

Full-wave Nonlinear Inverse Scattering for Acoustic and Electromagnetic Breast Imaging

by

Mark Spencer Haynes

A dissertation submitted in partial fulfillment
of the requirements for the degree of
Doctor of Philosophy
(Applied Physics)
in The University of Michigan
2012

Doctoral Committee:

Professor Mahta Moghaddam, Chair
Professor Paul Carson
Professor Jeffrey Fessler
Professor Kamal Sarabandi
Associate Research Scientist Leland Pierce

© Mark Spencer Haynes 2012
All Rights Reserved

To my Grandpa, Albert Maisel.

ACKNOWLEDGEMENTS

I would like to thank my faculty advisor and committee chair, Professor Mahta Moghaddam, for her years of support and encouragement.

I would like to thank the members of my committee: Professor Paul Carson, Professor Kamal Sarabandi, Professor Jeffrey Fessler, and Associate Research Scientist Leland Pierce, for their suggestions and critiques of this dissertation. I want to especially thank Professor Carson for his generous laboratory support throughout this work, as well as Dr. Pierce for invaluable conversations and discussions. I would also like to thank Doctor Marylin Roubidoux for instructing me in the field of radiology.

I would like to thank my many friends and colleagues in the Applied Physics Program, the Radiation Laboratory, the Basic Radiological Sciences Ultrasound Group, and the University community at large, for much collaboration, fun, and friendship over the years. Alphabetically: Sarah Barbrow, Edward Baskerville, Michael Benson, Karl Brakora, Meridith Brenner, Steven Clarkson, Nathan Crockett, Forest Doss, Xueyang Duan, William Fisher, Yuri Goykhman, Kevin Haworth, Jeffrey Herbsman, Fong Ming Hooi, Channing Huntington, Victor Lee, John Prensner, Sacha van der Spek, John Stang, Robert Willson, and Jane Witcomb.

I express my deepest gratitude to my close friends and family for their love and encouragement. I thank my brother Peter for always giving me perspective, my father for his unwavering enthusiasm, and, finally, my mother, to whom, as my father once said, I owe all my success.

TABLE OF CONTENTS

DEDICATION	ii
ACKNOWLEDGEMENTS	iii
LIST OF FIGURES	ix
LIST OF TABLES	xxiii
LIST OF APPENDICES	xxiv
ABSTRACT	xxv
CHAPTER	
I. Introduction	1
1.1 Motivation and Objectives	1
1.2 Previous Work	5
1.3 Thesis Overview	7
1.4 Dissertation Contributions	8
II. Acoustic Inverse Scattering Algorithm	10
2.1 Introduction	10
2.2 Theory and Formulation	12
2.2.1 Forward Model	12
2.2.2 Problem Specific Material Properties	13
2.3 Forward Solver	14
2.3.1 Neumann Series	14
2.3.2 Operator Norm for Three Contrasts	15
2.3.3 Computation of Series and Norm	17
2.4 Inverse Scattering Algorithm	18
2.4.1 Born Iterative Method	18
2.4.2 Cost Function	19
2.4.3 Conjugate Gradient Updates	23

2.4.4	Advantages of the Covariance-Based Cost Function	24
2.4.5	Strictly Positive Model Parameters	25
2.4.6	Comparison with the CSI Method	26
2.5	Results and Discussion	27
2.5.1	Series Solution Validation	27
2.5.2	Inverse Scattering Algorithm	29
2.6	Conclusion	38
III. Electromagnetic Inverse Scattering Algorithm		39
3.1	Introduction	39
3.2	Formulation	40
3.2.1	Volume Integral Equations	40
3.3	Born Iterative Method	42
3.3.1	Neumann Series for the Electromagnetic Forward Problem	42
3.3.2	Shanks Transformation	43
3.3.3	Cost Function	46
3.4	Numerical Examples	49
3.5	Conclusion	54
3.6	The Missing Link	56
IV. Antenna and Propagation Model for S-parameter Measurements		58
4.1	Introduction	58
4.2	Antenna Model	61
4.2.1	Electric Field Expansion	61
4.2.2	Antenna Model	62
4.2.3	Reciprocity Relations	63
4.3	Two Antenna Propagation Model	64
4.3.1	Two Fixed Antennas	64
4.3.2	Two Rotated Antennas	68
4.3.3	Required Number of Transmit Coefficients	70
4.3.4	Coordinate Origins	70
4.4	Scattering Objects	71
4.4.1	Single-Path Object Scattering	71
4.4.2	Multiple Scattering of Antennas and Objects	72
4.5	Determining Transmit Coefficients from Simulation	73
4.6	Experimental Validation	75
4.6.1	Determining a_o	78
4.6.2	Examples	78
4.6.3	Phasor Convention	82
4.6.4	Discussion of Errors	82
4.7	Conclusion	84

V. Vector Green’s Function for S-parameter Measurements of the Electromagnetic Volume Integral Equation	85
5.1 Introduction	85
5.2 Derivation	88
5.2.1 Volume Integral Equation	88
5.2.2 Antenna Model and Normalized Fields	88
5.2.3 Vector Green’s Function for S-parameters	90
5.2.4 Reciprocity Relation	96
5.2.5 Object-Centered Vector Green’s Function	98
5.2.6 Comparison with the Dyadic Green’s Function	101
5.2.7 Obtaining $\mathbf{g}(\mathbf{r})$	102
5.2.8 Generalization	103
5.3 Experimental Validation	105
5.3.1 Example 1	105
5.3.2 Example 2	107
5.3.3 Example 3	109
5.3.4 Example 4	113
5.3.5 Discussion of Errors	117
5.3.6 Summary of Experiments	119
5.4 Conclusion	119
VI. Free-space Electromagnetic Inverse Scattering Experiment	121
6.1 Introduction	121
6.2 Formulation with Source Characterization	123
6.2.1 Integral Equations for Characterized Sources and S-parameters	123
6.3 Born Iterative Method	125
6.3.1 Forward Solver	126
6.3.2 Cost Function	126
6.4 Experimental Setup	129
6.4.1 Antenna Characterization	130
6.4.2 Switching Matrix	132
6.4.3 VNA Calibration	133
6.4.4 Setup Diagnostics	134
6.4.5 Noise	134
6.5 Image Reconstructions	137
6.5.1 Discussion	147
6.6 Conclusion	149
VII. Microwave Breast Imaging Cavity Experiment	151
7.1 Introduction	151

7.2	VIEs and Characterization for Cavity Imaging	153
7.2.1	Integral Equations for Cavity S-parameter Measurements	153
7.2.2	Determining $\mathbf{e}_{inc}(\mathbf{r})$	156
7.2.3	Determining $\overline{\mathbf{G}}(\mathbf{r}, \mathbf{r}')$	157
7.2.4	Born Iterative Method for Cavities	159
7.3	Breast Imaging System Prototype	159
7.3.1	Liquid Coupling Medium	161
7.3.2	Antenna Design	162
7.3.3	System Parameters	162
7.3.4	Switching Matrix	163
7.3.5	VNA Calibration	163
7.4	Numerical Model	164
7.5	Image Reconstructions	168
7.5.1	Synthetic Data	168
7.5.2	Experimental Data	177
7.5.3	Discussion	181
7.6	Conclusion	183
VIII. Acoustic Inverse Scattering Experiment		184
8.1	Introduction	184
8.2	Multipole Propagation Model for Acoustics	186
8.2.1	Field Expansion and Translation Relations	186
8.2.2	Acoustic Source Scattering Matrix Formulation	187
8.2.3	Relation to Total Line Voltage	188
8.2.4	Propagation Model	189
8.3	Ultrasound Source Characterization	190
8.3.1	Hydrophone Characterization	191
8.3.2	Nonlinear Inversion of the Propagation Model	193
8.3.3	Conjugate Gradient Updates	196
8.3.4	Step length	197
8.3.5	Summary	201
8.4	Ultrasound Probe Characterization Experiment	202
8.4.1	Time Domain Data	204
8.4.2	Position Inversion Setup and Virtual Sources	206
8.4.3	Speed of Sound of Water	209
8.4.4	Position Inversion Results	210
8.4.5	Characterization Results	213
8.5	"Vector Green's" Formulation for Acoustics	218
8.5.1	Setup	218
8.5.2	Vector Green's Function analogue	220
8.5.3	Reciprocity Relation	221
8.6	Ultrasound Inverse Scattering Experiment	222
8.6.1	Rotator alignment	222

8.6.2	Image Reconstructions	225
8.7	Conclusion	235
IX.	Conclusion and Future Work	238
9.1	Conclusion	238
9.2	Future Research Directions	242
APPENDICES	246
A.1	Operator transpose for point receivers	247
B.1	Vector Wave Functions	250
B.1.1	Wave Function Conventions	250
B.1.2	Translation Addition Theorem	252
B.1.3	Rotation Addition Theorem	253
B.1.4	Computation of Addition Theorems	254
B.2	Reciprocity for Two Fixed Antennas	254
C.1	Special Cases of Vector Green's Function Integral	256
C.1.1	Far-Field	256
C.1.2	Born Approximation	258
C.1.3	Far-Field and Born Approximation	258
D.1	Cost Function and Step Length for a General Linear Problem	260
D.1.1	Cost Function	260
D.1.2	Step Length	261
D.2	Vector Green's function operator transpose	263
BIBLIOGRAPHY	265

LIST OF FIGURES

Figure

2.1	Magnitude of scattered field at receivers around 6λ cylinder with 5% contrast. Dashed: analytical; dotted: series solution.	27
2.2	Phase of scattered field at receivers around 6λ cylinder. Dashed: analytical; dotted: series solution. The phase in the backscatter direction begins to deteriorate.	28
2.3	Number of series terms needed for convergence vs. operator norm. The compressibility contrast of a 6λ cylinder was linearly stepped from 0 to 0.24, on a $10\lambda \times 10\lambda$ domain.	28
2.4	Source/receiver setup. $8\lambda \times 8\lambda$ domain.	29
2.5	a) Actual compressibility contrast. 2 cylinders each $2\lambda_{\min}$ in diameter. Peak contrast 0.2, lossless background, operator norm 0.31. b) Retrieved contrast with Born approximation. c) Retrieved contrast after 2 iterations. d) Retrieved contrast after 3 iterations.	31
2.6	Horizontal cut through lower cylinder. Solid: actual contrast; dashed: recovered contrast after 3 iterations.	31
2.7	a) Four sets of objects of 1, 4, 9, and 16 pixels equal to 90, 180, 270, and 360 micron widths. b) Compressibility contrast with 3 iterations.	32
2.8	a) Horizontal cut through third row of objects. b) Horizontal cut through fifth row of objects. Solid: actual contrast; dashed: recovered contrast after 4 iterations.	32
2.9	a) Compressibility and loss. Peak complex compressibility $0.2 + i0.02$ for both cylinders. b) Real part of compressibility contrast after 3 iterations. c) Imaginary part of compressibility contrast after 3 iterations	34

2.10	a) Horizontal cut through lower cylinder of real part of compressibility contrast. b) Horizontal cut through lower cylinder of imaginary part of compressibility contrast. Solid: actual contrast; dashed: recovered contrast after 3 iterations.	34
2.11	a) Compressibility and density. Peak compressive contrast of 0.2. Lossless background, inversion for compressibility only, with assumed relation $\delta\kappa = 2.4\delta\rho^{-1}$. b) Compressibility contrast after 3 iterations. c) Density contrast after 3 iterations.	35
2.12	a) Horizontal cut through lower cylinder of compressibility contrast. b) Horizontal cut through lower cylinder of density contrast. Solid: actual contrast; dashed: recovered contrast after 3 iterations. . . .	35
2.13	a) Compressibility only with background and object pixels each correlated. b) Compressibility contrast after 5 Born iterations.	36
2.14	Horizontal cut through lower cylinder. Solid: actual contrast; dashed: recovered contrast after 5 iterations.	36
2.15	Source/receiver setup. $50\lambda \times 50\lambda$ domain.	36
2.16	a) Domain is $50 \lambda_{\min} \times 50 \lambda_{\min}$. Compressibility only. Random distribution with two inclusions and peak contrast ± 0.08 . b) Compressibility contrast after 5 iterations.	37
2.17	Horizontal cut at $-6 \lambda_{\min}$. Solid: actual contrast; dashed: recovered contrast after 5 iterations. Low pass artifacts evident.	37
3.1	Linearly stepped relative permittivity of 1λ diameter sphere from 1 to 2.1	44
3.2	Scattered field solution for different terms the Neumann series and Neumann series with Shanks transformation of a 1λ sphere. Top row: Neumann series partial sums $\{10, 11, 12\}$. Bottom row: Neumann series partial sums with 3rd order Shanks transformation terms $\{4, 5, 6\}$	45
3.3	Transmit pulse, transmit spectrum and source configuration to test the electromagnetic inverse scattering algorithm.	50
3.4	Reconstructed object for Example 1 after 2 BIM iterations. Actual object shown at right.	51

3.5	Reconstructed object for Example 2 after 3 BIM iterations. Actual object shown at right.	51
3.6	Reconstructed object for Example 3 after 3 BIM iterations. Actual object shown at right.	52
3.7	Reconstructed object for Example 4 after 3 BIM iterations. Actual object shown at top.	52
3.8	Reconstructed object for Example 5 after 3 BIM iterations. Actual objects shown at right.	53
3.9	Reconstructed object for Example 6 after 3 BIM iterations. Actual objects shown at right.	54
3.10	Exploded view of reconstructed object for Example 7 after 3 BIM iterations. Actual objects shown at right.	55
3.11	Source geometry and reconstructed object for Example 8. Cylindrical arrangement of sources elongates the recovered object in the z-direction.	55
4.1	Antenna and transmission line setup. a_o and b_o are outgoing and incoming modes on the transmission line, respectively.	63
4.2	Two antenna setup in free space. The transmitting antenna is in frame i and the receiving antenna is in frame j	65
4.3	HFSS CAD model of probe-fed rectangular waveguide used to determine the transmit coefficients. The coordinate origin for the reference frame of the antenna is the center of the aperture. The de-embedded reference plane for the feeding transmission line is approximately half way up the extruding stalk to match the physical location of the VNA measurement reference plane.	76
4.4	Measured and simulated S_{11} for both waveguides. a) Magnitude of S_{11} . b) Phase of S_{11} . Dotted: HFSS simulation; Solid: waveguide 1 measured; Dashed: waveguide 2 measured.	77
4.5	Normalized magnitude of transmit coefficients, \mathbf{t}_a and \mathbf{t}_b , found using Eqn. (4.41) for the waveguide in Figure 4.3, with harmonics up to $l = 4$ at 5 GHz. The horizontal axis is the (l, m) index; the upper row is m , the lower row is l . Most of the field information is captured in the first few l	77

4.6	Example of anechoic chamber measurements of S_{21} . Waveguide apertures in photo are separated by 0.55 m and rotated 30 degrees.	79
4.7	Measured and predicted S_{21} for two distances. a) Magnitude of S_{21} . b) Phase of S_{21} . Waveguides are separated by $d_1 = 0.55$ m and $d_2 = 0.73$ m facing each other with no rotation. Solid line and circles: measured and predicted S_{21} , respectively, at d_1 . Dashed line and squares: measured and predicted S_{21} , respectively, at d_2 . Phase for d_2 is shifted by 360 degrees for display.	79
4.8	Measured and predicted S_{21} for two rotations. a) Magnitude of S_{21} . b) Phase of S_{21} . Waveguides are separated by 0.55 m and rotated about the z-axis of their coordinate systems by $a_1 = 15$ degrees, and $a_2 = 30$ degrees (also shown in Figure 4.6). Solid line and circles: measured and predicted S_{21} , respectively, for a_1 . Dashed line and squares: measured and predicted S_{21} , respectively, for a_2 . Phase for a_2 is shifted by 360 degrees for display.	80
4.9	Example of anechoic chamber measurements of S_{21} for a scatterer. The scatterer is a 2 inch diameter conducting sphere. Waveguide apertures in photo are separated by 0.85 m and rotated 40 degrees. The sphere is positioned near the boresights of the waveguide apertures.	82
4.10	Measured and predicted S_{21} of the incident, total and scattered field for the setup in Figure 4.9. a) Magnitude of S_{21} . b) Phase of S_{21} . Solid line and circles: measured and predicted incident field, respectively. Dashed line and triangles: measured and predicted total field, respectively. Dash-dot line and squares: measured and predicted scattered field. Phases for the total and scattered field are shifted by 360 and 720 degrees, respectively, for display.	83
5.1	Antenna and transmission line setup. The quantities a_o and b_o are outgoing and incoming voltages on the transmission line, respectively. The dotted line represents the nearest point of nonzero contrast and the maximum radius for the antenna multipole expansion.	93
5.2	Network model of two antennas and a scattering object. S-parameters are measured between the reference planes on the antenna transmission lines.	95
5.3	Antenna and transmission line setup for an object-centered scattering scenario. The quantities a_o and b_o are outgoing and incoming voltages on the transmission line, respectively. The dotted line represents the furthest point of non-zero contrast.	98

5.4	Setup for Example 1. The two waveguides are rotated 120 degrees around the target at distances of 16 inches each. The object consists of two acrylic spheres which are separated by approximately 5 cm.	107
5.5	Discretized object domain for Example 1. The two spheres have a diameter of 2.54 cm, a relative permittivity of 2.5 in a background of free-space, and are separated by approximately 5 cm. This discretization is used for both the VIE and BCGFFT.	108
5.6	Measured and predicted S_{21} of the scattered field for a pair of spheres and the setup in Figure 5.4. a) Magnitude. b) Phase. The results for two receiver angles are shown. Solid line and dots: measured and predicted S_{21} for a receiver at 180 degrees. Dashed line and triangles: S_{21} for a receiver at 120 degrees. The second set of phases is shifted by 360 degrees for display.	108
5.7	Setup for Example 2. The waveguide and acrylic sphere are supported by Styrofoam in an anechoic chamber. The sphere is held in a Styrofoam mount.	109
5.8	Close-up picture of one waveguide and the acrylic spheres used in Examples 1 and 2. The spheres are held in Styrofoam. The spheres in the pair are separated by approximately 5 cm.	110
5.9	Measured and predicted S_{11} of the scatter field for a single sphere and the setup in Figure 5.7. a) Magnitude. b) Phase.	110
5.10	HFSS CAD model for Example 3. Two different sized apertures are embedded in PEC walls. The object domain has four dielectric objects and is meshed with a sparse, unassigned grid to constrain the HFSS adaptive meshing.	111
5.11	Simulated and predicted S_{21} and S_{12} of the scattered field for the simulation in Figure 5.10. a) Magnitude. b) Phase. Solid line: S_{21} and S_{12} computed by HFSS, which are identical. Circles: S_{21} predicted by the VIE. Dots: S_{12} predicted by the VIE. While HFSS computes identical values for S_{21} and S_{12} , the VIE results in some asymmetries due to numerical error.	112
5.12	Simulated and predicted S_{11} and S_{22} of the scatter field for the simulation in Figure 5.10. a) Magnitude. b) Phase. Solid line and circles: simulated and predicted S_{11} . Dashed line and dots: simulated and predicted S_{22} . Phase of S_{22} is shifted by 360 degrees for display.	113

5.13	Dielectrically loaded waveguide for Example 4. The empty waveguide is shown at left, and the two nylon blocks making up the load and object domains are shown at right. The relative positions of the blocks and probes in the waveguide are outlined underneath. . . .	114
5.14	HFSS CAD model of the dielectrically loaded waveguide in Figure 5.13. The object domains are meshed with an unassigned sheet grid to constrain the adaptive meshing of HFSS. The waveguide is also enclosed in a large radiation box (not depicted). The coaxial lines extend to the radiation boundary and are de-embedded to the reference planes used by the VNA for the physical waveguide.	115
5.15	Measured, simulated, and predicted S_{21} of the scattered field for the setup in Figures 5.13 and 5.14. a) Magnitude. b) Phase. Solid line: measured S_{21} . Dashed line: S_{21} computed by HFSS. Dots: S_{21} predicted by the VIE and vector Green's function. Similar results were found for S_{12}	116
5.16	Measured, simulated, and predicted S_{11} and S_{22} of the scattered field for the setup in Figures 5.13 and 5.14. a) Magnitude. b) Phase. Phases of S_{22} are shifted by 360 degrees for display.	116
5.17	Simulated and predicted S_{21} and S_{12} of the scattered field for the simulation in Figure 5.10 with twice the spatial sampling and stricter HFSS convergence criteria than used in Example 3. a) Magnitude. b) Phase. Solid line: S_{21} and S_{12} computed by HFSS, which are identical. Circles: S_{21} predicted by the VIE. Dots: S_{12} predicted by the VIE. This shows that numerical errors can be controlled.	118
6.1	Network model of two antennas and a scattering object. S-parameters are measured between the reference planes on the antenna transmission lines.	125
6.2	Experimental setup in an anechoic chamber. One transmitter and 14 receivers are mounted on a nylon octagon which is supported on Styrofoam mounts. The objects are turned with a rotator (not visible). The transmitter and receives are connected to the VNA, where the receivers are selected with a SP16T solid-state switch.	129
6.3	a) HFSS CAD model of E-patch antenna in the vertical polarization. The patch is enclosed in a large radiation box (not shown). The transmission line was de-embedded to match the reference plane of the VNA in experiment. b) Actual antenna mounted in the setup for the horizontal polarization.	130

6.4	Magnitude and phase of simulated and measured S_{11} for the E-patch antennas. a) Magnitude. b) Phase. The solid line is simulated S_{11} from HFSS. The dashed and dotted lines represent the upper and lower bounds, respectively, of the variation of measured S_{11} across all 15 antennas before being used in the setup.	131
6.5	Normalized magnitude of transmit coefficients, $t_{(a)lm}$ and $t_{(b)lm}$, for the E-patch antenna in Figure 6.3, with harmonics up to $l = 3$ at 2.5 GHz. The horizontal axis is the (l,m) index; the upper row is m , the lower row is l . Most of the field information is captured in the first few l	132
6.6	Schematic of ideal antenna reference frame positions and rotations for the setup pictured in Figure 7.2. The transmitter frame is at the lower right. The dots represent the mounting holes on the nylon beams, which are separated by 1 inch.	133
6.7	Setup to test the antenna model by measuring the scattered field from a conducting sphere. The sphere has a diameter of 2 inches, and was centered in the setup.	135
6.8	Magnitude and phase of measured and predicted S_{21} of the incident, total and scattered fields of the conducting sphere in Figure 6.7 between the transmitter and receiver number 11. a) Magnitude. b) Phase. Solid line and circles: measured and predicted incident field S_{21} . Dashed line and triangles: measured and predicted total field S_{21} . Dash-dot line and squares: measured and predicted scattered field S_{21} . The incident and total field S_{21} appear nearly identical on these scales.	135
6.9	Histogram of the real part of S_{21} for the incident field of receiver 8 (across from the transmitter) at 2.5 GHz. The solid line is a Gaussian distribution with the same mean and variance of the data. The noise is equal to approximately -91 dB. Similar results are obtained for all measurements.	136
6.10	Reconstructed relative permittivity at 4 iterations of the BIM after 12 conjugate gradient iterations each using VV polarization data. a) Photo of Delrin rods. b) BIM iteration 1, i.e. Born approximation. c) Iteration 7. d) Iteration 12. The wavelength is that in a material of $\epsilon_r = 3$	140
6.11	a) Normalized residual for the conjugate gradient iterations for each successive BIM iteration. b) Vertical cut of the actual and reconstructed relative permittivity through the center of the two objects.	140

6.12	a) Reconstructed image of two Delrin rods using HH polarization data. b) Vertical cut of the actual and reconstructed relative permittivity through the center of the two objects.	141
6.13	a) Photo of Delrin block. b) Reconstructed relative permittivity after 12 BIM iterations. An outline of the actual block is superimposed on the image. c) Normalized residual for all iterations. d) Horizontal cut through the middle of the image for the actual and reconstructed object.	141
6.14	a) and c) Photo of PVC rings. b) and d) Reconstructed relative permittivity after 12 BIM iterations. An outline of the actual rings are superimposed on the images.	142
6.15	a) Photo of ring and rod combination. b) Reconstructed relative permittivity after 12 BIM iterations. An outline of the inner and outer diameter of the ring as well as the PVC rod is superimposed on the image.	143
6.16	a) and c) Photo of the metal rods at separates of 4cm and 6cm, respectively. b) and d) Reconstructed absolute conductivity in Siemens per meter after 12 BIM iterations.	144
6.17	a) Photo of ring and rod combination in the setup. b) Reconstructed relative permittivity after 12 BIM iterations. The algorithm failed to recover this object.	145
6.18	a) Photo of Delrin rod and block b) Reconstructed relative permittivity after 12 iterations. An outline of the actual objects is shown. The algorithm could not recover the contrasts of the objects.	146
6.19	a) Objects used to generate synthetic scattered field data. b) Reconstruction using synthetic data.	146
6.20	Image reconstructions from synthetic and experimental data using covariance operators to correlate pixels of homogeneous regions. a) Reconstruction using synthetic data. b) Reconstruction using experimental data.	147
7.1	Microwave network model of cavity and scattering object. S-parameters are measured between the reference planes on the transmission lines.	156

7.2	Breast imaging system prototype. The imaging cavity is connected to the VNA through a solid-state switching matrix. A rotator is mounted above and turns suspended objects for multiple transmitter views.	160
7.3	Imaging cavity. Twelve panels with three bow-tie antennas each are solder together and to a conducting plate.	160
7.4	HFSS CAD model of the imaging cavity. Twelve panels contain three bow-tie antennas each. The bottom of the cavity is PEC, it is filled with the coupling fluid up to the visible line, and the top surface radiates to air.	165
7.5	Measured and simulated magnitude and phase of incident S_{21} between each of the three transmitting antennas and all receivers. Solid: measured. Dots: HFSS. The groupings from left to right are the eleven receivers of each level (middle, top, bottom), repeated for the three transmitters (middle, top, bottom), plotted counterclockwise when viewed from above for a given receiver level. For example, data 38:48 are middle receivers and top transmitter. The magnitude and phase agree best for transmitters and receivers on the same level (i.e. data 1:11, 50:60, and 98:108).	166
7.6	HFSS CAD model of the imaging cavity with mesh of unassigned sheets to constrain the adapting meshing of HFSS for field interpolation. Sheets are spaced every 5 mm in each direction.	167
7.7	HFSS convergence with number of tetrahedra for each adaptive meshing step.	167
7.8	Cross cuts through the center of the cavity of the z-component of the incident electric field due to the middle transmitter. The scale is $20\log_{10}(Re\{E_{z,inc}\})$ of the unnormalized field. a) horizontal x-y, b) vertical x-z, c) vertical y-z planes.	169
7.9	HFSS model of a simple sphere use to generate synthetic scattered field S-parameters.	170
7.10	Reconstructions of a single sphere $(\epsilon_r, \sigma) = (40, 1)$ located at $(x,y,z) = (0,0,2\text{cm})$ of Example 1. Left and right columns are relative permittivity and conductivity, respectively. Top row is the Born approximation. Bottom row is BIM iteration 4. Here, iterations help retrieve the relative permittivity in c), but the Born approximation yielded better conductivity in b).	171

7.11	Reconstructions of a single sphere $(\epsilon_r, \sigma) = (40, 0)$ located at $(x,y,z) = (0,0,2\text{cm})$ of Example 1. Born iterations helped retrieve the relative permittivity in c), and are essential in recovering the conductivity in d).	172
7.12	Reconstructions of a single sphere $(\epsilon_r, \sigma) = (10, 1)$ located at $(x,y,z) = (0,0,2\text{cm})$ of Example 1. Born iterations helped the recovery of the low permittivity in c), but at the expense of the correct conductivity value which was better in with the Born approximation in b). . . .	173
7.13	Reconstructions of a single sphere $(\epsilon_r, \sigma) = (40, 0)$ located at $(x,y,z) = (0,0,2\text{cm})$ of Example 1. Born iterations helped bring out the proper conductivity value in d).	174
7.14	HFSS CAD numerical breast phantom of Example 2. The inclusion is 2 cm in diameter with relative permittivity and conductivity contrasts of 2:1. The skin layer is 2 mm thick.	174
7.15	Reconstructions of the HFSS numerical breast phantom in Example 2 after three iterations. Left and right columns are relative permittivity and conductivity, respectively. Rows top down are cuts at $x = 0$ cm, $y = 0$ cm, and $z = 2.5$ cm. The relative permittivity of the skin and inclusion are well recovered. The conductivity of the inclusion is recovered, but both images contain many artifacts.	175
7.16	HFSS CAD numerical breast phantom with skin layer, fat layer, glandular tissue and chest wall of Example 3. The inclusion is 1 cm in diameter with relative permittivity and conductivity contrasts of 2:1.	176
7.17	Reconstructions of the HFSS numerical breast phantom which includes the chest wall of Example 3. Left and right figures are relative permittivity and conductivity, respectively. The object could not be reconstructed.	176
7.18	Image reconstruction sensitivity to background permittivity. Left and right columns are relative permittivity and conductivity, respectively. Data was generated in background of $(21, 0.475)$. Reconstructions with background relative permittivities of $\{20, 20.5, 21, 21.5, 22\}$ for rows 1 through 5 respectively. Recovered contrasts of the sphere oscillate about the background.	178
7.19	Test objects and coupling fluid for Experiment 1. a) Single suspended acrylic sphere. b) Two acrylic spheres. c) Cavity filled with the coupling medium. Objects are suspended and rotated from the nylon platform.	179

7.20	Reconstructions of the single acrylic sphere of Experiment 1 shown in Figure 7.19(a). Left: relative permittivity. Right: conductivity. The permittivity is recovered well but the shape in the conductivity is not	180
7.21	Reconstructions of the two acrylic spheres of Experiment 1 shown in Figure 7.19(b). Left: relative permittivity. Right: conductivity. The permittivity is again recovered well but the shape in the conductivity is not.	180
7.22	Second cavity with antennas designed to operate at 915 MHz of Experiment 2. Three acrylic sphere are suspended (one visible). Cavity is filled with fluid for imaging.	181
7.23	Reconstruction of the relative permittivity and conductivity of three acrylic spheres using a cavity operating at 915 MHz from Experiment 2. The two spheres in plane are well recovered, and the third detected at the upper left of the image.	181
8.1	Photo of an early hydrophone characterization experiment. A transducer is gimbaled and mounted on a translator. The focus of the transducer is positioned at the center of rotation of the rotational stage. A hydrophone is also gimbaled and positioned with a 3-axis micropositioner.	192
8.2	Photo of setup for nonlinear source characterization and inverse scattering experiment.	203
8.3	Top view of transducer positions. Mounting holes are spaced 1 cm apart.	203
8.4	Typical time domain data for a water shot. The center element of one probe was fired and the signal was received by all the elements of the opposite probe. The color scale is digitized voltage.	204
8.5	Close up of the traces in Figure 8.4.	205
8.6	Time trace of the center receive element from the data in Figure 8.4.	205
8.7	Envelope of time trace in Figure 8.6. The time of flight is determined by the time of the envelope maximum less half the pulse width. . .	207

8.8	Actual and virtual sources and receivers. The signal fires at t_0 , emanates from the transducer at t_1 , arrives at the receiving transducer at t_2 , and is recorded at t_3 . The virtual source and receiver lump any delays into a spatial offset.	208
8.9	Actual and virtual sources and receivers. The signal fires at t_0 , emanates from the transducer at t_1 , arrives at the receiving transducer at t_2 , and is recorded at t_3 . The virtual source and receiver lump any delays into a spatial offset.	209
8.10	Photo of setup to determine the speed of sound of the water bath. From left to right: digital readout thermocouple, oscilloscope, pulser/receiver, micropositioner with transducer and reflection plate.	210
8.11	Photo of micropositioner with transducer to measure the speed of sound of the water bath.	211
8.12	Water speed of sound estimation from micropostioner and reflection measurements. Slope of the line is the speed of sound.	211
8.13	Water speed of sound with temperature from literature.	212
8.14	Split plot of the probe element positions. Bottom line and filled circles are the element locations of probe 1 (reference). Open circles are the element locations of probe 2 for all seven positions based on the position inversion values of Table 8.2. The y-axis is compressed.	213
8.15	Magnitude (a) and real part (b) of the incident field at 3.75 MHz for all transmit/receive pairs. Scale is magnitude and real part of digitized voltage.	214
8.16	Data of Figure 8.15 smoothed along the anti-diagonals.	215
8.17	Phase of incident field at 3.75 MHz. Anti-diagonal shows that the probes are not quite parallel and rotated about the z-axis.	215
8.18	Normalized residual as a function of conjugate gradient iteration number.	216
8.19	Normalized transmit coefficients. a) real part, b) imaginary part. Horizontal axis is the (l, m) harmonic index.	217

8.20	Magnitude and phase of measured and predicted data for a sampling of transmit and receive elements. a) Magnitude, b) phase. The apparent groups in the magnitude plot are receivers for a given transmit element.	217
8.21	Normalized magnitude of acoustic field in the transducer plane computed with the solved transmit coefficients.	218
8.22	Photo of 6-axis positioning arm used to place and rotate objects. . .	223
8.23	Close-up of metal rod. Rod is translated and rotated to	224
8.24	Diagram of transmissions and reflections used to align the rotator. .	224
8.25	Assorted targets of worm rubber, brass rods, and fishline to image. .	225
8.26	Diagram of sources and receivers used in the inverse scattering algorithm. The box outlines the imaging domain.	225
8.27	Photo of worm rubber target.	226
8.28	Magnitude of the scattered field for select rotations of the object in Figure 8.27.	227
8.29	Recovered compressibility and absorption contrast for the object in Figure 8.27. a) Compressibility. b) Absorption.	228
8.30	Photo of two metal filaments.	229
8.31	Recovered compressibility and absorption contrast for the object in Figure 8.30. a) Compressibility. b) Absorption.	229
8.32	Photo of two fish line filaments.	230
8.33	Recovered compressibility and absorption contrast for the object in Figure 8.32. a) Compressibility. b) Absorption.	231
8.34	Photo of worm rubber crescent.	231
8.35	Recovered compressibility and absorption contrast for the object in Figure 8.34. a) Compressibility. b) Absorption.	232
8.36	Photo of metal rod and worm rubber combination.	233

8.37	Recovered compressibility and absorption contrast for the object in Figure 8.36. a) Compressibility. b) Absorption.	233
8.38	Photo of worm rubber rectangle.	234
8.39	Recovered compressibility and absorption contrast for the object in Figure 8.38. a) Compressibility. b) Absorption.	235

LIST OF TABLES

Table

8.1	Comparison between ultrasound and microwave spatial scales	185
8.2	Position inversion results for seven transducer positions	213

LIST OF APPENDICES

Appendix

A.	Operator Transpose for Electromagnetic Inversion	247
B.	Vector Wave Functions	250
C.	Special Cases of Vector Green's Function VIE	256
D.	Cost Function of Linear Inverse Problems	260

ABSTRACT

Full-wave Nonlinear Inverse Scattering for Acoustic and Electromagnetic Breast Imaging

by

Mark S Haynes

Chair: Mahta Moghaddam

Acoustic and electromagnetic full-wave nonlinear inverse scattering techniques are explored in both theory and experiment with the ultimate aim of noninvasively mapping the material properties of the breast. There is evidence that benign and malignant breast tissue have different acoustic and electrical properties and imaging these properties directly could provide higher quality images with better diagnostic certainty. In this dissertation, acoustic and electromagnetic inverse scattering algorithms are first developed and validated in simulation. The forward solvers and optimization cost functions are modified from traditional forms in order to handle the large or lossy imaging scenes present in ultrasonic and microwave breast imaging. An antenna model is then presented, modified, and experimentally validated for microwave S-parameter measurements. Using the antenna model, a new electromagnetic volume integral equation is derived in order to link the material properties of the inverse scattering algorithms to microwave S-parameters measurements allowing direct comparison of model predictions and measurements in the imaging algorithms.

This volume integral equation is validated with several experiments and used as the basis of a free-space inverse scattering experiment, where images of the dielectric properties of plastic objects are formed without the use of calibration targets. These efforts are used as the foundation of a solution and formulation for the numerical characterization of a microwave near-field cavity-based breast imaging system. The system is constructed and imaging results of simple targets are given. Finally, the same techniques are used to explore a new self-characterization method for commercial ultrasound probes. The method is used to calibrate an ultrasound inverse scattering experiment and imaging results of simple targets are presented. This work has demonstrated the feasibility of quantitative microwave inverse scattering by way of a self-consistent characterization formalism, and has made headway in the same area for ultrasound.

CHAPTER I

Introduction

1.1 Motivation and Objectives

The modern imaging standard for breast cancer screening is mammography with ultrasound follow-up. A mammogram is the 2D projection of X-ray absorption of breast tissue. Any suspicious lesions detected by radiologists on a mammogram are followed up using an ultrasound hand probe. After analyzing the ultrasound image, a BiRads rating is assigned to the lesion assessing the certainty of malignancy or not, [1], after which recommendations are made for either biopsy, 6-month follow-up, or 12-month standard exam. Biopsy results are returned with their pathology after about a week, and further recommendations are made if necessary. The images for all positive cases and some negative cases are later reviewed by radiologists concurrent with the pathology report.

Between mammography and ultrasound, many lesions can be detected and diagnosed. Even still, most breast biopsies are benign. This is due in part from imaging uncertainties, the relatively low risk of biopsy, and the low tolerance, generally, for false negatives (i.e. lesions diagnosed as benign which were actually malignant), which all taken together lead to conservative care practices. As reported in [2], the sensitivity (ability to predict positive results, reducing false negatives) and specificity (ability to predict negative results, reducing false positives) of mammography alone

is about 70% and 75%, respectively. For ultrasound alone, they are about 80% and 35%, respectively. Breast MRI has recently been recommended for high-risk patients, [3], but the images are expensive and have a high false positive rate.

X-ray mammography has many benefits. It has the best resolution of any modality available and provides full coverage of the breast. It is also a relatively low-energy, low-dose X-ray modality as compared to X-ray CT or chest X-rays, because it only needs to image soft tissue. Some draw backs are that a mammogram is a 2D projection of a 3D object and that the variable breast properties throughout the population require highly trained radiologists to interpret the images. Also, X-ray radiation is ionizing, which is known to be harmful, and it is desirable to limit exposure as much as possible.

Ultrasound imaging also has many benefits. It is so far know to be safe, it is inexpensive, fast, has millimeter resolution or better, and is portable. However, images are only 2D slices in depth, they cannot be formed through bone or air, and are technician dependent. From a wave imaging stand point, the image quality is quite poor. Images are plagued with artifacts such as speckle, reverberations, lensing, ghost images, and shadowing. Highly trained radiologists are again required to interpret the images and artifacts are often used for diagnosis.

Mammographic and ultrasonic images are both anatomical in nature, meaning they show primarily tissue structure. Tissue function, such as malignancy, is inferred from shape, texture, and context, [4]. For example, shapes such as spickulations, spheres, or microlobulations indicate malignancy, while almond shaped lesions or those with smooth margins indicate benign masses. Cysts show up on ultrasound as homogeneous black regions (no sound reflected). Artifacts in the ultrasound images often aid the diagnosis of certain lesions, such as reverberations at cyst boundaries or shadowing which is often a sign of malignancy due to high attenuation.

The speed with which ultrasound images are formed is due in part because algo-

rithms are built on only the kinematic properties of waves. Ultrasound algorithms assume fixed speed of sound, ray approximations, and no diffraction, refraction or multiple scattering [5]. Ultrasound systems and algorithms essentially focus acoustic energy through the tissue and listen, in a way, for reflections due to tissue with different material properties than water. Ultrasound images are formed with a technique called dynamic receiver focusing. On transmit, in hardware, the signals of every transducer element on the probe (up to 128) are phased to focus the acoustic radiation to several coarse points at depth. In software, the received echoes are phased in order to focus at every pixel in the scene. The echoes are summed, and the result displayed as pixel intensity. The brightness of the pixels represents a measure of reflectivity of the tissue, or the degree to which the tissue properties differ from the background, but, due to the many assumptions, one can only make qualitative statements from these images about the actual material properties of the tissue.

This is just a small picture of breast imaging today, and, based on it, there are several areas of breast imaging we can look to improve. First, any modality avoiding the use of ionizing X-ray radiation is worth investigating, especially screening modalities to which large portions of the population are exposed. Second, the quality of ultrasound images might be improved by reconsidering the physics missing in those algorithms. Last, it is also worth investigating any type of imaging that provides additional quantitative diagnostic information aiding the task of diagnosis to better assess malignancy.

A candidate technology to improve breast imaging then is wave-based inverse scattering. Inverse scattering has a long history in oil exploration, acoustics, and electromagnetics. It is centered around the idea that, by using the complete physical description of wave phenomena, one can remotely and noninvasively map the actual material properties of objects under investigation. The methods apply equally to ultrasound and microwave imaging.

The real motivation for using inverse scattering methods is evidence that benign and malignant breast tissue have quantitatively different material properties, and that imaging these properties directly could provide higher quality images with better diagnostic certainty. In acoustics we are concerned with tissue speed of sound (i.e. compressibility and density) and absorption; in microwave we are concerned with relative permittivity and conductivity. The quantitative material differences of breast tissue are well known in acoustics; malignant tissue has higher speed of sound and more attenuation than surrounding healthy tissue. In microwave, evidence that the relative permittivity and conductivity of benign and malignant breast tissue differ is not as strong, but is still an area of investigation. Furthermore, microwave radiation is known to be non-ionizing. Also, quantitative images formed with inverse scattering techniques do not depend on the operator. While inverse scattering images have their own artifacts, they do not suffer from speckle or other artifacts found in traditional beamforming.

For all the possible benefits, inverse scattering is not without its own challenges. First of all, images must be formed using non-linear optimization techniques and the complete description of wave propagation. This is because probing waves must travel through all the intervening tissue to sense and return, and the optimization routine must unravel the effects of tissue from one area with those of another. This is computationally intensive. Also, because the received fields are necessarily measured outside the object, the inverse scattering problem is mathematically and inherently ill-posed and non-unique. The simultaneous imaging of more than one material property creates further ambiguity. On top of these, inverse scattering systems require very carefully calibration and source characterization, because they use the full description of waves. Addressing these issues in order to bring inverse scattering methods to a point where they can be clinically and commercially tested continues to be an active area of research. Addressing some of these challenges dominates much of the subject

of this dissertation.

At the outset of this work, the abstract goal was to use microwave and ultrasound inverse scattering methods to create quantitative maps of the material properties of breast tissue. After some work understanding and improving theoretical acoustic and electromagnetic inverse scattering algorithms, it was clear that in order to perform any type of experiment, several unanswered questions about calibration needed to be addressed. As a result, the bulk of this dissertation is concerned with the calibration and characterization of microwave and ultrasound inverse scattering imaging systems in the context of breast imaging. For the microwave problem, we systematically progress from the imaging algorithms, antenna model, propagation model, scattered field volume integral equation, and inverse scattering algorithm to eventually arrive at a solution and formulation for the numerical characterization of a near-field cavity-based breast imaging system. For the ultrasound problem, we apply some of the same techniques to explore a new area of self-characterization for commercial ultrasound probes.

While the work described in this dissertation never approached clinical use, much progress was made in understanding the next steps required for developing clinically viable inverse scattering imaging systems and the last chapter lists several areas for future work.

1.2 Previous Work

The application of inverse scattering to ultrasound and electromagnetic breast imaging has gained popularity because the acoustic or electrical contrasts of benign and malignant lesions have been reported to be different. For ultrasound, malignant lesions are known to have increased sound speed and attenuation compared to the background tissue [6, 7]. In microwave, there has been evidence that the dielectric properties differ between benign and malignant lesions [8, 9], though this remains an

active area of investigation [10, 11], because the microwave properties of breast have never been measured in vivo.

Inverse scattering methods that have been applied to acoustic breast imaging include kinematic backprojection [12], which yield images of wave speed and attenuation, first order approximations such as diffraction tomography [13, 14] based on the Born-approximation, and full-wave inverse scattering [15].

Only a few clinical ultrasound breast imaging systems exist which use inverse scattering algorithms. In ultrasound, the system described in [16, 15] uses ultrasound CT in conjunction with a gradient based full-wave optimization, but images of acoustic loss display artifacts near the skin/background interface. Several diffraction tomography systems have been tested in the last decades, [13, 17, 14, 12, 18], but images commonly suffer ringing artifacts. In [19, 20], several imaging algorithms have been tested on an experimental system to study the trade off between computation effort and image quality.

There has been substantial work done in developing microwave breast imaging algorithms in simulation. Time domain beamforming algorithms have received much attention, [21, 22, 23, 24, 25, 26]. These are usually based on shift-and-sum methods to focus volumetrically through inhomogeneous media. Full-wave, iterative nonlinear inverse scattering methods have been studied by several different groups, [27, 28, 29, 30, 31]. Other inversion methods based on shape, level-sets, genetic algorithms, priors, and global optimization have also been investigated in an effort to improve the performance of the inverse scattering problem in the context of breast imaging, [32, 33, 34, 35, 36].

A few microwave experimental and clinical systems exist. Some non-clinical inverse scattering experiments for breast imaging and biomedical applications have been built and tested, [37, 38, 39, 40]. A clinical system using gradient-based optimization has been studied in some depth [41]. Whole breast images are formed by splicing

2D slice approximations, but image quality is poor. Another clinical system, [42], is based on beamforming and radar backscatter images, but has not yet shown successful clinical results in discriminating benign and malignant tissue.

1.3 Thesis Overview

This dissertation contains nine chapters, including this one. Chapters II and III explain the acoustic and electromagnetic forward models and inverse scattering algorithms. For both the acoustic and electromagnetic problem, we use is the Born Iterative Method inverse scattering algorithm. We modify this algorithm from its traditional implementations with an eye toward experiment. We do this using a multi-variate covariance-based cost function which allows us to 1) minimize the functional with conjugate gradients avoiding the need to build and invert a large matrix, and 2) use the Gaussian interpretation of the least-squares problem to give us physically meaningful regularization, eliminating the need for arbitrary tuning parameters. The derivation of these algorithms is validated in simulation. Chapter IV describes the antenna model which forms the basis of our calibration method. We use it to derive an S-parameter based antenna and propagation model and show how we use simulation to obtain the antenna model parameters. Chapter V presents our use the antenna model to solve one of the outstanding problems of microwave experimental inverse scattering by developing a formalism to directly link the material properties of the object we want to image to the scattered field quantities we measure. We valid this formalism with several experiments. Chapter VI describes a microwave free-space inverse scattering experiment built to test the integration of the inverse scattering algorithm and the calibration formalism. We show how to make the algorithm, antenna characterization, and experiment consistent. The experiment demonstrates our ability to form images of dielectric constant without the use of calibration targets. In Chapter VII we combine all of these elements to characterize a cavity-

based microwave breast imaging system prototype. We outline the system, study the performance of the characterization in simulation, and present imaging examples from both simulation and experiment. In Chapter VIII we apply the findings of the microwave problem to the task of characterizing an acoustic inverse scattering experiment. We derive an analogous propagation model and calibration formalism. A new self-characterization technique is derived and tested which is based on the nonlinear inversion of the propagation model. Images of test objects are presented along with a discussion of the limitations of the setup. Finally, Chapter IX, summarizes and concludes the dissertation and gives several areas of future work.

1.4 Dissertation Contributions

Specific contributions of this dissertation include:

1. Chapter 2: Acoustic Born Iterative Method (BIM) with covariance-based cost function, conjugate gradient minimization, and Neumann series forward solver.
2. Chapter 3: Electromagnetic BIM with covariance-based cost function, conjugate gradient minimization, and Neumann series forward solver with Shanks transformation speed-up.
3. Chapter 4: S-parameter based antenna and propagation model with numerical characterization and experimental T-matrix scattering.
4. Chapter 5: Vector Green's function formulation for microwave S-parameter measurements of the electromagnetic scattered field volume integral equation.
5. Chapter 6: Experimental demonstration of BIM and vector Green's function. Showed image formation is possible without calibration targets.
6. Chapter 7: Numerically characterized breast imaging system prototype.

7. Chapter 8: Experimental test of Acoustic BIM, acoustic vector Green's function analogue, and ultrasound probe self-characterization based on the nonlinear inversion of an acoustic propagation model.

CHAPTER II

Acoustic Inverse Scattering Algorithm

2.1 Introduction

In breast ultrasound, it is well known that the speed of sound variation of breast tissue is $\pm 6\%$ of water [43]. This property has enabled for decades imaging by real-time volumetric beamforming. While ultrasound is an indispensable tool in medicine, the image resolution and quality of beamformed images are fundamentally limited by the assumptions inherent in the image formation: fixed speed of sound, ray approximation, and no multiple scattering [5]. Images are qualitative measures of backscatter, with artifacts such as speckle, shadowing, reverberations, and ghost images. Similar methods have been simulated in electromagnetics for the same application with similar effects [21, 22].

Generally, the inverse scattering problem can be classified as a constrained nonlinear optimization. Numerous techniques exist for the solutions in both acoustics and electromagnetics [44, 45, 46, 47, 27, 48, 49, 50]; most are iterative, gradient-based approaches because global, nonlinear optimization techniques, which require millions of forward solver evaluations, are not practical given the large number of unknowns.

The central contribution of this chapter is the unique selection, modification, and integration of components of the inversion algorithm to make large, full-wave quantitative inverse scattering feasible for ultrasound breast imaging. The choice of

forward solver, inversion method, and cost function were specifically motivated by the imaging domain size and known ranges of object contrasts. We combine the familiar concepts of the Born Iterative Method (BIM) and an efficient semi-analytical forward solver, with a covariance-based cost function, to tackle the specific problem of large, low-contrast acoustic inverse scattering.

Because soft tissue is weakly scattering in ultrasound, Born iterations are an appropriate inverse scattering method. The BIM has been shown to retrieve small objects with contrasts up to 3 times the background [44, 51]. The Distorted Born Iterative Method (DBIM) can retrieve objects with even higher contrasts [52, 51] and has been demonstrated experimentally for acoustics [45], but requires additional computation. The Born approximation alone is expected to break down for large objects, but an area not previously investigated is the applicability of Born iterations to domains of tens of wavelengths or larger.

We use the Neumann series solution for the forward solver [53] and extend it to three object contrasts. This solution is an $O(N \log N)$, volumetric, frequency domain technique that takes advantage of low contrast media to expand the field solution in a power series.

The inverse scattering problem is typically cast as a multivariate optimization for the image, often reducing to the problem of solving a series of ill-posed, linear systems. This system must be regularized in order to retrieve physically meaningful images. The choice of regularization is often more influential on the final image than including or excluding data or even the accuracy of forward model. A common choice of regularization is a Tikhonov tuning parameter [54, 44], the value of which must be determined by trial and error, and carries little intuition except that it is related to the spectral content of the linear system and also the image. For extremely large inversion domains, tuning parameters are not practical and cannot be easily determined. To avoid this, and to include physically meaningful regularization, we use a covariance

based cost-function [55, 56] from which we can set the regularization simply from our *a priori* knowledge of the range of image pixel values and experimental noise.

For now, we will only consider the inverse scattering problem in two dimensions. The following equations and formulation apply equally to 3D problems by only changing the background Green's function.

2.2 Theory and Formulation

2.2.1 Forward Model

The physics of the acoustic problem are captured by the following integral equation

$$\begin{aligned} \phi(\mathbf{x}) = & \phi_{inc}(\mathbf{x}) + k_o^2 \int g(\mathbf{x}, \mathbf{x}') \left(\delta\kappa(\mathbf{x}') + i \frac{\delta\alpha(\mathbf{x}')}{\kappa_o \omega} \right) \phi(\mathbf{x}') dV' \\ & + \int g(\mathbf{x}, \mathbf{x}') \nabla' \cdot \delta\rho^{-1}(\mathbf{x}') \nabla' \phi(\mathbf{x}') dV' \end{aligned} \quad (2.1)$$

$$k^2 = k_o^2 \left(1 + i \frac{\alpha_o}{\kappa_o \omega} \right) \quad (2.2)$$

where $k_o^2 = \omega^2 \rho_o \kappa_o$ is the lossless background wave number and $g(\mathbf{x}, \mathbf{x}')$ is the free-space Green's function with wave number k . The incident field, $\phi_{inc}(\mathbf{x})$, is the field in the absence of the object. We also define the following contrast functions

$$\frac{1}{\rho_o} \delta\rho^{-1}(\mathbf{x}) = \frac{1}{\rho(\mathbf{x})} - \frac{1}{\rho_o} \quad (2.3)$$

$$\kappa_o \delta\kappa(\mathbf{x}) = \kappa(\mathbf{x}) - \kappa_o \quad (2.4)$$

$$\delta\alpha(\mathbf{x}) = \alpha(\mathbf{x}) - \alpha_o \quad (2.5)$$

where ρ_o , κ_o and α_o are the background material constants. The quantities $\delta\rho^{-1}$ and $\delta\kappa$ are unitless, and $\delta\alpha$ is an absolute measure of loss with units of compressive loss.

We will refer to the complex compressibility as

$$\kappa_c = \delta\kappa + i\frac{\delta\alpha}{\kappa_o\omega}. \quad (2.6)$$

For $\mathbf{x} \notin V$, (2.1) is sometimes called the data equation, while for $\mathbf{x} \in V$ it is the object equation [46]. $\mathbf{x} \notin V$ are positions of field measurements. When the data equation is cast as a functional to be minimized, it is used to retrieve the contrasts. The object equation represents the solution to the forward problem for the field given the object. We will refer to the total field, $\phi(\mathbf{x})$, as the object field when it is in the integration domain

The inverse scattering solution is nonlinear because both the contrasts and object fields are unknowns and occur as a product in the data equation. The contrasts are constrained by our *a priori* knowledge of values and smoothness, as well as experimental noise; the object fields are constrained such that, for a given object, they must satisfy the wave equation, i.e. the object equation.

2.2.2 Problem Specific Material Properties

In the breast ultrasound problem, the speed of sound for all tissue is bounded between $\pm 6\%$ the speed of sound in water [6]. As reported in [43], the compressibility and density contrasts of human soft tissue vary no more than 20% about the background assumed to be water. Furthermore, these quantities are linearly proportional over the range of frequencies and tissues of interest with proportionality $\delta\kappa \sim 2.4\delta\rho^{-1}$. If this relation can be assumed for this problem, the number of unknowns in the inversion is greatly reduced, and, more importantly, the ambiguity in simultaneous retrieval of both quantities is eliminated while maintaining the physics of density variation [57].

Reported values of attenuation rate of breast tissue range from 0-4 dB/cm/MHz, [15, 58]. Together with the contrast ranges, the complex compressibility takes values

no more than $0.2 + i0.02$ and no less than $-0.2 + i0$. Imaging methods based on the Born approximation such as diffraction tomography [59, 14] are only good for contrasts of up to 0.01 as explained in [60, 52]. Thus, the contrasts for the breast imaging problem are beyond the validity of the standard Born approximation, but still weak enough that Born iterations are appropriate to solve the nonlinear problem.

2.3 Forward Solver

2.3.1 Neumann Series

Of the many techniques for the forward solution, few are well suited for large, low-contrast inhomogeneous media. Method of Moments (MoM) and the Finite Element Method require building and solving a large linear system, and Finite-Difference Time-Domain is grossly over sampled in both space and time. A full-wave time domain solver for ultrasound propagation in breast tissue based on spectral methods can be found in [61], [62], but requires storage of auxiliary domains. The forward solver adopted here is the Neumann or Born series solution [53, 47, 63]. This uses the fact that for small contrasts the operator norm of the Green's function integral is such that the field solution can be expanded in a power series of the incident field. Another similar iterative method, but for highly lossy background, is [64], where the MoM matrix is compressed to a diagonal, after which the matrix inverse and Born iterations are readily computed. A forward and inverse method using the Extended Born approximation and FFT to speed the forward solution and handle higher contrasts is [65, 66].

The Neumann series solution begins by writing (2.1) as single operator equation. With the source and frequency dependence assumed, we can write

$$\phi = \phi_{\text{inc}} + G\phi \tag{2.7}$$

where G is the integral-differential operator containing the Green's function and object contrasts acting on the field. The formal inverse of this equation is

$$\phi = (I - G)^{-1} \phi_{\text{inc}} \quad (2.8)$$

Similar to the approximation of $(1 - x)^{-1}$, if $\|G\| < 1$ as measured in a suitable norm, then the solution can be sought using the Neumann series

$$\phi = \sum_{i=0}^n G^i \phi_{\text{inc}} \quad (2.9)$$

where the number of series terms, n , needed for convergence depends on the value of the norm. The operator is an infinite space convolution which is readily computed with an $N-1$ zero-padded FFT, where N is the number of samples along the sides of the original domain. The zeroth and first order solutions give the well known Born and Extended-Born approximations, respectively. See [46] for discussions of these and other approximations as they relate to the formal inverse of the operator equation.

2.3.2 Operator Norm for Three Contrasts

The bounds of $\|G\|$ and the degree to which the peak contrasts and object spectral content affect series convergence have been thoroughly studied in [53, 47]. In these papers, the norm is only computed for the first term of the operator, involving compressibility and loss, and not for density. We wish to compute this norm quickly including all three contrasts.

As given in [53], the L_2 norm of a continuous, linear operator is bounded by a double integral over the object domain. Because the contrast functions are only non-zero in the integration domain, the limits of the first integration can be extended to infinity. The norm is then given as

$$\|G\|^2 < \|k\|_{L^2(\Omega \times \Omega)}^2 = \int_{\Omega} \int_{-\infty}^{\infty} |k(\mathbf{x}, \mathbf{x}')|^2 dV' dV \quad (2.10)$$

where $|k(\mathbf{x}, \mathbf{x}')|^2$ does not depend on the field. After applying integration by parts to the second term of (2.1) in order to factor the field from the integrand, and inserting the shifted argument of the Green's function

$$\begin{aligned} |k(\mathbf{x}, \mathbf{x}')|^2 &= |g(\mathbf{x} - \mathbf{x}') \left(k_o^2 \delta\kappa(\mathbf{x}) + \frac{ik_o^2}{\kappa_o \omega} \delta\alpha(\mathbf{x}) \right) \\ &\quad + \nabla' \cdot \delta\rho^{-1}(\mathbf{x}) \nabla' g(\mathbf{x} - \mathbf{x}')|^2 \end{aligned} \quad (2.11)$$

To speed the computation of the convolution using FFT, we must separate the shifted and unshifted functions in the square magnitude. It can be shown that the norm can be written as an integral over six functions

$$\begin{aligned} \|k\|_{L_2}^2 &= \int_{\Omega} N_1(\mathbf{x}) + N_2(\mathbf{x}) + N_3(\mathbf{x}) \\ &\quad + 2\Re \{-N_4(\mathbf{x}) - N_5(\mathbf{x}) + N_6(\mathbf{x})\} dV \end{aligned} \quad (2.12)$$

$$N_1(\mathbf{x}) = |h(\mathbf{x})|^2 ** |g(\mathbf{x})|^2 \quad (2.13)$$

$$N_{[2,3]}(\mathbf{x}) = |\delta\rho_{[x,y]}^{-1}(\mathbf{x})|^2 ** |g_{[x,y]}(\mathbf{x})|^2 \quad (2.14)$$

$$N_{[4,5]}(\mathbf{x}) = \left(h^*(\mathbf{x}) \delta\rho_{[x,y]}^{-1}(\mathbf{x}) \right) ** \left(g^*(\mathbf{x}) g_{[x,y]}(\mathbf{x}) \right) \quad (2.15)$$

$$N_6(\mathbf{x}) = \left((\delta\rho_x^{-1})^*(\mathbf{x}) \delta\rho_y^{-1}(\mathbf{x}) \right) ** \left(g_x^*(\mathbf{x}) g_y(\mathbf{x}) \right) \quad (2.16)$$

where $h(\mathbf{x})$ is

$$h(\mathbf{x}) = k_o^2 \left(\delta\kappa(\mathbf{x}) - \delta\rho^{-1}(\mathbf{x}) + \frac{i}{\kappa_o \omega} (\delta\alpha(\mathbf{x}) - \alpha_o \delta\rho^{-1}(\mathbf{x})) \right) \quad (2.17)$$

and where $**$ is an infinite-space 2D convolution, and $*$ is complex conjugation. These

expressions can be computed with 2D FFTs. The partial derivatives of the Green's function can be obtained analytically and are given below. The leading order of k_o , and so the nature of $h(\mathbf{x})$, contributes most to the value of the norm.

It can be seen that in 2D the norm depends on the difference of the contrasts. Thus, in cases where the compressibility and density contrasts follow one another, series convergence requires fewer terms. As stated earlier, this condition is met for biological tissue. The norm can be interpreted as a measure of correlation between the object contrasts and the Green's functions. Random collections of objects, containing little overall structure, tend to have smaller norms than highly structured objects, such as rings or disks.

2.3.3 Computation of Series and Norm

To avoid aliasing, we must compute the convolutions for the both the norm and the series by first sampling each function in the spatial domain, zero padding, FFT, multiplying, IFFT, and cropping. Numerically, best results were given by centering the Green's function in a domain with an odd number of samples. This requires sampling the singularities of the Green's function and its derivatives. While singularity extraction was carried out in the integral equation, we found that simply approximating the singularity sufficed. This is equivalent to low pass filtering the Green's function. Given the small sampling area of each pixel for grids sampled at $\lambda_{\min}/10$ or better, the difference between the contribution of the singularity and an approximation is small. When validated against the analytic solution, the magnitude and phase of the forward scattered field appeared unaffected. The 2D Green's function, derivatives and approximate values at the origin used were

$$g(k|\boldsymbol{\rho}|) = \frac{i}{4}H_0^{(1)}(k\rho) \quad (2.18)$$

$$\frac{\partial}{\partial[x, y]}g(k|\boldsymbol{\rho}|) = -\frac{ik}{4}H_1^{(1)}(k\rho) [\cos(\phi), \sin(\phi)] \quad (2.19)$$

$$\lim_{\rho \rightarrow 0} g(k|\boldsymbol{\rho}|) \approx 0.4 + i0.25 \quad (2.20)$$

$$\lim_{\rho \rightarrow 0} \frac{\partial}{\partial[x, y]}g(k|\boldsymbol{\rho}|) \approx 0 \quad (2.21)$$

The approximation for $g(k|\boldsymbol{\rho}|)$ is justified by considering the real and imaginary parts separately in the limit as $\rho \rightarrow 0$. We found a value of 0.4 was adequate for the real part of the singularity. We also found the norm required multiplication by the constant $1/(2\sqrt{M}\sqrt{N})$, where M and N are the number of samples along each side of the unpadded rectangular domain. This brought the value of the norm into the correct range where values on either side of 1 matched series convergence.

2.4 Inverse Scattering Algorithm

2.4.1 Born Iterative Method

The BIM iterations proceed as follows:

1. Assume the object field is the incident field (Born approximation).
2. Given the scattered field data, estimate the contrasts with the current object field by minimizing a cost function subject to suitable constraints.
3. Run forward solver with current contrasts. Store the updated object field.
4. Repeat at step 2 until convergence.

In effect, the BIM iterations successively linearize the nonlinear problem. The use of the forward solver enforces the constraint that the field satisfy the wave equation for a given object. The cost function enforces any constraints on the contrasts and is minimized with a conjugate gradient routine described below.

The BIM has been shown to be applicable for contrasts of up to 3 times the background in acoustics for both compressibility and density [44]. The BIM is aptly suited for the problem we are considering because the contrasts vary no more than 20% about the background, which is beyond the Born approximation but still weakly scattering.

2.4.2 Cost Function

The cost function used to estimate the contrasts follows that of [55],

$$2S(\mathbf{m}) = \|\mathbf{g}(\mathbf{m}) - \mathbf{d}\|_2^2 + \|\mathbf{m} - \mathbf{m}_a\|_2^2. \quad (2.22)$$

The vector \mathbf{d} contains the data, \mathbf{g} is the forward operator, and $\mathbf{g}(\mathbf{m})$ is the vector of predicted data. The forward operator, generally, can be a nonlinear function of the model parameter vector, \mathbf{m} . \mathbf{m}_a is a vector of *a priori* model parameter values.

If \mathbf{m} belongs to an unweighted space, and $\hat{\mathbf{m}}$ belongs to the analogous weighted space, then the L_2 norm is defined through the outer product of these spaces given by

$$\|\mathbf{m}\|_2^2 = (\hat{\mathbf{m}}, \mathbf{m}) = \mathbf{m}^t \mathbf{C}^{-1} \mathbf{m} \quad (2.23)$$

where \mathbf{C}^{-1} is the inverse covariance matrix.

Writing out the cost function using the definition of the norm with data and model inverse covariance matrices, we get

$$\begin{aligned}
2S(\mathbf{m}) &= (\mathbf{g}(\mathbf{m}) - \mathbf{d})^* \mathbf{C}_D^{-1} (\mathbf{g}(\mathbf{m}) - \mathbf{d}) \\
&\quad + (\mathbf{m} - \mathbf{m}_a)^* \mathbf{C}_M^{-1} (\mathbf{m} - \mathbf{m}_a)
\end{aligned} \tag{2.24}$$

where $*$ is conjugate transpose in the case of complex vectors, or simply transpose for real vectors.

This cost function has the statistical interpretation that both the predicted data, $\mathbf{g}(\mathbf{m})$, and separately model parameters, \mathbf{m} , are jointly Gaussian random variables with means \mathbf{d} and \mathbf{m}_a , respectively. The operators \mathbf{C}_D^{-1} and \mathbf{C}_M^{-1} assume their usual meaning in probability. If the elements of the data vector or model vectors are independent, then the corresponding inverse covariance operator is a diagonal matrix, with reciprocal variances given along the diagonals. Finding the set of model parameters that minimizes the cost function will give, at the same time, the most probable set of model parameters for the data.

We write a linear forward operator as \mathbf{G} , the transpose as \mathbf{G}^* and the adjoint as \mathbf{G}^\dagger . It can be shown that, [55],

$$\mathbf{G}^\dagger = \mathbf{C}_M \mathbf{G}^* \mathbf{C}_D^{-1} . \tag{2.25}$$

In wave scattering problems, the forward operator is the Green's function integral, mapping contrasts to scattered fields at receivers. Its transpose, which maps scattered fields at the receivers onto the object domain is, physically, a form of time reversal or backprojection.

For the BIM, the vector \mathbf{m} contains the pixel values of the contrasts; \mathbf{G} is the discretized Green's function integral with constant object field. The forward model is a linear function of model parameters and given by

$$\mathbf{G}\mathbf{m} = \mathbf{G}_1\mathbf{m}_1 + \mathbf{G}_2\mathbf{m}_2 + \mathbf{G}_3\mathbf{m}_3 . \quad (2.26)$$

The cost function is

$$\begin{aligned} 2S(\mathbf{m}) &= \|\mathbf{G}_1\mathbf{m}_1 + \mathbf{G}_2\mathbf{m}_2 + \mathbf{G}_3\mathbf{m}_3 - \mathbf{d}\|_D^2 \\ &\quad + \sum_{m=1}^3 \|\mathbf{m}_m - \mathbf{m}_{a,m}\|_{M,m}^2 \end{aligned} \quad (2.27)$$

with

$$\mathbf{G}_{1,2}(\cdot) = \eta_{1,2} \int g(\mathbf{x}_r, \mathbf{x}')(\cdot)\phi_s(\mathbf{x}')dV' \quad (2.28)$$

$$\mathbf{G}_3(\cdot) = \int g(\mathbf{x}_r, \mathbf{x}')\nabla' \cdot (\cdot)\nabla'\phi_s(\mathbf{x}')dV' \quad (2.29)$$

$$\mathbf{d} = \phi(\mathbf{x}_r) - \phi_{inc}(\mathbf{x}_r) \quad (2.30)$$

$$\mathbf{m}_1 = \delta\kappa(\mathbf{x}) \quad (2.31)$$

$$\mathbf{m}_2 = \delta\alpha(\mathbf{x}) \quad (2.32)$$

$$\mathbf{m}_3 = \delta\rho^{-1}(\mathbf{x}) \quad (2.33)$$

$$\eta_1 = k_o^2 \quad (2.34)$$

$$\eta_2 = \frac{ik_o^2}{\kappa_o\omega} \quad (2.35)$$

where \mathbf{x}_r is the position of receiver r , ϕ_s is the object field produced by a source s , and the frequency is not indexed. The data vectors are indexed over source, frequency, and receiver. The integral operators are linear and their transposes given by

$$\mathbf{G}_{1,2}^*(\cdot) = \eta_{1,2}^* \phi_s^*(\mathbf{x}) \int g^*(\mathbf{x}_r, \mathbf{x})(\cdot) d\mathbf{x}_r \quad (2.36)$$

$$\mathbf{G}_3^*(\cdot) = -\nabla \phi_s^*(\mathbf{x}) \cdot \nabla \int g^*(\mathbf{x}_r, \mathbf{x})(\cdot) d\mathbf{x}_r \quad (2.37)$$

where * on the right hand side represents complex conjugate. The integral over the receiver location becomes a sum for receivers at discrete points.

The gradient vector for each contrast is given by

$$\hat{\gamma}_m = \mathbf{G}_m^* \mathbf{C}_D^{-1} \mathbf{r} + \mathbf{C}_{M,m}^{-1} (\mathbf{m}_m - \mathbf{m}_{a,m}) \quad (2.38)$$

where $\mathbf{r} = \mathbf{G}\mathbf{m} - \mathbf{d}$ is the residual vector. Because the operators are linear, they are their own Frechet derivatives.

In this derivation, we assume the scattered field data are independent, so \mathbf{C}_D^{-1} is diagonal. We further assume that the contrast functions are independent. However, for an inversion where compressibility and density can be assumed to be linearly related, it is easier to substitute one for the other in the forward operator than enforce this condition through the covariance matrix spanning the three contrasts (see example below).

The contrasts are updated with the steepest descent vector

$$\gamma_m = \mathbf{C}_{M,m} \mathbf{G}_m^* \mathbf{C}_D^{-1} \mathbf{r} + \mathbf{m}_m - \mathbf{m}_{a,m} \quad (2.39)$$

$$= \mathbf{G}_m^\dagger \mathbf{r} + \mathbf{m}_m - \mathbf{m}_{a,m} \quad (2.40)$$

which is a vector in the model space and $\mathbf{G}_m^\dagger = \mathbf{C}_{M,m} \mathbf{G}_m^* \mathbf{C}_D^{-1}$ is the adjoint. The adjoint maps the residual (a data vector), through the weighted spaces to the model

space. When the same cost function is used with unweighted spaces, the gradient and steepest descent vectors are equal and terminology often interchanged in the literature [46, 67]. Notice that the steepest descent is the aggregate of all backprojected scattered field residuals; for additional discussion on this topic see [68].

2.4.3 Conjugate Gradient Updates

We use conjugate gradients to determine the contrasts which minimize the cost function. The updates for the model parameter vector are given by

$$\mathbf{m}_{mn} = \mathbf{m}_{m,n-1} - \alpha_n \mathbf{v}_{mn} \quad (2.41)$$

$$\mathbf{v}_{mn} = \boldsymbol{\gamma}_{mn} + \beta_n \mathbf{v}_{m,n-1} \quad (2.42)$$

where n is the iteration number, \mathbf{m}_{mn} is the running model parameter vector for a particular contrast, \mathbf{v}_n is the search direction, α_n is the step length, and n is the iteration number. The same step length is used for all contrasts at a given iteration. The search direction is a linear combination of the steepest descent and the previous search direction. The value of β_n is chosen to ensure that the gradient and steepest descent are conjugate in some sense [67]. We used the Polak-Ribiere step given by

$$\begin{aligned} \beta_n &= \sum_{m=1}^3 \frac{\langle \hat{\boldsymbol{\gamma}}_{mn} - \hat{\boldsymbol{\gamma}}_{mn-1}, \boldsymbol{\gamma}_{mn} \rangle}{\langle \hat{\boldsymbol{\gamma}}_{mn-1}, \boldsymbol{\gamma}_{mn-1} \rangle} \\ &= \sum_{m=1}^3 \frac{\langle \mathbf{C}_{M,m}^{-1} (\boldsymbol{\gamma}_{mn} - \boldsymbol{\gamma}_{mn-1}), \boldsymbol{\gamma}_{mn} \rangle}{\langle \mathbf{C}_{M,m}^{-1} \boldsymbol{\gamma}_{mn-1}, \boldsymbol{\gamma}_{mn-1} \rangle} \end{aligned} \quad (2.43)$$

where \langle, \rangle is a simple dot product. Choosing α_n to minimize the cost function at each step, it can be shown

$$\alpha_n = \frac{\sum_{m=1}^3 \Re \{(\mathbf{v}_{mn}, \boldsymbol{\gamma}_{mn})_{M,m}\}}{\|\sum_{m=1}^3 \mathbf{G}_m \mathbf{v}_{mn}\|_D^2 + \sum_{m=1}^3 \|\mathbf{v}_{mn}\|_{M,m}^2} \quad (2.44)$$

where \Re is the real part, and $(\cdot)_{M,m}$ represents the norm over the model space. The step length α_n is similar in form to the update parameter in [69]. In general, an analytic expression for this parameter is possible when derived in this manner if the cost function is a quadratic functional of linear operators.

2.4.4 Advantages of the Covariance-Based Cost Function

An attractive feature of the above cost function is that a complete linear system is never constructed, which is also true for other gradient based methods [46, 41]; the object contrast functions are simply updated. However, the use of a forward solver in the overall inversion algorithm does require storing the object field.

The greatest advantage of a covariance-based cost function is that it provides natural regularization through the inverse covariance matrices which are chosen at the beginning of the optimization and need not be changed. For example, if we know that contrasts vary no more than 10%, and each contrast pixel is independent, the covariance matrices are diagonal and choosing standard deviations of 0.2 is appropriate. Also, experimental noise is readily included in the optimization. The Gaussian interpretation of the data norm implies that the predicted data are corrupted by Gaussian noise. For example, with coherent imaging systems, averaging many single scene scattered field time traces is common to improve the signal to noise ratio. From these traces, the first order statistics, mean and standard deviation, can be found. These values are precisely the values used for \mathbf{d} and the diagonal of \mathbf{C}_D^{-1} .

If \mathbf{C}_M^{-1} is diagonal and a constant, the second term in the cost function reduces to Tikhonov regularization. Often in practice, when the Tikhonov tuning parameter is used with unweighted spaces, its optimal value, which changes with the experimental setup, must be determined by trial and error [44, 70, 67]. This is because the value of

a single tuning parameter must replace the effects of all the elements of the matrices \mathbf{C}_M^{-1} and \mathbf{C}_D^{-1} , which inherently adjust for each experimental setup and domain size. While a tuning parameter could be added to this cost function, it only changes the *a priori* variances of the contrasts, so is unnecessary. When dealing with large domains, it is not practical to recompute a tuning parameter for every variation of problem size and setup; the covariance-based cost function avoids just this.

Regularization by the model inverse covariance matrix can also be computationally efficient. In cases of mostly uncorrelated contrast pixel values, the covariance matrix is sparse. Furthermore, the full inverse is never computed; only the sparse system $\mathbf{C}_M \hat{\mathbf{m}} = \mathbf{m}$ must be solved. For the example in the following section, we solve the preconditioned system $\mathbf{C}_M^t \mathbf{C}_M \hat{\mathbf{m}} = \mathbf{C}_M^t \mathbf{m}$ using a conjugate gradient method for normal equations [71]. As the covariance matrix is symmetric, computing and storing the transpose is unnecessary. An example of this procedure can also be found in [56].

Due to the problem size, it is difficult to determine in real time whether the solution has been trapped in a local minimum. One way to avoid local minima is to better constrain the problem with more measurements and use of the covariance matrix. Another, but ad hoc, method is to limit the number of conjugate gradient steps before updating the field with the forward solver. This effectively creates smaller linearizations of the nonlinear problem.

2.4.5 Strictly Positive Model Parameters

Gaussian probability distributions are appropriate for contrasts taking both positive and negative values. However, compressive losses take strictly positive values when the background loss goes to zero, so Gaussian distributions, while practical and still useful in this context, are not technically correct. As addressed in [55], one solution is to use the log-normal distribution. This is beyond the scope of this work, but it is mentioned here for completeness.

2.4.6 Comparison with the CSI Method

The Contrast Source Inversion Method (CSI) [69] has gained recent popularity as an inversion method for biologic imaging [29], [72]. While the BIM and CSI share many similarities, and, while both methods are generally effective, some key differences in algorithm structure are illuminated here. The CSI method simultaneously minimizes functionals over the data and object equations by interleaving conjugate gradient updates of the contrasts and fields. First, because complete minimization of an object equation functional represents the solution to the forward problem, only after which the fields satisfy the wave equation, the contrasts in the CSI are updated with fields that are not wave fields. The BIM, on the other hand, by using a forward solver, effectively completes the minimization of an object functional before minimizing the data functional, therefore uses a wave field satisfying the wave equation to update the contrasts. Second, conjugate gradient iterations, in general, rely on the fact that the functional space is constant in order to use the history of the updates for that space to construct the Krylov subspaces out of which the solution is formed. By changing the functional space at each iteration, the CSI states that it avoids local minima [69], however, this is done at the expense of properly formed conjugate gradient updates. Lastly, the terms of the CSI cost function are given arbitrary normalizations, and many types of regularization have been tested for the CSI cost function, such as a total variation multiplicative constant. In the probabilistic interpretation of the least squares problem, such normalizations affect the *a priori* variances of the Gaussian distributions. Also, such multiplicative regularizers make the cost function more nonlinear. Even partial use of a model inverse covariance matrix adds sufficient regularization without increasing the nonlinearity of the cost function. Thus, the BIM is the inversion method of choice for our problem because the data and object equation constraints are fully enforced between steps, the conjugate gradient updates are well defined, and the form of regularization has a simple physical interpretation.

2.5 Results and Discussion

2.5.1 Series Solution Validation

The forward solver was validated in 2D against the analytic scattering solution of a cylinder [52]. Many combinations of contrast, domain size, and gridding were tested. A representative example is given.

Shown in Figs. 2.1 and 2.2, is the scattered field of a 6λ diameter cylinder with compressive contrast of 5%. The domain size was $10\lambda \times 10\lambda$ sampled at $\lambda/10$. The source is a point source located at 180 degrees (the backscatter direction) and 8λ from the origin, with unit amplitude and zero phase. The scattered field was computed at a radius of 10λ for all angles. The norm of this object had a value of 0.11, and 7 terms were needed for convergence. The convergence criterion used was that the mean pixel change for the field be less than 0.1% after adding an additional series term.

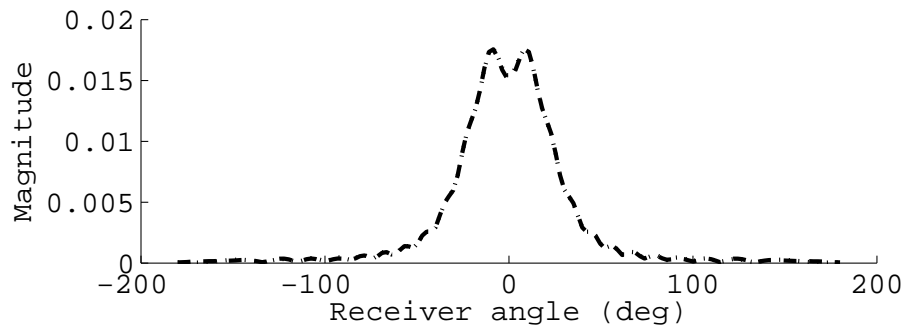


Figure 2.1: Magnitude of scattered field at receivers around 6λ cylinder with 5% contrast. Dashed: analytical; dotted: series solution.

Fig. 2.3 is an example of the number of series terms for convergence vs operator norm. The compressibility contrast of the cylinder was linearly stepped from 0-0.23. Smoother objects permit higher peak contrasts to give the same values of the norm. No more than 200 terms were summed.

The largest overall domain tested was $150\lambda \times 150\lambda$, with smoothly random objects of peak contrasts $\pm 20\%$. Convergence is achieved usually with 20 terms. Generally,

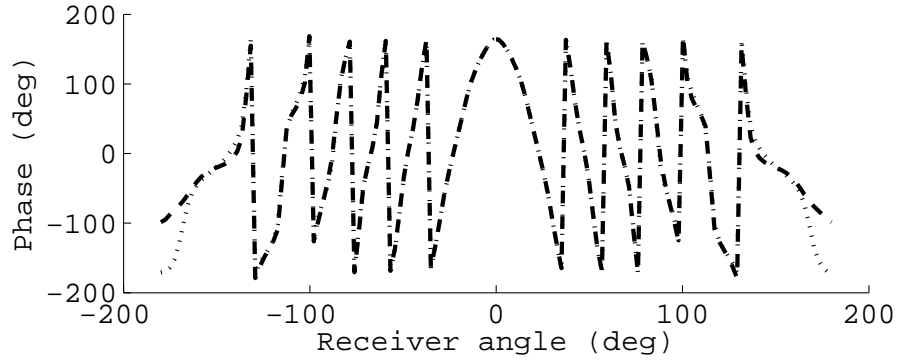


Figure 2.2: Phase of scattered field at receivers around 6λ cylinder. Dashed: analytical; dotted: series solution. The phase in the backscatter direction begins to deteriorate.

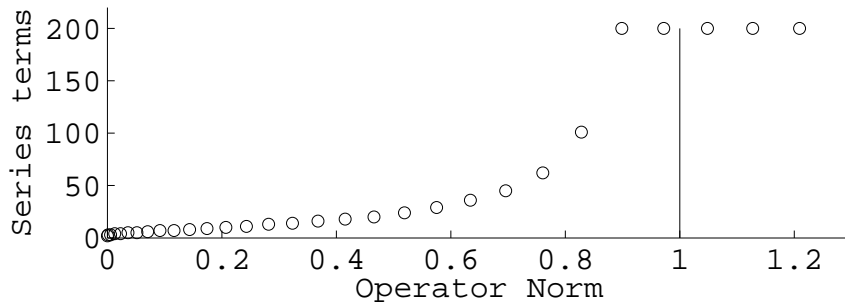


Figure 2.3: Number of series terms needed for convergence vs. operator norm. The compressibility contrast of a 6λ cylinder was linearly stepped from 0 to 0.24, on a $10\lambda \times 10\lambda$ domain.

background loss, even as little as 1% imaginary to real part in the wavenumber, tends to reduce the norm and speed convergence; similar effects are demonstrated in [47] but for small domains.

2.5.2 Inverse Scattering Algorithm

The transmit waveform is a modulated Gaussian with the -10-dB frequency band from 0.5-1.5 MHz. The background speed of sound is 1500 m/s, with smallest free space wavelength, λ_{\min} , equal to 1mm. For Examples 1-5, there are 20 point sources, with unit amplitude and zero phase, and 20 point receivers collocated with the sources, as shown in Fig. 2.4. Twenty complex frequency samples are used for a total of 16000 data points. For Example 6, 256 sources and receivers were used with 20 frequencies. The pixel size is $0.09\lambda_{\min}$, equal to 90 microns. Synthetic scattered pressure field data had magnitudes on the order of $1e-3$ (Pa); the standard deviation for predicted data used for all examples was $1e-5$, which is approximately 1% Gaussian noise. Twelve series terms were used for the forward solver. Eight conjugate gradient steps were used when minimizing the cost function. The operator norm was computed for each object at the highest transmit frequency before the inversion; the values are reported below. No more than 3-5 inversion iterations were typically needed to recover the contrasts with mean pixel error of 5% relative to the actual contrasts.

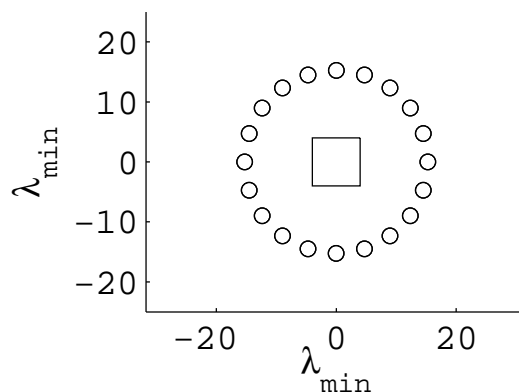


Figure 2.4: Source/receiver setup. $8\lambda \times 8\lambda$ domain.

Storage requirements for the unknowns are $O(N)$; storage requirements for the object fields are $O(N_f N_s N)$, where N_f , N_s , N are the number of frequencies, sources, and unknown pixels, respectively. For 2D rectangular domains, the forward solver requires $O(N_f N_s N_t N \log N)$ operations, where N_t are the number of terms required for the Neumann series to converge. The total run time for the inversion of the $8\lambda_{\min} \times 8\lambda_{\min}$ domains was typically 5-15 minutes using 64-bit Matlab on a Linux desktop with an Athlon 64 processor and 4 GB of RAM.

We used a Fourier-based compression scheme for the object fields and pre-computed data equation Green's functions. Spectral components with greater than 0.1% magnitude of the maximum were stored and uncompressed when needed. This procedure yielded at least a 100-fold decrease in required memory, with an increase in computation time determined by the 2D FFTs used to compress and uncompress the data.

Example 1, shown in Figs. 2.5 and 2.6, is the reconstruction of two cylinders $2\lambda_{\min}$ in diameter with peak contrast 0.2 at different stages of the BIM. The background is lossless and the operator norm is 0.31. A contrast standard deviation of 0.2 is used uniformly. Similar results are obtained for cylinders of only density and only loss. Because we use a diagonal inverse covariance matrix, low pass filter artifacts of the type for Tikhonov regularization are apparent in the reconstruction.

Example 2, Figs. 2.7 and 2.8, demonstrate the resolution limits of the algorithm. There are four sets of objects of 1, 4, 9, and 16 pixels wide equal to 90, 180, 270, and 360 microns, respectively. Compressibility only and a contrast of 0.2. Single objects smaller than $\lambda_{\min}/2$ are detected, but a pair of objects are only distinguished when they are separated by a distance around $\lambda_{\min}/2$. While small objects are detected, their peak contrasts are not recovered.

Example 3, Figs. 2.9 and 2.10 is the reconstruction of a complex compressibility profile with peak complex compressibility $0.2 + i0.02$ for both cylinders. The back-

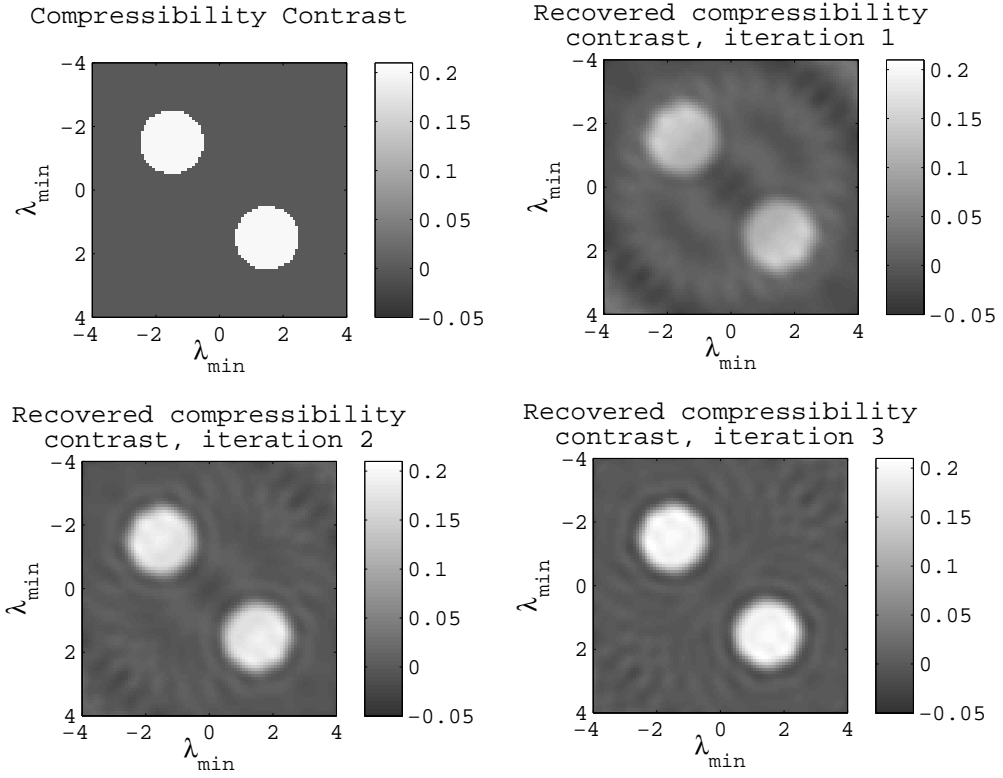


Figure 2.5: a) Actual compressibility contrast. 2 cylinders each $2\lambda_{\min}$ in diameter. Peak contrast 0.2, lossless background, operator norm 0.31. b) Retrieved contrast with Born approximation. c) Retrieved contrast after 2 iterations. d) Retrieved contrast after 3 iterations.

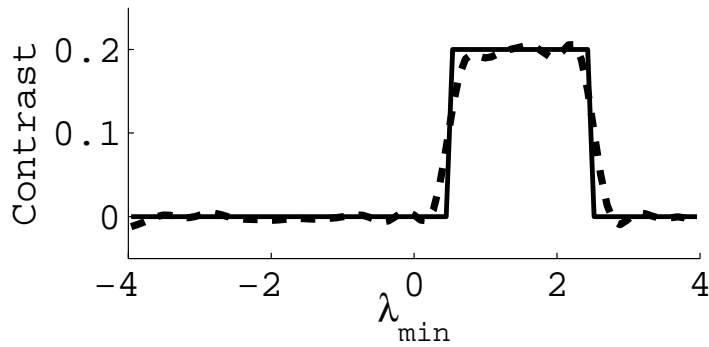


Figure 2.6: Horizontal cut through lower cylinder. Solid: actual contrast; dashed: recovered contrast after 3 iterations.

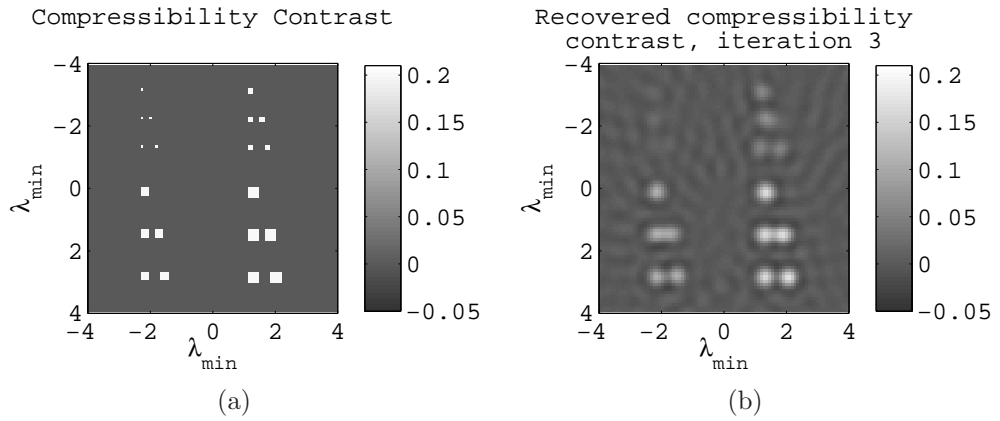


Figure 2.7: a) Four sets of objects of 1, 4, 9, and 16 pixels equal to 90, 180, 270, and 360 micron widths. b) Compressibility contrast with 3 iterations.

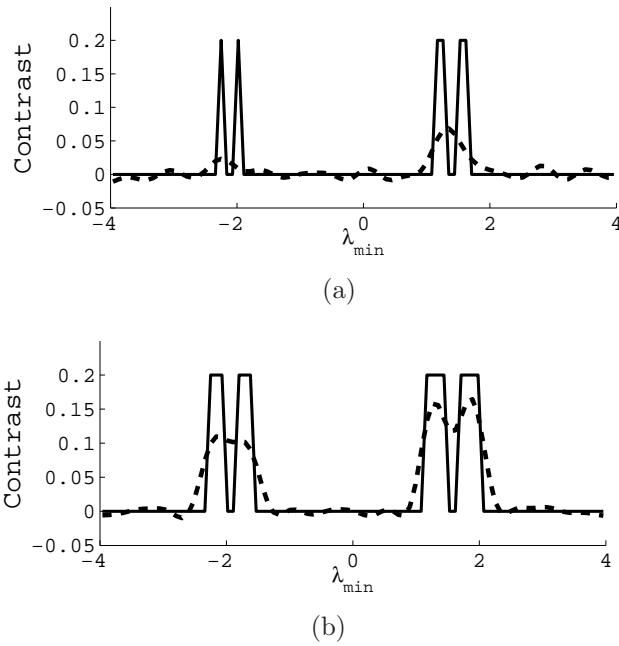


Figure 2.8: a) Horizontal cut through third row of objects. b) Horizontal cut through fifth row of objects. Solid: actual contrast; dashed: recovered contrast after 4 iterations.

ground is lossless and a standard deviation of 0.2 and 0.04 is used for the real and imaginary parts, respectively. The operator norm is 0.31. Note that the recovered imaginary part is 25% of the actual value. The ambiguity in recovering the real and imaginary parts of the complex compressibility result because 1) the inversion must separate the scattered field contributions of the two contrast functions which are summed in the integral equation; this is inherently ambiguous, 2) by adding a second contrast we have doubled the number of unknowns for the same number of data points, even though the optimization is still over-determined, and 3) because the contribution to the scattered field of the imaginary part is an order of magnitude smaller than the real part and the algorithm is not sensitive enough to recover it without additional *a priori* information.

Example 4, Figs. 2.11 and 2.12, is the reconstruction of both compressibility and density under the assumption that they are linearly related. The peak compressive contrast is 0.2. The inversion is for compressibility only, with the assumed relation $\delta\kappa = 2.4\delta\rho^{-1}$. Standard deviation of 0.2 used for all pixels, with an operator norm 0.36.

Example 5, Figs. 2.13 and 2.14, demonstrates use of the model covariance matrix to improve image sharpness. The background and object pixels each correlated with themselves. The peak contrast is 0.2 and a standard deviation of 0.3 used for all pixels. A crosscorrelation coefficient of 0.004 used in both regions. The edges of the cylinders in the reconstruction are more sharp than would be without the correlation.

Finally, Example 6, is the reconstruction of a $50\lambda_{\min} \times 50\lambda_{\min}$ domain of random compressibility with two inclusions and peak contrast ± 0.08 . A standard deviation of 0.2 used for all pixels and 5 iterations were used. Data from 80 sources, 80 receivers were collocated at a radius of $45\lambda_{\min}$, shown in Figure 2.5.2, and 20 frequencies were used for a total of 256,000 data points for 245,000 unknowns. Reconstructions are shown in Figures 2.16 and 2.17. Overall features are recovered well.

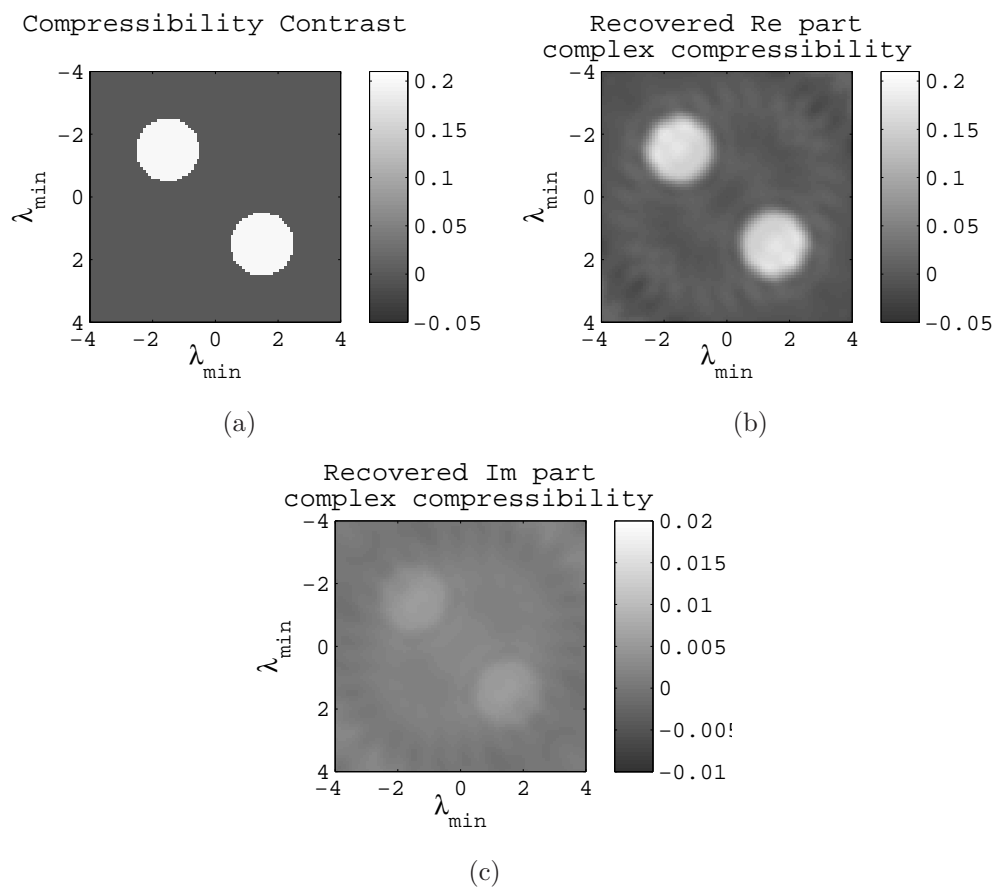


Figure 2.9: a) Compressibility and loss. Peak complex compressibility $0.2 + i0.02$ for both cylinders. b) Real part of compressibility contrast after 3 iterations. c) Imaginary part of compressibility contrast after 3 iterations

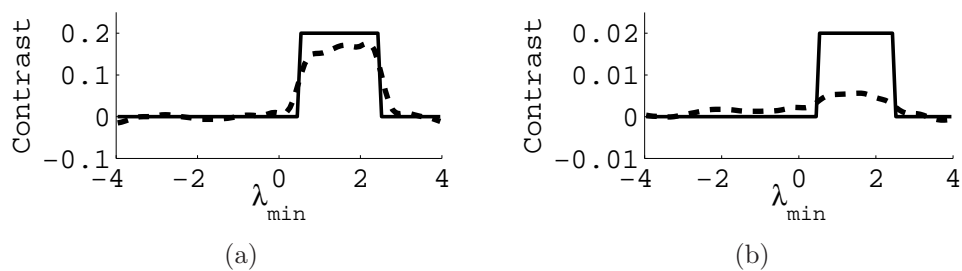


Figure 2.10: a) Horizontal cut through lower cylinder of real part of compressibility contrast. b) Horizontal cut through lower cylinder of imaginary part of compressibility contrast. Solid: actual contrast; dashed: recovered contrast after 3 iterations.

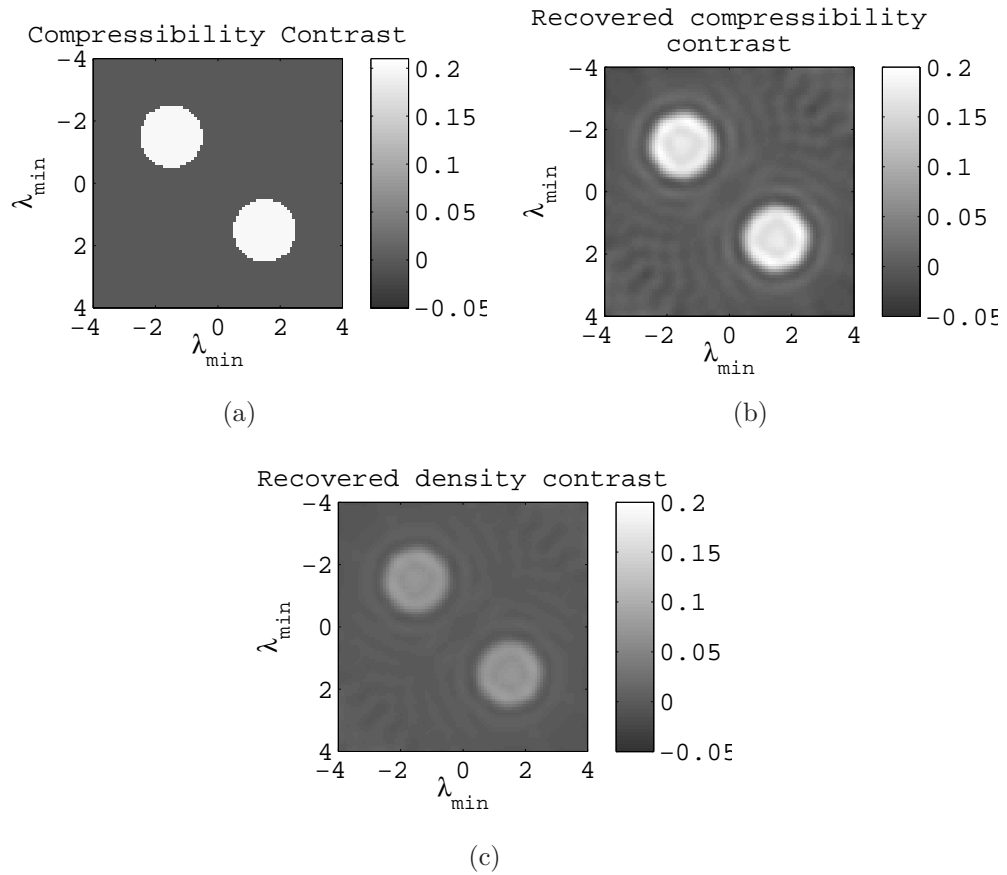


Figure 2.11: a) Compressibility and density. Peak compressive contrast of 0.2. Lossless background, inversion for compressibility only, with assumed relation $\delta\kappa = 2.4\delta\rho^{-1}$. b) Compressibility contrast after 3 iterations. c) Density contrast after 3 iterations.

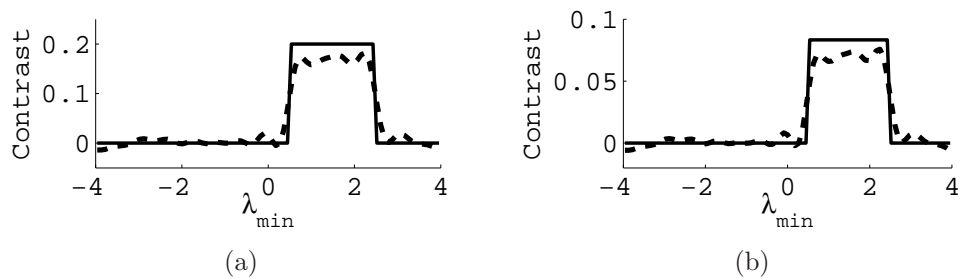


Figure 2.12: a) Horizontal cut through lower cylinder of compressibility contrast. b) Horizontal cut through lower cylinder of density contrast. Solid: actual contrast; dashed: recovered contrast after 3 iterations.

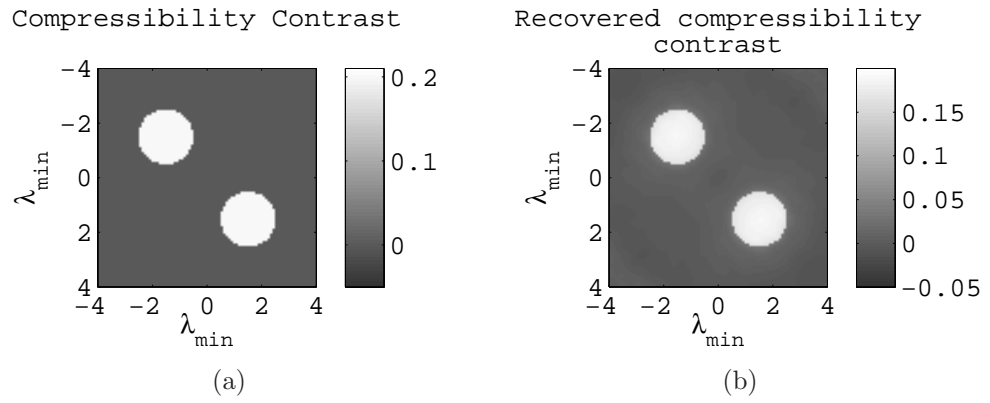


Figure 2.13: a) Compressibility only with background and object pixels each correlated. b) Compressibility contrast after 5 Born iterations.

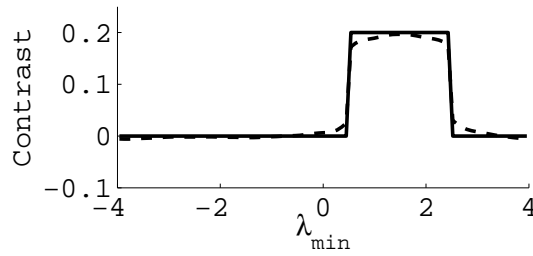


Figure 2.14: Horizontal cut through lower cylinder. Solid: actual contrast; dashed: recovered contrast after 5 iterations.

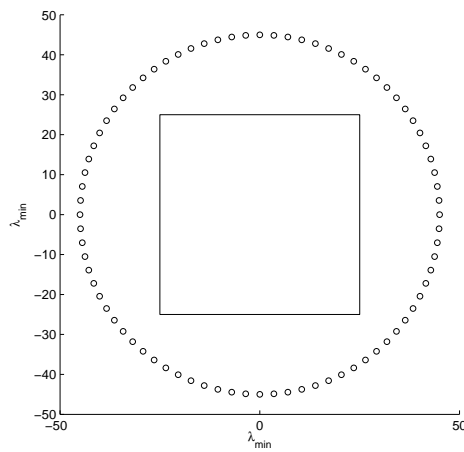


Figure 2.15: Source/receiver setup. $50\lambda \times 50\lambda$ domain.

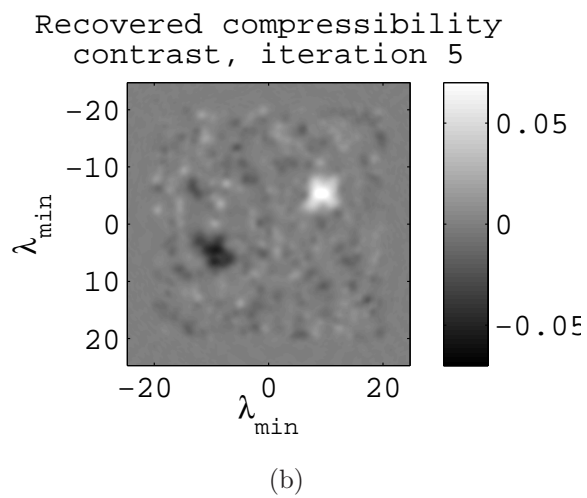
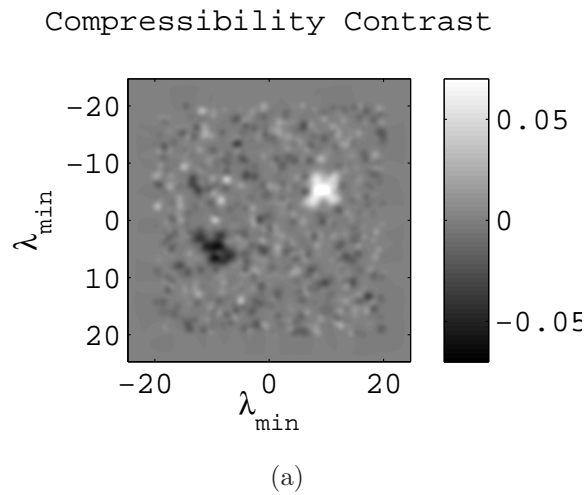


Figure 2.16: a) Domain is $50 \lambda_{\min} \times 50 \lambda_{\min}$. Compressibility only. Random distribution with two inclusions and peak contrast ± 0.08 . b) Compressibility contrast after 5 iterations.

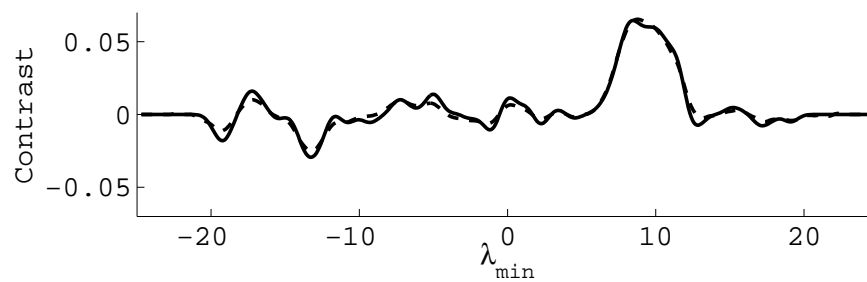


Figure 2.17: Horizontal cut at $-6 \lambda_{\min}$. Solid: actual contrast; dashed: recovered contrast after 5 iterations. Low pass artifacts evident.

The run time for the $50\lambda_{\min} \times 50\lambda_{\min}$ object domain was 9 hours per Born iteration using Matlab on a 64-bit Linux desktop with 4 Gb of RAM, which includes one run of the forward solver and one cost function minimization. This is due to the nonlinear increase in computation with the number of unknowns, as the gradient is a triple nested loop over source, receiver and frequency, where the product of the number of sources, receivers and frequencies scales with the unknowns. Note also that so far no particular attempt has been made to optimize the code, or to run the code in a more efficient language such as Fortran.

Extending the method to 3D only requires changing the form of the Green's function; the structure of the inversion algorithm is the same. The storage scales as the 2D problem. The forward solver requires 3D FFTs, which still gives $O(N\log N)$ for the forward solver. Because the algorithm loops over source, receiver, and frequency, where the product of these three quantities scale with the number of unknowns, the computation for the algorithm scales nonlinearly with the number of unknowns.

2.6 Conclusion

In this chapter, we have presented an iterative inverse scattering method suitable for ultrasound breast imaging. The forward solver, inversion method, and cost function were specifically selected for the size of the problem and expected range of contrasts. The Neumann series as forward solver is well suited to simulate the scattering of large, low contrast, inhomogeneous domains. Also, the covariance based cost function has physically meaningful regularization which avoids trial and error when determining a tuning parameter. Finally, Born iterations can retrieve the expected material contrasts with high accuracy in few iterations; contrasts can be retrieved to within 5% of the actual and resolution of at least $\lambda_{\min}/2$ and often better, is possible. Also, we have included density variation in the formulation, and demonstrated object retrieval when compressibility and density are linearly related.

CHAPTER III

Electromagnetic Inverse Scattering Algorithm

3.1 Introduction

The microwave breast imaging problem is currently the application of many electromagnetic inverse scattering algorithms, such as the Contrast Source Inversion, and Distorted Born Iterative Method. The goal is to image both the permittivity and conductivity of the soft tissue. Evidence suggests that there is a quantitative difference in the material parameters between benign and malignant tissue, which if imaged might provided an addition diagnostic tool, though the degree of diagnostic potential is still under investigation. Assuming the use of a coupling medium with a relative permittivity of 30, the imaging domain at frequencies between 1-10 GHz is in the tens of wavelengths in three dimensions. The size of the domain is large compared to those tested by most inverse scattering algorithms. The goal is to choose the elements of the inverse scattering algorithm to handle these larger domains.

The highest relative permittivity expected is that of water, which, with a background relative permittivity of 30, has a contrast of no more than 3:1. We choose Born iterations as the inversion scheme as it has been shown capable of recovering contrasts this high. Born iterations alternate estimates of the objects and object fields by first estimating the object via the cost function assuming constant object field, then use this object in the forward solver to update the field. The forward

solver we have chosen is the Neumann series solution. The series solution is applicable for objects of low contrast (less than 1) or some loss. A contrast of 3:1 is normally not valid, but we expect high conductive losses in the tissue. The series solution is an $O(N \log N)$ volumetric solver, good for large domains. We estimate objects by minimizing a multi-variate covariance-based cost functional with conjugate gradients. This procedure eliminates the need to build, store or solve a large matrix system because the functional is simply minimized, and natural regularization is provided by inverse data and model covariance matrices. Tuning parameters are eliminated because the elements of the covariance matrices are provided by our a priori knowledge of the experimental noise and range of contrasts. Solving a matrix system with tuning regularization is not practical for this problem.

We have specifically chosen the elements of this inverse scattering algorithm to handle large imaging domains. We have initially tested this algorithm in three dimensions for full-vector data and object fields on domains of several wavelengths and retrieved objects of contrasts of 2:1 with half-wavelength resolution of the smallest wavelength in the transmit spectrum.

3.2 Formulation

3.2.1 Volume Integral Equations

The electric field volume integral equation (VIE) for an inhomogeneous distribution of permittivity and conductivity is given by

$$\mathbf{E}(\mathbf{r}) = \mathbf{E}_{inc}(\mathbf{r}) + k_o^2 \int \overline{\mathbf{G}}(\mathbf{r}, \mathbf{r}') \cdot \left(\delta\epsilon(\mathbf{r}') + \frac{i\delta\sigma(\mathbf{r}')}{\epsilon_b\omega} \right) \mathbf{E}(\mathbf{r}') dV' \quad (3.1)$$

where $\mathbf{E}(\mathbf{r})$ and $\mathbf{E}_{inc}(\mathbf{r})$ are the total and incident fields, respectively, and \mathbf{r} is the position vector. The quantity $k_o^2 = \omega^2 \mu_o \epsilon_b$ is the lossless background wave number and $\epsilon_b = \epsilon_o \epsilon_{rb}$ is the background permittivity with relative permittivity ϵ_{rb} . The

object contrast functions are defined

$$\epsilon_b \delta\epsilon(\mathbf{r}) = \epsilon(\mathbf{r}) - \epsilon_b \quad (3.2)$$

$$\delta\sigma(\mathbf{r}) = \sigma(\mathbf{r}) - \sigma_b \quad (3.3)$$

where σ_b is the background conductivity. The quantity $\delta\epsilon(\mathbf{r})$ is unitless and $\delta\sigma(\mathbf{r})$ is an absolute measure of conductivity with units of Siemens per meter and $\overline{\mathbf{G}}(\mathbf{r}, \mathbf{r}')$ is the background dyadic Green's function.

In free space, this is given by,

$$\overline{\mathbf{G}}(\mathbf{r}, \mathbf{r}') = \left[\overline{\mathbf{I}} + \frac{\nabla' \nabla'}{k^2} \right] g(\mathbf{r}, \mathbf{r}') \quad (3.4)$$

where

$$g(\mathbf{r}, \mathbf{r}') = \frac{e^{ikr}}{4\pi r} \quad (3.5)$$

with $r = |\mathbf{r} - \mathbf{r}'|$. The background wave number, k , is given by

$$k^2 = k_o^2 \left(1 + i \frac{\sigma_b}{\epsilon_b \omega} \right) \quad (3.6)$$

Defining the scattered field as

$$\mathbf{E}_{sca}(\mathbf{r}) = \mathbf{E}(\mathbf{r}) - \mathbf{E}_{inc}(\mathbf{r}) \quad (3.7)$$

and restricting the observation point \mathbf{r} to points outside the object region in Eqn. (3.1), we can write the VIE for the scattered field concisely as

$$\mathbf{E}_{sca}(\mathbf{r}) = \int \overline{\mathbf{G}}(\mathbf{r}, \mathbf{r}') \cdot \mathcal{O}(\mathbf{r}') \mathbf{E}(\mathbf{r}') dV' \quad (3.8)$$

where we define the following object function

$$O(\mathbf{r}) = k_o^2 \left(\delta\epsilon(\mathbf{r}) + i \frac{\delta\sigma(\mathbf{r})}{\epsilon_b\omega} \right) \quad (3.9)$$

In the context of inverse scattering, Eqn. (3.1) represents the solution to the wave equation in the object domain, while Eqn. (3.8) relates the material contrasts to scattered field measurements taken outside the object domain. Depending on the inversion algorithm, these two equations are used in combination to recover both the contrasts and the total fields.

3.3 Born Iterative Method

The Born Iterative Method (BIM) and the related Distorted Born Iterative method (DBIM) have been extensively studied in theory, [52, 73, 74, 51, 75]. In effect, the BIM successively linearizes the nonlinear problem by alternating estimates of the contrasts and the object fields according to the following algorithm:

1. Assume the object fields are the incident field (Born approximation).
2. Given the measured scattered field data, estimate the contrasts with the current object fields by minimizing a suitable cost function.
3. Run the forward solver with current contrasts. Store the updated object field.
4. Repeat at step 2 until convergence.

3.3.1 Neumann Series for the Electromagnetic Forward Problem

The use of the forward solver in the BIM enforces the constraint that the object fields satisfy the wave equation for the current object at each iteration. We will continue the use of the Neumann series solution that was used for the acoustic problem in the previous chapter. As mentioned then, the converge properties are better for

lossy backgrounds. In the microwave breast imaging problem, we expect to use a background coupling medium with some loss, see Chapter VII for an example. Writing Eqn. 3.1 in operator form

$$\mathbf{E} = \mathbf{E}_{inc} + \overline{\mathbf{G}} \cdot \mathbf{E} \quad (3.10)$$

then the solution in terms of the formal inverse is

$$\mathbf{E} = (\overline{\mathbf{I}} - \overline{\mathbf{G}})^{-1} \mathbf{E} \quad (3.11)$$

which for sufficiently operator norms $\|\overline{\mathbf{G}}\| < 1$ can be solved with the series

$$\mathbf{E} = \sum_{n=1}^N (\overline{\mathbf{G}})^n \mathbf{E}_{inc} \quad (3.12)$$

The norm of the operator is given by

$$\|\overline{\mathbf{G}}\| < k_o^2 \int \int |\overline{\mathbf{G}}(\mathbf{x}, \mathbf{x}')|^2 \left| \delta\epsilon(\mathbf{r}') + \frac{i\delta\sigma(\mathbf{r}')}{\epsilon_b\omega} \right|^2 dV' dV \quad (3.13)$$

which can be computed efficiently using 3D FFTs and is a measure of correlation between the object and the background dyadic Green's function.

For example, the operator norm as a function of relative permittivity for a sphere with a diameter of 1λ is given in Figure 3.1, where the relative permittivity is stepped from 1 to 2.1. Convergence is achieved when the change in the magnitude of the field solution is on average less than 1 percent by adding the next term. The behavior is similar to the that in the acoustic problem.

3.3.2 Shanks Transformation

As shown previously, and also for the acoustic problem, the number of terms necessary for convergence for objects which yield operator norms near 1 can be between

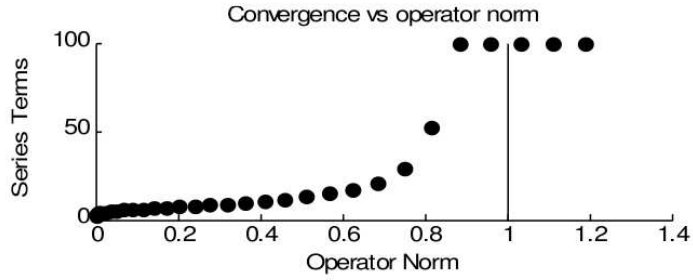


Figure 3.1: Linearly stepped relative permittivity of 1λ diameter sphere from 1 to 2.1 50-200 terms, which can be computationally prohibitive. A method to accelerate the convergence of a series which oscillates about the final solution is called Shanks transformation [76]. This is a nonlinear transformation which, in effect, cancels the oscillatory behavior of the series. Given a sequence of partial sums A_n the Shanks transformation is given by

$$S(A_n) = \frac{A_{n+1}A_{n-1} - A_n^2}{A_{n+1} - 2A_n + A_{n-1}} \quad (3.14)$$

This transformation generally only requires the first six or seven partial sums and can be applied in succession to achieve high order transformations for more rapid convergence. This transformation is computed over fields of the partial sums of the Neumann series point by point.

An example of the effect of the Shanks transformation on the field solution is shown in Figure 3.2. Shown are real parts of the z-component of the scattered electric field of a 1λ sphere. The relative permittivity of the background and sphere are 30 and 60 respectively. A dipole source is located 10λ to the right of the domain. The background is lossless. The field in the horizontal plane for the Neumann series terms $\{10, 11, 12\}$, and then 3rd order Shanks transformation for terms $\{4, 5, 6\}$ are shown. The field solution under the Neumann series oscillates, while that for the Shanks transformation has already converged.

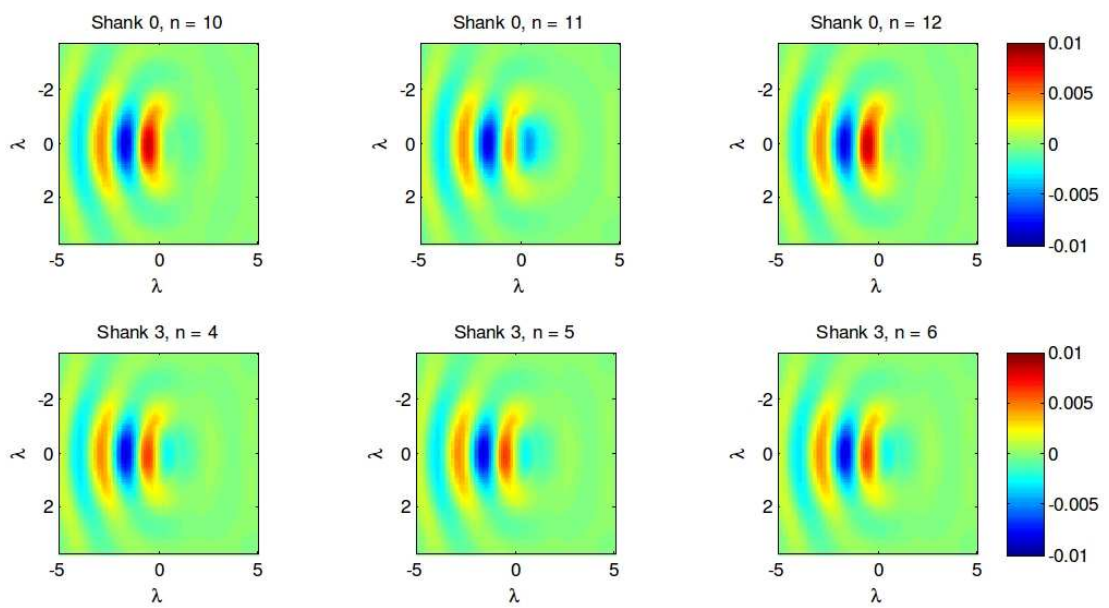


Figure 3.2: Scattered field solution for different terms the Neumann series and Neumann series with Shanks transformation of a 1λ sphere. Top row: Neumann series partial sums $\{10, 11, 12\}$. Bottom row: Neumann series partial sums with 3rd order Shanks transformation terms $\{4, 5, 6\}$.

This transformation was retrospectively tested with success for the acoustic problem in 2D and 3D.

As an aside, for several years a few Applied Physics colleagues and I would meet weekly in a group we called Applied Theory to discuss our work and mulch ideas. My thanks to William Fisher who suggested trying the Shanks transformation on the Neumann series after he ran across it buried in a math methods book. Also, transformations like this one, I think, have several new applications in wave physics. For instance, rapid computation of analytic scattering solutions, such as the Mie solution, or accelerating perturbation series for random media.

3.3.3 Cost Function

The choice of the cost function is not trivial, because it and the form of regularization often have more effect on the final image than the number of data points. Unlike traditional formulations of the BIM, which build and solve a linear system of equations over a discretized Eqn. (3.8) to update the contrasts, we minimize a functional over Eqn. (3.8) using the multi-variate covariance-based cost function of [55]. We use this cost function for the same reasons it was used in the acoustic problem, 1) it has the probabilistic interpretation that the model parameters and forward model predictions are Gaussian random variables, for which inverse covariance operators provide physically meaningful regularization, the parameters of which come directly from experiment, avoiding the need for tuning parameters, 2) it gives a unified framework for analytically deriving the transpose of the forward operator in weighted spaces, and 3) we can minimize this cost function with conjugate gradients avoiding the need to build and solve a large linear system of equations. This cost function and its meaning are described in more detail in [55] and Appendix D.1.1.

At each iteration when we estimate the contrast, we assume the object field is constant. The scattered field integral with constant object field is then a linear

operator acting on the contrast. With this in mind, we write the cost function as

$$2F(\mathbf{m}) = \|\mathbf{G}_1\mathbf{m}_1 + \mathbf{G}_2\mathbf{m}_2 - \mathbf{d}\|_D^2 + \sum_{m=1,2} \|\mathbf{m}_m - \mathbf{m}_{a,m}\|_{M,m}^2 \quad (3.15)$$

where

$$[\mathbf{G}_m]_{ji} = c_m \int \overline{\mathbf{G}}_j(\mathbf{x}_j, \mathbf{x}') \cdot (\cdot) \mathbf{E}_i(\mathbf{x}') dV' \quad (3.16)$$

$$[\mathbf{d}]_{ji} = \mathbf{E}_{ji,\text{sca}} \quad (3.17)$$

$$\mathbf{m}_1 = \delta\epsilon(\mathbf{x}) \quad (3.18)$$

$$\mathbf{m}_2 = \delta\sigma(\mathbf{x}) \quad (3.19)$$

$$\mathbf{m}_{a,1} = \delta\epsilon_{a \text{ priori}}(\mathbf{x}) \quad (3.20)$$

$$\mathbf{m}_{a,2} = \delta\sigma_{a \text{ priori}}(\mathbf{x}) \quad (3.21)$$

$$c_1 = k_o^2 \quad (3.22)$$

$$c_2 = k_o^2 \frac{i}{\epsilon_b \omega} \quad (3.23)$$

with frequency dependence understood. The quantities i and j index source and receiver respectively. The vector \mathbf{x}_j is the location of the received scattered field, and $\mathbf{E}_i(\mathbf{x}')$ is the total field in the object domain due to the transmitter. The quantity \mathbf{G} is the forward operator, and $\mathbf{G}_1\mathbf{m}_1 + \mathbf{G}_2\mathbf{m}_2$ is a vector of forward model predictions. The quantity \mathbf{d} is the data vector containing the measured scattered fields. The vectors \mathbf{m}_1 and \mathbf{m}_2 contain the relative permittivity and conductivity contrast pixel values, respectively, for a discretized domain. The vectors $\mathbf{m}_{a,1}$ and $\mathbf{m}_{a,2}$ contain our *a priori* knowledge of the contrast pixel values. We have assumed that the permittivity and conductivity contrasts are independent so each has its own regularization term. The vector norms are defined over the data and model spaces, respectively, through

inverse covariance operators. See Appendix D.1.1.

The gradient vector and steepest descent vectors for the two model vectors are also independent and given by

$$\hat{\boldsymbol{\gamma}}_m = \mathbf{G}_m^* \mathbf{C}_D^{-1} \mathbf{r} + \mathbf{C}_{M,m}^{-1} (\mathbf{m}_m - \mathbf{m}_{a,m}) \quad (3.24)$$

$$\boldsymbol{\gamma}_m = \mathbf{C}_{M,m} \mathbf{G}_m^* \mathbf{C}_D^{-1} \mathbf{r} + \mathbf{m}_m - \mathbf{m}_{a,m} \quad (3.25)$$

for $m = 1, 2$, and where $\mathbf{r} = \mathbf{G}(c_1 \mathbf{m}_1 + c_2 \mathbf{m}_2) - \mathbf{d}$, is the residual. The transpose of the forward operator is similar for both object functions and for a single datum is given by

$$\mathbf{G}_m^* \mathbf{E}_{ji,sca} = c_m^* \mathbf{E}_i^*(\mathbf{x}) \cdot \overline{\mathbf{G}}^*(\mathbf{x}, \mathbf{x}_j) \cdot \mathbf{E}_{ji,sca} \quad (3.26)$$

where $*$ is simply the conjugate. The complete operation of the transpose is a sum over its application to all the data, and can be thought of as a form of aggregate backprojection, which maps data quantities onto the object domain. We note that the transposes for the permittivity and conductivity only differ by a constant. See Appendix D.2 for the derivation of the operator transpose.

The conjugate gradient updates of the model parameters are

$$\mathbf{m}_{mn} = \mathbf{m}_{mn-1} - \alpha_n \mathbf{v}_{mn} \quad (3.27)$$

$$\mathbf{v}_{mn} = \boldsymbol{\gamma}_{mn} + \beta_{mn} \mathbf{v}_{mn-1} \quad (3.28)$$

For β_{mn} , we used the Polak-Ribiere step given by

$$\beta_{mn} = \frac{\langle \mathbf{C}_{M,m}^{-1} (\boldsymbol{\gamma}_{mn} - \boldsymbol{\gamma}_{mn-1}), \boldsymbol{\gamma}_{mn} \rangle}{\langle \mathbf{C}_{M,m}^{-1} \boldsymbol{\gamma}_{mn-1}, \boldsymbol{\gamma}_{mn-1} \rangle} \quad (3.29)$$

where \langle, \rangle is a simple dot product. Choosing α_n to minimize the cost function at each step, it can be shown that (see Appendix D.1.2),

$$\alpha_n = \frac{\Re \{ \sum_{m=1}^2 (\mathbf{v}_{mn}, \boldsymbol{\gamma}_{mn})_{M,m} \}}{\|\mathbf{s}_n\|_D^2 + \sum_{m=1}^2 \|\mathbf{v}_{mn}\|_{M,m}^2} \quad (3.30)$$

where $\mathbf{s}_n = \mathbf{G}(c_1 \mathbf{v}_{1n} + c_2 \mathbf{v}_{2n})$.

3.4 Numerical Examples

In this section we give several numerical examples of the performance of the electromagnetic inverse scattering algorithm on small imaging domains. These were done simply to confirm the formulation as derived. We used the forward solver to compute synthetic scattered field data which were used as measured scattered field data.

For the following examples, the imaging domain and source configuration are shown in Figure 3.3. The we used 20 frequency points from 1-3 GHz. The background relative permittivity is 30. There are 24 collocated source and receiver positions. The sources are 3-vector Hertzian dipoles and the scattered field was measured in all three Cartesian directions at the same points. We test a hemi-spherical source geometry to mimic a source arrangement in a breast imaging setup, though the imaging domain for now is only $2 \lambda_{min} \times 2 \lambda_{min} \times 2 \lambda_{min}$ due to computation limits, where λ_{min} is the smallest free space wavelength in the transmit spectrum. The domain was sampled at $\lambda_{min}/10 = 1.7$ mm. In the cost function, we gave the data 1% Gaussian noise, and restricted the permittivity and conductivity contrasts to within ± 10 of the background. These values were chosen at the outset for use in the data and model inverse covariance matrices and were not changed during the inversion.

Example 1: Shown in Figure 3.4 are the reconstructions of a single 1λ diameter sphere with a relative permittivity of 33, which is a 10% contrast. We have also made the imaginary part of the background wave number 1 percent that of the real

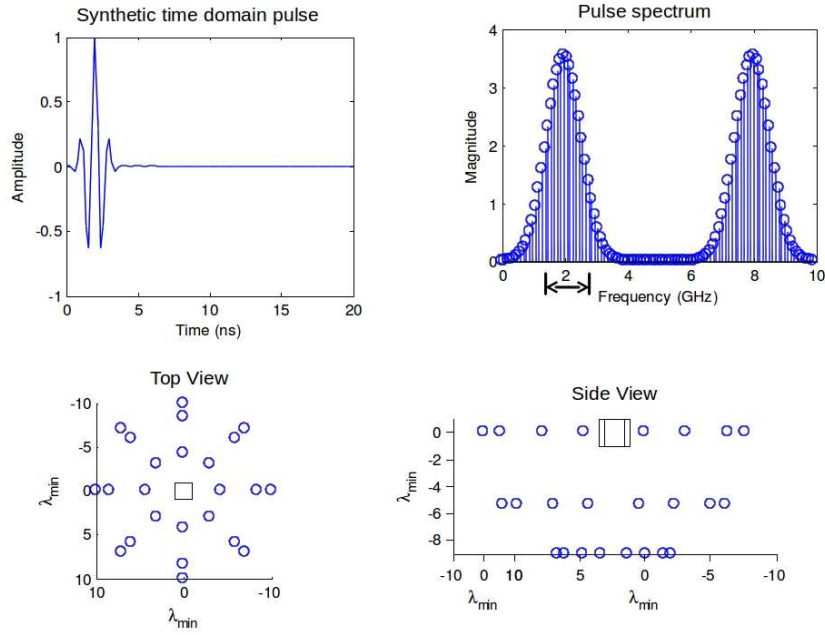


Figure 3.3: Transmit pulse, transmit spectrum and source configuration to test the electromagnetic inverse scattering algorithm.

part. The object shape and permittivity contrast are well recovered after only 2 BIM iterations.

Example 2: Shown in Figure 3.5 are the reconstructions of a single $\lambda/6$ diameter sphere with a relative permittivity of 60, which is a 100% contrast. Same background as Example 1. The object shape and permittivity contrast are well recovered.

Example 3: Shown in Figure 3.6 are the reconstructions of a single λ diameter sphere with a conductivity of 1 Siemens/m, which is a 100% contrast. Same background as Example 1. The object shape and conductivity are well recovered.

Example 4: Shown in Figure 3.7 are the reconstructions of two $\lambda/2$ diameter spheres with relative permittivities of 60. The object shape and location are well recovered, but the contrast is very underestimated. This is the result of the small size of the object and the form of regularization we have used.

Example 5: Shown in Figure 3.8 are the reconstructions of two $\lambda/2$ diameter

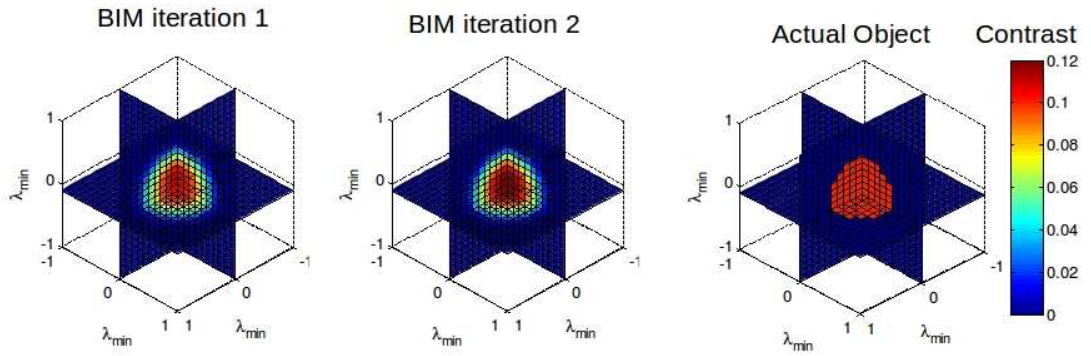


Figure 3.4: Reconstructed object for Example 1 after 2 BIM iterations. Actual object shown at right.

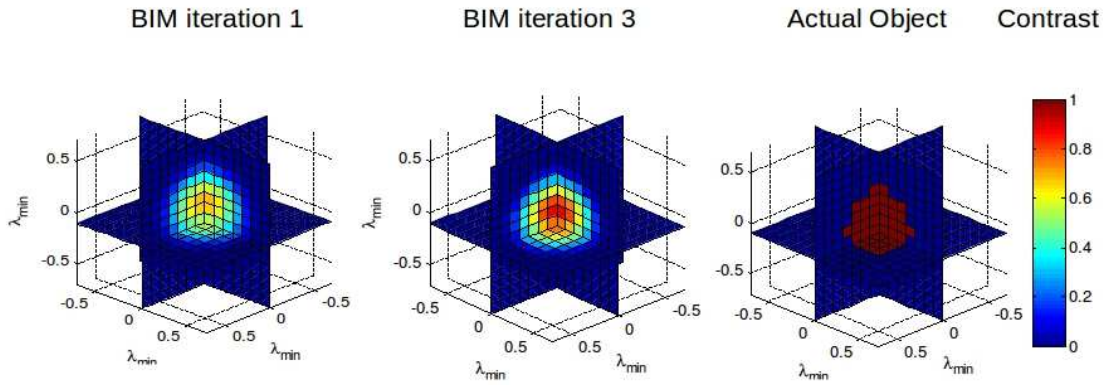


Figure 3.5: Reconstructed object for Example 2 after 3 BIM iterations. Actual object shown at right.

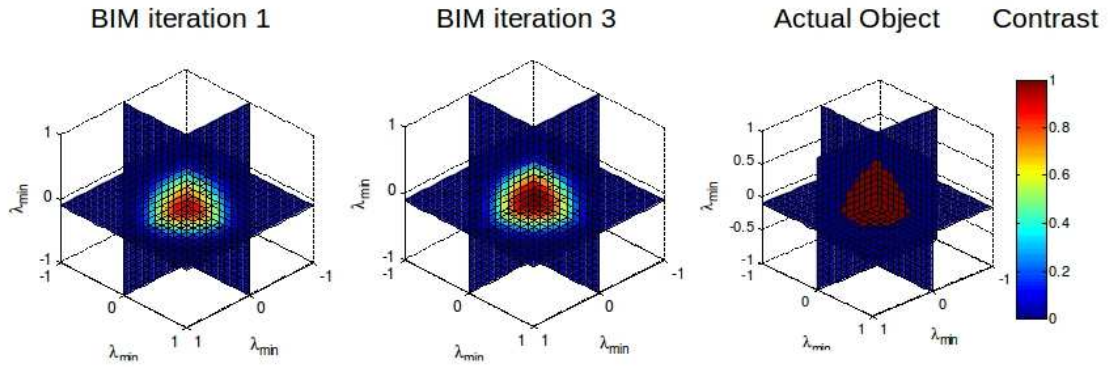


Figure 3.6: Reconstructed object for Example 3 after 3 BIM iterations. Actual object shown at right.

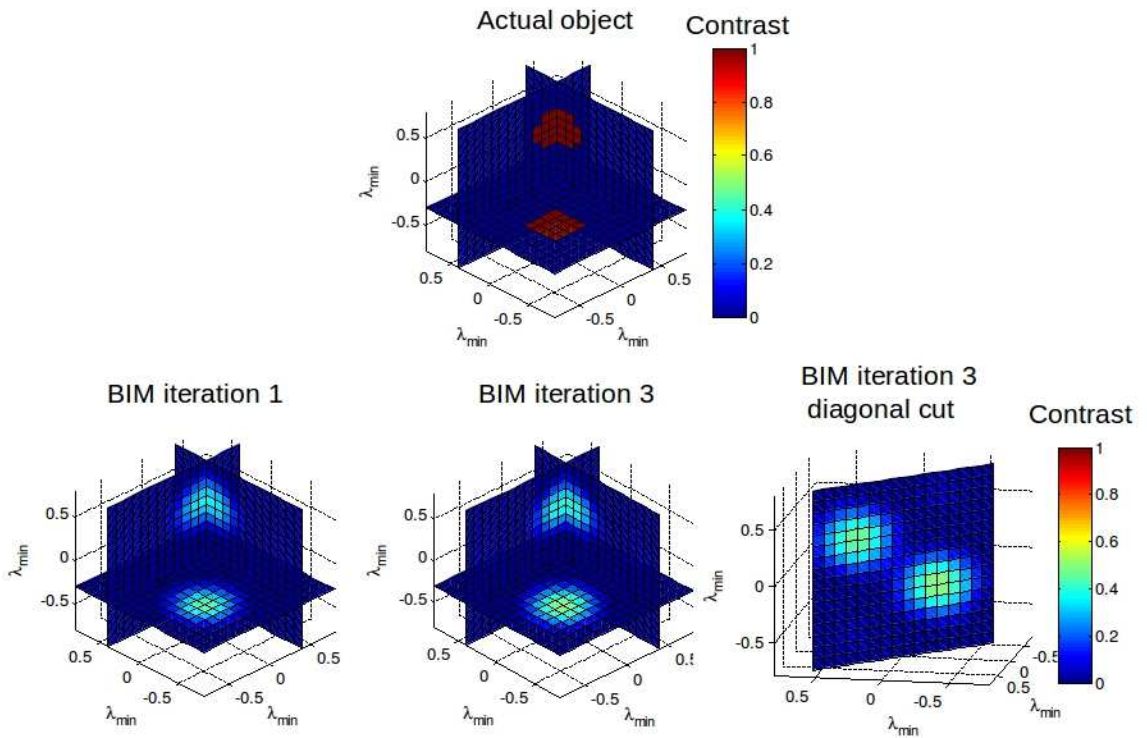


Figure 3.7: Reconstructed object for Example 4 after 3 BIM iterations. Actual object shown at top.

spheres each with a relative permittivity and conductivity of 45 and 0.5 Siemens/m, respectively. The object shape and locations are found, but the conductivity is very underestimated (the scale is reduced by factor of 5). This begins to show the inherent ambiguity of simultaneous retrieval of both relative permittivity and conductivity in the inverse scattering problem.

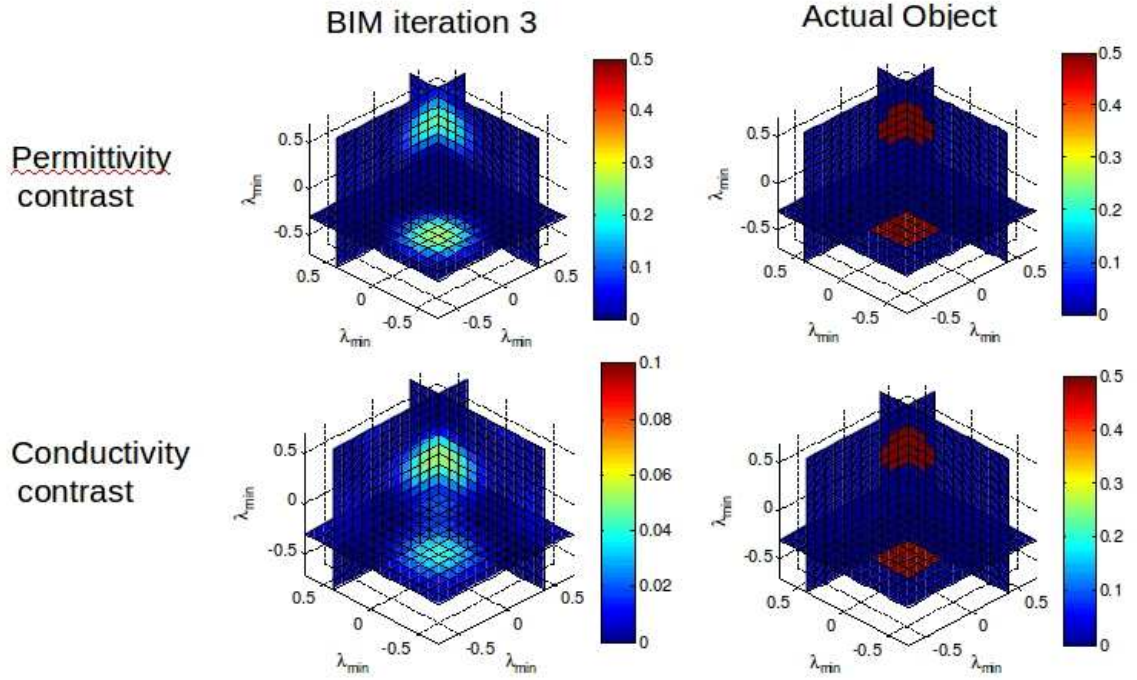


Figure 3.8: Reconstructed object for Example 5 after 3 BIM iterations. Actual objects shown at right.

Example 6: Shown in Figure 3.9 are the reconstructions of two $\lambda/2$ diameter spheres one with a relative permittivity of 45 the other with a conductivity of 0.5 Siemens/m. The permittivity is shape and locations is similar to that in the previous example, but the conductivity is very underestimated (the scale is reduced by factor of 10) and shows two objects. This very clearly demonstrates ambiguity in the retrieval of both relative permittivity and conductivity.

Example 7: Shown in Figure 3.10 are the reconstructions of a random distribution of relative permittivity with values from 15-45. The image is a blurred version of the

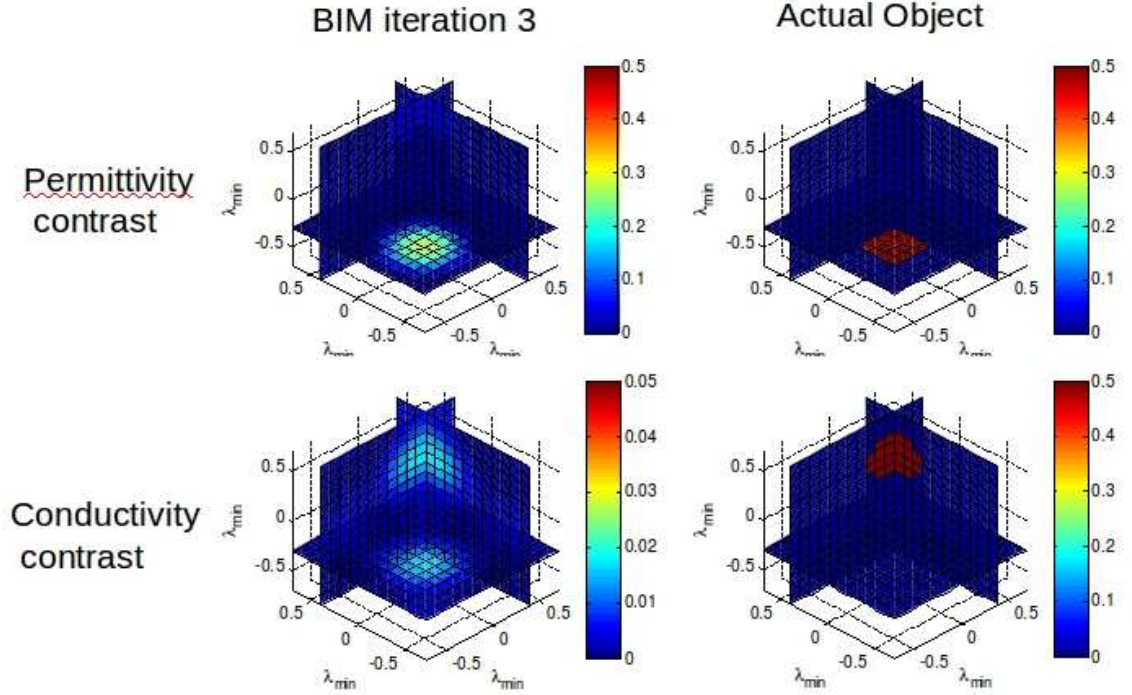


Figure 3.9: Reconstructed object for Example 6 after 3 BIM iterations. Actual objects shown at right.

actual, but even small permittivity fluctuations are recovered.

Example 8: Finally, we demonstrate the effect of the source geometry on the reconstructions. We arrange a similar number of sources in a cylindrical geometry. The object is the same sphere from Example 1. The source geometry and reconstructions are shown in Figure ???. The recovered sphere is elongated in the z -direction.

3.5 Conclusion

In this chapter, we have derived and numerically demonstrated a new version of the electromagnetic inverse scattering algorithm. The key features are the use of the Neumann series and Shanks transformation for the forward solver, the covariance-based cost function for which we could set the regularization parameters at the outset, and conjugate gradient minimization to avoid storing a large system of equations and

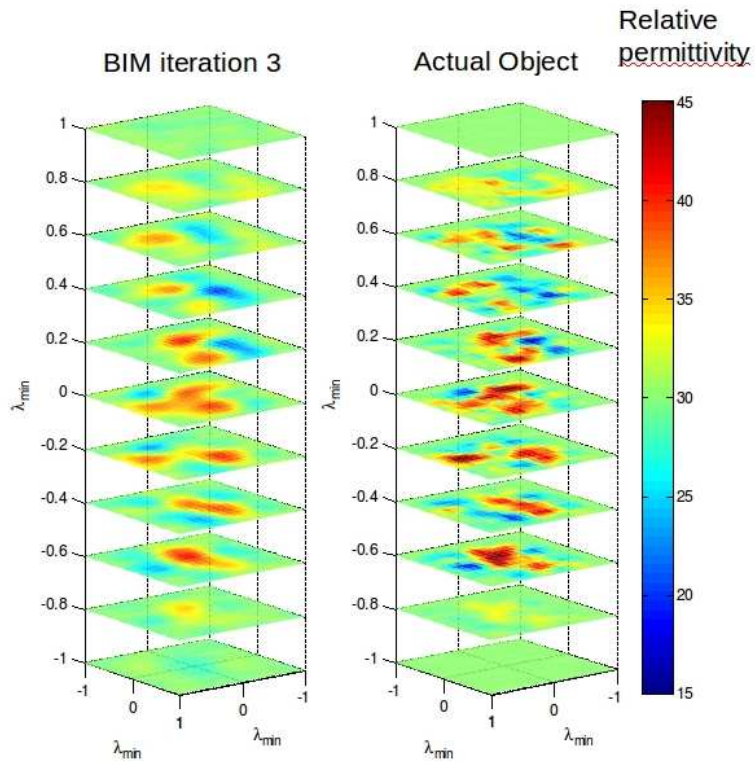


Figure 3.10: Exploded view of reconstructed object for Example 7 after 3 BIM iterations. Actual objects shown at right.

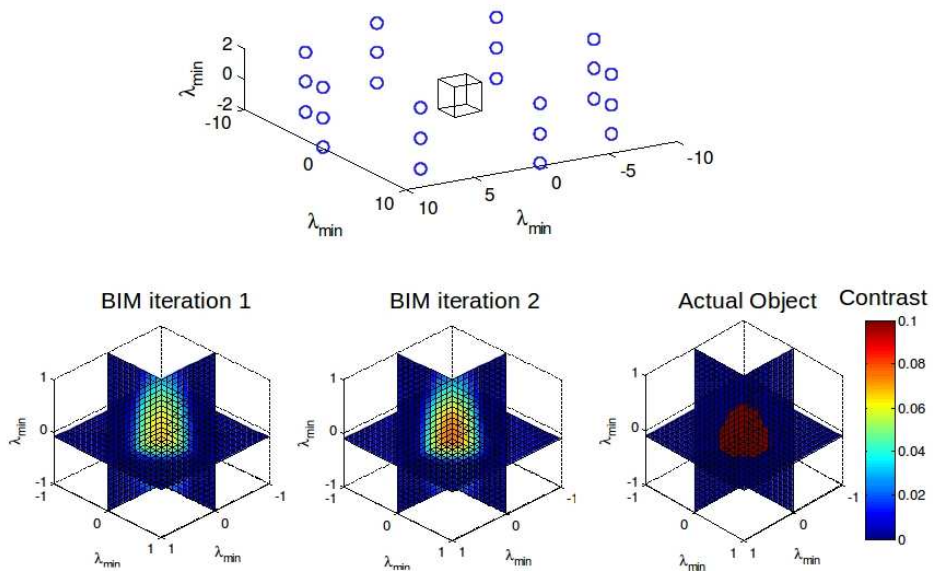


Figure 3.11: Source geometry and reconstructed object for Example 8. Cylindrical arrangement of sources elongates the recovered object in the z -direction.

solving them by matrix inversion.

The examples given were meant to be small to allow quick study of the algorithm. These showed 1) that the algorithm was derived correctly, 2) reconstructions of only relative permittivity or conductivity for solid or random distributions is quite good, and 3) there is inherent ambiguity in the simultaneous retrieval of both permittivity and conductivity, which corroborates the findings of the acoustic inverse scattering problem. Although the imaging domains were small, provided the number of data remains commensurate with the number of unknowns, the size of the domain can be increased without altering the algorithm.

3.6 The Missing Link

The next step is to test both the acoustic and electromagnetic inverse scattering algorithms in experiment. This requires us to calibrate an experimental measurement system by characterizing the sources. We must do this for two main reasons. First, inversion algorithms must have the actual incident field throughout the object domain. In simulation our knowledge of the incident field is essentially perfect, but determining it in experiment is not trivial. The incident field is required for the forward solver, the initial guess of the BIM, and, as will be shown in Chapter V, the scattered field volume integral. Second, the measurements in the acoustic and electromagnetic algorithms are field quantities, either pressure fields or electric fields. This is the traditional treatment in the area of theoretical inverse scattering. However, field measurements present a hurdle when taking these algorithms to experiment. That is because no one, in the history of physics, has ever measured a field quantity directly. We measure forces, and the force of an electric field on an electron is a voltage. For acoustics, we relate the pressure fields to voltages at the output of piezoelectric devices. Thus, there is a missing link between the algorithms as we derive them and the measurements as we take them and this issue is seemingly absent from the majority of inverse

scattering literature. Finding this link, in order to perform meaningful experiments, is the subject of the next few chapters.

CHAPTER IV

Antenna and Propagation Model for S-parameter Measurements

4.1 Introduction

In this chapter, we focus our attention on modeling the fields radiated from an antenna and linking the fields to measurement quantities. Specifically, we show how to obtain the antenna model parameters with simulation, and we derive a propagation model predicting the S-parameter measurements between two antennas. While this discussion and that for the next few chapters is in the context of microwaves, almost any treatment in electromagnetics can be reworked for acoustics.

Two-way propagation models are useful in a variety of microwave communication and measurements scenarios [77, 78, 79, 80]. While antenna radiation patterns and gain might accurately model long range measurements, these are not always convenient to use in full-wave scattering experiments where targets can occupy a large field of view and spatial field distributions are needed. Inverse scattering methods, such as those presented in Chapters II and III, use free-space radiated field distributions as the starting point for iterative algorithms. Also, in the case of receivers, measured output voltages are angle dependent weighted sums of all incoming fields. If we want to predict the output voltage due to incoming fields from many directions, then doing

so, for instance, by integrating over the antenna current distributions [81, 82] can be difficult. Furthermore, S-parameters, which are voltage ratios, are an accurate and often available measurement. Thus, a compact way is needed to relate the spatial distributions of fields radiated and received by antennas to the S-parameters that would be measured between them.

The source-scattering matrix formulation in [83, 84, 85, 86] provides the framework for our S-parameter and propagation model. Specifically, the source-scattering formulation relates modes on a feeding transmission line to the multipole fields radiated and received by an antenna. It assumes the antenna response is linear and captures the effect through a set of model parameters called transmit and receive coefficients. Because the source-scattering formulation is based on the multipole expansion, the fields radiated or received by different antennas in different reference frames are easily related through the use of the addition theorems for vector wave functions [52]. Finally, when considering the modes on the feeding transmission line of multiple antennas radiating and receiving in the presence of each other, we can relate the transmit coefficients of each antenna to S-parameter measurements between them. This forms the basis of our derivation.

Accurately determining the transmit coefficients of an antenna is vital to their use in the propagation model and spatially computing radiated fields. Similar to [83], the approach in [87] uses multipole fields to study antenna interactions, in this case the mutual impedances between multiple stationary antennas. However, in both [83] and [87], the transmit coefficients or multipole coefficients are assumed known or found analytically for simple antennas. These transmit coefficients are also the same as those sought in near-field antenna measurements systems [85]. Near-field antenna systems require precise positioning, sophisticated probe calibration, and are generally expensive ventures. Instead of using a near-field measurement system or analytic methods, we use simulation to approximately determine the transmit coefficients. For

instance, if a CAD model accurately represents the physical structure of an antenna, the fields computed in simulation serve as estimates of probeless field measurements. These simulated fields can then be used to invert the antenna model for the transmit coefficients. We demonstrate this procedure below as an effective use of simulation in place of expensive measurements.

A method to account for the mutual coupling of antennas based on the source-scattering matrix has been developed in theory [86]. Even though we do not consider the multiple scattering between antennas here, we show how to include single-path T-matrix scattering of near-by objects in the propagation model. T-matrices are readily included because they are derived with the same multipole fields as those used in the propagation model [52].

We validate both the propagation model and the inclusion of T-matrix scattering with several experiments using the apertures of two probe-fed waveguides as the antennas. The experiments were done between 4-6 GHz. We show that the magnitude of the predicted S-parameters between the two waveguides matches measurements to better than 2 dB, in most cases, and the phase is better than 10 degrees. This means the model is accurate to $\lambda/10$ (i.e. 36 degrees), which is a common metric for many microwave systems.

This model shows promise for use in a range of laboratory-scale experiments. First, because the antenna model parameters can be estimated with simulation, access to a near-field antenna range is not required to characterize an antenna. Also, the S-parameters predicted by the model are the same as those measured by a vector network analyzer. These two features allow fast development of small-scale scattering and propagation experiments, as well as full antenna characterization. Specifically, this model can be used for the first time to experimentally validate N-scatterer T-matrix solutions, [88], and is a starting point in order to model the multiple scattering of antennas in near-field setups if the antenna T-matrices are known. It can also be

used for diagnostics in multi-antenna setups. Finally, because the antenna characterization is directly related to field measurements, it can be used to implement inverse scattering algorithms.

As a note, we use the vector wave function conventions of [52]; therefore, the normalization constants in the following derivations differ slightly from [83, 84, 87, 85].

4.2 Antenna Model

4.2.1 Electric Field Expansion

Let the total electric and magnetic fields around an antenna be expressed by the multipole expansion

$$\mathbf{E}(\mathbf{r}) = \sum_{lm} [a_{lm}\mathbf{M}_{lm}(\mathbf{r}) + b_{lm}\mathbf{N}_{lm}(\mathbf{r}) + c_{lm}\Re\mathbf{M}_{lm}(\mathbf{r}) + d_{lm}\Re\mathbf{N}_{lm}(\mathbf{r})] \quad (4.1)$$

$$\mathbf{H}(\mathbf{r}) = \frac{k}{i\omega\mu} \sum_{lm} [a_{lm}\mathbf{N}_{lm}(\mathbf{r}) + b_{lm}\mathbf{M}_{lm}(\mathbf{r}) + c_{lm}\Re\mathbf{N}_{lm}(\mathbf{r}) + d_{lm}\Re\mathbf{M}_{lm}(\mathbf{r})] \quad (4.2)$$

where \mathbf{r} is the position vector, k is the wavenumber of the medium, ω is the operating frequency in radians, and μ is the background permeability. $\mathbf{M}_{lm}(\mathbf{r})$ and $\mathbf{N}_{lm}(\mathbf{r})$ are the free-space vector wave functions, and \Re means the regular part of the corresponding spherical Bessel function. The conventions for vector wave functions follow [52], which are also given in Appendix B.1.1. The quantities a_{lm} and b_{lm} are the expansion coefficients for outgoing waves, and c_{lm} and d_{lm} are the coefficients for incoming waves. The number of harmonics needed to represent a field produced by an antenna is $O(kd)$, where d is the largest dimension of the antenna.

4.2.2 Antenna Model

We model the full antenna response following the source-scattering matrix formulation [83, 84, 85]. The antenna is connected to a shielded transmission line, show in Figure 4.1, where a_o and b_o are complex outgoing and incoming modes, respectively, on the transmission line. We relate the modes on the transmission line to the electric field expansion coefficients through a linear model

$$b_o = a_o \Gamma + \sum_{lm} (u_{(c)lm} c_{lm} + u_{(d)lm} d_{lm}) \quad (4.3)$$

$$a_{lm} = t_{(a)lm} a_o + \sum_{l'm'} (S_{(ac)lm,l'm'} c_{l'm'} + S_{(ad)lm,l'm'} d_{l'm'}) \quad (4.4)$$

$$b_{lm} = t_{(b)lm} a_o + \sum_{l'm'} (S_{(bc)lm,l'm'} c_{l'm'} + S_{(bd)lm,l'm'} d_{l'm'}) \quad (4.5)$$

where Γ is the reflection coefficient looking into the antenna. The quantities $u_{(c)lm}$ and $u_{(d)lm}$ are receive coefficients which convert incoming field harmonics to b_o . Similarly, $t_{(a)lm}$ and $t_{(b)lm}$ are transmit coefficients which convert a_o to outgoing field harmonics. The terms $S_{(xy)lm,l'm'}$ capture the passive scattering properties of the antenna, similar to a T-matrix. An in depth explanation of this model is found in [83].

The antenna model can be written in matrix notation as

$$b_o = a_o \Gamma + \begin{bmatrix} \mathbf{u}_c^t & \mathbf{u}_d^t \end{bmatrix} \begin{bmatrix} \mathbf{c} \\ \mathbf{d} \end{bmatrix} \quad (4.6)$$

$$\begin{bmatrix} \mathbf{a} \\ \mathbf{b} \end{bmatrix} = a_o \begin{bmatrix} \mathbf{t}_a \\ \mathbf{t}_b \end{bmatrix} + \begin{bmatrix} \mathbf{S}_{ac} & \mathbf{S}_{ad} \\ \mathbf{S}_{bc} & \mathbf{S}_{bd} \end{bmatrix} \begin{bmatrix} \mathbf{c} \\ \mathbf{d} \end{bmatrix} \quad (4.7)$$

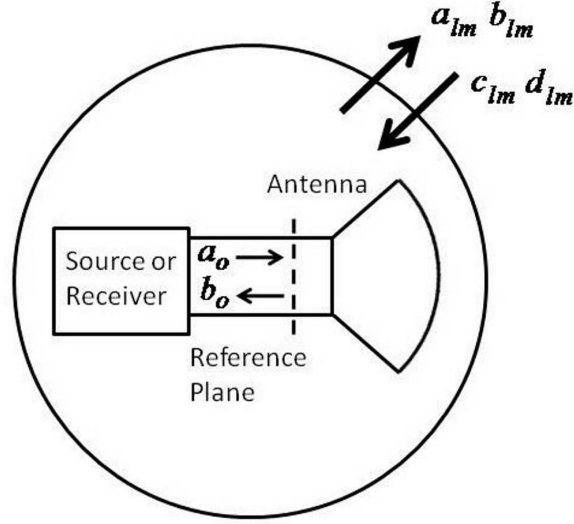


Figure 4.1: Antenna and transmission line setup. a_o and b_o are outgoing and incoming modes on the transmission line, respectively.

4.2.3 Reciprocity Relations

Assuming the antennas are reciprocal, we can establish the following relations between transmit and receive coefficients and between the scattering matrices by evoking the reciprocity theorem for electromagnetics. Following the steps in [83] and [85], with our convention for vector wave functions, see Appendix B.1.1, we arrive at the following reciprocity relations:

$$u_{(c)lm} = \frac{Z_o}{2k\omega\mu} l(l+1)(-1)^m t_{(a)l,-m} \quad (4.8)$$

$$u_{(d)lm} = \frac{Z_o}{2k\omega\mu} l(l+1)(-1)^m t_{(b)l,-m} \quad (4.9)$$

$$S_{(ac)l'm',lm} = c_{lm,l'm'} S_{(ac)l-m,l'-m'} \quad (4.10)$$

$$S_{(bc)l'm',lm} = c_{lm,l'm'} S_{(ad)l-m,l'-m'} \quad (4.11)$$

$$S_{(ad)l'm',lm} = c_{lm,l'm'} S_{(bc)l-m,l'-m'} \quad (4.12)$$

$$S_{(bd)l'm',lm} = c_{lm,l'm'} S_{(bd)l-m,l'-m'} \quad (4.13)$$

$$c_{lm,l'm'} = \frac{l(l+1)}{l'(l'+1)} (-1)^{m+m'} \quad (4.14)$$

where Z_o is the characteristic impedance of the feeding transmission line. The index-dependent multiplying factor in Eqn. (4.14) differs from [83] because the spherical harmonics in the vector wave functions we use are not fully normalized.

Equation (4.8) relates transmit and receive coefficients on the \mathbf{M}_{lm} field harmonics, while Eqn. (4.9) relates transmit and receive coefficients on the \mathbf{N}_{lm} field harmonics. No cross terms and no mixing between $u_{(c,d)lm}$ and $t_{(a,b)lm}$ indicates that \mathbf{M}_{lm} and \mathbf{N}_{lm} harmonics are transmitted and received independently.

4.3 Two Antenna Propagation Model

4.3.1 Two Fixed Antennas

Having established the antenna model, we now derive an expression for the S-parameter, S_{21} , that would be measured between two antennas. Let two antennas be separated by some distance in free space, shown in Figure 4.2. One antenna transmits in reference frame i and the other receives in reference frame j . Each antenna has its own field expansion and set of transmit coefficients, indexed with i and j , respectively. In the following derivation, unprimed indices, lm , index sums in the transmitter frame, while primed indices, $l'm'$, index sums in the receiver frame.

We make the following assumptions,

1. There are no incoming waves in the transmitter frame (i.e., $c_{lm}^i = d_{lm}^i = 0$).
2. The receiver is purely receiving (i.e., the receiver transmission line is matched looking into its source, or $a_o^j = 0$).
3. There is no multiple scattering between the two antennas or between the antennas and other objects (i.e., $S_{(xy)lm,l'm'} = 0$).

Applying the assumptions for the transmitting antenna to Eqns. (4.1), (4.4), and (4.5), we can write the total electric field in the frame of the transmitter as a purely

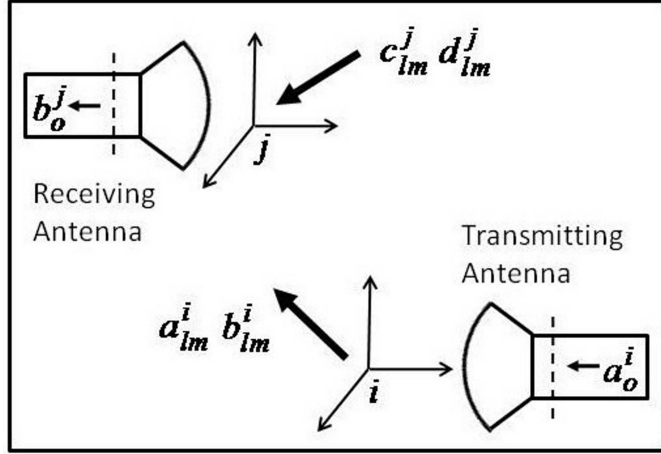


Figure 4.2: Two antenna setup in free space. The transmitting antenna is in frame i and the receiving antenna is in frame j .

radiating wave

$$\mathbf{E}(\mathbf{r}_i) = \sum_{lm} [a_{lm}^i \mathbf{M}_{lm}(\mathbf{r}_i) + b_{lm}^i \mathbf{N}_{lm}(\mathbf{r}_i)] \quad (4.15)$$

with outgoing field coefficients

$$a_{lm}^i = t_{(a)lm}^i a_o^i \quad (4.16a)$$

$$b_{lm}^i = t_{(b)lm}^i a_o^i \quad (4.16b)$$

Applying the assumptions for the receiving antenna to Eqns. (4.1), and (4.3), we can write the incoming field in the receiver frame as

$$\mathbf{E}(\mathbf{r}_j) = \sum_{l'm'} [c_{l'm'}^j \Re \mathbf{M}_{l'm'}(\mathbf{r}_j) + d_{l'm'}^j \Re \mathbf{N}_{l'm'}(\mathbf{r}_j)] \quad (4.17)$$

where the incoming mode on the receiver transmission line is

$$b_o^j = \sum_{l'm'} \left(u_{(c)l'm'}^j c_{l'm'}^j + u_{(d)l'm'}^j d_{l'm'}^j \right) \quad (4.18)$$

Next, we expand the outgoing fields from frame i as incoming fields in frame j using the translation addition theorem for vector spherical harmonics [52], see Appendix B.1.2. The field coefficients in each frame are related by

$$c_{l'm'}^j = \sum_{lm} \left(A_{l'm',lm}^{ji} a_{lm}^i + B_{l'm',lm}^{ji} b_{lm}^i \right) \quad (4.19a)$$

$$d_{l'm'}^j = \sum_{lm} \left(B_{l'm',lm}^{ji} a_{lm}^i + A_{l'm',lm}^{ji} b_{lm}^i \right) \quad (4.19b)$$

where $A_{l'm',lm}^{ji}$ and $B_{l'm',lm}^{ji}$ are the translation matrices with spherical Hankel functions for the radial part. We use $(\cdot)^{ji}$ to indicate that the translation matrices are evaluated with the vector that points from the origin of frame i to that of frame j .

Substituting (4.16) into (4.19), then (4.19) into (4.18) we have

$$\begin{aligned} b_o^j &= a_o^i \sum_{l'm'} \left[u_{(c)l'm'}^j \sum_{lm} \left(A_{l'm',lm}^{ji} t_{(a)lm}^i + B_{l'm',lm}^{ji} t_{(b)lm}^i \right) \right. \\ &\quad \left. + u_{(d)l'm'}^j \sum_{lm} \left(B_{l'm',lm}^{ji} t_{(a)lm}^i + A_{l'm',lm}^{ji} t_{(b)lm}^i \right) \right] \end{aligned} \quad (4.20)$$

Defining the reciprocity constant as $c_r = \frac{Z_o}{2k\omega\mu}$ and the normalization index $n_{lm} = l(l+1)(-1)^m$, we use the reciprocity relations in Eqns. (4.8) and (4.9) to replace the receive coefficients of the receiving antenna with its transmit coefficients,

$$\begin{aligned}
b_o^j &= a_o^i \sum_{l'm'} c_r n_{l'm'} \left[t_{(a)l',-m'}^j \sum_{lm} \left(A_{l'm',lm}^{ji} t_{(a)lm}^i + B_{l'm',lm}^{ji} t_{(b)lm}^i \right) \right. \\
&\quad \left. + t_{(b)l',-m'}^j \sum_{lm} \left(B_{l'm',lm}^{ji} t_{(a)lm}^i + A_{l'm',lm}^{ji} t_{(b)lm}^i \right) \right]
\end{aligned} \tag{4.21}$$

Taking $-m' \rightarrow m'$, only $A_{l'm',lm}^{ji}$ and $B_{l'm',lm}^{ji}$ are affected, because the sums commute and the normalization is unaffected. This gives:

$$\begin{aligned}
b_o^j &= a_o^i \sum_{l'm'} c_r n_{l'm'} \cdot \left[t_{(a)l',m'}^j \sum_{lm} \left(A_{l',-m',lm}^{ji} t_{(a)lm}^i + B_{l',-m',lm}^{ji} t_{(b)lm}^i \right) \right. \\
&\quad \left. + t_{(b)l',m'}^j \sum_{lm} \left(B_{l',-m',lm}^{ji} t_{(a)lm}^i + A_{l',-m',lm}^{ji} t_{(b)lm}^i \right) \right]
\end{aligned} \tag{4.22}$$

Finally, thinking of the two antennas as the ports of a two-port network, together with the conditions above (matched receiver), we can identify the S-parameter, $S_{ji} = b_o^j/a_o^i$,

$$\begin{aligned}
S_{ji} &= \sum_{l'm'} c_r n_{l'm'} \cdot \left[t_{(a)l',m'}^j \sum_{lm} \left(A_{l',-m',lm}^{ji} t_{(a)lm}^i + B_{l',-m',lm}^{ji} t_{(b)lm}^i \right) \right. \\
&\quad \left. + t_{(b)l',m'}^j \sum_{lm} \left(B_{l',-m',lm}^{ji} t_{(a)lm}^i + A_{l',-m',lm}^{ji} t_{(b)lm}^i \right) \right]
\end{aligned} \tag{4.23}$$

So we have formally related the transmit coefficients of each antenna to S-parameter measurements between them. This was possible because we began with an antenna model relating the field harmonics to the modes on the feeding transmission line. It can be shown (see Appendix B.2) that Eqn. (4.23) is reciprocal, that is $S_{ji} = S_{ij}$. The notation, S_{ji} , can be read similarly to its use for multi-port networks, where this is the S-parameter measured by a receiver in frame j due to a transmitter in frame i .

Having demonstrated the basic derivation of the model, we will adopt matrix notation for the remainder of the chapter. We use the indexing convention in [89]. For sums up to order L for all m , there are $L^2 + 2L$ harmonics. The matrix index of the lm harmonic is $l^2 + l + m$. Rewriting the propagation model, we have

$$S_{ji} = \begin{bmatrix} (\mathbf{t}_a^j)^t & (\mathbf{t}_b^j)^t \end{bmatrix} \begin{bmatrix} \mathcal{N} & 0 \\ 0 & \mathcal{N} \end{bmatrix} \begin{bmatrix} \mathbf{A}'_{ji} & \mathbf{B}'_{ji} \\ \mathbf{B}'_{ji} & \mathbf{A}'_{ji} \end{bmatrix} \begin{bmatrix} \mathbf{t}_a^i \\ \mathbf{t}_b^i \end{bmatrix} \quad (4.24)$$

where t denotes the transpose, $[\mathcal{N}]_{lm,lm} = c_r n_{lm}$ is a diagonal matrix of normalization indices, and matrix prime, $'$, denotes evaluating the row indices of the matrix at $m' \rightarrow -m'$.

4.3.2 Two Rotated Antennas

Equation (4.24) can be generalized for antennas which are rotated in their frames. Assume, as before, that there are no additional sources and that there is no multiple scattering. Let the transmitting antenna be initially centered in the unrotated frame i . The antenna is then rotated to a frame, i' , where the rotation is described by its three Euler angles about the origin of i . The antenna transmits, as before, with transmit coefficients \mathbf{t}_a^i and \mathbf{t}_b^i , but now produces outgoing field coefficients in the rotated frame, \mathbf{a}' and \mathbf{b}' , given by

$$\begin{bmatrix} \mathbf{a}' \\ \mathbf{b}' \end{bmatrix} = a_o^i \begin{bmatrix} \mathbf{t}_a^i \\ \mathbf{t}_b^i \end{bmatrix} \quad (4.25)$$

Let the outgoing field coefficients in the unrotated frame be \mathbf{a} and \mathbf{b} . These are related to Eqn. (4.25) through the rotation addition theorem for vector wave functions [90, 91, 92] (see also Appendix B.1.3):

$$\begin{bmatrix} \mathbf{a} \\ \mathbf{b} \end{bmatrix} = \begin{bmatrix} \mathbf{D}_i^* & 0 \\ 0 & \mathbf{D}_i^* \end{bmatrix} \begin{bmatrix} \mathbf{a}' \\ \mathbf{b}' \end{bmatrix} \quad (4.26)$$

where \mathbf{D}_i is the rotation matrix describing the rotation from i to i' and $*$ is conjugate transpose. Next, using the translation relations we expand Eqn. (4.26) as incoming harmonics in the unrotated receiver frame

$$\begin{bmatrix} \mathbf{c} \\ \mathbf{d} \end{bmatrix} = \begin{bmatrix} \mathbf{A}_{ji} & \mathbf{B}_{ji} \\ \mathbf{B}_{ji} & \mathbf{A}_{ji} \end{bmatrix} \begin{bmatrix} \mathbf{a} \\ \mathbf{b} \end{bmatrix} \quad (4.27)$$

Let the receiver be initially unrotated in frame j with receive coefficients \mathbf{u}_c^j and \mathbf{u}_d^j . We then rotate it to a frame j' . From the rotation addition theorem, the incoming field coefficients in the rotated receiver frame, \mathbf{c}' and \mathbf{d}' , are given by

$$\begin{bmatrix} \mathbf{c}' \\ \mathbf{d}' \end{bmatrix} = \begin{bmatrix} \mathbf{D}_j & 0 \\ 0 & \mathbf{D}_j \end{bmatrix} \begin{bmatrix} \mathbf{c} \\ \mathbf{d} \end{bmatrix} \quad (4.28)$$

where \mathbf{D}_j describes the rotation from j to j' . The incoming mode on the receiver transmission line is now

$$b_o^j = \begin{bmatrix} (\mathbf{u}_c^j)^t & (\mathbf{u}_d^j)^t \end{bmatrix} \begin{bmatrix} \mathbf{c}' \\ \mathbf{d}' \end{bmatrix} \quad (4.29)$$

Substituting (4.25)-(4.28) into (4.29) we have

$$b_o^j = a_o^i \begin{bmatrix} (\mathbf{u}_c^j)^t & (\mathbf{u}_d^j)^t \end{bmatrix} \cdot \begin{bmatrix} \mathbf{D}_j & 0 \\ 0 & \mathbf{D}_j \end{bmatrix} \begin{bmatrix} \mathbf{A}_{ji} & \mathbf{B}_{ji} \\ \mathbf{B}_{ji} & \mathbf{A}_{ji} \end{bmatrix} \begin{bmatrix} \mathbf{D}_i^* & 0 \\ 0 & \mathbf{D}_i^* \end{bmatrix} \begin{bmatrix} \mathbf{t}_a^i \\ \mathbf{t}_b^i \end{bmatrix} \quad (4.30)$$

Dividing by a_o^i , applying the reciprocity relations, and multiplying the matrices, we have

$$S_{ji} = \begin{bmatrix} (\mathbf{t}_a^j)^t & (\mathbf{t}_b^j)^t \end{bmatrix} \begin{bmatrix} \mathbf{A}_1 & \mathbf{A}_2 \\ \mathbf{A}_3 & \mathbf{A}_4 \end{bmatrix} \begin{bmatrix} \mathbf{t}_a^i \\ \mathbf{t}_b^i \end{bmatrix} \quad (4.31)$$

where

$$\mathbf{A}_1 = \mathbf{A}_4 = \mathcal{N}\mathbf{D}'_j\mathbf{A}_{ji}\mathbf{D}_i^* \quad (4.32)$$

$$\mathbf{A}_2 = \mathbf{A}_3 = \mathcal{N}\mathbf{D}'_j\mathbf{B}_{ji}\mathbf{D}_i^* \quad (4.33)$$

We are using the i and j indices of \mathbf{D}_i and \mathbf{D}_j to implicitly index rotations in a particular frame. If the antennas are not rotated, $\mathbf{D}_i = \mathbf{D}_j = \mathbf{I}$, the matrix prime moves to the translation matrices and this reduces to the propagation model for two fixed antennas. Equation (4.31) is also reciprocal (see Appendix B.2).

4.3.3 Required Number of Transmit Coefficients

The transmit coefficients represent the excitation-independent multipole expansion of the field radiated by the antenna. Hence, as stated previously, the number of harmonics needed to represent the antenna field is roughly $O(kd)$ where d is the largest dimension of the antenna and k is the operating wave number. Computationally, we must always truncate the expansion, but should do so only after this condition is met.

4.3.4 Coordinate Origins

The placement of an antenna in its reference frame is arbitrary but affects the number of expansion coefficients needed to model the fields. Consider an infinitesimal dipole placed precisely at the origin. Only the $l = 1$ harmonics are needed to represent this source. If, however, the dipole is moved off the origin, then all harmonics are

needed out to $O(kd)$, because, even though the dipole is a concentrated source, the source region now has dimension d relative to the origin. Thus, in order to limit the number of expansion harmonics, the origin of the antenna frame and the antenna itself should be as coincident as possible.

Furthermore, the fact that the transmit coefficients are independent of the excitation means that there are no additional requirements on the positions of the frame origins relative to the antennas. For instance, the origins need not be placed at the phase centers of the antennas. The transmit coefficients also capture all internal propagation effects from the transmission line reference plane to the radiating fields. For instance, if the physical antenna were connected through a long rigid coax cable, then the phase delay arising from the cable length is accounted for in the transmit coefficients. All that matters is that the transmission line reference plane and the antenna coordinate origin be consistent for a particular set of transmit coefficients.

4.4 Scattering Objects

4.4.1 Single-Path Object Scattering

If an object is present, with a known T-matrix, then we can easily include single-path scattering in the propagation model. The scattered field coefficients in the frame of the scatterer are given by

$$\begin{bmatrix} \mathbf{a}_s \\ \mathbf{b}_s \end{bmatrix} = \begin{bmatrix} \mathbf{T}_s^{MM} & \mathbf{T}_s^{MN} \\ \mathbf{T}_s^{NM} & \mathbf{T}_s^{NN} \end{bmatrix} \begin{bmatrix} \mathbf{c}_s \\ \mathbf{d}_s \end{bmatrix} \quad (4.34)$$

where \mathbf{a}_s and \mathbf{b}_s , and also \mathbf{c}_s and \mathbf{d}_s are the scattered and incident field coefficients, respectively. The matrices \mathbf{T}_s^{xy} are T-matrix blocks relating the corresponding incident and scattered field wave harmonics. Assuming the scatterer and antenna reference frames are parallel, we can account for the incident and single-path scattered field in

the antenna model by making the following substitution for the translation matrices

$$\begin{bmatrix} \mathbf{A}_{ji} & \mathbf{B}_{ji} \\ \mathbf{B}_{ji} & \mathbf{A}_{ji} \end{bmatrix} \rightarrow \begin{bmatrix} \mathbf{A}_{ji} & \mathbf{B}_{ji} \\ \mathbf{B}_{ji} & \mathbf{A}_{ji} \end{bmatrix} + \begin{bmatrix} \mathbf{A}_{js} & \mathbf{B}_{js} \\ \mathbf{B}_{js} & \mathbf{A}_{js} \end{bmatrix} \begin{bmatrix} \mathbf{T}_s^{MM} & \mathbf{T}_s^{MN} \\ \mathbf{T}_s^{NM} & \mathbf{T}_s^{NN} \end{bmatrix} \begin{bmatrix} \mathbf{A}_{si} & \mathbf{B}_{si} \\ \mathbf{B}_{si} & \mathbf{A}_{si} \end{bmatrix} \quad (4.35)$$

where \mathbf{A}_{si} and \mathbf{B}_{si} translate fields from the frame of the transmitter to the frame of the scatterer, and \mathbf{A}_{js} and \mathbf{B}_{js} translate fields from the scatterer to the receiver. If the scatterer is rotated, then this too can be accounted for by including rotation matrices on both sides of the T-matrix. Notice that for any combination of single-path scattering, the form of Eqn. (4.31) will not change; transmit coefficients will multiply the outside of a 2x2 block matrix containing some linear combination of rotation and translation matrices.

Like the fields from an antenna, the required number of harmonics needed to accurately represent the scattered field from an object is $O(kd)$, where d is the largest dimension of the scatterer. Furthermore, the \mathbf{A} and \mathbf{B} translation matrices need not be square should the scatterer and antenna transmit coefficients require a different number of harmonics.

4.4.2 Multiple Scattering of Antennas and Objects

Modeling the mutual coupling of the antennas using the source-scattering formulation has been addressed in theory [86]. For our model, however, the assumptions used to derive Eqns. (4.24), (4.31), and (4.35) limit the validity of these expressions to situations where single-path scattering and propagation between two antennas or between an antenna and an object are reasonable. Even still, the propagation model is readily applicable to full-wave T-matrix methods.

If the incoming field coefficients in Eqns. (4.4) and (4.5) represent the incident

field and we replace the source-scattering matrices in the same equations with the T-matrices of the antennas, then we can account for all multiple scattering between the antennas and objects by finding the N-scatterer solution. T-matrix solution methods abound, some examples are [52, 93, 88, 94]. These usually begin with the object T-matrices in isolation, and yield the object T-matrices in the presence of all other scatterers. Demonstrating this application is beyond the scope of this chapter, but is the next step in extending this model to account for all multiple scattering between antennas and objects.

4.5 Determining Transmit Coefficients from Simulation

The transmit coefficients, \mathbf{t}_a and \mathbf{t}_b , are also those sought in near-field antenna measurements [85]. In near-field systems, the coefficients are determined directly by performing the inverse Fourier transform over densely sampled spherical measurements. While the coefficients are in principle determined exactly, near-field antenna characterization requires precise position alignment and probe calibration.

In the absence of a near-field measurement system, one can determine the transmit coefficients approximately from simulation. In simulation we can directly sample the electric field radiated by an antenna. Provided an antenna's numerical CAD model and physical construction are nearly the same, we can substitute actual field measurements (which are never possible) with simulated field measurements. We can then estimate the transmit coefficients by setting up an inverse problem to simply invert the expression for the electric field given in Eqn. (4.1).

Let a single antenna be purely radiating ($\mathbf{a} = a_o \mathbf{t}_a$ and $\mathbf{b} = a_o \mathbf{t}_b$). In simulation, we compute the electric field at points \mathbf{r}_n , where n indexes spatial samples. Writing Eqn. (4.1) in matrix notation for a single point

$$\mathbf{E}(\mathbf{r}_n) = a_o \begin{bmatrix} \mathbf{M}(\mathbf{r}_n) & \mathbf{N}(\mathbf{r}_n) \end{bmatrix} \begin{bmatrix} \mathbf{t}_a \\ \mathbf{t}_b \end{bmatrix} \quad (4.36)$$

We can write this as a linear system over all measurements

$$\mathbf{b} = \mathbf{A}\mathbf{x} \quad (4.37)$$

with

$$\mathbf{x} = \begin{bmatrix} \mathbf{t}_a \\ \mathbf{t}_b \end{bmatrix} \quad (4.38)$$

$$[\mathbf{b}]_n = \mathbf{E}(\mathbf{r}_n)/a_o \quad (4.39)$$

$$[\mathbf{A}]_n = \begin{bmatrix} \mathbf{M}(\mathbf{r}_n) & \mathbf{N}(\mathbf{r}_n) \end{bmatrix} \quad (4.40)$$

where the electric field vector components are stacked row-wise in \mathbf{b} and \mathbf{A} , and the lm harmonic index is column-wise for \mathbf{A} . The field measurements are normalized by the outgoing mode on the transmission line, indicating again that the transmit coefficients are independent of the excitation.

We determine \mathbf{x} , and thus the transmit coefficients, by solving the normal equations of Eqn. (4.37) with Tikhonov regularization.

$$\mathbf{x} = (\mathbf{A}^* \mathbf{A} + \gamma \mathbf{I})^{-1} \mathbf{A}^* \mathbf{b} \quad (4.41)$$

where $*$ is conjugate transpose and \mathbf{I} is the identity matrix.

The number of harmonics needed to represent the antenna field dictates the number of unknowns in the inverse problem. For expansions out to $l = L$, the total number of complex unknowns is $2(L^2 + 2L)$. At least this many complex numeric

field measurements are required to make Eqn. (4.37) overdetermined. Furthermore, these measurements should sample all three components of the field in order to better constrain the problem and yield better estimates for the transmit coefficients.

Because we are determining the transmit coefficients through an inversion procedure, also known as parameter estimation or fitting, we are finding the transmit coefficients of an equivalent source, not the actual source. In general, fitting problems can only be expected to make accurate model predictions in the vicinity of the measurements used for inversion. Antenna problems have the beneficial property that, once an observer is in the far-field, there is no new information about the field at further distances from the antenna. Thus, if the field in Eqn. (4.36) is computed in the far-field of the antenna, we can expect field points beyond those to be reasonably well predicted. We cannot say the same for points in the near-field for the same situation. Furthermore, due to the nature of the multipole expansion, we cannot use field measurements within the dimension d to find the transmit coefficients. So, if we want the transmit coefficients to produce accurate fields in the near-field, then we must use field samples in the near-field but outside d .

4.6 Experimental Validation

To validate Eqn. (4.31) experimentally, we constructed two, hollow, probe-fed brass waveguides to be the antennas. These structures were chosen with the rationale that they could be accurately simulated in Ansoft HFSS. The waveguide body and aperture are the radiating objects we wish to test.

The reason for the use of HFSS is two fold, 1) we need a full-wave simulation to provide numeric field measurements to invert Eqn. (4.36), 2) HFSS can easily model the transmission line feeding the physical waveguide so that we can match the S-parameter reference planes used in simulation to those used by the vector network analyzer (VNA) in measurement.

The waveguides were designed with WR-187 specifications to operate between 3.95-5.85 GHz. The probes feeding the waveguides were SMA female flange mount connectors with an extended dielectric. The positions of the probes were optimized in HFSS for best matching at 5 GHz. After construction, we carefully measured the waveguide dimensions and used these dimensions for field simulations. The CAD model is shown in Figure 4.3. The HFSS transmission line feeding the waveguide had the same inner dimensions and dielectric constant as the SMA probe. This line was de-embedded to the same reference plane of the physical waveguide that would be used by the VNA. The coordinate origin for the antenna reference frame to be used in the propagation model was placed at the center of the waveguide aperture, as shown in Figure 4.3.

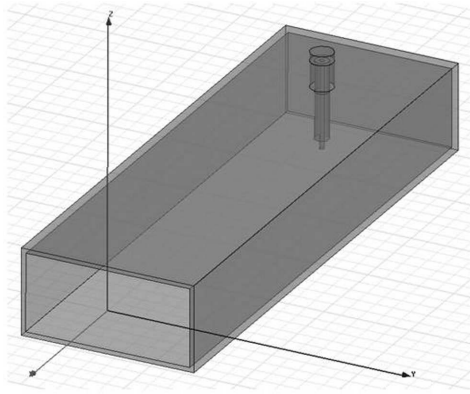


Figure 4.3: HFSS CAD model of probe-fed rectangular waveguide used to determine the transmit coefficients. The coordinate origin for the reference frame of the antenna is the center of the aperture. The de-embedded reference plane for the feeding transmission line is approximately half way up the extruding stalk to match the physical location of the VNA measurement reference plane.

The value of S_{11} of each physical waveguide was measured and compared with simulation, as shown in Figure 4.4. Away from resonance, these were accurate to within 5 degrees of phase, and near resonance these were within 20 degrees, confirming that the CAD model was accurate.

Returning to simulation, we sampled the simulated fields radiated by the aperture

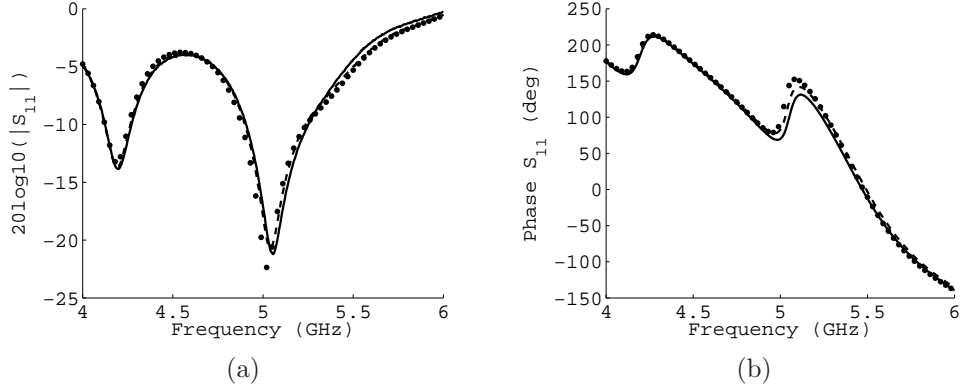


Figure 4.4: Measured and simulated S_{11} for both waveguides. a) Magnitude of S_{11} . b) Phase of S_{11} . Dotted: HFSS simulation; Solid: waveguide 1 measured; Dashed: waveguide 2 measured.

on a sphere with a radius of 20 cm, at 2700 points uniformly distributed on the sphere. Using these numerical field measurements, we solved Eqn. (4.41) for the waveguide transmit coefficients, with harmonics up to $l=10$, for a total of 240 unknown transmit coefficients. We found no regularization was needed in Eqn. (4.41). Transmit coefficients were found at 21 frequencies between 4-6 GHz. The transmit coefficients at 5 GHz up to $l = 4$ are shown in Figure 4.5.

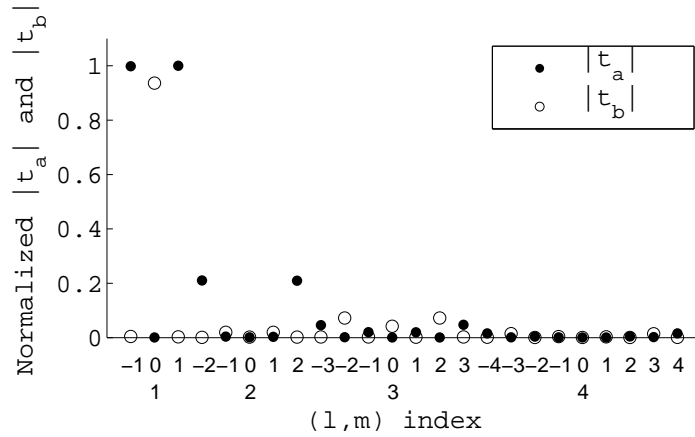


Figure 4.5: Normalized magnitude of transmit coefficients, \mathbf{t}_a and \mathbf{t}_b , found using Eqn. (4.41) for the waveguide in Figure 4.3, with harmonics up to $l = 4$ at 5 GHz. The horizontal axis is the (l, m) index; the upper row is m , the lower row is l . Most of the field information is captured in the first few l .

4.6.1 Determining a_o

The normalization, a_o , in Eqn. (4.39), was determined from the source definitions in HFSS. The input source had an average power of 1 Watt and zero phase. The characteristic impedance of the transmission line computed during simulation, Z_o , was 48.5 Ω . From transmission line analysis, the average power on the line is given by

$$P_{ave} = \frac{|a_o|^2}{2Z_o} \quad (4.42)$$

Rearranging we have

$$|a_o| = \sqrt{2Z_o P_{ave}} \quad (4.43)$$

The coefficient a_o has zero phase because the reference plane of transmission line in the HFSS CAD model matched that of the VNA reference plane of the physical waveguide.

This normalization is applied twice in the propagation model: once for the transmit coefficients of the transmitter and again for the transmit coefficients of the receiver. Thus, with an average simulated source power of 1 Watt, the propagation model is scaled by a factor of $1/(2Z_o)$. Here we assume that the line impedance computed by HFSS is the same as the line impedance of the SMA cables used to connect the VNA to the waveguides.

4.6.2 Examples

Measurements were taken from 4-6 GHz in the University of Michigan Radiation Laboratory anechoic chamber, shown in Figure 4.6. The waveguides pictured are attached to a rigid Styrofoam board and suspended on a Styrofoam pedestal.

Example 1, shown in Figure 4.7, is the magnitude and phase of measured and



Figure 4.6: Example of anechoic chamber measurements of S_{21} . Waveguide apertures in photo are separated by 0.55 m and rotated 30 degrees.

predicted S_{21} for the two antennas separated at two different distances facing one another. Both sets of data are displayed. The distances were 0.55 m and 0.73 m. For both, the magnitude of the model predictions was accurate to better than 1.5 dB. The phase was accurate to better than 10 degrees overall.

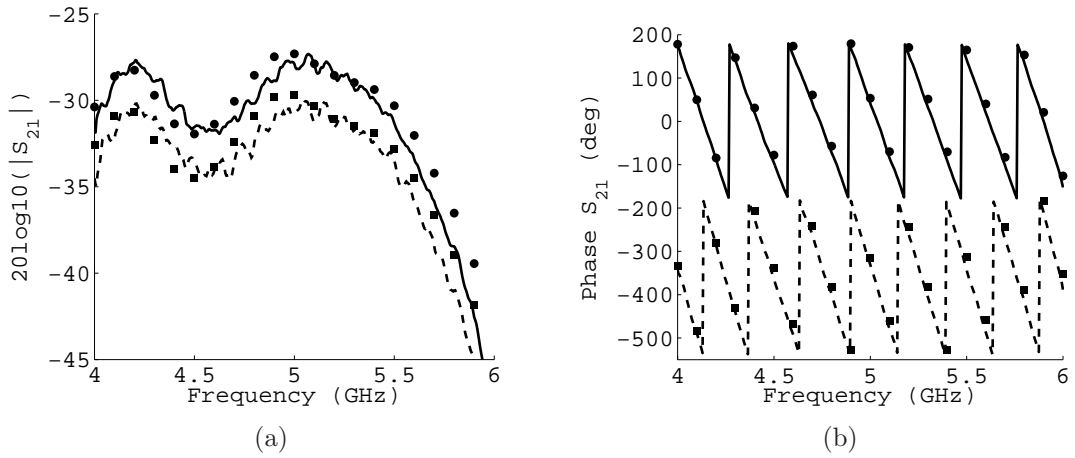


Figure 4.7: Measured and predicted S_{21} for two distances. a) Magnitude of S_{21} . b) Phase of S_{21} . Waveguides are separated by $d_1 = 0.55$ m and $d_2 = 0.73$ m facing each other with no rotation. Solid line and circles: measured and predicted S_{21} , respectively, at d_1 . Dashed line and squares: measured and predicted S_{21} , respectively, at d_2 . Phase for d_2 is shifted by 360 degrees for display.

Example 2, shown in Figure 4.8, is the magnitude and phase of measured and predicted S_{21} for the two waveguides when they are rotated. The data for two sets

of rotations is displayed. The first set is when each waveguide was rotated about the z-axis away from a facing position by 15 degrees. The second set is when both waveguides are rotated by 30 degrees. See also Figure 4.6. The magnitude of the model predictions was accurate to better than 2 dB. The phase of the predictions matched the measurements as well as Example 1.

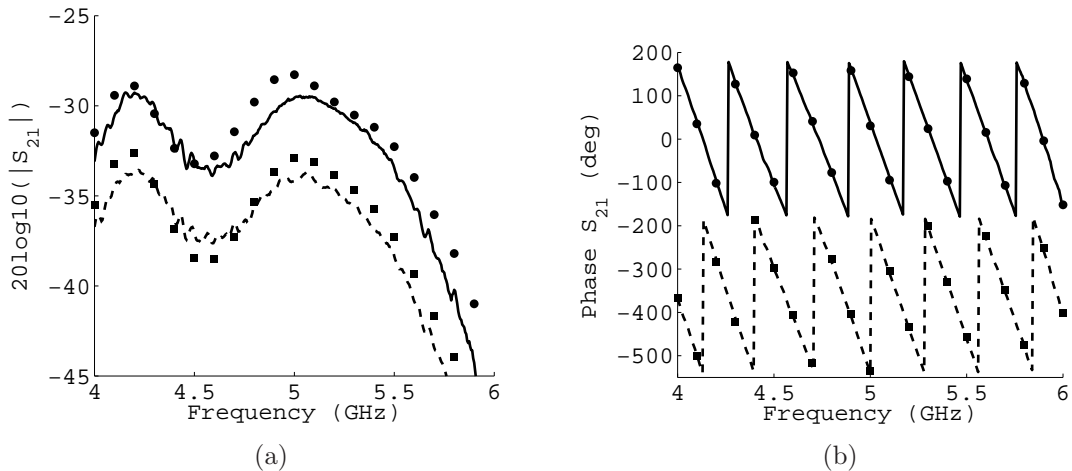


Figure 4.8: Measured and predicted S_{21} for two rotations. a) Magnitude of S_{21} . b) Phase of S_{21} . Waveguides are separated by 0.55 m and rotated about the z-axis of their coordinate systems by $a_1 = 15$ degrees, and $a_2 = 30$ degrees (also shown in Figure 4.6). Solid line and circles: measured and predicted S_{21} , respectively, for a_1 . Dashed line and squares: measured and predicted S_{21} , respectively, for a_2 . Phase for a_2 is shifted by 360 degrees for display.

For Example 3, we demonstrate the use of Eqn. (4.35) to predict the single-path scattered field of an object from its T-matrix. The setup is shown in Figure 4.9. The object is a conducting sphere with a diameter of 2 inches. In the setup, it is held in a Styrofoam cup and placed near the boresight of each antenna. The waveguides pictured are rotated 40 degrees toward the object, and separated by 0.85 m.

The T-matrix of a PEC sphere can be found by solving the boundary condition problem with Eqn. (4.1). The T-matrix is diagonal with elements given by

$$[\mathbf{T}_s^{MM}]_{lm,lm} = -\frac{j_l(ka)}{h_l^{(1)}(ka)} \quad (4.44)$$

$$[\mathbf{T}_s^{NN}]_{lm,lm} = -\frac{j_l'(ka)}{h_l^{(1)'}(ka)} \quad (4.45)$$

and $\mathbf{T}_s^{MN} = \mathbf{T}_s^{NM} = 0$. The quantity a is the radius of the sphere, and $j_l(ka)$ and $h_l^{(1)}(ka)$ are the spherical Bessel and Hankel functions, respectively. Prime denotes a derivative with the form

$$z_l'(x) = \frac{1}{x} \frac{\partial}{\partial x}(xz_l(x)) \quad (4.46)$$

Figure 4.10 shows the magnitude and phase of measured and predicted S_{21} for the incident, total, and scattered fields. The corresponding S-parameters are defined as

$$S_{ji,\text{tot}} = S_{ji,\text{inc}} + S_{ji,\text{sca}} \quad (4.47)$$

where $S_{ji,\text{inc}}$ is measured in the absence of the scatterer, $S_{ji,\text{tot}}$ is measured in the presence of the scatterer, and $S_{ji,\text{sca}}$ is the contribution from the scatterer alone. The scattered field contribution can never be measured directly, but is determined by subtracting the incident field from the total field. This subtraction has the added benefit of eliminating some systematic errors, for example any multipath effects between the two antennas which do not also occur between the antennas and the object.

The magnitude of the model predictions for the scattered field in Figure 4.10 was accurate to better than 1.5 dB. The phase was accurate to better than 10 degrees overall. Similar results were obtained for rotations of [0, 10, 20, 30, 45] degrees.



Figure 4.9: Example of anechoic chamber measurements of S_{21} for a scatterer. The scatterer is a 2 inch diameter conducting sphere. Waveguide apertures in photo are separated by 0.85 m and rotated 40 degrees. The sphere is positioned near the boresights of the waveguide apertures.

4.6.3 Phasor Convention

The vector wave functions we use have $e^{ikr-i\omega t}$ phasor convention. HFSS, however, uses $e^{-jkr+j\omega t}$. Thus, we had to conjugate the simulated field measurements before using them to determine the transmit coefficients in Eqn. (4.37).

Furthermore, we found that the phasor convention of the VNA is that of HFSS. This was determined from technical notes and is consistent with the observation that the phase of simulated and measured S_{11} match. Thus, we need to conjugate Eqns. (4.23) and (4.31) when comparing predictions and measurements. The data displayed include this adjustment.

4.6.4 Discussion of Errors

There are several sources of error that may contribute to differences between the measured and predicted S-parameters. The first major source of error is the estimation procedure used to determine transmit coefficients, Eqn. (4.41). When experimenting with different normalizations for the vector wave functions, we found that predicted S_{21} could change by as much as 0.5 dB (at -30 dB signal levels) for different normalizations. The second major source of error is the lack of multiple

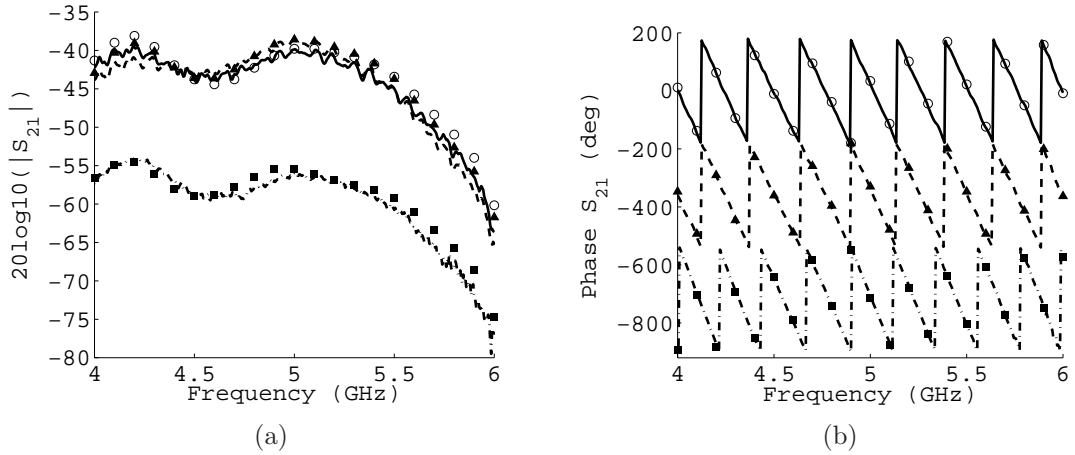


Figure 4.10: Measured and predicted S_{21} of the incident, total and scattered field for the setup in Figure 4.9. a) Magnitude of S_{21} . b) Phase of S_{21} . Solid line and circles: measured and predicted incident field, respectively. Dashed line and triangles: measured and predicted total field, respectively. Dash-dot line and squares: measured and predicted scattered field. Phases for the total and scattered field are shifted by 360 and 720 degrees, respectively, for display.

scattering in the model. The waveguides are directive enough that objects in their bore sight 2-3 m away will noticeably influence the measurements. A third source of error are uncertainties in the values for position and rotation. Position and rotation measurements were taken by hand with uncertainties of a few millimeters in position and a few degrees in rotation. At 6 GHz in free space, the wavelength is 5 cm, so a 5 mm position error is already an error of $\lambda/10$, or 36 degrees. Another source of error was the agreement between the HFSS CAD model and the physical waveguide. From Figure 4.4, we see the most disagreement between measured and simulated S_{11} is near resonance, where the phase differs by as much as 20 degrees. Finally, truncating the sums and any numeric error arising from the translation and rotation matrix multiplications, while undoubtedly present, are considered small relative to the previously listed errors. This is because the transmit coefficients decay quickly for larger l (see Figure 4.5) and because numerical computation of translation and rotation via the addition theorems are nearly exact so long as the correct number of

harmonics are used.

4.7 Conclusion

In this chapter, we derived a model relating the multipole expansions of the fields of two antennas to S-parameter measurements between them. We also showed how numerical simulation can be used to approximately determine the antenna model parameters. We experimentally validated the model using two rectangular waveguides as antennas. Model predictions matched measurements to better than 2 dB in magnitude and better than 10 degrees in phase.

The work in this chapter has a wide range of potential applications. First, it is now very simple to test T-matrix scattering methods on laboratory scales. This is because the propagation model only requires scalar computations based on the locations of antennas. As a demonstration, my colleague, Jessie Duan, used this model to experimentally validate aggregate T-matrix methods. This model now allows accurate and simple testing of multipole scattering methods with network analyzer based experiments. Second, this propagation model is simple enough to be used for inversion methods which could be designed to either find the transmit coefficients, perform multi-sensor diagnostics, or make corrections to models based on experimental data. These ideas are pursued in more depth in Chapter VIII.

In the next chapter, we will use this antenna model to derive a formal link between the integral equations used in the inverse scattering algorithm to S-parameter measurements that would be taken in an experimental imaging system.

CHAPTER V

Vector Green's Function for S-parameter Measurements of the Electromagnetic Volume Integral Equation

5.1 Introduction

In the electric field volume integral equation (VIE), the dyadic Green's function can be used either to determine the total field solution inside the object domain or to move the field quantities inside the object domain to observed fields outside the object domain. While this type of formulation is indispensable for analytical and numerical studies, the vector fields predicted by the VIE in the latter case cannot be observed directly in measurement. That is, actual measurements of fields are performed with antennas or probes, the outputs of which are voltages, which are scalar quantities. Thus, in order to directly link the material contrasts of the VIE to scalar measurement quantities, we need a kernel which, instead of relating fields to fields, relates fields to scalars.

The primary motivation for the work in this chapter is a lack of attention to full-wave antenna models in both theoretical and experimental scattering and inverse scattering. Forward and inverse algorithms based on the VIE commonly use infinitesimal dipole sources and full vector data when analyzing scattering phenomena or

when forming images, [73, 74]. While dipole sources, plane wave sources, or antenna gain patterns, might be adequate for many systems, [95, 96, 97, 98], an additional modeling step, or antenna characterization, is still required to properly link the fields collected by an antenna to its output voltage. Polarimetric remote sensing systems are often calibrated using the radar cross section of trihedral corner reflectors [99, 100], which is appropriate for investigations of rough-surface scattering or other random media for which absolute phase measurements are not required or defined. Full-wave systems, however, such as those for inverse scattering, which 1) use absolute phase, 2) deal with near-fields, or 3) illuminate objects and receive fields from large fields of view, require more complete antenna models. Calibration for far-field scattering systems using spheres has been done successfully in a few cases [101, 102].

Even with the proper use of standard calibration targets for experimental scattering and inverse scattering, a method to directly link the VIE to measurement quantities for both near-field and far-field experiments using a full-wave antenna model is missing. Furthermore, the measurement of choice in microwave engineering is often the set of S-parameters, or some other voltage ratio, due to the ease and accuracy of calibrating a vector network analyzer (VNA), as well as the familiarity and meaning of S-parameters. Thus, we not only want to link the VIE directly to measurement quantities, we also want to link it to S-parameter measurements.

We will show that the antenna model from the previous chapter, when used in conjunction with the VIE, can manifest itself as a new kernel. This new kernel is a vector which moves field quantities in the object region to a scalar voltage on the transmission line. Because of the role this new kernel serves in the VIE, we call it a vector Green's function. We then show that this vector Green's function can be used to predict an object's scattered field S-parameters measured in a mono-static or bi-static antenna system.

To further distinguish the vector Green's function from the standard dyadic Green's

function, we note that the vector Green’s function is used only in a measurement role. It is analogous to when the observation point argument of the dyadic Green’s function is evaluated at a receiver location. The vector Green’s function, however, implicitly includes the antenna model. The vector Green’s function is not used to simulate the forward scattering of an object, nor is it to be confused with the vector Green’s functions named in [103], where it is one column of the dyadic Green’s function, or [104], where it is defined by the gradient of the scalar green’s function.

It can be shown using reciprocity that the dyadic Green’s function is related to the incident field produced by an infinitesimal source. Analogously, we show that the vector Green’s function is related to the incident field produced by an antenna, and formally find the proper scaling factors.

Even though our primary derivation is for antennas and objects in free-space, we justify that the relationship between the vector Green’s function and the antenna incident field holds whether or not there exist closed form expressions for either. This implies that we can use simulation to estimate the vector Green’s function for any complex measurement geometry where it will include all background multiple scattering not included in the VIE object function. This will be useful later when we move to cavity-based imaging geometries.

We validate the vector Green’s function formulation with several experiments. We demonstrate the use of the vector Green’s function in free space using two probe fed waveguides to measure scattering from dielectric spheres. Then, we show how to obtain the vector Green’s function numerically for near-field scenarios, and demonstrate this use with a combination of simulation and experiment.

We include expressions for far-field and Born approximations in Appendix C.1. The following derivation can also be applied to acoustic waves and sources, which will be presented in Chapter VIII.

5.2 Derivation

5.2.1 Volume Integral Equation

The domain and scattered field volume integral equations (VIE) for an inhomogeneous distribution of permittivity and conductivity are again, respectively,

$$\mathbf{E}(\mathbf{r}) = \mathbf{E}_{inc}(\mathbf{r}) + k_o^2 \int \overline{\mathbf{G}}(\mathbf{r}, \mathbf{r}') \cdot \left(\delta\epsilon(\mathbf{r}') + \frac{i\delta\sigma(\mathbf{r}')}{\epsilon_b\omega} \right) \mathbf{E}(\mathbf{r}') dV' \quad (5.1)$$

and

$$\mathbf{E}_{sca}(\mathbf{r}) = \int \overline{\mathbf{G}}(\mathbf{r}, \mathbf{r}') \cdot O(\mathbf{r}') \mathbf{E}(\mathbf{r}') dV' \quad (5.2)$$

where the scattered field is defined

$$\mathbf{E}_{sca}(\mathbf{r}) = \mathbf{E}(\mathbf{r}) - \mathbf{E}_{inc}(\mathbf{r}) \quad (5.3)$$

and the object function is

$$O(\mathbf{r}) = k_o^2 \left(\delta\epsilon(\mathbf{r}) + i \frac{\delta\sigma(\mathbf{r})}{\epsilon_b\omega} \right) \quad (5.4)$$

5.2.2 Antenna Model and Normalized Fields

We model the full antenna response following the source-scattering matrix formulation explained in the previous chapter [83, 84, 85], but use a simplified version

$$b_o = \sum_{lm} (u_{(c)lm} c_{lm} + u_{(d)lm} d_{lm}) \quad (5.5)$$

$$a_{lm} = a_o t_{(a)lm} \quad (5.6)$$

$$b_{lm} = a_o t_{(b)lm} \quad (5.7)$$

The quantities $u_{(c)lm}$ and $u_{(d)lm}$ are again the receive coefficients which convert incoming field harmonics to b_o . Similarly, $t_{(a)lm}$ and $t_{(b)lm}$ are transmit coefficients which convert a_o to outgoing field harmonics.

Here, we have made the following assumptions about the antenna model 1) there is no multiple scattering between the antenna and other antennas or objects, and 2) the transmission line is matched looking into the source or receiver.

Given the assumptions above, the incident field produced by a transmitting antenna is composed of only outgoing waves. Using the antenna model, we can write the incident field in the frame of the transmitter as

$$\mathbf{E}_{inc}(\mathbf{r}) = \sum_{lm} (a_{lm}\mathbf{M}_{lm}(\mathbf{r}) + b_{lm}\mathbf{N}_{lm}(\mathbf{r})) \quad (5.8)$$

$$= a_o \sum_{lm} (t_{(a)lm}\mathbf{M}_{lm}(\mathbf{r}) + t_{(b)lm}\mathbf{N}_{lm}(\mathbf{r})) \quad (5.9)$$

$$= a_o \mathbf{e}_{inc}(\mathbf{r}) \quad (5.10)$$

where we define $\mathbf{e}_{inc}(\mathbf{r})$ as the normalized incident field. This is a field produced by only the transmit coefficients, and can be thought of as the excitation-independent multipole expansion. \mathbf{E}_{inc} has units of V/m and a_o has units of V, so \mathbf{e}_{inc} has units of 1/m.

Next, consider the total field, which is the solution of Eqn. (5.1) given the object contrasts and incident field. Even though the total field results from solving an integral equation, it is still only linearly proportional to the source excitation. Letting the solution of Eqn. (5.1) be represented by the operator inverse, and substituting Eqn. (5.10), we can write the total field as

$$\mathbf{E}(\mathbf{r}) = (\bar{\mathbf{I}} - \bar{\mathbf{G}}O)^{-1} \mathbf{E}_{inc}(\mathbf{r}) \quad (5.11)$$

$$= a_o (\bar{\mathbf{I}} - \bar{\mathbf{G}}O)^{-1} \mathbf{e}_{inc}(\mathbf{r}) \quad (5.12)$$

$$= a_o \mathbf{e}(\mathbf{r}) \quad (5.13)$$

where we define $\mathbf{e}(\mathbf{r})$ as the normalized total field. This is the field solution resulting from a normalized incident field. That is, the field solution due to a source described by only the transmit coefficients. Similar to $\mathbf{e}_{inc}(\mathbf{r})$, $\mathbf{e}(\mathbf{r})$ also has units of 1/m.

5.2.3 Vector Green's Function for S-parameters

The dyadic Green's function, which is the kernel of the VIE, serves to move field quantities inside the object region to field quantities outside the object region. In practice, though, we can never measure fields directly; we measure a voltage response at the terminals of an antenna. We need an additional modeling step to convert the fields at observation points to voltages. The antenna model described previously, [83, 84, 85, 105], is one mechanism to do this. When this antenna model is used in conjunction with the VIE, we will show that it manifests itself concisely as a new kernel, which, instead of transforming fields to fields, transforms fields to scalars. That is, the new kernel will move field quantities inside the object region directly to scalar measurement quantities. This kernel is a vector as opposed to a dyad, and so we call it the vector Green's function. Finally, because the antenna model we use links the fields of an antenna to the voltages on its feeding transmission line, we show, using the concept of normalized fields, that the vector Green's function we derive is specialized for S-parameter measurements.

In order to use the antenna model, we must first expand the scattered field from the VIE as incoming waves in the reference frame of the receiver. We begin with the

addition theorem for the free-space dyadic Green's function from [52],

$$\overline{\mathbf{G}}(\mathbf{r}, \mathbf{r}') = ik \sum_{lm} \frac{1}{l(l+1)} \left[\Re \mathbf{M}_{lm}(\mathbf{r}) \hat{\mathbf{M}}_{lm}(\mathbf{r}') + \Re \mathbf{N}_{lm}(\mathbf{r}) \hat{\mathbf{N}}_{lm}(\mathbf{r}') \right] \quad (5.14)$$

where hat, $\hat{\cdot}$, denotes conjugating the angular part of the vector wave function. The dyad is formed by taking the outer product of $\Re \mathbf{M}_{lm}(\mathbf{r})$ and $\hat{\mathbf{M}}_{lm}(\mathbf{r}')$, and of $\Re \mathbf{N}_{lm}(\mathbf{r})$ and $\hat{\mathbf{N}}_{lm}(\mathbf{r}')$. Here, \mathbf{r} and \mathbf{r}' are position vectors in the frame of the receiver where $|\mathbf{r}| < |\mathbf{r}'|$. Substituting Eqn. (5.14) into the VIE, Eqn. (5.2), we have

$$\mathbf{E}_{sca}(\mathbf{r}) = \int \left(ik \sum_{lm} \frac{1}{l(l+1)} \left[\Re \mathbf{M}_{lm}(\mathbf{r}) \hat{\mathbf{M}}_{lm}(\mathbf{r}') + \Re \mathbf{N}_{lm}(\mathbf{r}) \hat{\mathbf{N}}_{lm}(\mathbf{r}') \right] \right) \cdot \mathbf{O}(\mathbf{r}') \mathbf{E}(\mathbf{r}') dV' \quad (5.15)$$

Exchanging the order of integration and summation, and collecting the terms being integrated, the scattered field of the VIE can be written as incoming fields in the frame of the receiver as

$$\mathbf{E}_{sca}(\mathbf{r}) = \sum_{lm} (c_{lm} \Re \mathbf{M}_{lm}(\mathbf{r}) + d_{lm} \Re \mathbf{N}_{lm}(\mathbf{r})) \quad (5.16)$$

where the expansion coefficients are

$$c_{lm} = \frac{ik}{l(l+1)} \int \hat{\mathbf{M}}_{lm}(\mathbf{r}') \cdot \mathbf{O}(\mathbf{r}') \mathbf{E}(\mathbf{r}') dV' \quad (5.17)$$

$$d_{lm} = \frac{ik}{l(l+1)} \int \hat{\mathbf{N}}_{lm}(\mathbf{r}') \cdot \mathbf{O}(\mathbf{r}') \mathbf{E}(\mathbf{r}') dV' \quad (5.18)$$

Note that the argument of the wave functions is directionally dependent, where \mathbf{r}' points from the origin of the receiver frame to an integration location. However, for the object and the total field, \mathbf{r}' simply keeps track of the integration location.

The quantity $O(\mathbf{r})\mathbf{E}(\mathbf{r})$ can be thought of as a collection of infinitesimal dipole current sources. The vector wave functions in the integrands of Eqns. (5.17) and (5.18) effectively translate the fields radiated from these dipoles so as to be expanded as incoming waves in the frame of the receiver. We can compare this action to the translation of dipole fields in the context of T-matrix methods [52]. The multipole expansion of an infinitesimal dipole has at most three harmonics: $(l, m) = (1, -1), (1, 0), (1, 1)$. Thus, translating dipole fields using the translation matrices for vector spherical harmonics, [52], only requires the first three columns of the matrices. The matrix entries have Hankel functions for the radial part, and the vector argument points from the dipole to the receiver. The wave functions in the integrands of Eqns. (5.17) and (5.18) act as these columns. While these also have Hankel radial parts, the vector argument points from the receiver to the dipole, hence the angular conjugate. Thus, we see that the incoming field coefficients are the aggregates of all translated dipole fields.

We can now interpret the condition $|\mathbf{r}| < |\mathbf{r}'|$ more carefully. The observation points \mathbf{r} are restricted to a sphere with a radius less than the radius of the nearest point of integration in Eqns. (5.17) and (5.18), which is the nearest point of non-zero contrast. In other words, the radius for the field expansion of the receiver cannot overlap the object. See Figure 5.1.

We also point out that the right hand vector of each term of the dyadic outer product serves to translate the scattered fields, while the left hand vector serves to expand the scattered field as incoming waves in the frame of the receiving antenna.

Now that we have the expansion coefficients for the scattered field in the frame of the receiver, we substitute Eqns. (5.17) and (5.18) into the antenna model, Eqn. (5.5), giving

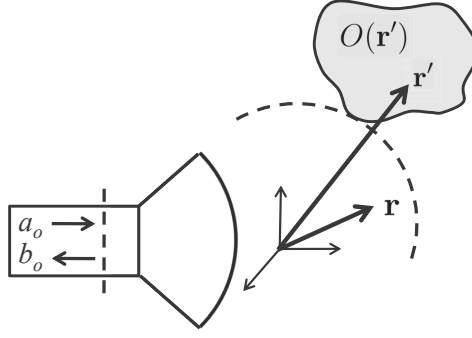


Figure 5.1: Antenna and transmission line setup. The quantities a_o and b_o are outgoing and incoming voltages on the transmission line, respectively. The dotted line represents the nearest point of nonzero contrast and the maximum radius for the antenna multipole expansion.

$$b_o = \sum_{lm} \left[u_{(c)lm} \frac{ik}{l(l+1)} \int \hat{\mathbf{M}}_{lm}(\mathbf{r}') \cdot O(\mathbf{r}') \mathbf{E}(\mathbf{r}') dV' + u_{(d)lm} \frac{ik}{l(l+1)} \int \hat{\mathbf{N}}_{lm}(\mathbf{r}') \cdot O(\mathbf{r}') \mathbf{E}(\mathbf{r}') dV' \right] \quad (5.19)$$

Exchanging the order of integration and summation again and factoring out the object and total field we have

$$b_o = \int \sum_{lm} \frac{ik}{l(l+1)} \left(u_{(c)lm} \hat{\mathbf{M}}_{lm}(\mathbf{r}') + u_{(d)lm} \hat{\mathbf{N}}_{lm}(\mathbf{r}') \right) \cdot O(\mathbf{r}') \mathbf{E}(\mathbf{r}') dV' \quad (5.20)$$

The term multiplying the object and total field acts as a Green's function. It is a vector which moves the vector quantity $O(\mathbf{r}') \mathbf{E}(\mathbf{r}')$ to a scalar, b_o . Letting the vector Green's function be $\mathbf{g}(\mathbf{r})$, we can write the incoming voltage on the transmission line due to the scattered field as

$$b_o = \int \mathbf{g}(\mathbf{r}') \cdot O(\mathbf{r}') \mathbf{E}(\mathbf{r}') dV' \quad (5.21)$$

where

$$\mathbf{g}(\mathbf{r}') = ik \sum_{lm} \frac{1}{l(l+1)} \left(u_{(c)lm} \hat{\mathbf{M}}_{lm}(\mathbf{r}') + u_{(d)lm} \hat{\mathbf{N}}_{lm}(\mathbf{r}') \right) \quad (5.22)$$

The vector Green's function for the free-space VIE is a sum of dipole translations weighted by the receive coefficients of the antenna. It directly links field quantities in the object domain to the incoming voltage on the receiver transmission line.

Next, consider a bi-static system with two antennas, one transmitting in reference frame i , the other receiving in reference frame j , shown in Figure 5.2, and subject to the assumptions in Section 5.2.2. Let the receiver vector Green's function be labeled $\mathbf{g}_j(\mathbf{r})$ and let the total field in the object be $\mathbf{E}_i(\mathbf{r})$, which is the unnormalized total field due to the transmitter. Equation (5.21) then becomes

$$b_o^j = \int \mathbf{g}_j(\mathbf{r}') \cdot O(\mathbf{r}') \mathbf{E}_i(\mathbf{r}') dV' \quad (5.23)$$

Finally, dividing both sides by the outgoing voltage on the transmission line of the transmitter, a_o^i , with the conditions before (matched receiver), we can identify the S-parameter, $S_{ji} = b_o^j/a_o^i$,

$$S_{ji} = \int \mathbf{g}_j(\mathbf{r}') \cdot O(\mathbf{r}') \mathbf{e}_i(\mathbf{r}') dV' \quad (5.24)$$

where $\mathbf{e}_i(\mathbf{r}')$ is the normalized total object field produced by the transmitter.

Thus, we have transformed the traditional scattered field volume integral equation into one suitable for S-parameter measurements. The notation, S_{ji} , can be read similarly to its use for multi-port networks, where this is the scattered field S-parameter measured by a receiver in frame j due to a transmitter in frame i .

While Eqn. (5.24) has been derived in a bi-static S_{21} measurement setup, it also applies to monostatic S_{11} measurements. The S-parameters are measured between the reference planes on the antenna transmission lines, so that the antennas and the object scattering are represented by a 2-port microwave network, shown in Figure 5.2.

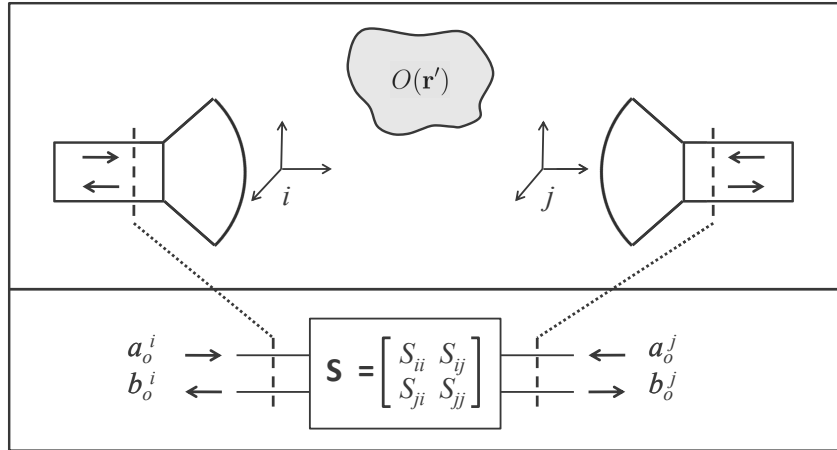


Figure 5.2: Network model of two antennas and a scattering object. S-parameters are measured between the reference planes on the antenna transmission lines.

To summarize, we arrived at an expression in terms of S-parameters because we used an antenna model relating transmission line voltages to multipole fields, as well as the concept of normalized fields.

As stated in the introduction, the vector Green's function is only used in a measurement role; it is not used to simulate the forward scattering of an object. In order to determine the total field or normalized total field in the object domain, one must solve Eqn. (5.1) or Eqn. (5.11) in its entirety using one of numerous techniques, e.g. Conjugate gradient FFT, Neumann series, Finite difference time domain, etc., [106, 107, 108, 53, 109]. The forward solvers also require knowledge of the incident field throughout the object domain. In the context of this model, the normalized incident field is computed using Eqn. (5.10). Lastly, in experiment, we can never measure the scattered field directly, but can obtain it by subtracting the S-parameters for the

total and incident fields,

$$S_{ji,\text{sca}} = S_{ji,\text{tot}} - S_{ji,\text{inc}} \quad (5.25)$$

where $S_{ji,\text{inc}}$ is measured in the absence of the object, and $S_{ji,\text{tot}}$ is measured in the presence of the object.

5.2.4 Reciprocity Relation

Making use of the antenna coefficient reciprocity relations, Eqns. (4.8) and (4.9), we can write $\mathbf{g}(\mathbf{r})$ in terms of the transmit coefficients as

$$\mathbf{g}(\mathbf{r}) = \frac{iZ_0}{2\omega\mu} \sum_{lm} (-1)^m \left(t_{(a)l,-m} \hat{\mathbf{M}}_{lm}(\mathbf{r}) + t_{(b)l,-m} \hat{\mathbf{N}}_{lm}(\mathbf{r}) \right) \quad (5.26)$$

$$= \frac{iZ_0}{2\omega\mu} \sum_{lm} (-1)^m \left(t_{(a)lm} \hat{\mathbf{M}}_{l,-m}(\mathbf{r}) + t_{(b)lm} \hat{\mathbf{N}}_{l,-m}(\mathbf{r}) \right) \quad (5.27)$$

The second relation comes from taking $m \rightarrow -m$ where the sum commutes and $(-1)^m$ is unaffected. We can simplify this further. $\hat{\mathbf{M}}_{lm}(\mathbf{r})$ is the same as $\mathbf{M}_{lm}(\mathbf{r})$ with the angular harmonics conjugated

$$\hat{\mathbf{M}}_{lm}(\mathbf{r}) = \nabla \times [\mathbf{r}z_l(kr)Y_{lm}^*(\theta, \phi)] \quad (5.28)$$

Using the identity $Y_{lm}^* = (-1)^m Y_{l,-m}$, we can show

$$\hat{\mathbf{M}}_{l,-m}(\mathbf{r}) = (-1)^m \mathbf{M}_{lm}(\mathbf{r}) \quad (5.29)$$

The same relation is true for $\mathbf{N}_{lm}(\mathbf{r})$. Using this in Eqn. (5.27), the vector Green's function becomes

$$\mathbf{g}(\mathbf{r}) = \frac{iZ_0}{2\omega\mu} \sum_{lm} (t_{(a)lm}\mathbf{M}_{lm}(\mathbf{r}) + t_{(b)lm}\mathbf{N}_{lm}(\mathbf{r})) \quad (5.30)$$

which is the expansion for the normalized incident field multiplied by a scaling factor

$$\mathbf{g}(\mathbf{r}) = \frac{iZ_0}{2\omega\mu} \mathbf{e}_{inc}(\mathbf{r}) \quad (5.31)$$

or

$$\mathbf{g}(\mathbf{r}) = -\frac{Z_o}{2a_o} \frac{1}{i\omega\mu} \mathbf{E}_{inc}(\mathbf{r}) \quad (5.32)$$

We see that the vector Green's function used in the VIE for a receiver can be interpreted as the incident field produced by that antenna in transmit mode and scaled by factors characterizing the transmission line. This form of the vector Green's function means we can bypass the step of determining the antenna transmit and receive coefficients, if we can obtain and store the incident field with other means, such as simulation.

Recall that the transmit and receive coefficients are related formally through reciprocity, so Eqn. (5.31) is a statement of reciprocity for this type of problem. This equation is another way of expressing the idea that an antenna receives the same way it transmits.

Substituting Eqn. (5.31) into Eqn. (5.24) we can write the VIE in terms of the normalized incident and total fields as

$$S_{ji} = \frac{iZ_0^j}{2\omega\mu} \int \mathbf{e}_{inc,j}(\mathbf{r}') \cdot \mathbf{O}(\mathbf{r}') \mathbf{e}_i(\mathbf{r}') dV' \quad (5.33)$$

where Z_0^j is the characteristic impedance of the receiver transmission line. Note that

$\mathbf{e}_{inc,j}(\mathbf{r}')$ and $\mathbf{e}_i(\mathbf{r}')$ are fields transmitted by the receiver and transmitter, respectively.

Finally, dimensional analysis shows that Eqn. (5.24) is self consistent. From Eqn. (5.31), it can be shown that $\mathbf{g}(\mathbf{r})$ is unitless. The object function, $O(\mathbf{r})$, has units of $1/(\text{m}^2)$, and the normalized total field has units of $1/\text{m}$. Replacing these in Eqn. (5.24), we have

$$S_{ji} = \int \mathbf{g}_j(\mathbf{r}') \cdot O(\mathbf{r}') \mathbf{e}_i(\mathbf{r}') dV' \rightarrow (1) = \int (1) \left(\frac{1}{\text{m}^2}\right) \left(\frac{1}{\text{m}}\right) (\text{m}^3) \quad (5.34)$$

5.2.5 Object-Centered Vector Green's Function

Previously, we derived the vector Green's function for a receiver-centered scattering situation. In principle, given the condition $|\mathbf{r}| < |\mathbf{r}'|$, the object can surround the receiver. In practice, however, multiple antennas usually surround the object. Thus, we will rework the antenna model and derivation for an object-centered situation, where we will be dealing with the condition $|\mathbf{r}'| < |\mathbf{r}|$.

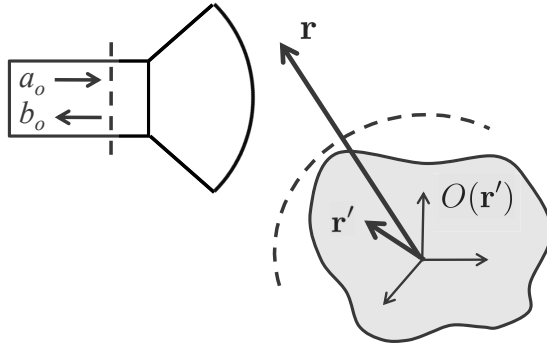


Figure 5.3: Antenna and transmission line setup for an object-centered scattering scenario. The quantities a_o and b_o are outgoing and incoming voltages on the transmission line, respectively. The dotted line represents the furthest point of non-zero contrast.

We begin by considering the setup in Figure 5.3. The multipole expansion of the electric field is the same as before, but now it is expanded in the frame of the object instead of the antenna. The antenna model is

$$b_o = \sum_{lm} (u_{(a)lm} a_{lm} + u_{(b)lm} b_{lm}) \quad (5.35)$$

$$c_{lm} = a_o t_{(c)lm} \quad (5.36)$$

$$d_{lm} = a_o t_{(d)lm} \quad (5.37)$$

The quantities $u_{(a)lm}$ and $u_{(b)lm}$ are the receive coefficients which convert outgoing field harmonics in the frame of the object to b_o . Similarly, c_{lm} and d_{lm} are transmit coefficients which convert a_o to incoming field harmonics in the frame of the object. The derivation of the reciprocity relations between the antenna transmit and receive coefficients is nearly identical to that used to derive Eqns. (4.8) and (4.9), and the following analogous relations can be shown:

$$u_{(a)lm} = \frac{Z_o}{2k\omega\mu} l(l+1)(-1)^m t_{(c)l,-m} \quad (5.38)$$

$$u_{(b)lm} = \frac{Z_o}{2k\omega\mu} l(l+1)(-1)^m t_{(d)l,-m} \quad (5.39)$$

Next, we consider the dyadic Green's function under the condition $|\mathbf{r}'| < |\mathbf{r}|$, which is

$$\overline{\mathbf{G}}(\mathbf{r}, \mathbf{r}') = ik \sum_{lm} \frac{1}{l(l+1)} \left[\mathbf{M}_{lm}(\mathbf{r}) \Re \hat{\mathbf{M}}_{lm}(\mathbf{r}') + \mathbf{N}_{lm}(\mathbf{r}) \Re \hat{\mathbf{N}}_{lm}(\mathbf{r}') \right] \quad (5.40)$$

Substituting this into the VIE we get the scattered field in terms of outgoing coefficients in the frame of the object

$$\mathbf{E}_{sca}(\mathbf{r}) = \sum_{lm} [a_{lm}\mathbf{M}_{lm}(\mathbf{r}) + b_{lm}\mathbf{N}_{lm}(\mathbf{r})] \quad (5.41)$$

where

$$a_{lm} = \frac{ik}{l(l+1)} \int \Re \hat{\mathbf{M}}_{lm}(\mathbf{r}') \cdot O(\mathbf{r}') \mathbf{E}(\mathbf{r}') dV' \quad (5.42)$$

$$b_{lm} = \frac{ik}{l(l+1)} \int \Re \hat{\mathbf{N}}_{lm}(\mathbf{r}') \cdot O(\mathbf{r}') \mathbf{E}(\mathbf{r}') dV' \quad (5.43)$$

The integration vector \mathbf{r}' now points from the origin of the object frame to an integration point still in the object domain. The vector wave functions in the integrands are translating the dipole fields to the origin of the object frame. We see that a_{lm} and b_{lm} are the coefficients for the multipole expansion of the scattered field radiating from the object. This also means that the antennas cannot be inside a sphere with a radius smaller than the furthest point of non-zero contrast from the origin of the object frame, shown in Figure 5.3. Substituting these into the new antenna model we again get

$$b_o = \int \mathbf{g}(\mathbf{r}') \cdot O(\mathbf{r}') \mathbf{E}(\mathbf{r}') dV' \quad (5.44)$$

but this time

$$\mathbf{g}(\mathbf{r}') = ik \sum_{lm} \frac{1}{l(l+1)} \left(u_{(a)lm} \Re \hat{\mathbf{M}}_{lm}(\mathbf{r}') + u_{(b)lm} \Re \hat{\mathbf{N}}_{lm}(\mathbf{r}') \right) \quad (5.45)$$

The last steps in Section 5.2.3 can be used to find the scattered field S-parameter that would be measured between a transmitter and receiver. The incident field from the antenna is now expanded as incoming waves in the frame of the object, and, following the steps of Section 5.2.4, we can arrive at the same relation between the vector Green's function and the incident field, Eqn. (5.31).

5.2.6 Comparison with the Dyadic Green's Function

Here we compare the result of Eqn. (5.32) to the method of determining the dyadic Green's function using the fields of infinitesimal dipoles. The incident field due to an arbitrary current distribution is given by

$$\mathbf{E}_{inc}(\mathbf{r}) = i\omega\mu \int \overline{\mathbf{G}}(\mathbf{r}, \mathbf{r}') \cdot \mathbf{J}(\mathbf{r}') dV' \quad (5.46)$$

Let the current source be an infinitesimal dipole at location \mathbf{r}_p with strength I and direction $\hat{\mathbf{p}}$,

$$\mathbf{J}(\mathbf{r}') = I\hat{\mathbf{p}}\delta(\mathbf{r}' - \mathbf{r}_p) \quad (5.47)$$

Substituting this into the integral we have

$$\mathbf{E}_{inc}(\mathbf{r}, \mathbf{r}_p) = i\omega\mu I \overline{\mathbf{G}}(\mathbf{r}, \mathbf{r}_p) \cdot \hat{\mathbf{p}} \quad (5.48)$$

or

$$\overline{\mathbf{G}}(\mathbf{r}, \mathbf{r}_p) \cdot \hat{\mathbf{p}} = \frac{1}{i\omega\mu I} \mathbf{E}_{inc}(\mathbf{r}, \mathbf{r}_p) \quad (5.49)$$

We can find the columns of the dyadic Green's function by finding the incident field due to three orthogonal dipoles in turn. Using the reciprocity of the dyadic Green's function, [52, 51], we can swap the arguments, \mathbf{r} and \mathbf{r}_p , which will give us the dyadic Green's function used in the VIE to predict observed scattered fields at the point \mathbf{r}_p by integrating over the points \mathbf{r} . In principle, this technique can be used for any problem geometry, not only free-space, and has been used in simulation for nonlinear inverse scattering algorithms [51].

Comparing the multiplying constant in Eqn. (5.49) to that found for the vector Green's function in Eqn. (5.32) shows they differ by a factor of $-Z_o/2$ with a_o in place

of I . We see then that the line voltage, a_o , which normalizes the incident field for the vector Green's function is analogous to the strength of the dipole source, I , which normalizes the incident field for the dyadic Green's function. Thus, collapsing the dyad to a vector using the antenna model results in a constant which only depends on the feeding transmission line and antenna reciprocity.

From the above treatment of the dyadic Green's function, we might have expected the vector Green's function to be related to the incident field, but it took the use of a full antenna model to elucidate the proper multiplying constant in Eqn. (5.32).

5.2.7 Obtaining $\mathbf{g}(\mathbf{r})$

Determining the antenna transmit and receive coefficients is difficult. These are the same transmit and receive coefficients that can be obtained from near-field antenna measurements [85]. Near-field systems are expensive ventures, which require precise positioning and probe calibration. Alternatively, these coefficients can be estimated using simulation as we did in Chapter IV, and [105], from which we can compute $\mathbf{g}(\mathbf{r})$ using Eqn. (5.22) or Eqn. (5.30). However, from Eqn. (5.31), we see it is sufficient to simply know the incident field, which we can choose to determine through measurement or estimate with simulation.

To see how to normalize excitation-dependent fields from a simulator, we substitute the normalized fields from Eqns. (5.10) and (5.13) into Eqn. (5.33)

$$S_{ji} = \frac{i}{2\omega\mu} \frac{Z_o^j}{a_o^j a_o^i} \int \mathbf{E}_{inc,j}(\mathbf{r}') \cdot O(\mathbf{r}') \mathbf{E}_i(\mathbf{r}') dV' \quad (5.50)$$

If we are given the average transmit power on the transmission line, P_{ave} , and the characteristic impedance, then from transmission line analysis the magnitude of a_o is given by, [110],

$$|a_o| = \sqrt{2Z_o P_{ave}} \quad (5.51)$$

The phase of a_o is found by comparing the transmission line reference plane used to determine the simulated fields to those used in measurement by, for instance, a vector network analyzer (VNA). In practice, it may be difficult to determine this phase, so it is best to try to make these reference planes the same, in which case, the phase of a_o will be zero.

If the transmission lines of the transmitter and receiver have the same characteristic impedances, as would be the case for most multi-sensor imaging applications, and the S-parameter reference planes are appropriately aligned between simulation and measurement, then the factor of Z_o drops out of Eqn. (5.50) so it becomes independent of the type of transmission line

$$S_{ji} = \frac{i}{4\omega\mu} \frac{1}{\sqrt{P_{ave,i}P_{ave,j}}} \int \mathbf{E}_{inc,j}(\mathbf{r}') \cdot O(\mathbf{r}') \mathbf{E}_i(\mathbf{r}') dV' \quad (5.52)$$

5.2.8 Generalization

Although the vector Green's function was derived in a free-space scattering scenario, from the results of Eqns. (5.31) and (5.32), we see that the vector Green's function 1) only depends on the antenna incident field and transmission line, and 2) appears to be independent of the basis functions used for the field expansion. This implies that we can generalize the derivation of Section 5.2.3 to any geometry under certain assumptions.

In general, the addition theorem for the dyadic Green's function for a source free region can be written [103, 111]

$$\overline{\mathbf{G}}(\mathbf{r}, \mathbf{r}') = \sum_{\mu} [k' \mathbf{M}_{\mu}(\mathbf{r}) \mathbf{M}_{\mu}^*(\mathbf{r}') + k'' \mathbf{N}_{\mu}(\mathbf{r}) \mathbf{N}_{\mu}^*(\mathbf{r}')] \quad (5.53)$$

where $\mathbf{M}_{\mu}(\mathbf{r})$ and $\mathbf{N}_{\mu}(\mathbf{r})$ are the electric and magnetic (or vice versa) solenoid vector wave functions [52], with adjoints (or inverses) $\mathbf{M}^*(\mathbf{r})$ and $\mathbf{N}^*(\mathbf{r})$ and k' and k'' are their normalizations. There will be conditions on the position vectors \mathbf{r} and \mathbf{r}' specific to the prescribed coordinate system, just as there are for the free-space dyadic Green's function. For example, there exist the analytical solutions of the dyadic Green's function for a z -oriented PEC cylinder, [103, 111], where there are conditions on z and z' .

Assuming that an addition theorem of the form in Eqn. (5.53) exists for a particular geometry, and assuming that the antenna fields can be expanded in the vector wave functions that make up the addition theorem, then we can carry out a derivation that is identical to the one in Section 5.2.3, regardless of the form of $\mathbf{M}_{\mu}(\mathbf{r})$ and $\mathbf{N}_{\mu}(\mathbf{r})$. If the antennas and medium are reciprocal, we will arrive at the same reciprocity relation between the vector Green's function and the incident field, Eqn. (5.31). The term $-Z_o/2a_o$ will always remain because it depends only on the feeding transmission line and electromagnetic reciprocity. The term $1/(i\omega\mu)$ remains as well because it comes from the source term in Maxwell's equations. We have already given one example of this generalization by reworking the derivation of the vector Green's function in Section 5.2.5 for the object-centered scattering situation.

The implications of this generalization are that Eqns. (5.31) and (5.32) will hold whether or not we can find closed-form expressions for the vector wave functions. We need only obtain the incident field, which we can measure experimentally after proper probe calibration, or estimate with simulation. We provide examples in Section 5.3, in both simulation and experiment, to support this generalization.

We also mention that, while the vector Green's function in Eqn. (5.24) serves the purpose of a Green's function by acting as the kernel of the VIE, calling it such

implies that it is the impulse solution to a linear differential or partial differential equation, [112]. In a way it is: while the dyadic Green's function is the solution to an infinitesimal dipole source, the incident field is the solution to the entire source, found by the superposition of dipole solutions that make up the source. However, Green's functions also have completeness relations, [113]. Developing this formalism, if it exists and makes sense to do so, is left for future work, and so we use the name Green's function because of the role it serves as a kernel of the VIE. In the end, we might think of the vector Green's function as the impulse response of an antenna-object microwave network.

5.3 Experimental Validation

We performed several experiments to validate the use of the vector Green's function with the VIE. First, we demonstrate that we can predict the S_{21} scattered field S-parameters from known objects using the VIE and vector Green's function in a free-space scenario. Next, we show we can also predict the S_{11} scattered field of objects close to an antenna. Third, we show with simulation that we can predict 2-port scattered field S-parameters in a near-field scenario for which we can only compute and store the incident and total fields, but otherwise have no knowledge of the types of basis functions that could satisfy the wave equation. Fourth, and last, we compare simulated, predicted, and measured 2-port scattered field S-parameters for a cavity-like experiment. The last two examples support the generalization of Section 5.2.8.

5.3.1 Example 1

First, we compare measured and predicted scattered field S_{21} in free space for a pair of dielectric spheres.

We use the same two identical waveguides from the previous chapter as the trans-

mitter and receiver. The waveguides and spheres are shown in Figure 5.4. The waveguides are characterized using Ansoft HFSS and the method described in Chapter IV. The average power on the transmission line is 1 Watt, so line voltage is given by $a_o = \sqrt{2Z_o}$. The transmit coefficients can then be used in Eqn. (5.10) to compute the normalized incident field at any points around the antenna except those in the very near-field.

The setup for this example is shown in Figure 5.4. The waveguides are placed on a Styrofoam board which is suspended on a Styrofoam pedestal in an anechoic chamber. Measurements were taken between 4-6 GHz. The transmitter and receiver are positioned 40.6cm away from the scatterers. The transmitter is fixed and the receiver is positioned in 15 degree increments about the center from 90 to 180 degrees relative to the transmitter. The spheres are acrylic and identical, having a diameter of 2.54 cm and a relative permittivity of 2.5 and assumed lossless. The spheres are held in a Styrofoam support and separated by approximately 5 cm.

We predict S_{21} using Eqn. (5.33) at 21 discrete frequencies between 4-6 GHz. First, we define an object domain encompassing the two spheres with dimensions 9cm \times 9cm \times 5cm. We discretize the object domain with a regular spacing of 2.5 mm, which is $\sim \lambda/20$ at 6 GHz in a material with relative permittivity of 2.5. The discretized domain and the dielectric contrast of the pair of spheres are shown in Figure 5.5. Then using the transmit coefficients and Eqn. (5.10) we compute the normalized incident field of the transmitter at all points in the object domain. This is used to compute the normalized total field in the object region using the Bi-Conjugate Gradient FFT (BCGFFT), [106, 107, 108]. We use this forward solver because the size of the contrasts of the acrylic spheres are too large for the Neumann series.

Next, we compute the normalized incident field for each receiver location at all points in the object domain, which are used in Eqn. (5.31) to obtain the vector Green's function for each receiver location. Finally, the normalized total field and

vector Green's functions are used in Eqn. (5.33), where we evaluate the integral by summing over the cubic voxels.

Figure 5.6 shows the magnitude and phase of measured and predicted S_{21} for the scattered field for the pair of spheres at receiver angles of 120 degrees and 180 degrees (see also Figure 5.4). We see that the magnitude of measured and predicted S_{21} agree to better than 2 dB across the band (at -50 dB levels or less). The phase agrees overall to better than 20 degrees.

This example shows that we can use the VIE in conjunction with the vector Green's function and a numerical volumetric forward solver to predict S_{21} for the scattered field with a phase much better than $\lambda/10$, i.e., 36 degrees, which is a common metric for many microwave systems.



Figure 5.4: Setup for Example 1. The two waveguides are rotated 120 degrees around the target at distances of 16 inches each. The object consists of two acrylic spheres which are separated by approximately 5 cm.

5.3.2 Example 2

In this example, we use Eqn. (5.33) to predict S_{11} for the setup in Figure 5.7. We use the same procedure as Example 1, however, here we predict the scattered field S_{11} for a single acrylic sphere.

One waveguide is supported by Styrofoam in an anechoic chamber, show in Figure

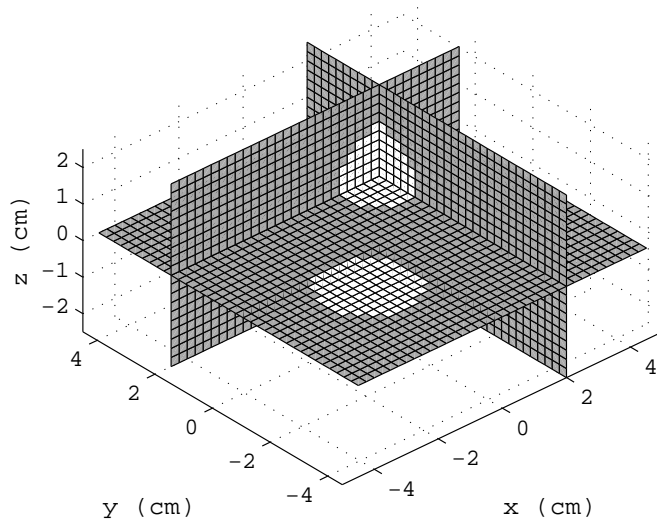


Figure 5.5: Discretized object domain for Example 1. The two spheres have a diameter of 2.54 cm, a relative permittivity of 2.5 in a background of free-space, and are separated by approximately 5 cm. This discretization is used for both the VIE and BCGFFT.

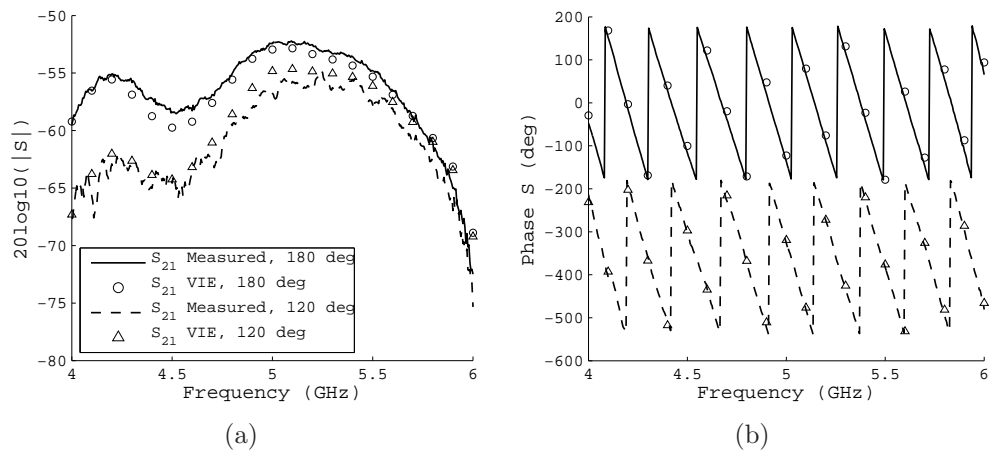


Figure 5.6: Measured and predicted S_{21} of the scattered field for a pair of spheres and the setup in Figure 5.4. a) Magnitude. b) Phase. The results for two receiver angles are shown. Solid line and dots: measured and predicted S_{21} for a receiver at 180 degrees. Dashed line and triangles: S_{21} for a receiver at 120 degrees. The second set of phases is shifted by 360 degrees for display.

5.7. The sphere is held in a Styrofoam and placed two inches in front of the waveguide and one inch to the side of the boresight. We included the Styrofoam holder in the incident field measurement, and it is shown in Figure 5.8.

After evaluating the incident field in the object domain, the normalized total field in the object region is computed again with the BCGFFT. The same incident field is used for the vector Green’s function because we are predicting S_{11} .

From Figure 5.9, we see that the magnitude of measured and predicted S_{11} agree well up to 5 GHz and differ by about 2 dB through 5.6 GHz. The phase agrees to within 10 degrees up to 5.6 GHz. It is clear from the phase that we lose sensitivity above 5.6 GHz. We also attribute the difference in magnitude between measurements and predictions to the lack of multiple scattering in the model, especially as the object becomes electrically larger. Furthermore, the location of the sphere is near the radius of the source dimension for the multipole expansion of the waveguide fields, which will render the incident field computation invalid. Even with these errors, this example demonstrates that reasonable predictions of S_{11} are possible.

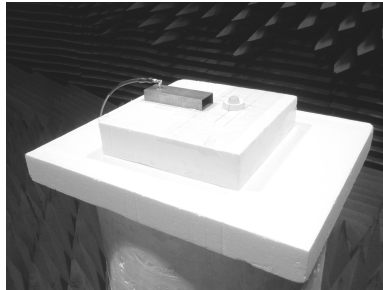


Figure 5.7: Setup for Example 2. The waveguide and acrylic sphere are supported by Styrofoam in an anechoic chamber. The sphere is held in a Styrofoam mount.

5.3.3 Example 3

In this example, we test the vector Green’s function and VIE in simulation. We compare simulated and predicted scattered field S-parameters of an arbitrary distribution of inhomogeneous dielectric objects in a near-field scenario using HFSS. We

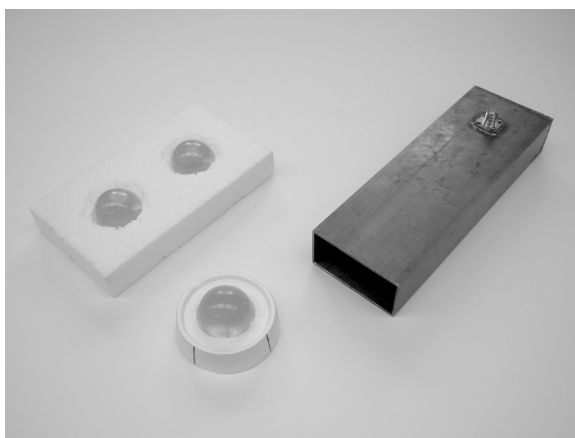


Figure 5.8: Close-up picture of one waveguide and the acrylic spheres used in Examples 1 and 2. The spheres are held in Styrofoam. The spheres in the pair are separated by approximately 5 cm.

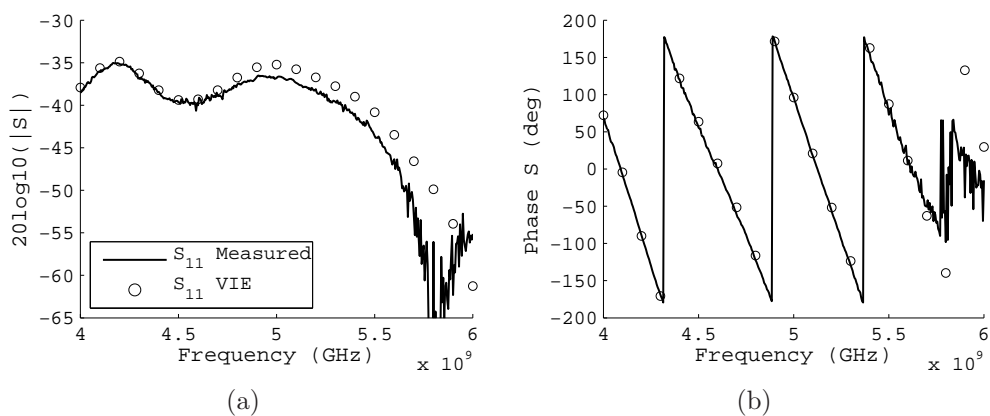


Figure 5.9: Measured and predicted S_{11} of the scatter field for a single sphere and the setup in Figure 5.7. a) Magnitude. b) Phase.

make no assumptions about the nature of the field solution. This example supports the argument that Eqn. (5.31) holds for any geometry.

The simulation domain is shown in Figure 5.10. The simulation region has dimensions of $32\text{cm} \times 38\text{cm} \times 20\text{cm}$, and the object domain is $8\text{cm} \times 10\text{cm} \times 9\text{cm}$. The 2-ports are apertures in PEC walls. The dimensions of the apertures for ports 1 and 2 correspond to WR-430 and WR-187 waveguides, respectively, with characteristic impedances of 250 Ohms and 450 Ohms. The other four sides of the simulation region are radiation boundaries. The dielectric objects are a Teflon sphere, cylinder, and two blocks, with permittivities of 2.1.

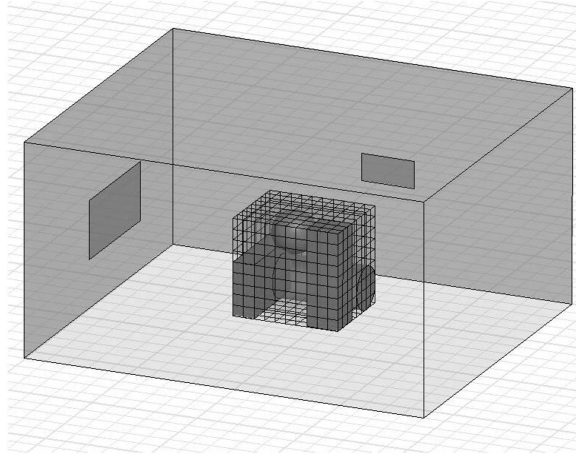


Figure 5.10: HFSS CAD model for Example 3. Two different sized apertures are embedded in PEC walls. The object domain has four dielectric objects and is meshed with a sparse, unassigned grid to constrain the HFSS adaptive meshing.

We use HFSS to both simulate the 2-port S-parameters as well as estimate the incident and total fields in the object region. Because of the proximity of the objects to the apertures, this is a near-field problem where the multiple scattering between the PEC walls and the objects is included in both the incident and total fields.

First, the direct 2-port scattered field S-parameters were simulated between 3-4 GHz, which we treat as the measurement. Next, the incident and total fields were computed by HFSS in the object domain at 21 discrete frequencies between 3-4 GHz.

The fields were sampled on a fine Cartesian grid across the object domain. The grid spacing was 2.5 mm, which is $\sim \lambda/20$ at 4 GHz in Teflon. Because HFSS computes volume fields by interpolating across the finite element mesh, we superimposed a sparse grid of unassigned sheets through the domain before simulation (shown in Figure 5.10). We have found that this sparse grid helps constrain the adaptive meshing of HFSS providing more accurate interpolation on the finely sampled Cartesian grid. The surface sheets of the sparse grid are separated by 9 mm in all three dimensions, which is $\sim \lambda/6$. The sampled incident and total fields were then used in Eqn. (5.50) to predict all four S-parameters. The integral was computed with the trapezoidal method. The average power on the transmission lines are again 1 Watt, so the line voltages are given by $a_o^i = \sqrt{2Z_o^i}$ and $a_o^j = \sqrt{2Z_o^j}$, specific to each port.

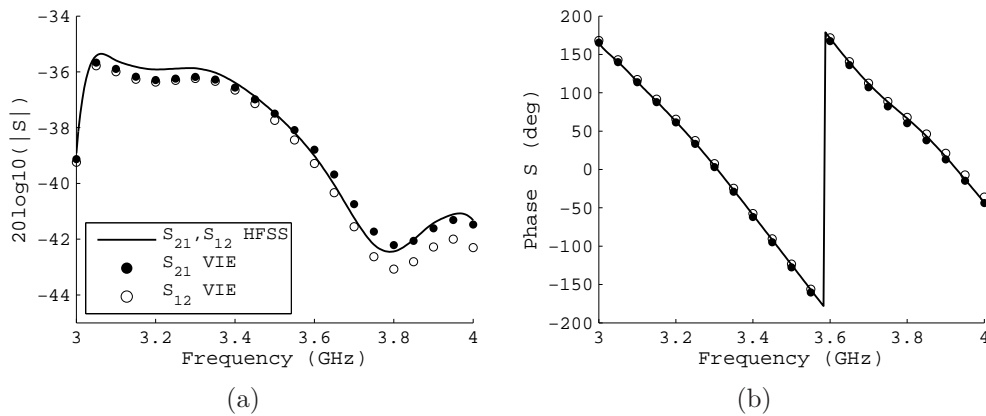


Figure 5.11: Simulated and predicted S_{21} and S_{12} of the scattered field for the simulation in Figure 5.10. a) Magnitude. b) Phase. Solid line: S_{21} and S_{12} computed by HFSS, which are identical. Circles: S_{21} predicted by the VIE. Dots: S_{12} predicted by the VIE. While HFSS computes identical values for S_{21} and S_{12} , the VIE results in some asymmetries due to numerical error.

Figures 5.11 and 5.12 show simulated and predicted 2-port scattered field S-parameters. Overall, simulated and predicted S_{21} and S_{12} agree to within 1 dB in magnitude and 8 degrees in phase, while S_{11} and S_{22} agree to within 2 dB in magnitude and 10 degrees in phase. The system is reciprocal, so all values of S_{21} and S_{12} should be equal. The HFSS simulation yields identical values, but some asymmetries

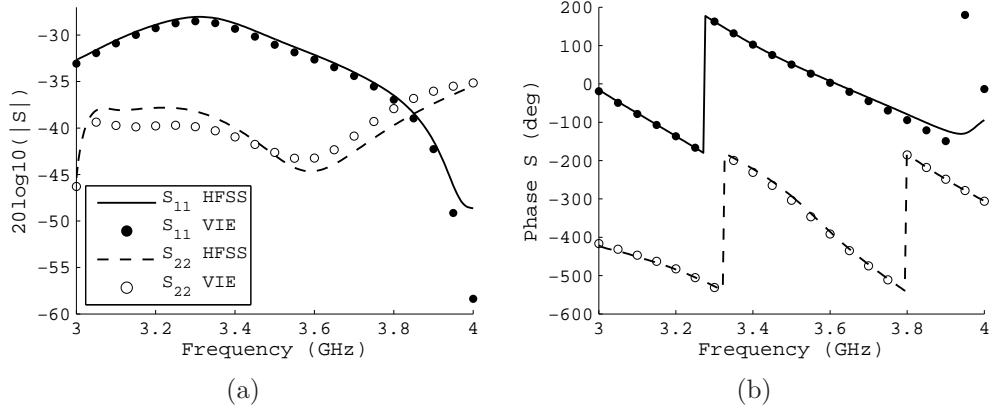


Figure 5.12: Simulated and predicted S_{11} and S_{22} of the scatter field for the simulation in Figure 5.10. a) Magnitude. b) Phase. Solid line and circles: simulated and predicted S_{11} . Dashed line and dots: simulated and predicted S_{22} . Phase of S_{22} is shifted by 360 degrees for display.

are present between predicted S_{21} and S_{12} , which we attributed to interpolation and numerical integration errors. These data confirm the generalization in Section 5.2.8, that we can use the incident field as the vector Green's function in the absence of analytical expressions.

Finally, from technical notes we know that HFSS computes generalized S-parameters, which are normalized to the impedance of the transmission lines in order for the transmitted power to be given by $|a_o|^2$ [110]. We define S-parameters, however, by the line voltages, see also [110]. Thus, in order to compare HFSS and Eqn. (5.50), we multiply Eqn. (5.50) by $\sqrt{Z_o^i}/\sqrt{Z_o^j}$. The data in Figures 5.11 and 5.12 include this adjustment.

5.3.4 Example 4

For the last example, we compare simulated and predicted 2-port scattered field S-parameters to experimental measurements. The simulations and predictions follow the procedure in Example 3, but we validate with an experiment. The structure we tested was a dielectrically loaded waveguide. The physical waveguide and dielectric load are shown in Figure 5.13, and its HFSS CAD model is shown in Figure 5.14.

This example also supports the argument that Eqn. (5.31) holds for any geometry.

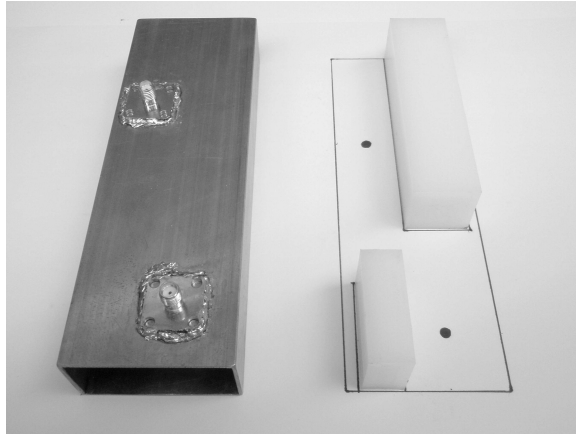


Figure 5.13: Dielectrically loaded waveguide for Example 4. The empty waveguide is shown at left, and the two nylon blocks making up the load and object domains are shown at right. The relative positions of the blocks and probes in the waveguide are outlined underneath.

The waveguide body is the same as those used in Examples 1 and 2, but the ends of the waveguide are left open to prevent cavity resonances which may lead to inaccurate HFSS simulations. The probes are SMA female flange mounts with an extended dielectric. One probe is located 1.91cm inward from one corner along both axes, and the other is located 2.54cm and 1.27cm inward from the other corner.

The dielectric load is composed of two rectangular, nylon blocks having a relative permittivity of 2.93 and assumed lossless. The blocks were machined to fit tightly in the vertical direction to limit the air gap at the metal surface and preserve the dielectric-metal boundary conditions. The blocks had dimensions of 3.78cm \times 1.34cm \times 2.28cm and 9.26cm \times 2.33cm \times 2.28cm. The probe locations and block dimensions were chosen to break any structural symmetries.

Measurements were performed between 4-6 GHz in an anechoic chamber (not pictured). In order to accurately model the positions of the nylon blocks in the CAD model, we first inserted and aligned the dielectric blocks in the physical waveguide. These locations were recorded and used in HFSS. In experiment, we then measured the total field S-parameters first, after which we removed the blocks and measured

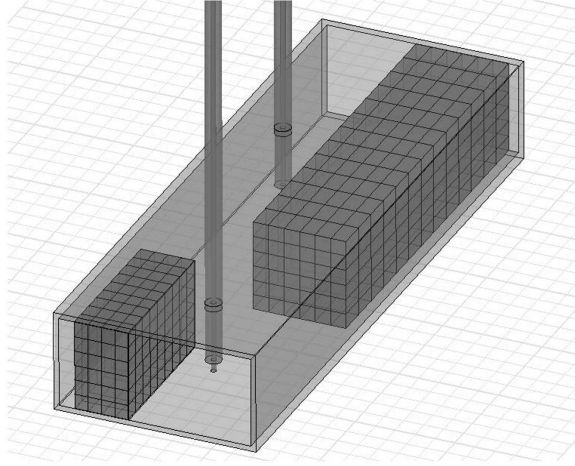


Figure 5.14: HFSS CAD model of the dielectrically loaded waveguide in Figure 5.13. The object domains are meshed with an unassigned sheet grid to constrain the adaptive meshing of HFSS. The waveguide is also enclosed in a large radiation box (not depicted). The coaxial lines extend to the radiation boundary and are de-embedded to the reference planes used by the VNA for the physical waveguide.

the incident field S-parameters, the difference being the scattered field S-parameters.

The simulated and predicted scattered field S-parameters were computed just as in Example 3. The incident and total fields were computed at 41 discrete frequencies between 4-6 GHz. Because both dielectric blocks contribute to the scattered field, the incident and total fields were computed by HFSS in both object regions and the VIE was integrated over both. In addition, the HFSS probes were de-embedded so that the simulation reference planes matched the reference planes used by the vector network analyzer (VNA). This de-embedding correction was also applied to the computed incident and total fields.

Figures 5.15 and 5.16 show the magnitude and phase of measured, simulated, and predicted scattered field S-parameters. The magnitude of simulated and predicted S_{21} match to better than 0.2 dB, and both match the measurements to better than 2 dB across the band. The phases of all three agree to better than 8 degrees. Similar results were obtained for S_{12} . The magnitude of S_{11} of all three quantities agrees to within 1 dB, and the phase better than 10 degrees. S_{22} , however, does not agree as well in

magnitude due in part to the sensitivity of reflection measurements near resonance. The S_{22} phases diverge at resonance, but are otherwise within 10 degrees. Note that the magnitude of S_{22} is greater than 0 dB in the range from 4-5 GHz, because the scattered field magnitude can be greater than the incident or total fields individually. This can be confirmed mathematically by applying the triangle inequality to Eqn. (7.6), [114].

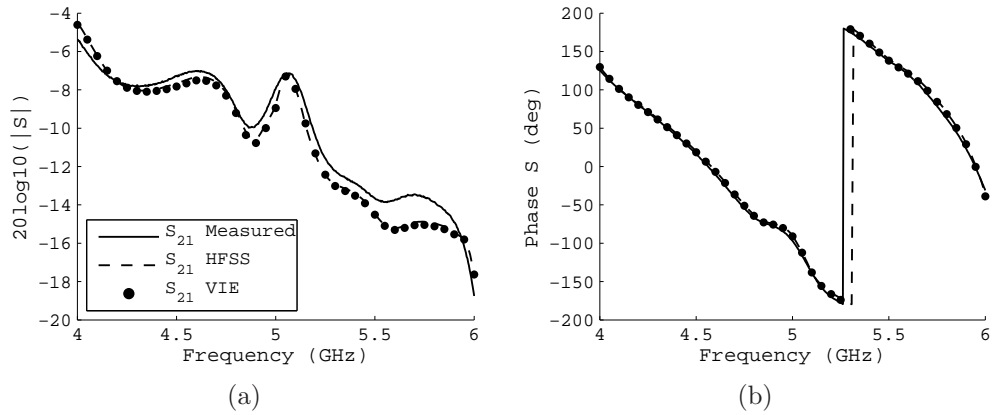


Figure 5.15: Measured, simulated, and predicted S_{21} of the scattered field for the setup in Figures 5.13 and 5.14. a) Magnitude. b) Phase. Solid line: measured S_{21} . Dashed line: S_{21} computed by HFSS. Dots: S_{21} predicted by the VIE and vector Green's function. Similar results were found for S_{12} .

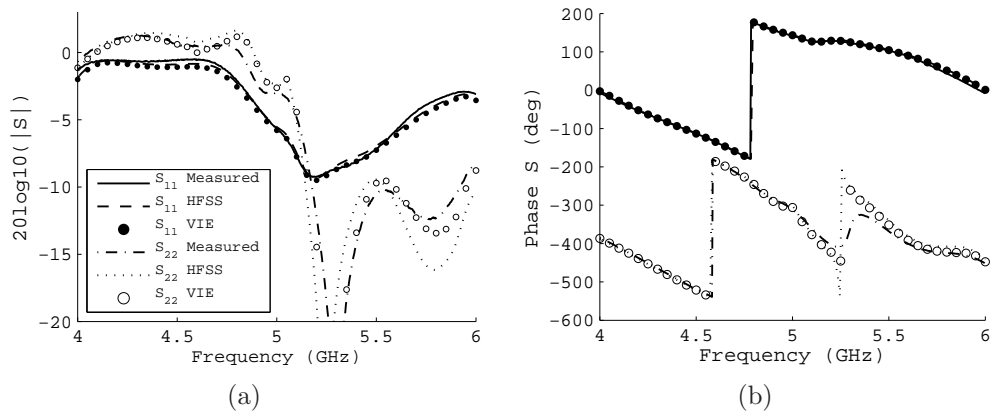


Figure 5.16: Measured, simulated, and predicted S_{11} and S_{22} of the scattered field for the setup in Figures 5.13 and 5.14. a) Magnitude. b) Phase. Phases of S_{22} are shifted by 360 degrees for display.

5.3.5 Discussion of Errors

While the measurements and predictions match well in each example, we need to briefly discuss some sources of error.

For Examples 1 and 2, we can trace the errors through the computational steps. First, and probably the largest contribution to error for the free-space predictions, is the fitting procedure used for the transmit coefficients of the antenna model [105]. This uses a least squares criterion to find an equivalent multipole expansion to fields generated by HFSS. The accuracy of the fit depends on the accuracy of HFSS and number of field data used to find the multipole expansion. The next source of error is the evaluation of the incident field used for the vector Green's function and the BCGFFT. This is obtained by summing over a finite number of the free-space vector wave functions, where inaccuracies will undoubtedly be present. The third source of error is the normalized total field solution given by the BCGFFT. While we validated the BCGFFT with analytical solutions, the spheres must be approximated with their discretized counterparts. Finally, the computation of the VIE itself will be prone to integration errors even for high spatial sampling rates. For Example 2, we have the additional problem that the object is so close to the waveguide that the multipole expansion for the field may not be accurate, and that the effects of multiple scattering, which are non-negligible at that range, are not included in the vector Green's function or the total field computation. Furthermore, the positions and angles of antennas and objects in the experiments were measured by hand, and VNA measurements are subject to some, though small, calibration errors. Last, there is uncertainty in our knowledge of the dielectric constant of the acrylic spheres.

Errors in Example 3 are purely numerical. This example also helps to show us the internal consistency of HFSS. The largest source of error is the interpolation of the FEM CAD mesh to obtain the volume fields. We tried to mitigate this with the undefined, sparse sheet grid.

In order to show that some numerical errors can be controlled, we re-simulated the object in Example 3. The HFSS convergence criteria was tightened from $\Delta S = 0.02$ to $\Delta S = 0.005$. The spatial sampling of the unassigned sheet grid was double to $\sim \lambda/12$, and the sampling of the interpolation and VIE integration points were doubled to $\sim \lambda/40$ in Teflon. A total of 12000 tetrahedra were used in this simulation, which is large given a simulation region of only a few wavelengths. The resulting simulated and predicted S_{21} are shown in Figure 5.17. The magnitudes now agree to within 0.2 dB and phases differ by no more than 1 degree (as compared to 1 dB and 10 degrees, respectively, in Example 3). Similar results were obtained for the other S-parameters. This shows that some of the numerical errors can be controlled with sufficient computation.

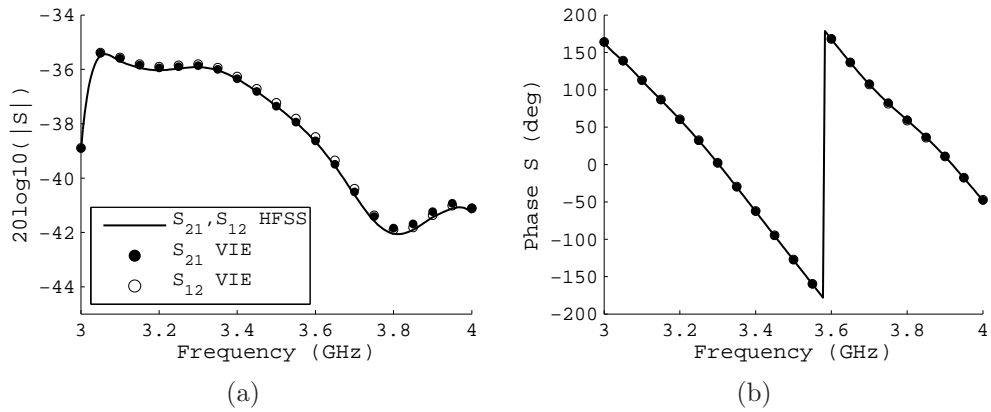


Figure 5.17: Simulated and predicted S_{21} and S_{12} of the scattered field for the simulation in Figure 5.10 with twice the spatial sampling and stricter HFSS convergence criteria than used in Example 3. a) Magnitude. b) Phase. Solid line: S_{21} and S_{12} computed by HFSS, which are identical. Circles: S_{21} predicted by the VIE. Dots: S_{12} predicted by the VIE. This shows that numerical errors can be controlled.

Finally, for Example 4, differences between measured and predicted scattered field S-parameters are due in large part to CAD model inaccuracies and structural resonances that cannot be accurately simulated. This example is also affected by HFSS interpolation errors, VIE integration errors, and uncertainties in the dielectric constant of the objects.

5.3.6 Summary of Experiments

The four examples we presented in this chapter demonstrate the use of the vector Green's function and VIE in simulation and measurement.

Examples 1 and 2 demonstrated that we can predict scattered field S-parameters for objects in free space by using the vector Green's function, the VIE, and a full-wave antenna model. The antenna model allowed us to compute the normalized incident field in the object domain, which we used for the vector Green's function and to find the normalized total field using a volumetric forward solver.

Examples 3 and 4 demonstrated that the methods in this chapter apply to arbitrarily complex geometries, which can include near-field effects. We have shown that we need only obtain the incident field to find the vector Green's function. We can use the VIE and S-parameters to study scattering phenomena of inhomogeneous material in near-field scenarios, such as cavities, where the background multiple scattering can be accounted for by the vector Green's function.

5.4 Conclusion

In this chapter, we derived a vector Green's function for S-parameter measurements of the electric-field volume integral equation for inhomogeneous media. This formulation directly links the object properties to microwave measurements through a source model in a way that can be used for many applications. We have demonstrated how to obtain the vector Green's function from simulation and validated the model with both simulation and experiment in near-field and free-space scenarios.

This formulation effectively solves one of the outstanding problems in inverse scattering. Instead of calibrating a system to convert voltage measurements back to predicted scattered fields, we now have a forward model that directly predicts the voltage measurements, in this case microwave S-parameters. In these examples,

we were essentially validating the forward model of an inverse scattering algorithm. That is, given complete knowledge of the object to be imaged, how accurately can one predict the measurements? Only then does it make sense to run the model in reverse. The elegance of the method lies in the fact that the scattering, simulated incident field, and network analyzer measurements are formally and efficiently related. We need nothing more than the incident field in order to include the behavior of an antenna in the integral equation.

This formulation also has applications for using simulation to experimentally study the electrical properties of material. For instance, cavity based dielectric measurements, where we can parametrically simulate complicate devices and set up an inversion based on the S-parameter integral equation. Its simplicity also expands the use of network analyzer measurements to validate analytical forward scattering models of dielectric objects on laboratory scales. This provides the incident field for use in a forward model, that forward model computes the total field by the method under investigation, and the vector Green's function and scattered field VIE relates everything to the measurement for comparison. One of the next steps is to prove the method for surface integral techniques and random or rough scattering.

In the next chapter, we will prove the use of the vector Green's function and VIE in inverse scattering by using it as the core of a free-space S-parameter based inverse scattering algorithm and experiment.

CHAPTER VI

Free-space Electromagnetic Inverse Scattering Experiment

6.1 Introduction

While microwave inverse scattering has been extensively studied in theory [52, 73, 74, 115, 116, 117, 118, 46, 69, 51, 119], comparatively few experiments have demonstrated their use in practice, [95, 96, 97, 120, 121, 102, 98, 75]. One of the most difficult aspects of experimental inverse scattering is source characterization. That is, how to relate the electric field predictions in the algorithms to antenna voltage measurements in experiment. This problem is not usually treated comprehensively when developing algorithms or when performing experiments. The purpose of the algorithm and experiment in this chapter is to demonstrate how to use the full-wave antenna model and vector Green's function formulation from Chapters IV and V to make an inverse scattering algorithm and S-parameter-based experiment consistent.

As demonstrated in Chapters II and III, inverse scattering algorithms estimate material contrasts by comparing forward model predictions of fields to measurements using a cost function. The forward model is a volume integral equation giving the scattered electric field at observations points. However, the same scattered field cannot be measured directly in experiment; we measure a voltage response at the output

of an antenna. To properly compare forward model predictions to measurements, these two quantities must have the same dimensions. We can either calibrate our setup to convert measured voltages to measured scattered fields, or use an antenna model to convert predicted scattered fields to predicted voltages. The overarching philosophy of this work has been the latter, with the belief that is the most complete, intuitive, and rigorous.

The choice of whether to calibrate a setup or characterize an antenna depends on what assumptions apply in the experiment. For [101], far-field assumptions apply. A precisely located calibration target is used to determine a single complex parameter relating voltage measurements to plane wave amplitudes. Voltage measurements are mapped back to scattered fields, which, in this case, has worked with great success, [120, 102, 98, 121, 95]. However, we often cannot make plane wave assumptions, for instance in small laboratory setups where the antennas are in the quasi near-field, or use calibration targets, for instance, in half space inverse problems [51, 75]. In these cases, we must absolutely characterize the antenna response with a model to map scattered field predictions to voltage predictions. This necessarily changes the forward model and affects the downstream implementation of the inversion algorithm.

The goal here is to test the antenna model, vector Green's function formulation, and BIM in a free-space inverse scattering experiment. The overall structure of the BIM given in Chapter III is largely unchanged. However, our forward model now predicts scattered field S-parameters. This required rederiving the gradients and operator transposes in the conjugate gradient minimization steps. We will show how the values of the entries of the data and model covariance matrices are selected from experiment. We will also show what must be done to make the S-parameter based forward model consistent with the experiment.

We form images of the 2D dielectric profiles of finite cylindrical objects using a full 3D inverse scattering algorithm and 2D source geometry. The shapes of different

objects are discernible even though the contrast value is often underestimated. We also show that the algorithm breaks down for large contrast objects too closely spaced for this source geometry.

6.2 Formulation with Source Characterization

6.2.1 Integral Equations for Characterized Sources and S-parameters

First, we will make the domain VIE and scattered field VIE consistent. We essentially did this in Example 1 of Chapter V, where we simulated the volumetric scattering of the two acrylic spheres and predicted the scattered field S-parameters using the vector Green's function, but here we will point out the equations explicitly for the inverse scattering algorithm.

We write Eqn. (5.1) in terms of the normalized incident and total fields by dividing both sides by a_o ,

$$\mathbf{e}(\mathbf{r}) = \mathbf{e}_{inc}(\mathbf{r}) + \int \overline{\mathbf{G}}(\mathbf{r}, \mathbf{r}') \cdot O(\mathbf{r})\mathbf{e}(\mathbf{r}')dV' \quad (6.1)$$

This is the integral equation we will use to represent the forward scattering solution. It is solved with the same methods used to solve Eqn. (5.1), e.g. FDTD, CGFFT, Neumann Series [47, 106], but with $\mathbf{e}_{inc}(\mathbf{r})$ used in place of $\mathbf{E}_{inc}(\mathbf{r})$.

Using the vector Green's function formulation from Chapter V, the two-port scattered field S-parameter, $S_{ji,sca}$, measured between the two antennas in the presence of an object is again given by

$$S_{ji,sca} = \int \mathbf{g}_j(\mathbf{r}) \cdot O(\mathbf{r})\mathbf{e}_i(\mathbf{r})dV \quad (6.2)$$

where $\mathbf{e}_i(\mathbf{r})$ is the normalized total object field produced by the transmitter and $\mathbf{g}_j(\mathbf{r})$ is the vector Green's function kernel for the receiver. This assumes any multiple

scattering between the antennas and object is negligible. The vector Green's function is again

$$\mathbf{g}_j(\mathbf{r}) = \frac{iZ_0^j}{2\omega\mu} \mathbf{e}_{inc,j}(\mathbf{r}) \quad (6.3)$$

where ω is the operating frequency in radians, μ is the background permeability, and Z_0^j is the characteristic impedance of the receiver transmission line.

Equations (6.1) and (6.2) are the integral equations we will use for the inverse scattering algorithm. They consistently link the physics of the electromagnetic inverse scattering problem to an S-parameter measurement system through a full-wave antenna model. The antenna model allows us to compute fields that are properly normalized for S-parameter measurements to be used in Eqns. (6.1), (6.2), and (6.3). If the antenna transmit coefficients and locations are known accurately enough, then no other step is required to calibrate a free-space experimental inverse scattering system except to calibrate the transmission line reference planes. Equation (6.2), in fact, requires less storage and computation than Equation (5.2) where we would have used the dyadic Green's function in order to compute vector fields.

Finally, in experiment, we can never measure the scattered field S-parameter directly, but can obtain it by subtracting the S-parameters for the total and incident fields

$$S_{ji,sca} = S_{ji,tot} - S_{ji,inc} \quad (6.4)$$

where $S_{ji,inc}$ is measured in the absence of the object, and $S_{ji,tot}$ is measured in the presence of the object.

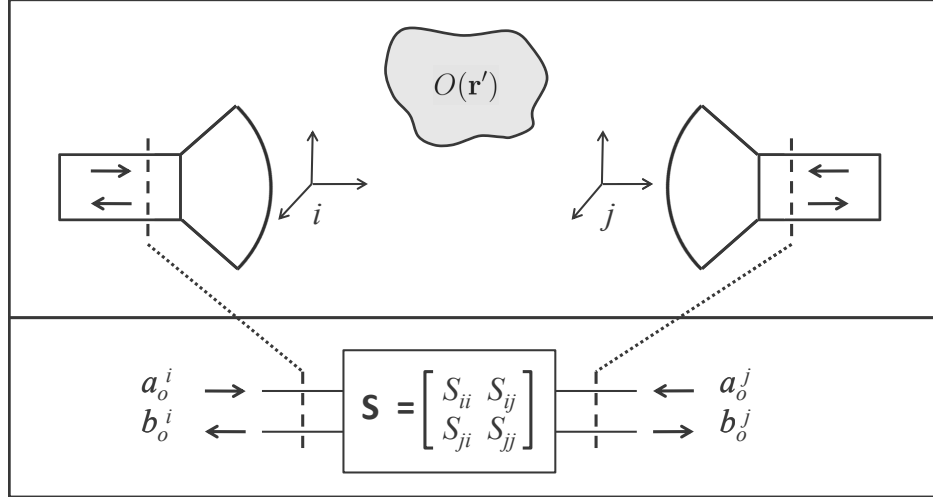


Figure 6.1: Network model of two antennas and a scattering object. S-parameters are measured between the reference planes on the antenna transmission lines.

6.3 Born Iterative Method

Our aim is to test the BIM in experiment using the new integral equations which include the source model. Compared to studies of the BIM and the related DBIM in theory [52, 73, 74, 51, 75], it has been implemented only a few times in experiment, [102, 122].

While implementing the forward solver with Eqn. (6.1) is standard enough, we will develop the cost function around Eqn. (6.2). This scattered field integral operator is substantially different from traditional forms, [68, 69], and that presented in Chapter III, and will affect our derivation of the minimization steps, specifically the operator transpose.

We mention here that the choice of the BIM over other inversion algorithms has been mainly for historical reasons, it being among many in the literature not extensively tested in experiment. The BIM, though, distinctly separates the data misfit functional from the forward solver, and this has provided clarity in consistently linking the two to experiment.

6.3.1 Forward Solver

For this free-space experiment, we use the BCGFFT for the forward solver [106, 107, 108]. This because the Neumann series may not be able to handle objects with relative permittivities of 3 or higher, which we expect for some plastics, such as Nylon. Even still, the BCGFFT was validated against the Neumann series up to contrasts of 2:1 and validated against the Mei scattering solution up to contrasts of 4:1.

6.3.2 Cost Function

Unlike traditional formulations of the BIM, which build and solve a linear system of equations over Eqn. (5.2) to update the contrasts, or develop the algorithm around point sources and receivers, as we did in Chapter III, we will minimize a functional over Eqn. (6.2) using the multi-variate covariance-based cost function of [55].

As before, at each iteration when we estimate the contrast, we assume the object field is constant. The scattered field integral with constant object field is then a linear operator acting on the contrast. With this in mind, we write the cost function as

$$2F(\mathbf{m}) = \|\mathbf{G}_1\mathbf{m}_1 + \mathbf{G}_2\mathbf{m}_2 - \mathbf{d}\|_D^2 + \sum_{m=1,2} \|\mathbf{m}_m - \mathbf{m}_{a,m}\|_{M,m}^2 \quad (6.5)$$

where the forward operator is now

$$[\mathbf{G}_m]_{ji} = c_m \int \mathbf{g}_j(\mathbf{r}') \cdot (\cdot) \mathbf{e}_i(\mathbf{r}') dV' \quad (6.6)$$

$$[\mathbf{d}]_{ji} = S_{ji, \text{sca}} \quad (6.7)$$

$$\mathbf{m}_1 = \delta\epsilon(\mathbf{r}) \quad (6.8)$$

$$\mathbf{m}_2 = \delta\sigma(\mathbf{r}) \quad (6.9)$$

$$\mathbf{m}_{a,1} = \delta\epsilon_{a \text{ priori}}(\mathbf{r}) \quad (6.10)$$

$$\mathbf{m}_{a,2} = \delta\sigma_{a \text{ priori}}(\mathbf{r}) \quad (6.11)$$

$$c_1 = k_o^2 \quad (6.12)$$

$$c_2 = k_o^2 \frac{i}{\epsilon_b \omega} \quad (6.13)$$

with frequency dependence understood. The quantity \mathbf{G} is the forward operator, and $\mathbf{G}_1 \mathbf{m}_1 + \mathbf{G}_2 \mathbf{m}_2$ is a vector of forward model predictions. The quantity \mathbf{d} is the data vector containing the measured scattered field S-parameters. The vectors \mathbf{m}_1 and \mathbf{m}_2 contain the relative permittivity and conductivity contrast pixel values, respectively, for a discretized domain. The vectors $\mathbf{m}_{a,1}$ and $\mathbf{m}_{a,2}$ contain our *a priori* knowledge of the contrast pixel values. We have assumed that the permittivity and conductivity contrasts are independent so each has its own regularization term. The vector norms are defined over the data and model spaces, respectively, through inverse covariance operators. See Appendix D.1.1.

The gradient vector and steepest descent vectors for the two model vectors are also independent and given by

$$\hat{\gamma}_m = \mathbf{G}_m^* \mathbf{C}_D^{-1} \mathbf{r} + \mathbf{C}_{M,m}^{-1} (\mathbf{m}_m - \mathbf{m}_{a,m}) \quad (6.14)$$

$$\gamma_m = \mathbf{C}_{M,m} \mathbf{G}_m^* \mathbf{C}_D^{-1} \mathbf{r} + \mathbf{m}_m - \mathbf{m}_{a,m} \quad (6.15)$$

for $m = 1, 2$, and where $\mathbf{r} = \mathbf{G}(c_1\mathbf{m}_1 + c_2\mathbf{m}_2) - \mathbf{d}$, is the residual. The transpose of the forward operator is similar for both object functions

$$\mathbf{G}_m^* \mathbf{u} = c_m^* \sum_{ji} (\mathbf{g}_j(\mathbf{r}) \cdot \mathbf{e}_i(\mathbf{r}))^* u_{ji} \quad (6.16)$$

where $*$ is simply the conjugate, and the vector \mathbf{u} is a vector in the weighted data space. As before, the transpose can be thought of as a form of aggregate backprojection, which maps data quantities onto the object domain. Here we are backprojecting scattered field S-parameter data. Again, the transposes for the permittivity and conductivity only differ by a constant. See Appendix D.2 for the derivation of Eqn. (6.16). The operator transpose differs from those derived traditionally for full-wave scattering problems, [68, 69], because we have used an integral equation which predicts S-parameters instead of fields.

The conjugate gradient updates of the model parameters are

$$\mathbf{m}_{mn} = \mathbf{m}_{mn-1} - \alpha_n \mathbf{v}_{mn} \quad (6.17)$$

$$\mathbf{v}_{mn} = \gamma_{mn} + \beta_{mn} \mathbf{v}_{mn-1} \quad (6.18)$$

For β_{mn} , we used the Polak-Ribiere step given by

$$\beta_{mn} = \frac{\langle \mathbf{C}_{M,m}^{-1} (\gamma_{mn} - \gamma_{mn-1}), \gamma_{mn} \rangle}{\langle \mathbf{C}_{M,m}^{-1} \gamma_{mn-1}, \gamma_{mn-1} \rangle} \quad (6.19)$$

where \langle, \rangle is a simple dot product. Choosing α_n to minimize the cost function at each step, it can be shown that (see Appendix D.1.2),

$$\alpha_n = \frac{\Re \{ \sum_{m=1}^2 (\mathbf{v}_{mn}, \gamma_{mn})_{M,m} \}}{\|\mathbf{s}_n\|_D^2 + \sum_{m=1}^2 \|\mathbf{v}_{mn}\|_{M,m}^2} \quad (6.20)$$

where $\mathbf{s}_n = \mathbf{G}(c_1 \mathbf{v}_{1n} + c_2 \mathbf{v}_{2n})$.

6.4 Experimental Setup

To test the inverse scattering algorithm in conjunction with the source characterization, we constructed the setup shown in Figure 6.2. Fifteen antennas are mounted to a ridged nylon octagon. The octagon is supported on eight, 4-foot Styrofoam pedestals in an anechoic chamber. One antenna transmits, while the other 14 receive. The receivers are connected through a SP16T solid-state switching matrix that was designed and assembled in-house. 2-port S-parameter measurements were taken with an Agilent PNA-5230A Vector Network Analyzer from 2.4-2.8 GHz between the transmitter and any one receiver. A rotator with a Styrofoam pedestal was aligned in the center of the octagon to rotate test objects and provide multiple transmitter views.

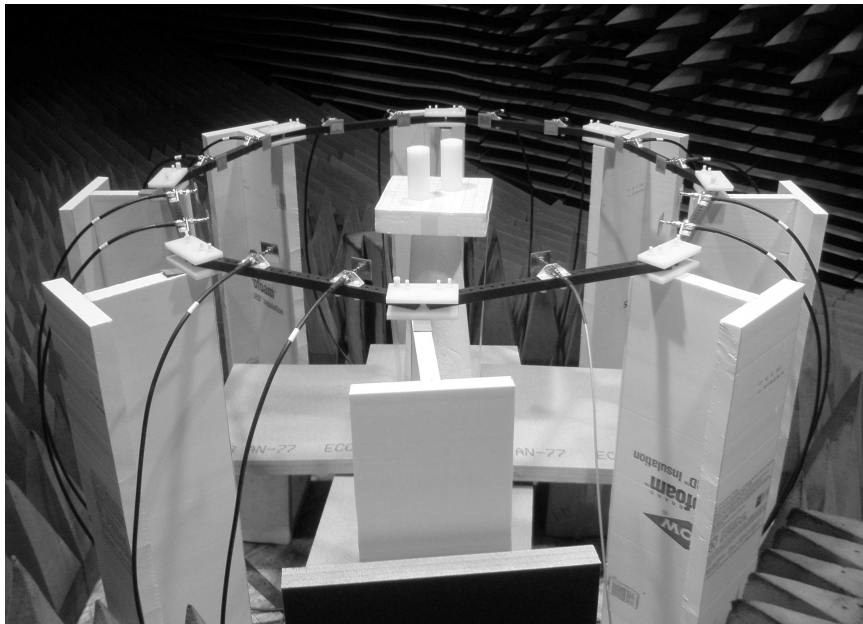


Figure 6.2: Experimental setup in an anechoic chamber. One transmitter and 14 receivers are mounted on a nylon octagon which is supported on Styrofoam mounts. The objects are turned with a rotator (not visible). The transmitter and receives are connected to the VNA, where the receivers are selected with a SP16T solid-state switch.

6.4.1 Antenna Characterization

The antennas were designed and characterized using Ansoft HFSS and the technique described in Chapter IV. The HFSS CAD model is shown in Figure 6.3. The antennas are E-patch antennas, [123], where the dimensions of the patch are $4\text{cm} \times 2.5\text{cm}$ on a $5\text{cm} \times 5\text{cm}$ substrate of 1/8 inch FR4. The size of the patch gaps and location of the feed were optimized to give a -10 dB bandwidth between 2.45-2.75 GHz. We chose this antenna for its moderate increase in bandwidth over a square patch with only a small additional design effort. This gave us a wider margin of error when fabricating many antennas as well as the option to use a few more frequencies about the center frequency when forming images.

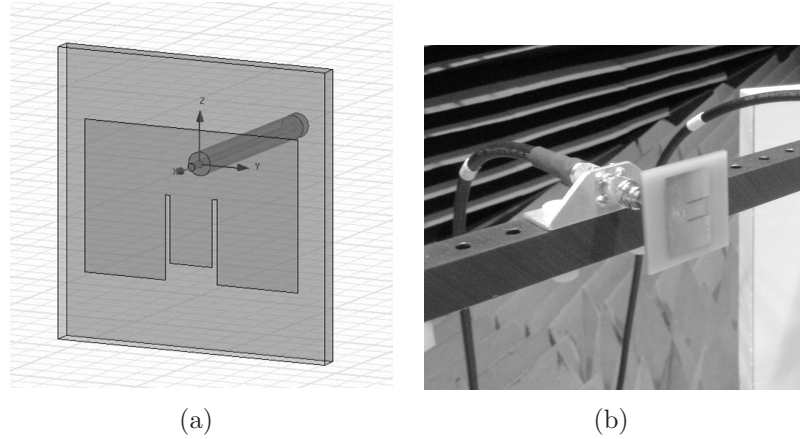


Figure 6.3: a) HFSS CAD model of E-patch antenna in the vertical polarization. The patch is enclosed in a large radiation box (not shown). The transmission line was de-embedded to match the reference plane of the VNA in experiment. b) Actual antenna mounted in the setup for the horizontal polarization.

Before completing the characterization, we compare measured and simulated S_{11} of the antennas in isolation before being used in the setup. Figure 6.4 shows the magnitude and phase of simulated S_{11} as well as the upper and lower bounds of measured S_{11} across all 15 antennas used in the setup. The overall phase variation was less than 10 degrees, except near the two resonances, even though the magnitude can differ by as much as 6 dB. From our experience with this characterization technique,

large differences in measured and simulated S_{11} do not directly translate to large differences between measured and predicted S_{21} , so we treat the antennas identically. Also, the S-parameter reference plane of the CAD model matched that used by the VNA in measurement (see VNA Calibration below).

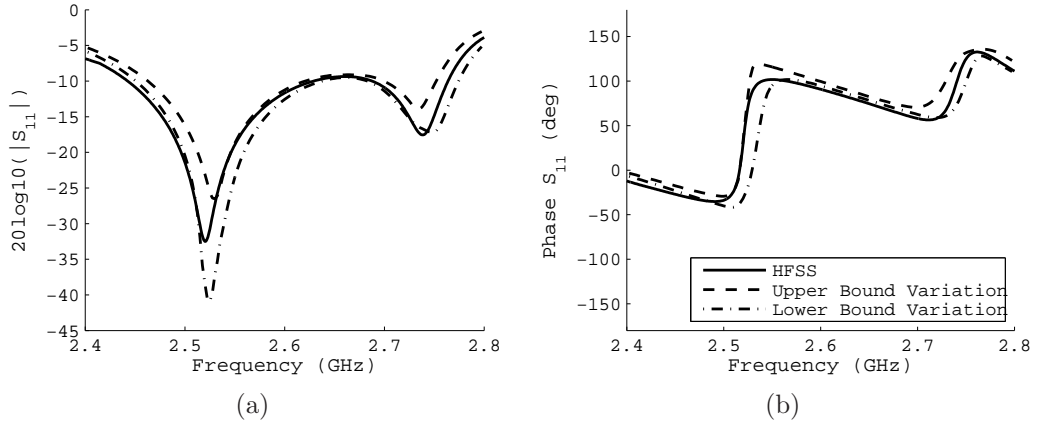


Figure 6.4: Magnitude and phase of simulated and measured S_{11} for the E-patch antennas. a) Magnitude. b) Phase. The solid line is simulated S_{11} from HFSS. The dashed and dotted lines represent the upper and lower bounds, respectively, of the variation of measured S_{11} across all 15 antennas before being used in the setup.

When estimating the transmit coefficients, we choose the coordinate origin of the antenna reference frame as the intersection of the center conductor and the ground plane of the patch. In simulation, the radiated electric field was computed relative to this origin on four spheres with radii of [20 50 100 150] cm at 2500 points uniformly on each sphere. The antenna transmit coefficients were estimated as in [105] up to harmonics of $l = 5$ for all m . The transmit coefficients at 2.5 GHz up to $l = 3$ are shown in Figure 6.5. Most of the field information is captured in the first few l , showing the dipole nature of the antenna. We obtain the transmit coefficients for antennas in rotated frames using the rotation addition theorem for vector spherical harmonics, [105], which allows us to compute the incident field for any antenna location and polarization from the same set of transmit coefficients.

The patch antennas are linearly polarized, so we tested two principal polarizations,

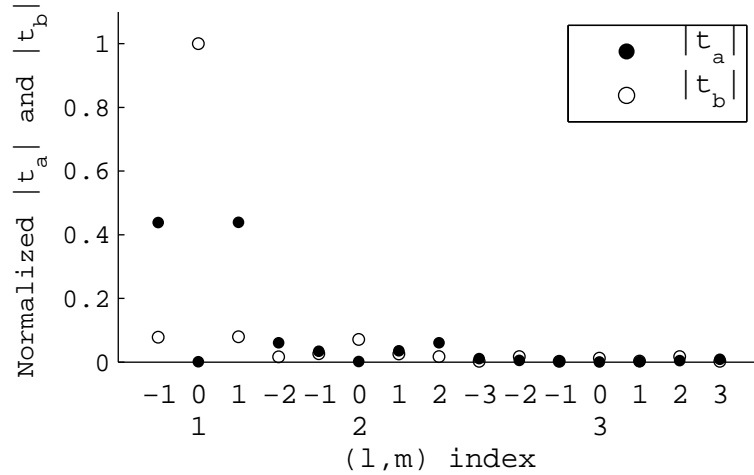


Figure 6.5: Normalized magnitude of transmit coefficients, $t_{(a)lm}$ and $t_{(b)lm}$, for the E-patch antenna in Figure 6.3, with harmonics up to $l = 3$ at 2.5 GHz. The horizontal axis is the (l,m) index; the upper row is m , the lower row is l . Most of the field information is captured in the first few l .

vertical and horizontal relative to the plane of the antennas, labeled V and H. To achieve different polarizations, the antennas were rotated about the connector and adjusted with a hand level.

The locations of the antenna reference frames in the setup were determined by measuring their relative locations on the nylon octagon. A schematic of the ideal positions and rotations of the antenna reference frames are shown in Figure 6.6. The receivers are numbered 1-14 counterclockwise from the transmitter as viewed from above.

6.4.2 Switching Matrix

The receivers were connected through a SP16T solid-state switching matrix that was designed and assembled in house. The switching matrix has two layers of SP4T Hittite HMC241QS16 non-reflective switches controlled with a computer parallel port. The operating band of the switching matrix is between 0.1-3 GHz. The overall loss of a path in the switching matrix is no worse than 2 dB across the band. We measured the switch path isolation to be better than -35 dB between 1-3 GHz, which means

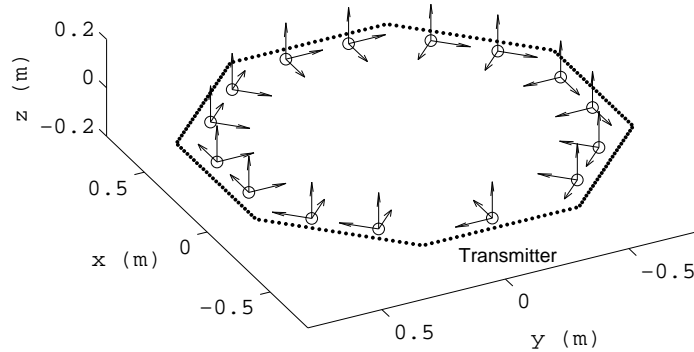


Figure 6.6: Schematic of ideal antenna reference frame positions and rotations for the setup pictured in Figure 7.2. The transmitter frame is at the lower right. The dots represent the mounting holes on the nylon beams, which are separated by 1 inch.

scattered field measurements between two antennas that differ by more than 35 dB cannot be reliably measured.

6.4.3 VNA Calibration

Two-port VNA calibrations were accomplished between the transmitter and each receiver. The S-parameter reference planes were calibrated to the points where the antennas were connected to the mounts. These reference planes are identical to that in the HFSS CAD model used to solve for the antenna transmit coefficients thus making the measurements and antenna characterization consistent.

To calibrate the VNA, the antennas were first removed from their mounts. While calibrating, we left the unused ports open with the rationale that the one-way switch isolation of -35 dB provided sufficient matching to the open ports. Short-open-load measurements for a 1-port calibration were taken for each antenna. Next, we measured the through path between the transmitter and each receiver with a 10' SMA cable. In software, we combined the 1-port and through measurements to accomplish

a 2-port short-open-load-through (SOLT) calibration with arbitrary through between the transmitter and each receiver. Although standard 2-port calibrations would have sufficed, this technique was developed with an eye toward multi-transmitter systems.

6.4.4 Setup Diagnostics

Before collecting data for inversion, we tested the setup by comparing measured and predicted S_{21} of the incident, total, and scattered fields for the conducting sphere in Figure 6.7, using the propagation model in Chapter IV. We tested both VV and HH polarizations. Note that the sphere is not used as a calibration target, it is only used to confirm the accuracy of the antenna characterization and our knowledge of the antenna reference frames.

Figure 6.8 shows the measured and predicted S_{21} for the VV polarization of the incident, total and scattered field of a conducting sphere measured between the transmitter and receiver 11. The magnitude agrees to within 2 dB and the phase is accurate to better than 20 degrees across the band from 2.4-2.7 GHz. Similar results were obtained for each transmitter-receiver pair and HH polarization. Given the accuracy of the predicted phase, we expect the incident field when computed in the object domain to be accurate to better than $\lambda/5$ throughout.

We found that scattered field cross pole measurements for small objects were not consistent with model predictions, likely because their magnitude was below the isolation levels of the switch, and so we excluded cross pole measurements from future measurements.

6.4.5 Noise

In the probabilistic interpretation of the cost function, the data vector \mathbf{d} represents the mean of the forward model Gaussian distributions. We assume the data are independent, so the data inverse covariance operator is a diagonal matrix with in-



Figure 6.7: Setup to test the antenna model by measuring the scattered field from a conducting sphere. The sphere has a diameter of 2 inches, and was centered in the setup.

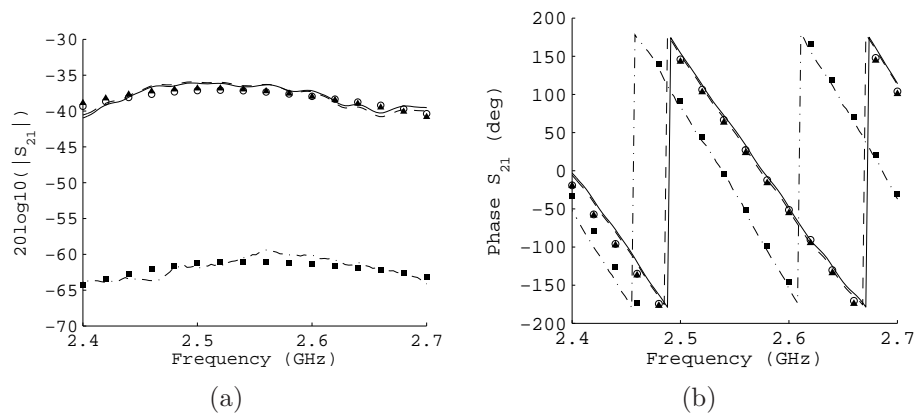


Figure 6.8: Magnitude and phase of measured and predicted S_{21} of the incident, total and scattered fields of the conducting sphere in Figure 6.7 between the transmitter and receiver number 11. a) Magnitude. b) Phase. Solid line and circles: measured and predicted incident field S_{21} . Dashed line and triangles: measured and predicted total field S_{21} . Dash-dot line and squares: measured and predicted scattered field S_{21} . The incident and total field S_{21} appear nearly identical on these scales.

verse variances given along the diagonal. By using these distributions, we necessarily assume the measurements are corrupted by Gaussian random noise.

The values of the means and variances for the Gaussian distributions are determined directly from the statistics of the measurements. For instance, in radar, we often average many data takes of the same viewing geometry to improve the signal to noise ratio. These averages, in addition to the variances, are precisely the quantities used for the entries of the inverse covariance matrix. As an aside, the data vectors in the cost function are complex, but are assigned a single value for the variance. This treatment automatically assumes that the real and imaginary parts of the data are independent with the same value for the variance.

To determine the noise of the system, we saved 12000 individual S_{21} measurements of the incident field for each receiver. A histogram of the real part of a typical S_{21} measurement at 2.5 GHz is shown in Figure 6.9. The random noise is clearly Gaussian with a standard deviation of $2.68\text{e-}05$, which is approximately -91 dB. The noise includes the effects of the VNA, the switch, and the background. Results at each receiver and each frequency varied between -88 dB and -92 dB, for both real and imaginary parts of S_{21} . It was enough to assign a single variance with a value of -90 dB for all the data, which is the value we use when forming the images.

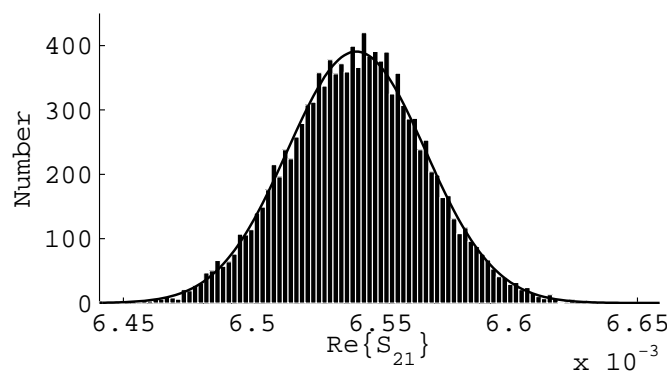


Figure 6.9: Histogram of the real part of S_{21} for the incident field of receiver 8 (across from the transmitter) at 2.5 GHz. The solid line is a Gaussian distribution with the same mean and variance of the data. The noise is equal to approximately -91 dB. Similar results are obtained for all measurements.

When taking data for inversion, we did not complete a full histogram, due to time constraints. For our setup, we averaged 20 samples of each measurement to use for the mean, and use the value of the variance above for the noise.

6.5 Image Reconstructions

The images we form are 2D cross sections of finite cylindrical objects using the full 3D inverse scattering algorithm. We use the cylindrical nature of the objects only as *a priori* information, where we assume we know the vertical extent of the object. We do this because it is difficult to collect enough data in a 2D source geometry to make the inverse problem overdetermined for a fully 3D object. Furthermore, we already know that the point spread function of a 2D source geometry is elongated in the vertical direction, which would corrupt 3D images. Also, it is simply not correct to use a 2D inversion algorithm in a 3D experiment, unless the objects are very tall and the incident fields are nearly cylindrical or plane waves. Thus, the full 3D forward solver and inversion algorithm are used to form images of 2D cross sections.

Most of the images we form are of permittivity only, because the objects consist of plastic cylinders and bars. We give one example of imaging conductivity only, where the objects are thin metal rods.

The object domain used for the forward solver and the scattered field volume integral was $30 \times 30 \times 30$ cm. This was large enough to encompass rotated objects which had heights of 15 cm. The domain was meshed at $\lambda/8$ in a material with relative permittivity of 3. This gave a domain that is $41 \times 41 \times 41$ pixels on a side. The discretization size was chosen so that the number of pixels of the zero padded domains for FFTs in the BCGFFT were $2N - 1 = 81$, which has a prime factorization of 3^4 . We also accept the possibility of some discretization errors given that this discretization may be coarser than $\lambda/10$ for high contrast objects. The 2D cross section, and thus the number of unknowns in the inverse problem for a single

contrast function, has $41 \times 41 = 1681$ pixels.

The objects were rotated to 72 positions in 5 degree increments. Using data from all 14 receivers gives 1008 complex data points per frequency for a single polarization. Thus reconstructions of permittivity with only one frequency have effectively 2016 data points, making the inverse problem overdetermined.

The antenna transmit coefficients were found at 20 frequencies between 2.4 and 2.7 GHz, and we have the option of using any of these frequencies in the inversion algorithm. After experimenting with different combinations of frequencies, we found that using a single frequency, or only two or three well separated frequencies, yielded the best results in terms of reconstructing the object shapes and contrasts. This is because data separated by 10-20 MHz in frequency will have free-space wavelengths that differ by less than 1 percent, which makes these data nearly redundant. Redundant data will contribute to numerical error more than they help the inversion.

In the cost function, we took the inverse covariance operators to be diagonal, meaning both the data and, separately, the image pixels, are independent. The value for the data variance was the noise. The standard deviations of the model parameters (i.e., relative permittivity) was set to 10, which is sufficient to regularize the problem without penalizing high contrasts. See Section 7.5.3 for further discussion on the regularization.

Each image is formed with 12 iterations of the BIM. An iteration consists of one run of the forward solver and 12 conjugate gradient iterations to minimize the cost function. We chose this number of iterations for the conjugate gradient because most of the work of the conjugate gradient is done in first couple of iterations and we saw that this number was repeatably sufficient for the the norm of the residual to bottom out, after which there was no noticeable change to the object estimate. Also, the number of BIM iterations was repeatably sufficient to achieve overall convergence. The computation time and storage to form a single image were 2 hours and 0.5 GB

RAM per frequency, respectively, for code written in Fortran on a Linux desktop with an AMD Phenom II quadcore processor and 16 GB RAM.

Example 1: Pair of Delrin rods

Shown in Figure 6.10, a pair of Delrin rods are approximately 5 cm in diameter, 15 cm tall, and have a relative permittivity of 2.3. Also shown are the reconstructions at BIM iterations {1,7,12}. The images were formed with VV data with the three frequencies {2.5, 2.6, 2.7} GHz. An outline of the locations of the actual objects is superimposed on the final image, which were measured during the experiment. The objects are detected at the correct locations, and the peak relative permittivity in the last iteration is approximately 1.8. Figure 6.11 shows a cross section of the actual and reconstructed permittivities. Also shown is the residual during the conjugate gradient minimization for each BIM iteration. The residual resets at the beginning of each iteration because we always begin the minimization with a zero object. The behavior of the residual at the 6th iteration is attributed either to the nonlinearity of the problem or error accumulation. Similar features were observed in the residuals in about one quarter of the examples which follow.

Next, using the same parameters, we formed an image of the two Delrin rods using HH data, shown in Figure 6.12. The objects are detected but the contrast is quite underestimated.

Example 2: Delrin block

Figure 6.13 shows the reconstruction after 12 BIM iterations using VV data at 2.5 GHz. Also shown is an outline of the actual block. The block is 5.5cm \times 8cm \times 15cm, with a relative permittivity of 2.3. While the shape is reasonably recovered, the contrast is only 40% of the actual. We attribute this to the fact that the block is electrically small, and the peak contrast of subwavelength objects are often not recovered given the type of regularization used in this algorithm.

Example 3: Two different PVC rings

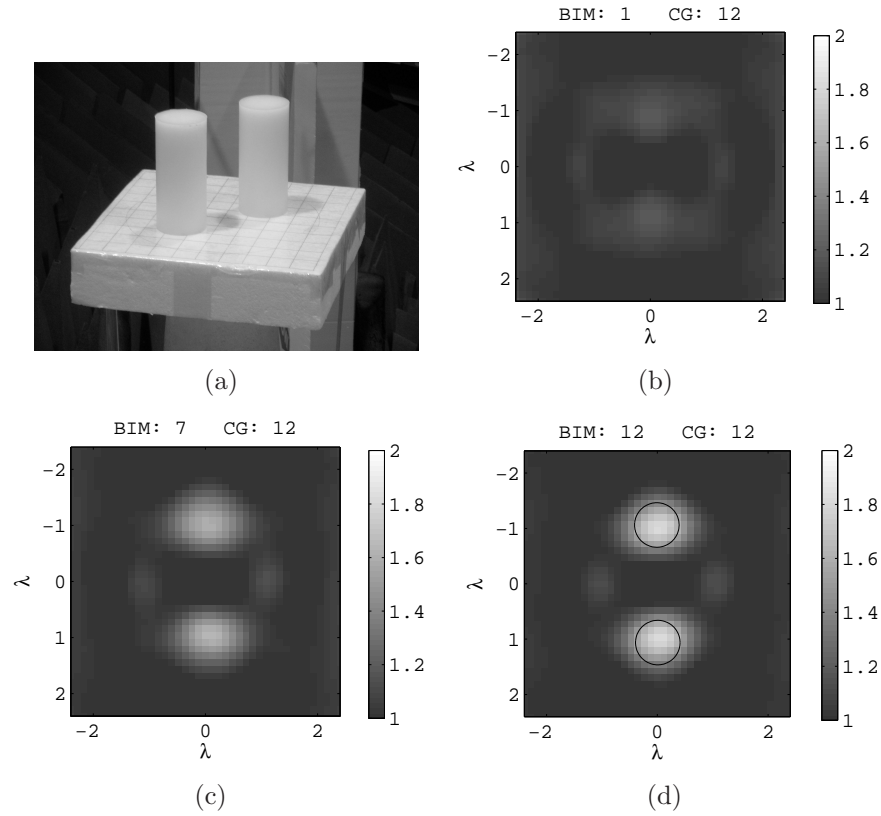


Figure 6.10: Reconstructed relative permittivity at 4 iterations of the BIM after 12 conjugate gradient iterations each using VV polarization data. a) Photo of Delrin rods. b) BIM iteration 1, i.e. Born approximation. c) Iteration 7. d) Iteration 12. The wavelength is that in a material of $\epsilon_r = 3$.

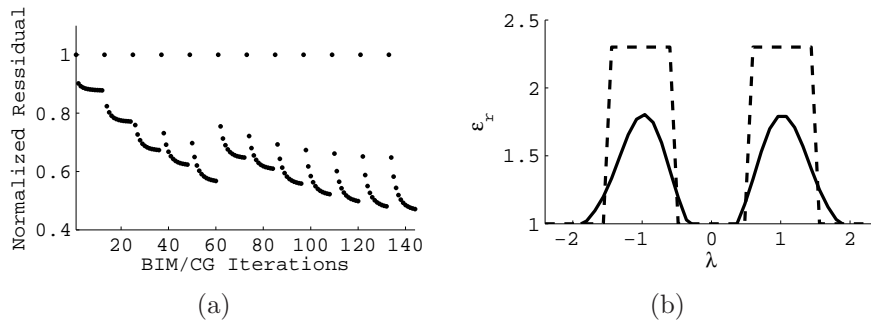


Figure 6.11: a) Normalized residual for the conjugate gradient iterations for each successive BIM iteration. b) Vertical cut of the actual and reconstructed relative permittivity through the center of the two objects.

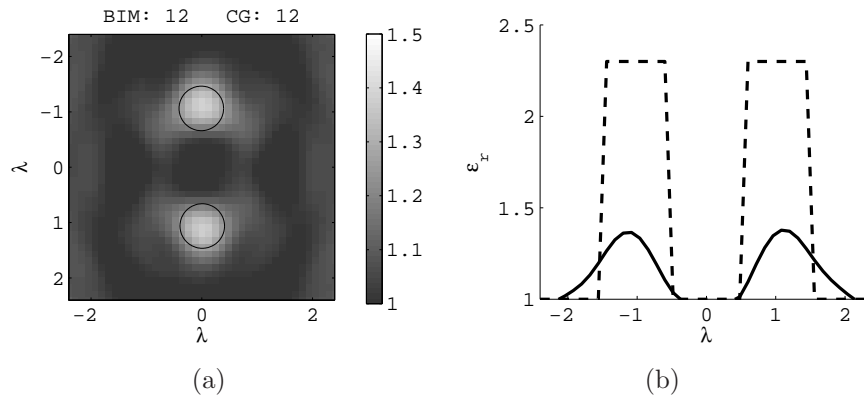


Figure 6.12: a) Reconstructed image of two Delrin rods using HH polarization data. b) Vertical cut of the actual and reconstructed relative permittivity through the center of the two objects.

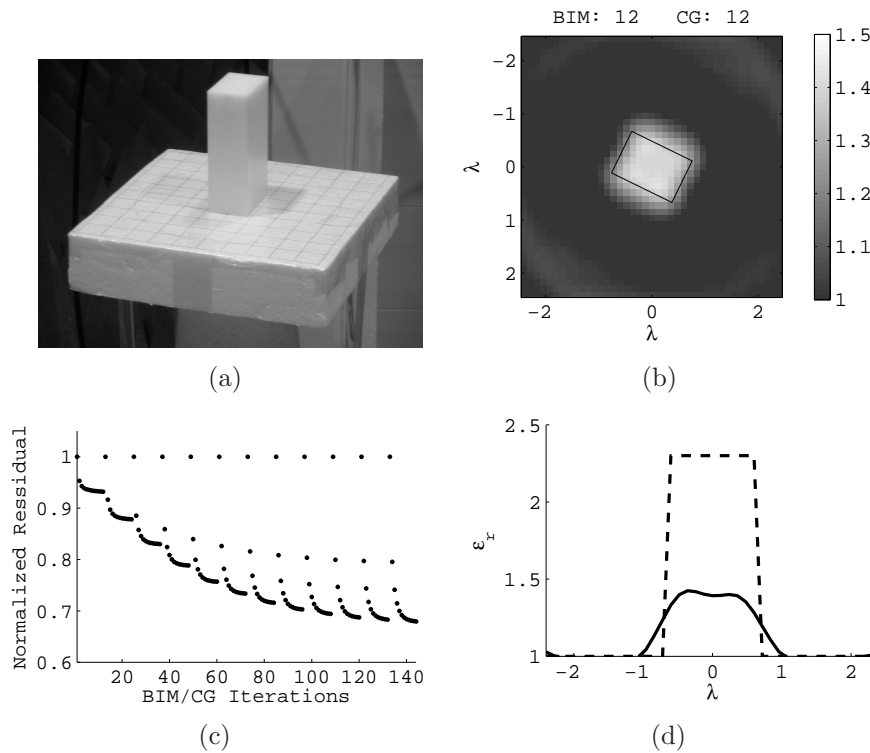


Figure 6.13: a) Photo of Delrin block. b) Reconstructed relative permittivity after 12 BIM iterations. An outline of the actual block is superimposed on the image. c) Normalized residual for all iterations. d) Horizontal cut through the middle of the image for the actual and reconstructed object.

Shown in Figure 6.14, the rings had diameters of 10 cm and 17 cm, respectively, both with thicknesses of 7.5mm. The reconstruction after 12 BIM iterations using VV data and the three frequencies $\{2.5, 2.6, 2.7\}$ GHz is also shown as well as an outline of each ring. The rings have a relative permittivity of 2.7. The overall shape of the rings is recovered well, but the peak contrast is underestimated due mostly to resolution limits, because the ring thickness is about $\lambda/8$. The apparent object in the center of the large ring is an artifact.

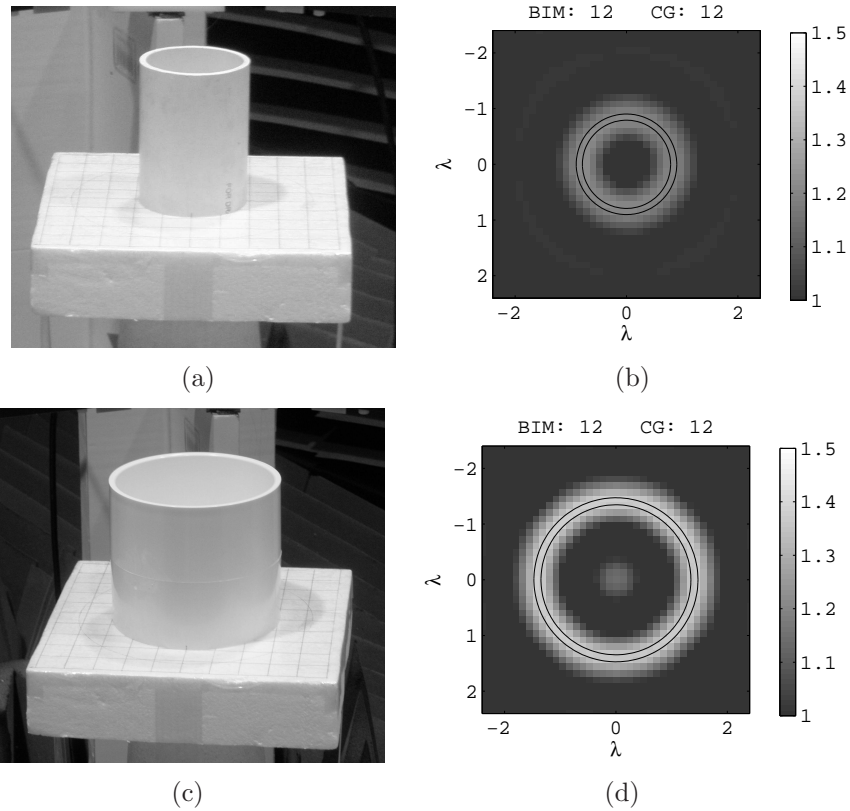


Figure 6.14: a) and c) Photo of PVC rings. b) and d) Reconstructed relative permittivity after 12 BIM iterations. An outline of the actual rings are superimposed on the images.

Example 4: PVC rod in rings

We enclosed a 5 cm diameter PVC rod in two different rings, shown in Figure 6.15. The first ring is the small PVC ring used in Example 3. The second ring is a large cardboard ring with a 18cm diameter and 5mm thickness, where this ring and rod

combination is also offset from the center. The relative permittivity of the PVC rod is 2.7. The reconstruction after 12 BIM iterations using VV data and the three frequencies $\{2.5, 2.6, 2.7\}$ GHz is shown in Figure 6.15 as well as an outline of the actual locations of the ring and the PVC rod. Both the rod and the ring are distinguishable in each case. The recovered peak relative permittivity of the rod in each image is 2.2. The cardboard ring is faintly visible, even with a thickness of $\lambda/12$.

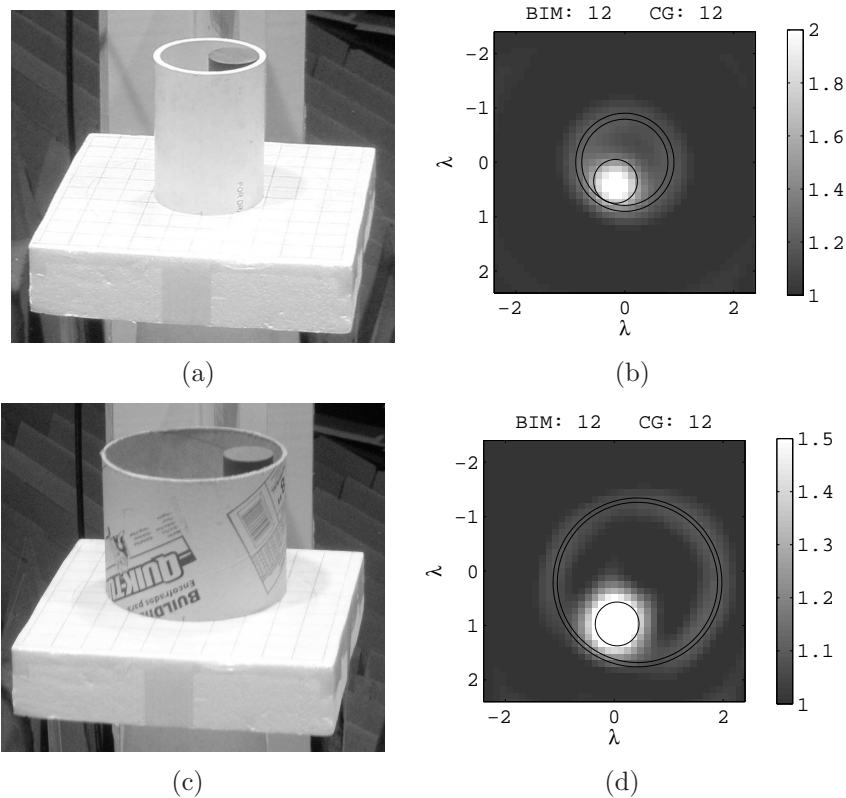


Figure 6.15: a) Photo of ring and rod combination. b) Reconstructed relative permittivity after 12 BIM iterations. An outline of the inner and outer diameter of the ring as well as the PVC rod is superimposed on the image.

Example 5: Thin metal rods

In this example, we attempted to image two very thin metal rods out of curiosity to study resolution, with the rationale that metal rods act as impulses in both space and conductivity. The rods are held in a Styrofoam mount, as shown in Figure 6.16. The images were formed at 2.5 GHz with VV polarization data. Also shown are the

reconstructed images for rods separated by 4cm and 6cm, respectively. The rods are distinguishable in the images at a 6 cm separation, which is $\lambda/2$ at 2.5 GHz in free space.

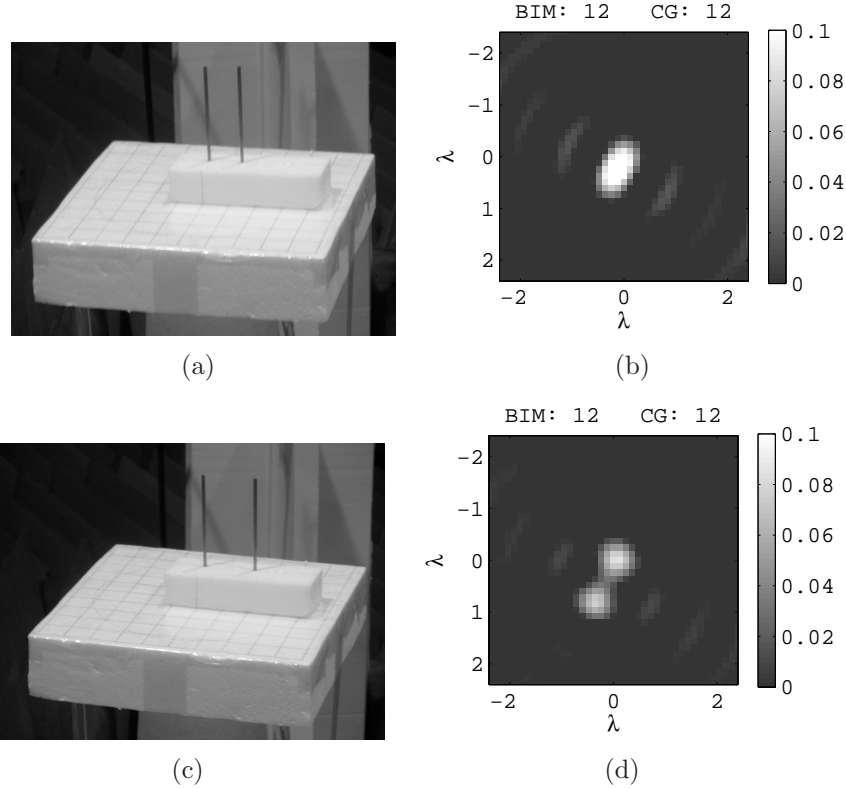


Figure 6.16: a) and c) Photo of the metal rods at separates of 4cm and 6cm, respectively. b) and d) Reconstructed absolute conductivity in Siemens per meter after 12 BIM iterations.

Example 6: High contrast limit I

There were some objects that could not be recovered by the algorithm. Similar to Example 4, we attempted to image the PVC rod enclosed by the 17cm PVC ring, shown in Figure 6.17. However, the algorithm failed to recover the objects properly after 12 iterations. Given that the PVC ring can be imaged by itself (Figure 6.14) and that the PVC rod with a cardboard ring can be imaged (Figure 6.15), the failure of the algorithm to recover the combination suggests that the nonlinearity of strong scattering interactions might have been too great for the algorithm to start from the Born approximation.

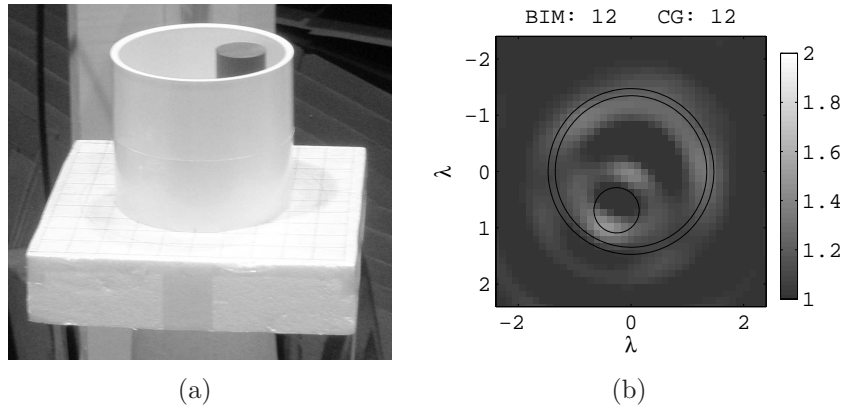


Figure 6.17: a) Photo of ring and rod combination in the setup. b) Reconstructed relative permittivity after 12 BIM iterations. The algorithm failed to recover this object.

Example 7: High contrast limit II

Here we attempted to image a combination of objects, shown in Figure 6.18. The objects are a Delrin rod and block each having a relative permittivity of 2.3. The algorithm failed to recover the contrasts correctly. To diagnose the problem, we ran the algorithm with synthetic data. The forward model still includes the antenna characterization and the reconstruction represents the image we could best expect for the same state of the algorithm. The ideal object and its reconstruction are shown in Figure 6.19. The image shows that the algorithm is capable of recovering this object to a point, which suggests that modeling errors (i.e., differences between the assumed experimental setup and the actual setup) are too large for the object to be recovered from experimental data, without additional a priori knowledge.

Next we tested the algorithm assuming we know the shapes of the objects a priori, but not the contrasts. We accomplish this regularization using the model inverse covariance matrix, [55, 56, 124]. We correlate the pixels within each homogeneous region with themselves, but leave the regions uncorrelated. We also assume we know the background to be free space and so set the variance of these pixels to be nearly zero. The value for the variance of pixels in the two dielectric regions was 10. Figure 6.20 shows the reconstructions for synthetic and experimental data. The reconstruc-

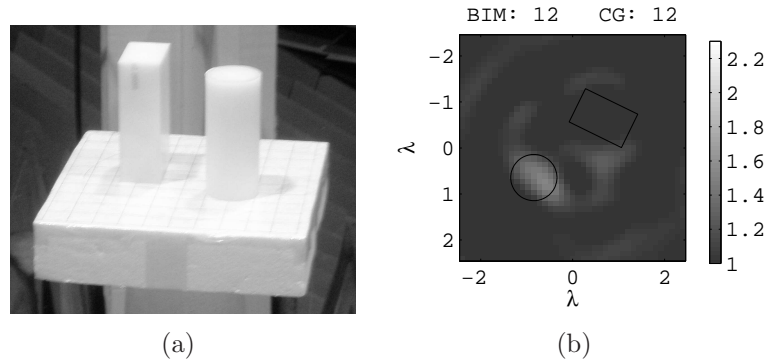


Figure 6.18: a) Photo of Delrin rod and block b) Reconstructed relative permittivity after 12 iterations. An outline of the actual objects is shown. The algorithm could not recover the contrasts of the objects.

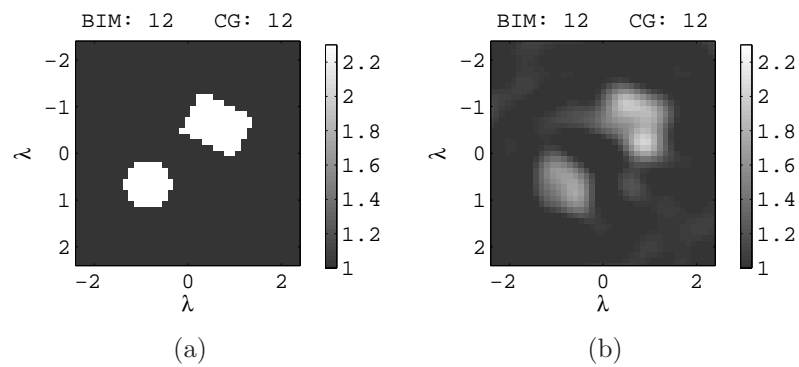


Figure 6.19: a) Objects used to generate synthetic scattered field data. b) Reconstruction using synthetic data.

tion from synthetic data recovers the contrast value quite well, while the experimental data underestimates the contrast value of the cylinder with the block faintly visible. This suggests that modeling errors are the underlying source of the discrepancy.

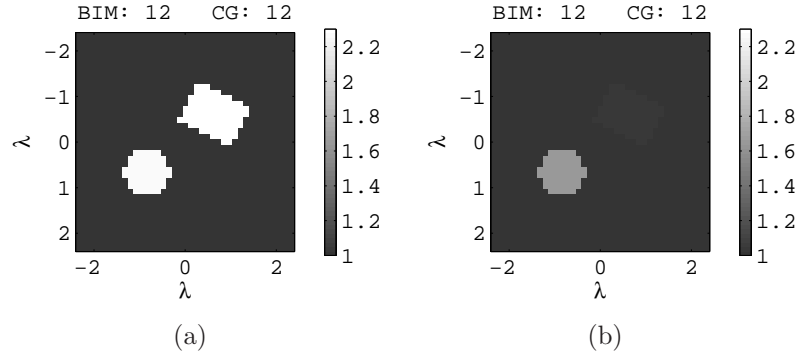


Figure 6.20: Image reconstructions from synthetic and experimental data using covariance operators to correlate pixels of homogeneous regions. a) Reconstruction using synthetic data. b) Reconstruction using experimental data.

6.5.1 Discussion

In general, the inversion algorithm with experimental data was able to recover the shapes of low contrast objects. However, it could not recover objects with too high a contrast. In the cases where objects were recovered the reconstructed contrasts were underestimated, as shown in Examples 1-4. The achievable resolution of the system is at least $\lambda/2$, as demonstrated in Example 5. Example 7 shows that the algorithm is capable of recovering high contrast objects when given synthetic data but not experimental data, which suggests the presence of modeling errors.

By developing an inverse scattering system based on an absolute source characterization, we are trading the convenience of calibrating the system using targets with the need to accurately model the experimental setup. That is, we rely solely on the numerical antenna characterization and our knowledge of their locations and orientations to link the S-parameter measurements to the physics of our algorithms. We do not have an additional correction procedure after setting up the experiment and

calibrating the VNA. The integration of the absolute source characterization with the inversion algorithm is the feature we set out to test. It makes an inverse scattering system more realistic, by enabling imaging in situations where calibration targets are unavailable, such as half-space problems. However, this means that any discrepancies between the forward model and the physical setup will remain uncorrected. Because the BIM is capable of recovering all the tested objects and their contrasts in simulation, we believe that in experiment the accumulation of many small modeling errors (e.g., transmit coefficient estimation errors, antenna position, rotator alignment, multiple scattering, calibration drift), accounts for most of the imperfections in the reconstructions.

Another complication is that the inverse scattering problem is nonlinear and non-unique, both of which are due to, but not exclusively due to, the source geometry and the strength of the scattering within the objects. In general, the BIM is capable of recovering contrasts as high as 3:1 in simulation for sources which surround the object in 2D or 3D, [74, 75]. For our experiment, even though we accounted for the cylindrical nature and finite height of our objects, we used a 3D algorithm with a 2D source geometry, which means the space of all possible measurements is incomplete. We suspect that while modeling errors and possibly the source geometry contributed to the low contrast estimations in Examples 1-4, the addition of stronger scattering and the sensitivity of a more nonlinear problem, led to the resulting images of Examples 6-7.

As stated previously, we regularize the inversion through the data and model inverse covariance operators and it is their Gaussian interpretations that allow us to physically and experimentally justify the values we use in each. However, treating the inverse model covariance operator as a diagonal matrix with equal diagonal elements, as we have done with most of the reconstructions, has had the effect of low-pass filtering the images. This is the same effect as when a Tikhonov tuning parameter is

used to solve similar inverse scattering problems via matrix inversion [74], the difference being that the value in our case comes directly from experiment. Higher-order regularizations exist, which can enforce different constraints on the image, such as total variation used to automatically preserve block-like structures [125, 67]. Higher-order regularization, however, is generally accomplished with non-linear operators, and therefore comes with two main caveats in the context of our cost function. First, the step length, α , in the conjugate gradient minimization, cannot be found analytically and must be sought through line minimization. Line minimization is very common but can increase the computational complexity of the algorithm. Second, and more importantly, the relationship between non-linear regularization and the Gaussian interpretation of the least-squares problem is unclear. The Gaussian model is very powerful, especially in experiment, but the model covariance matrix we use captures only the linear relations between unknowns. To link the nonlinear regularizers to the Gaussian model, we might 1) find a model covariance matrix, which approximates the non-linear regularizers, 2) attempt to generalize the model covariance operator to include high-order moments, or 3) seek a hybrid solution. Linking non-linear regularization and the Gaussian model, so that the reconstructions might benefit from both, remains a topic of study.

6.6 Conclusion

In this chapter, we demonstrated the use of the antenna model, vector Green's function formulation and BIM in experimental inverse scattering. We used the antenna model and vector Green's function to modify the traditional inverse scattering volume integral equations so that they are consistent with VNA S-parameter measurements. This absolute source characterization allowed us to directly compare measurements to model predictions in the inverse scattering algorithm without using calibration targets in experiment, and is one of the first demonstrations of its kind.

We successfully reconstructed 2D dielectric profiles of 3D objects. The inversion algorithm recovered object shape and contrast with mixed success given the constraints of the imaging setup. We also showed how a priori knowledge of random noise, contrast limits, and shape regularize the inverse problem in a covariance-based cost function.

The techniques in this experiment open up the area of network analyzer based microwave inverse scattering, because there is now a clear procedure for characterization. These methods also apply to situations where targets cannot be easily used to calibrate a scene, in, for instance, through-wall imaging or ground penetrating radar.

In the next chapter, we will use the concepts proven here as the foundation for characterizing and forming images with a cavity-based breast imaging system prototype.

CHAPTER VII

Microwave Breast Imaging Cavity Experiment

7.1 Introduction

A number of experimental systems for microwave breast imaging have been developed in recent years. These systems test full-wave inverse scattering algorithms [41, 126, 127, 37] as well as synthetic aperture beam focusing techniques [21, 42, 23]. While imaging algorithms abound in the literature, techniques to properly model, characterize, and calibrate these systems have lagged behind algorithm development. Investigators have started to identify characterization as a major task which must be addressed in order to fully evaluate the efficacy of microwave imaging for breast cancer detection. Part of this evaluation involves separating modeling errors from intrinsic algorithm artifacts in the final images. Thus, there has been a need for accurate models of experimental systems, as well as methods which efficiently incorporate these models into the imaging algorithms.

The task of characterizing a microwave breast imaging system for inverse scattering, as compared to a free-space system, is complicated by several factors. Specifically, the antennas are not isolated in the background media, but exist as part of the surrounding structure. Also, compact arrangements of many antennas creates a cavity-like imaging geometry, and the transmitter incident fields include all background multiple scattering. Finally, the antennas and object are in each others near-fields,

so object-cavity scattering should be modeled.

In trying to characterize breast imaging systems, investigators have turned to full numerical simulation. The antenna cavity in [128] was modeled using Ansoft HFSS, and only used for antenna design and sensitivity analysis. In [97], dipole sources of an inverse scattering experiment were modeled with HFSS, and calibration constants used to scale the antenna incident fields. HFSS has also been used to obtain antenna incident fields in a near-field, and open, antenna setup, [129], however, ad hoc methods have been used to calibrate the scattered field S-parameter data for the inverse scattering algorithm. In more recent work, [130], CST Microwave Studio was used to study and tune antenna performance in a breast imaging cavity. Also, finite-volume time-domain solvers of [131] modeled wide-band antennas for time domain beam focusing. The most complete work to date is [132], where an FEM forward solver is used to simulate the entire breast in the presence of the antennas, but computational complexity remains a challenge. Despite the growing use of numerical solvers to model breast imaging systems, there has been no formal way of incorporating the results from full-wave numerical models into the imaging algorithms.

The task of characterizing any inverse scattering system can generally be divided into three parts: 1) determining the incident fields produced by the antennas in the absence of the object, 2) determining the background dyadic Green's function, i.e., modeling the interactions between the object and its surroundings if necessary, and 3) linking the volume integrals in the imaging algorithms to measurable transmit and receive voltages.

In this chapter, we will use the vector Green's formulation we developed in Chapter V and HFSS to effectively solve parts 1) and 3) of this characterization problem for cavity-like breast imaging geometries, where we make the numerical characterization and inverse scattering algorithm consistent with an S-parameter based experiment.

The inverse scattering algorithm we use is the Born Iterative Method (BIM) with

multivariate-covariance cost function [133, 124, 55]. This cost function allows us to experimentally choose the regularization parameters based on our prior knowledge of system noise and expected range of permittivities.

We will again use the BIM as the inverse scattering algorithm, same as Chapter VI. The forward solver used in the BIM requires the background dyadic Green's function and finding it constitutes part 2) of the characterization problem mentioned above. For convenience we use the lossy free-space dyadic Green's function and give some numerical and experimental justification for this. Fully modeling the multiple scattering between the breast and the imaging structure in the forward solver is not trivial and some discussion is devoted to this.

We validate these methods with a combination of simulation and experiment. We first present the vector Green's function formalism of Chapter V in the context of cavity problems. We then explain our experimental setup which consists of a cylindrical imaging cavity with printed antennas, solid-state switching matrix and water/oil coupling medium. The HFSS numerical model is presented and the simulation results are compared to experiment. We form 3D images of the relative permittivity and conductivity using both HFSS synthetic data and experimental data for simple targets. We also present findings on the sensitivity of image reconstructions to the accuracy of modeling the background electrical properties.

7.2 VIEs and Characterization for Cavity Imaging

7.2.1 Integral Equations for Cavity S-parameter Measurements

In Chapter VI, we showed that is possible to transform the domain VIE and scattered field VIE so that they are consistent with an S-parameter based measurement system. We showed that the resulting equations were valid for both free-space and cavity-like geometries, and went on to validate the free-space case with the inverse

scattering experiment in Chapter VI. Here, we will summarize the results for a cavity geometry.

Consider the cavity depicted in Figure 7.1. An object to be imaged is placed in the middle of the cavity. The cavity is filled with a background material having a permittivity and conductivity of ϵ_b and σ_b , respectively. The cavity is lined with radiating apertures, which could be antennas. Each aperture has its own feeding transmission line and S-parameter reference plane.

We define the normalized incident and total fields throughout the cavity due to a transmitting aperture as

$$\mathbf{e}_{inc}(\mathbf{r}) = \mathbf{E}_{inc}(\mathbf{r})/a_o \quad (7.1)$$

$$\mathbf{e}(\mathbf{r}) = \mathbf{E}(\mathbf{r})/a_o \quad (7.2)$$

where a_o is the transmit voltage measured with respect to the S-parameter reference plane. The normalized incident field captures all background multiple scattering not present between the object and the cavity.

Let transmitting apertures be indexed with i and those receiving indexed with j . We can write domain VIE in terms of the normalized incident and total fields produced by a transmitter as

$$\mathbf{e}_i(\mathbf{r}) = \mathbf{e}_{inc,i}(\mathbf{r}) + \int \overline{\mathbf{G}}(\mathbf{r}, \mathbf{r}') \cdot O(\mathbf{r}') \mathbf{e}_i(\mathbf{r}') dV' \quad (7.3)$$

This is the integral equation we will use to represent the forward scattering solution. The normalized total field is the field solution in the object domain and, with the appropriate dyadic Green's function for the cavity, includes the scattering interactions between the object and the cavity.

From Chapter V, the two-port scattered field S-parameter, $S_{ji,sca}$, measured be-

tween the transmission line reference planes of two apertures in the presence of an object is given by

$$S_{ji,sca} = \int \mathbf{g}_j(\mathbf{r}') \cdot O(\mathbf{r}') \mathbf{e}_i(\mathbf{r}') dV' \quad (7.4)$$

where $\mathbf{e}_i(\mathbf{r})$ is the normalized total object field produced by the transmitter and $\mathbf{g}_j(\mathbf{r})$ is the vector Green's function kernel for the receiver. Again, $\mathbf{g}_j(\mathbf{r})$ is related to the normalized incident field of the receiver as

$$\mathbf{g}_j(\mathbf{r}) = -\frac{Z_0^j}{2i\omega\mu} \mathbf{e}_{inc,j}(\mathbf{r}) \quad (7.5)$$

To reiterate, this is the incident field throughout the cavity, which includes all background multiple scattering not present between the object and the cavity.

Equations (7.3) and (7.4) are the integral equations we will use for the inverse scattering algorithm. They consistently link the electric field volume integral equations to an S-parameter measurement system. We need only determine the normalized incident fields in the object domain and the background dyadic Green's function; no other step is required to characterize the system, except to calibrate the transmission line reference planes.

Lastly, in experiment, we never measure scattered field S-parameters directly, but obtain them by subtracting the S-parameters for the total and incident fields

$$S_{ji,sca} = S_{ji,tot} - S_{ji,inc} \quad (7.6)$$

where $S_{ji,inc}$ is measured in the absence of the object, and $S_{ji,tot}$ is measured in the presence of the object.

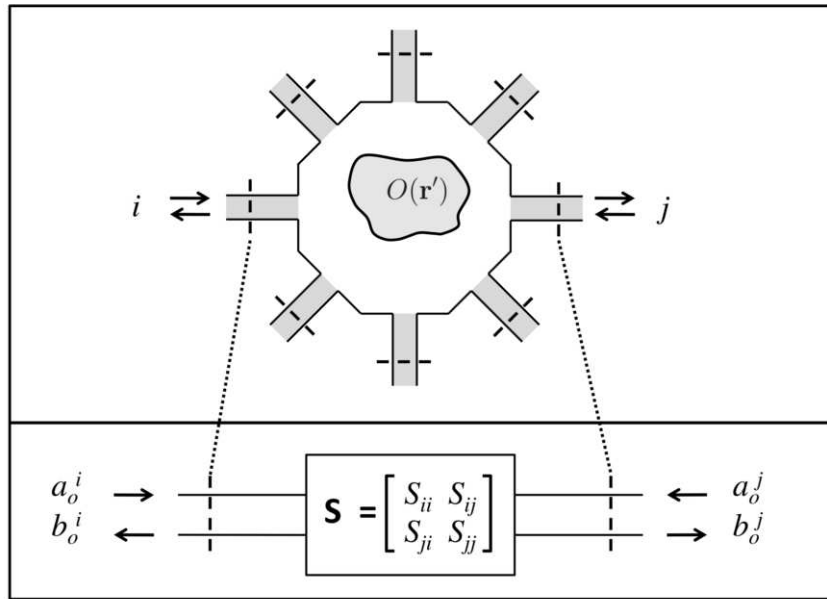


Figure 7.1: Microwave network model of cavity and scattering object. S-parameters are measured between the reference planes on the transmission lines.

7.2.2 Determining $\mathbf{e}_{inc}(\mathbf{r})$

The normalized incident field is required in both Eqns. (7.3) and (7.5), and is required for every aperture. We can either measure it experimentally or estimate it with simulation. Experimentally mapping the fields requires proper probe calibration and has the added complication in a cavity that the probe-wall interactions cannot be neglected. An alternative approach, and the one we adopt for this chapter, is to estimate the normalized incident field with simulation. This can be done provided that we have a computer aided design (CAD) model that accurately represents the cavity. It is also possible in simulation to model the feeding transmission lines and line voltages in order to assign an S-parameter reference plane that is identical to the reference plane used by a vector network analyzer for the physical measurement. We will show how we use Ansoft HFSS to accomplish this.

7.2.3 Determining $\overline{\mathbf{G}}(\mathbf{r}, \mathbf{r}')$

As stated in the introduction, determining the background dyadic Green's function is non-trivial, especially for arbitrary cavity geometries. Despite this, for the immediate investigation, we use the free-space dyadic Green's function under the condition that the background medium is extremely lossy. Though not strictly correct, this approximation is convenient provided the multiple scattering throughout the cavity is limited by the background loss. It also allows us, for the time being, to retain use of an FFT based volumetric forward solver. We give examples later evaluating this assertion. There are several approaches for determining or approximating the background dyadic Green's function for arbitrary geometries which we list as work for future investigation:

Analytical dyadic Green's function. There exist analytical solutions of the dyadic Green's function for some simple cavity geometries, such as cubes or cylinders, [?], which might approximately model certain cavity based imaging setups. These solutions, however, will likely not include finer details such as antenna plating, connectors, substrate material, or open-ended cavities, such as those used for breast imaging. Analytic solutions though lend themselves to the possibility of retaining some convolution structure in the VIE so fast forward solvers can be used, (e.g. fast half space solutions, [134], applied to multi-sided cavities). Determining the dyadic Green's function analytically becomes a formidable task as the geometry complicates, where simulation may be better suited.

Full numeric simulation. The most complete solution is to fully simulate the object and cavity using a numeric simulator, which will capture all the multiple scattering between the object and the cavity. However, unlike a dyadic Green's function, which only needs to be found once for a particular geometry and the values of which are only need on the interior of the object domain, this method must simulate the cavity structure outside the object domain in every instance of the simulation. When used

in an inverse scattering algorithm, which might compute the domain VIE for each source, frequency and iteration, then repeatedly simulating the cavity structure adds to the already high computational burden. In addition, some simulation methods are better at simulating surfaces or antennas, such as MoM or FEM, while others are better for inhomogeneous media, such as FDTD or CGFFT, so choosing the proper technique or hybrid is difficult.

Numerical dyadic Green's function. If analytical solutions are not accurate enough, then one must determine the dyadic Green's function numerically. This requires simulating three orthogonal dipoles in turn at every point in the object domain and recording the response at every other point in the domain. The dyadic Green's function is symmetric, so half of the combinations are redundant, and while the convolution nature of the VIE is destroyed, some computational speed up is possible for symmetric operators. This technique however, requires accurate modeling around the dipole singularity, which can be difficult. In the case of PEC structures, the technique in [135] computes the dyadic Green's function by finding an array of image dipoles outside the cavity, which avoids the complications from the singularity. The main advantage of determining the dyadic Green's function numerically is that once found, we no longer need to simulate the cavity structure and can turn our attention to optimizing the computation of the dyadic Green's function.

Approximate solutions. If the background loss is sufficiently high, so that the resonances of the cavity are damped, then we can approximate the dyadic Green's function. This can be done by adopting an analytical solution (e.g. free-space, or cavity), or by, for instance, developing a perturbation method. Adopting the free-space dyadic Green's function (or a perturbation on it) also allows us to retain the convolution structure of the VIE and FFT based forward solvers, which may be more beneficial to the inverse scattering algorithm than modeling higher-order multiple scattering.

7.2.4 Born Iterative Method for Cavities

The imaging algorithm we use is the same Born Iterative Method (BIM) inverse scattering algorithm as was used in the free-space experiment in Chapter VI. The cost function and conjugate gradient minimization remain unchanged. For the forward solver, because we use the lossy free-space dyadic Green's function to model the internal scattering, we use the BCGFFT. The one major assumption is the use of the free-space dyadic Green's function which ignores the breast-cavity scattering interactions. In a lossless background medium this would not work, however, we have some allowance given that the background coupling medium we use is so lossy.

7.3 Breast Imaging System Prototype

The breast imaging system prototype we built is shown in Figure 7.2. The imaging structure is a cavity, shown in Figure 7.3, which was created by soldering twelve vertical panels of microwave substrate together and soldering the collection to a conducting base. Opposite panels are separated by 15 cm, and the cavity is 17 cm tall. Three antennas are printed on each panel for a total of 36 antennas. In the prototype, the three antennas of one panel are used as transmitters while all other antennas are receivers. The transmit antennas are switched with a Dowkey SP6T electromechanical switch. The receivers are connected through a SP33T solid-state switching matrix that was designed and assembled in-house. 2-port S-parameter measurements were taken with an Agilent PNA-5230A Vector Network Analyzer at 2.75 GHz between each transmitter and any one receiver. This frequency was chosen as a compromise between resolution and switch performance which rolls off above 3 GHz. A rotator was mounted above the cavity and aligned in the center of the cavity. Test objects are suspended with fishline and rotated to provide multiple transmitter views.

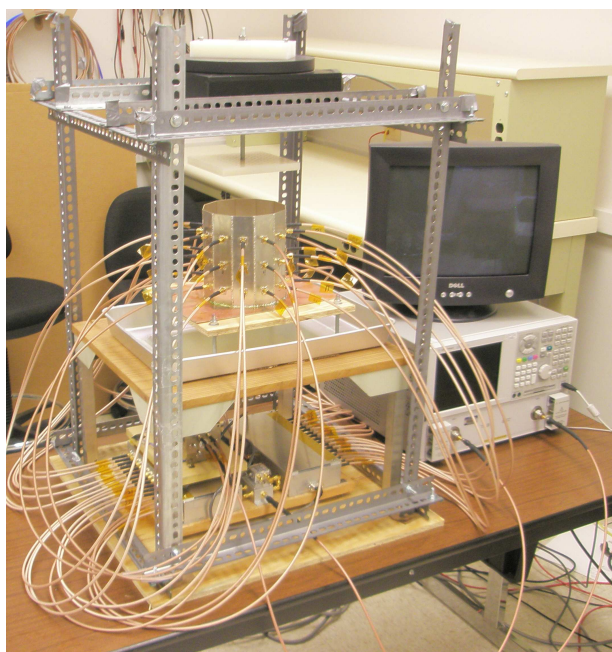


Figure 7.2: Breast imaging system prototype. The imaging cavity is connected to the VNA through a solid-state switching matrix. A rotator is mounted above and turns suspended objects for multiple transmitter views.

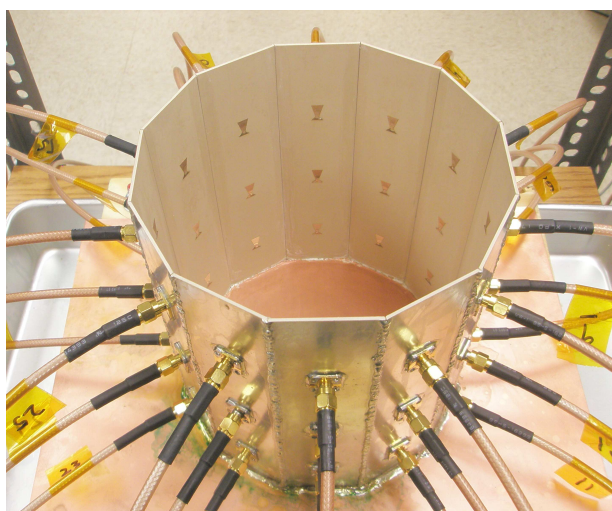


Figure 7.3: Imaging cavity. Twelve panels with three bow-tie antennas each are solder together and to a conducting plate.

7.3.1 Liquid Coupling Medium

We expect breast tissue to have a relative permittivity between 10-60 [10]. Without a matching medium, much of the incident power would be reflected at the breast/air interface reducing the sensitivity of the system, [136]. Also, the contrast ratio between the object and the background would be too high for the BIM inverse scattering algorithm to converge.

The matching medium we use is an oil/water emulsion developed in previous work [137]. This fluid is designed to balance the high permittivity and high conductivity of water with the low permittivity and low conductivity of oil, in order to achieve a fluid with moderate permittivity while limiting loss as much as possible. We are also able to tune the microwave properties of this emulsion by adjusting the oil/water ratio. We aimed for a relative permittivity value around 20, which brings the maximum permittivity contrast to about 3:1. The fluid mixture we used was 65%/35% oil/water.

The electrical properties of the fluid were initially measured using the Agilent 85070E slim form dielectric probe. The measured properties at 2.75 GHz were $(\epsilon_r, \sigma) = (24, 0.34)$. Relative permittivity is unitless; the units of conductivity used throughout the paper are Siemens/m. However, when using this value in the numerical model (presented below) the magnitude of cross-cavity S_{21} was too high and the phase was shifted compared to measurements. We obtained the best model agreement for $(\epsilon_r, \sigma) = (21, 0.475)$, and are the values we use through the chapter. We suspect that the probe area may be too small to accurately measure the bulk properties of the mixture, but the fluid otherwise appears homogeneous for propagation at 2.75 GHz. We are still investigating this effect.

When taking data, we fill the cavity with the coupling fluid to a height which is 0.5 cm below the top edge. This fluid height is accounted for in the numerical model. Any fluid displacement from adding or removing test objects is compensated in order to keep the height constant. We have also found the emulsion to be stable

over the course of measurements, which we confirmed by comparing transmission measurements before and after we take data for imaging.

7.3.2 Antenna Design

The antennas are bow-tie patch antennas, similar to the antennas in [128, 138]. They are single frequency, vertical polarization. The bow-tie was chosen to give more degrees of freedom to help impedance match the antenna to the coupling fluid. The vertical polarization was chosen for best illumination of the object and other antennas in the cylindrical geometry. The substrate material is Rogers RO3210, with 50 mil thickness and reported dielectric constant of 10.2. The antennas were originally designed to operate at 2.8 GHz in the cavity filled with a fluid with $(\epsilon_r, \sigma) = (24, 0.34)$, however, after iterating, we found best performance at 2.75 GHz in a fluid of $(\epsilon_r, \sigma) = (21, 0.475)$.

7.3.3 System Parameters

In determining the system noise and isolation requirements, the minimum expected signal determines the required noise level, and the maximum relative magnitude between signals on adjacent channels determines the required switch path isolation. From previous numerical studies of cavity-like breast imaging with similar emulsion properties, [139], we expect the scattered field S_{21} magnitude of small inclusions to be in the range from -100 to -50 dB, and signals between adjacent antennas to differ by as much as -30 dB. This means that the noise of our measurements must be less than -100 dB, which is achievable by our VNA with averaging and an IF bandwidth of 100 kHz or less. Also, the switching matrix paths must be isolated by at least -30 dB.

7.3.4 Switching Matrix

The receivers were connected through a SP33T solid-state switching matrix that was designed and assembled in house. The matrix consists of two custom SP16T solid state switching matrices, and a cascaded pair of Minicircuits SPDT switches. Each SP16T switch is composed of two layers of SP4T Hittite HMC241QS16 non-reflective switches which are buffered at the output by a third layer consisting of a single SPDT Hittite HMC284MS8GE on each path. The buffer layer was added to increase interpath isolation. The switch is controlled with an embedded digital board and computer parallel port. The operating band of the switching matrix is between 0.1-3 GHz. The overall loss of a path through the SP33T matrix is no worse than 8 dB across the band. We measured the switch path isolation to be better than -55 dB between 1-3 GHz, which meets the criteria above.

7.3.5 VNA Calibration

Two-port VNA calibrations were accomplished between each transmitter and each receiver. The S-parameter reference planes were calibrated to the points where the cables connect to the antenna. These reference planes are identical to those in the HFSS CAD model (presented below). While calibrating, we left the unused ports open with the rationale that the one-way switch isolation of -55 dB provided sufficient matching to the open ports. Short-open-load measurements for a 1-port calibration were taken for each antenna. Next, we measured the through path between the transmitter and each receiver using a connector. In software, we combined the 1-port and through measurements to accomplish a 2-port short-open-load-through (SOLT) calibration with arbitrary through between each transmitter and receiver for a total of 99 separate 2-port calibrations. The calibration for a particular transmitter/receiver pair is recalled in the VNA before taking data.

7.4 Numerical Model

We use Ansoft HFSS to numerically model the cavity, similar to [139]. We use it several ways. First, we model the feeding transmission lines in order to assign S-parameter reference planes that are identical in both simulation and experiment. Second, we estimate the normalized incident fields due to the transmitters throughout the cavity for use in Eqns. (7.3) and (7.5), where the normalized incident fields now include all background multiple scattering not present between the object and the cavity. Also, we use the model to generate synthetic scattered field S-parameters of numerical targets in order to study the performance of the inverse scattering algorithm given the source geometry and system parameters.

Figure 7.4 shows the HFSS CAD model of the 12 sided cavity. The model includes the panel thickness and dielectric constant, bottom conductor, probe feed, coupling fluid properties, and height of the fluid. Same as in the experiment, the cavity is filled to a height that is 0.5 cm below the top (seen as the line below the top edge of the cavity). The remaining 0.5 cm is air with a radiating boundary condition. The outer boundary of the cavity is PEC.

Next we compare measured and simulated incident S-parameters in order to access the accuracy of the model. Figure 7.5 shows the magnitude and phase, respectively, of the measured and simulated incident S-parameters between each transmitter and all receivers. The magnitude and phase agree best when the receivers are on the same level as the transmitter. In this case, the magnitude agrees generally to within 3 dB, for all three levels, and the phase agrees to within 30 degrees, which is approximately $\lambda/10$, a common metric for many microwave systems. For measurements between antenna levels in Figure 7.5, the agreement is not as good in magnitude, but the phase error remains similar to the previous cases. For cross-level measurements, the agreement is not as good in magnitude, but similar phase. This also shows that the one-way path loss across the cavity is approximately -50 dB, so we expect any multiple

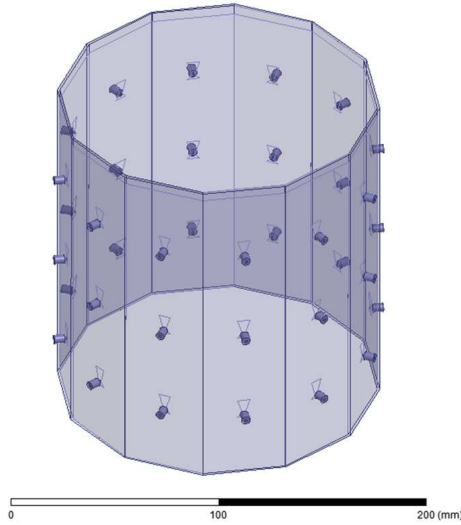
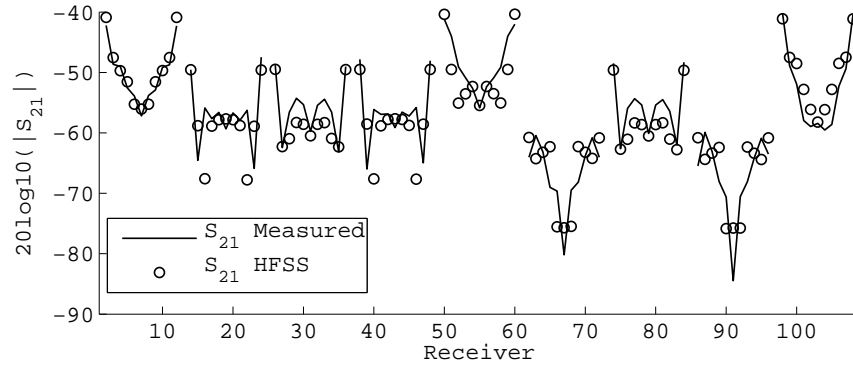


Figure 7.4: HFSS CAD model of the imaging cavity. Twelve panels contain three bow-tie antennas each. The bottom of the cavity is PEC, it is filled with the coupling fluid up to the visible line, and the top surface radiates to air.

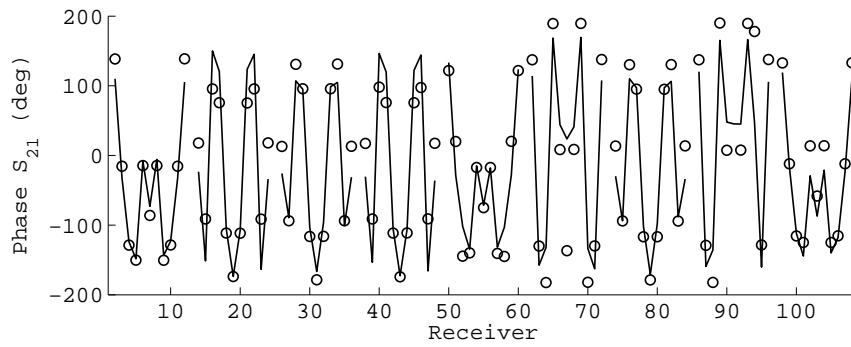
scattering to be localized. This partially justifies our approximating the cavity dyadic Green's function with the lossy free-space dyadic Green's function.

When computing the incident fields, the center of the cavity was meshed with a coarse Cartesian grid of sparse unassigned sheets, shown in Figure 7.6. Sheets are spaced every 5 mm in the x , y and z directions. The spacing is approximately $\lambda/5$ at 2.75 GHz in the fluid with relative permittivity of 21. We have found that this helps constrain the adaptive meshing of HFSS when we obtain the incident fields by interpolating the FEM mesh onto a fine Cartesian grid as we did in Chapter V.

When simulating the structure, with or without scattering targets, we use a convergence criterion of $\Delta S = 0.02$ which is generally reached in 7 adaptive meshing iterations. A typical simulation completed with approximately 1.4 million tetrahedra using 23.5 GBytes of RAM and swap space to obtain a full 36×36 S-matrix. Simulations took approximately 25 hours on a dual 2 GHz E5504 Intel Xeon (2x Quad



(a)



(b)

Figure 7.5: Measured and simulated magnitude and phase of incident S_{21} between each of the three transmitting antennas and all receivers. Solid: measured. Dots: HFSS. The groupings from left to right are the eleven receivers of each level (middle, top, bottom), repeated for the three transmitters (middle, top, bottom), plotted counterclockwise when viewed from above for a given receiver level. For example, data 38:48 are middle receivers and top transmitter. The magnitude and phase agree best for transmitters and receivers on the same level (i.e. data 1:11, 50:60, and 98:108).

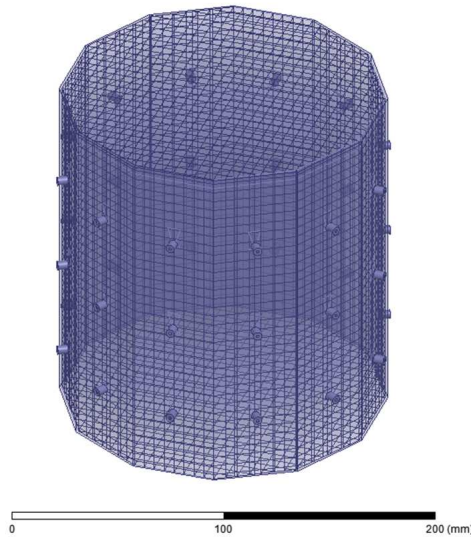


Figure 7.6: HFSS CAD model of the imaging cavity with mesh of unassigned sheets to constrain the adapting meshing of HFSS for field interpolation. Sheets are spaced every 5 mm in each direction.

Core) desktop with 24 GBytes of RAM. Figure 7.7 shows a typical convergence rate as a function of tetrahedra.

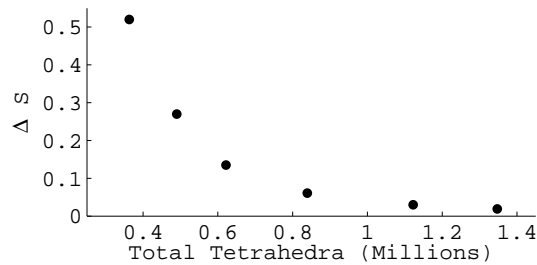


Figure 7.7: HFSS convergence with number of tetrahedra for each adaptive meshing step.

We obtained the incident fields for only the three transmitters. The incident fields for the receivers were obtained through rotation, where we assume the 12 panels of the experimental cavity are identical. The incident fields were sampled on a $17 \text{ cm} \times 17 \text{ cm} \times 18 \text{ cm}$ grid with 1 mm spacing, which is $\lambda/24$ at 2.75 GHz in a fluid with relative permittivity 21. In simulation, the average transmit power was 1 Watt, so, from

transmission line analysis, the line voltage is given by $a_o = \sqrt{(2P_{ave}Z_o)} = \sqrt{(2Z_o)}$, which is used in Eqns. (7.1) and (7.2). The phase of a_o is zero because the S-parameter reference planes of the HFSS model and the experimental cavity were identical.

Figure 7.8 shows three cross cuts of the z-component of the incident electric field through the center of the cavity for the center transmitter in a fluid of relative permittivity of 21 and conductivity 0.475 at 2.75 GHz. The coordinate origin is at the center of the cavity, and the transmitter is located on the positive x axis. The effects of the cavity on the incident field are seen in Figure 7.8(a) where the fields are guided by the walls of the cavity; the coaxial feeds are also visible; the fluid-air interface is visible in Figures 7.8(b) and 7.8(c).

7.5 Image Reconstructions

7.5.1 Synthetic Data

We first test the BIM and numerical characterization using synthetic data from HFSS. This is to assess the performance of the algorithm and source geometry under near ideal circumstances. We simulated the scattered field S-parameters of simple numerical objects and use these data as measurements in the inversion algorithm. HFSS scattered field data includes any multiple scattering between the object and the cavity. The background medium had a relative permittivity of 21 and a conductivity of 0.475 Siemens/m. The incident fields were computed with these background parameters and used in volume integral equations.

Example 1: We first used HFSS to simulate the scattered field S-parameters for a single 1.5 cm diameter sphere located at $(x,y,z) = (0,0,2\text{cm})$ with four combinations of relative permittivity and conductivity: (40, 1), (40, 0), (10, 1), (10, 0). The HFSS model is shown in Figure 7.9. Figures 7.10 - 7.13 show images of the first and fourth BIM iterations for each object. As shown, in some cases, the BIM steps were essential

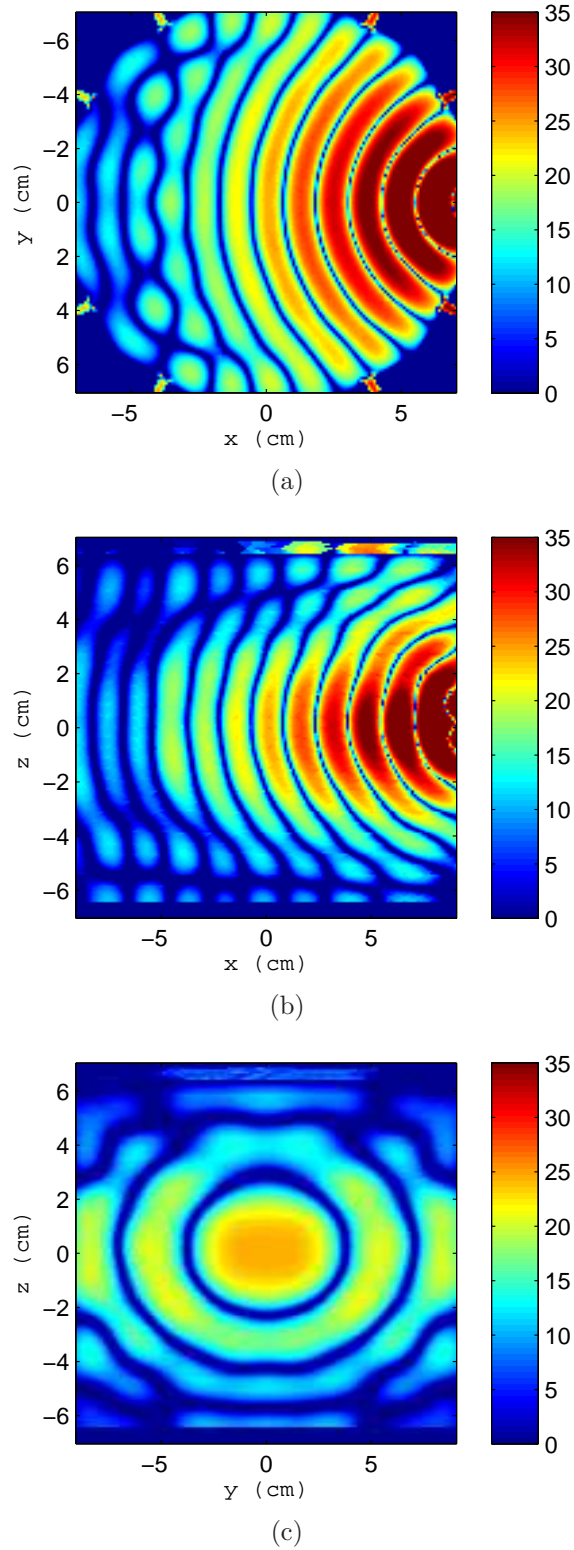


Figure 7.8: Cross cuts through the center of the cavity of the z-component of the incident electric field due to the middle transmitter. The scale is $20\log_{10}(|\text{Re}\{E_{z,inc}\}|)$ of the unnormalized field. a) horizontal x-y, b) vertical x-z, c) vertical y-z planes.

in recovering the correct property values of the sphere, in other cases, the relative permittivity was improved at the expense of the conductivity value. These images show that the source geometry and numerical characterization are adequate for the retrieval of some object property combinations, but not others. This fact, together with the visible artifacts, suggests that the images could be improved with a denser source geometry.

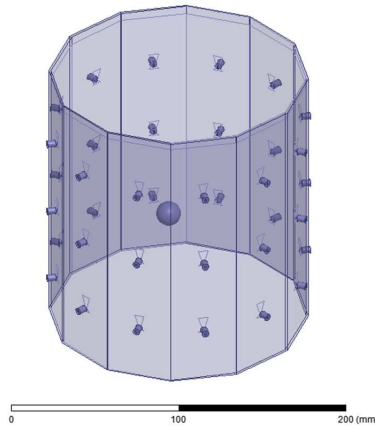


Figure 7.9: HFSS model of a simple sphere use to generate synthetic scattered field S-parameters.

Example 2: Next we imaged a more anatomical, albeit unrealistic, numerical breast phantom. The numerical phantom is shown in Figure 7.14. The breast is 9 cm at the widest point, and 6 cm deep. The outer layer is 2 mm thick and meant to mimic a mismatch layer, for example a layer with an effective permittivity representing both skin and subcutaneous fat. The inclusion is 2 cm in diameter. The dielectric properties of the outer layer, glandular tissue, and inclusion, respectively, are $(\epsilon_r, \sigma) = \{(10, 0.3), (23, 0.475), (42, 0.8)\}$. We assume we know the volume region of the breast, so mask that volume excluding all other points during inversion. Figure 7.15 shows the reconstructed relative permittivity and conductivity after 3 iterations for three cuts. The relative permittivities of the inclusion and the skin layer are well recovered. The conductivity of the inclusion is also recovered, but the skin is not.

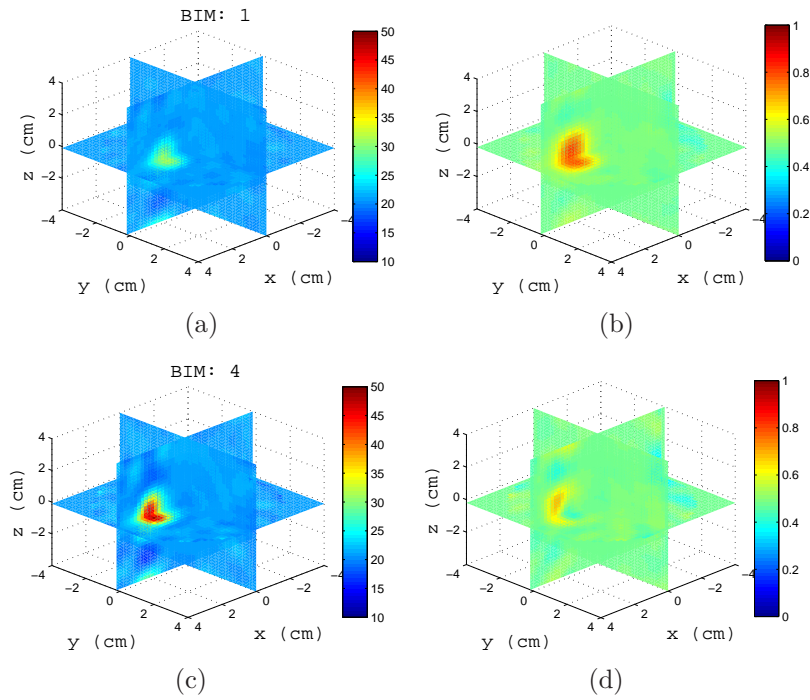


Figure 7.10: Reconstructions of a single sphere $(\epsilon_r, \sigma) = (40, 1)$ located at $(x,y,z) = (0,0,2\text{cm})$ of Example 1. Left and right columns are relative permittivity and conductivity, respectively. Top row is the Born approximation. Bottom row is BIM iteration 4. Here, iterations help retrieve the relative permittivity in c), but the Born approximation yielded better conductivity in b).

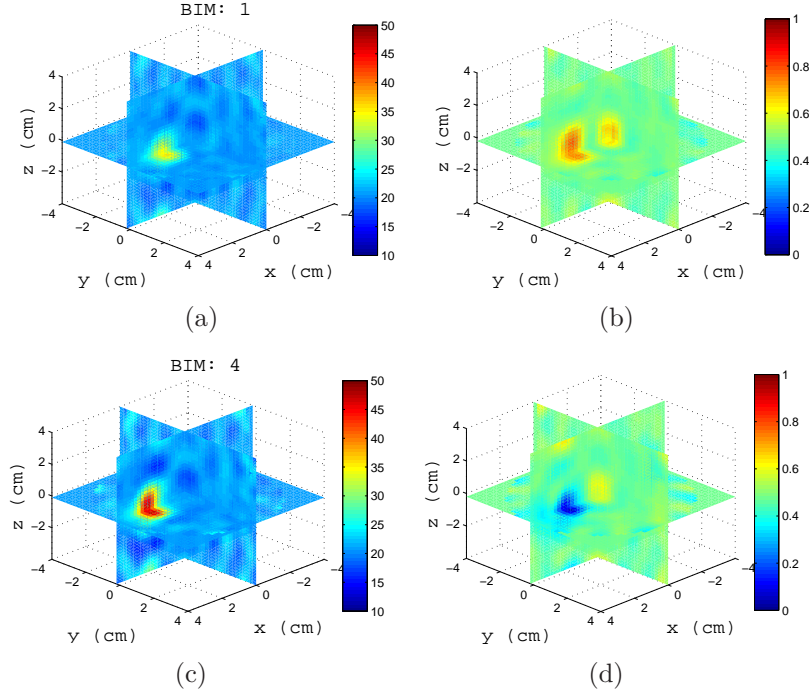


Figure 7.11: Reconstructions of a single sphere $(\epsilon_r, \sigma) = (40, 0)$ located at $(x,y,z) = (0,0,2\text{cm})$ of Example 1. Born iterations helped retrieve the relative permittivity in c), and are essential in recovering the conductivity in d).

Both sets of images suffer from artifacts; the twelve-pointed pattern in Figures 7.15(e) and 7.15(f) is due to the sparse spatial sampling of the antennas and indicates that the images can be improved with more angular views.

Example 3: To push the algorithm, we imaged a phantom which included a skin layer, fat layer, glandular tissue, chest wall, and inclusion, with relative permittivity and conductivity, respectively, of $(45, 1.6)$, $(5.1, 0.16)$, $(21, 0.475)$, $(52, 2.0)$, and $(40, 1.0)$. The HFSS model is shown in Figure 7.16. The reconstructions are shown in Figure 7.17. In this case the algorithm failed to recover the contrasts. This suggests that either 1) the object is too different from the background for the BIM to converge, 2) object-cavity interactions are too strong to use the free-space dyadic Green's function, or 3) images cannot be constructed if the chest wall is not modeled, meaning that it is necessary to model the chest wall for the incident fields and the dyadic Green's function.

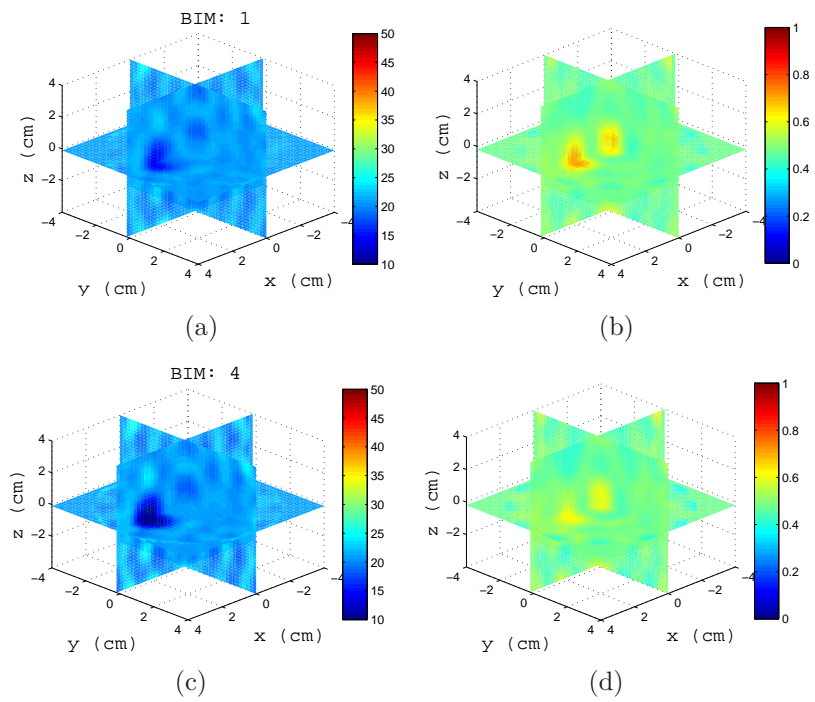


Figure 7.12: Reconstructions of a single sphere $(\epsilon_r, \sigma) = (10, 1)$ located at $(x,y,z) = (0,0,2\text{cm})$ of Example 1. Born iterations helped the recovery of the low permittivity in c), but at the expense of the correct conductivity value which was better in with the Born approximation in b).

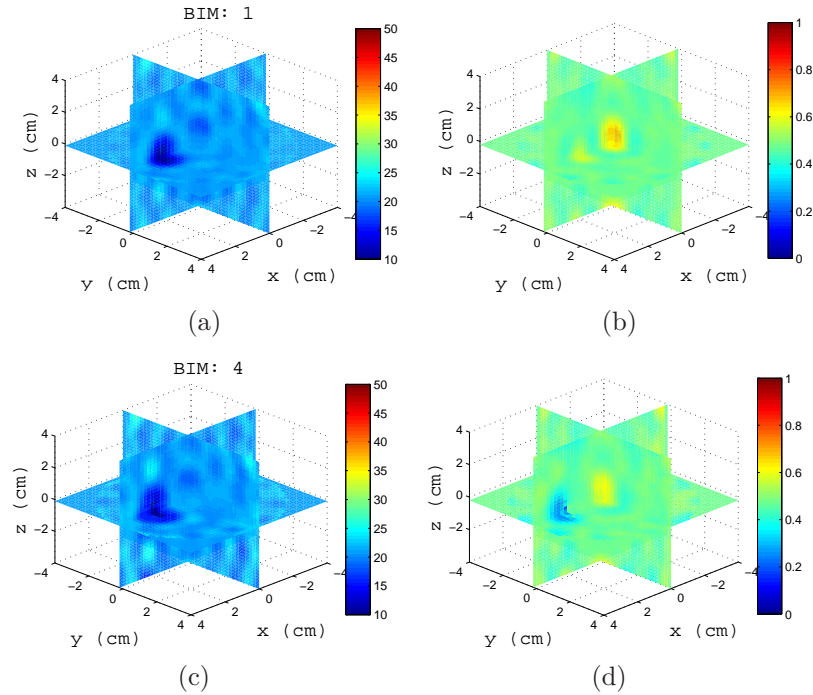


Figure 7.13: Reconstructions of a single sphere $(\epsilon_r, \sigma) = (40, 0)$ located at $(x,y,z) = (0,0,2\text{cm})$ of Example 1. Born iterations helped bring out the proper conductivity value in d).

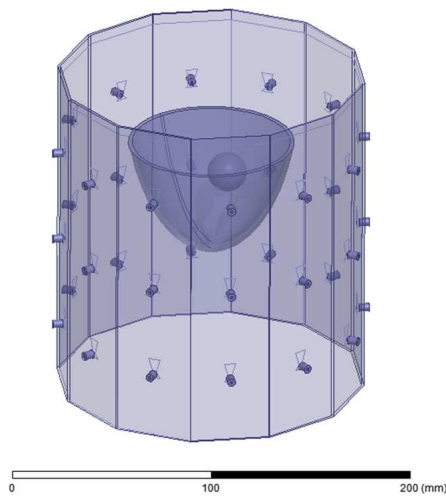


Figure 7.14: HFSS CAD numerical breast phantom of Example 2. The inclusion is 2 cm in diameter with relative permittivity and conductivity contrasts of 2:1. The skin layer is 2 mm thick.

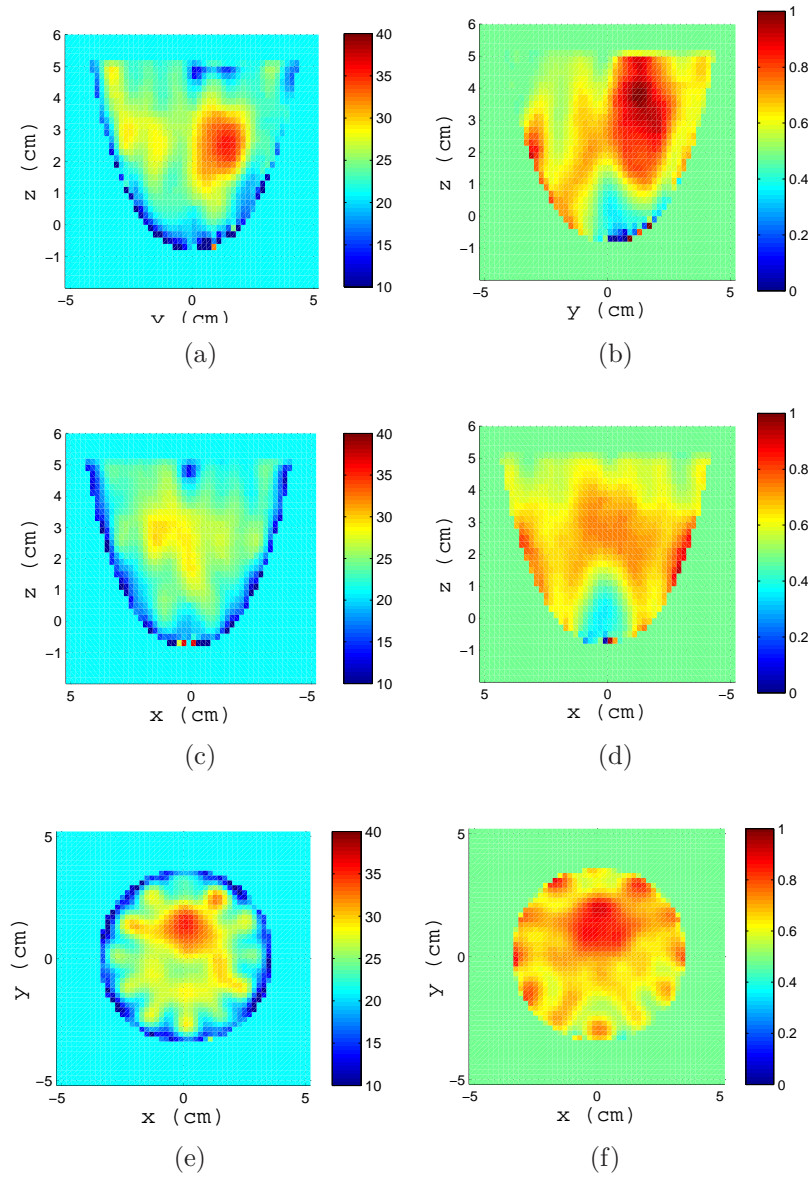


Figure 7.15: Reconstructions of the HFSS numerical breast phantom in Example 2 after three iterations. Left and right columns are relative permittivity and conductivity, respectively. Rows top down are cuts at $x = 0$ cm, $y = 0$ cm, and $z = 2.5$ cm. The relative permittivity of the skin and inclusion are well recovered. The conductivity of the inclusion is recovered, but both images contain many artifacts.

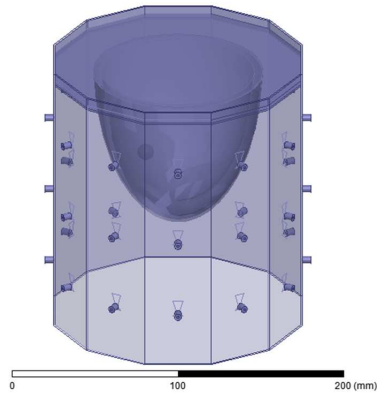


Figure 7.16: HFSS CAD numerical breast phantom with skin layer, fat layer, glandular tissue and chest wall of Example 3. The inclusion is 1 cm in diameter with relative permittivity and conductivity contrasts of 2:1.

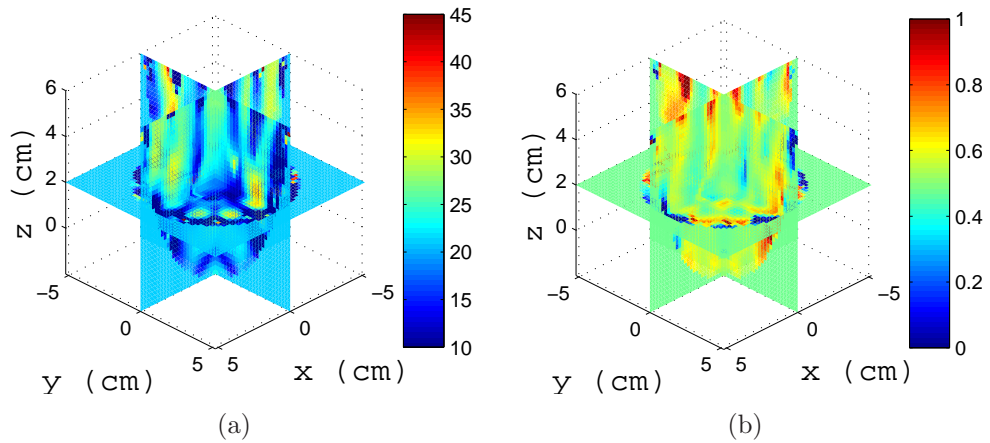


Figure 7.17: Reconstructions of the HFSS numerical breast phantom which includes the chest wall of Example 3. Left and right figures are relative permittivity and conductivity, respectively. The object could not be reconstructed.

Example 4: Finally, we studied the effects of different background permittivities when forming images. This represents a case in experiment where the measurements are taken in a fluid with some set of properties, but the fluid properties we use in the model are slightly off. We formed images using HFSS scattered field data of the sphere with $(\epsilon_r, \sigma) = (40, 0)$ in a background of $(\epsilon_b, \sigma) = (21, 0.475)$, but where we use incident fields from five different background permittivities: $\{20, 20.5, 21 \text{ (again)}, 21.5, 22\}$ and the same conductivity.

Figure 7.18 shows 3D cross cuts at the fourth BIM iteration for all five backgrounds. Figures 7.18(e) and 7.18(f) are the correct images. Notice that an error in the background permittivity of 1, or 5%, is enough for the reconstructed object contrast to oscillate, demonstrating that reconstructions are very sensitive to our knowledge of the background properties.

7.5.2 Experimental Data

In the experimental system, we imaged simple plastic objects as well as gelatin breast phantoms. The objects were suspended from a platform and rotated to 12 positions in 30 degree increments. Scattered field S-parameter measurements from each position were combined to yield a full 36×36 S-parameter matrix which was used in the inverse scattering algorithm.

Experiment 1: We imaged a single acrylic sphere, shown in Figure 7.19. The diameter of the sphere was 2.54 cm, with properties $(\epsilon_r, \sigma) = (2.7, 0)$. The sphere was located at approximately $(x,y,z) = (1.5 \text{ cm}, 1.5 \text{ cm}, 0)$. Figure 7.20, shows the reconstructions after 4 iterations of the x-y plane. The inversion domain is masked so that only a cylindrical region containing the rotated object is imaged. We also imaged two acrylic spheres, shown in Figure 7.19. Figure 7.21, shows the reconstructions after 4 iterations. In both cases, the relative permittivity is recovered, and the conductivity contrast is correctly valued but the shape is incorrect. There are also many artifacts

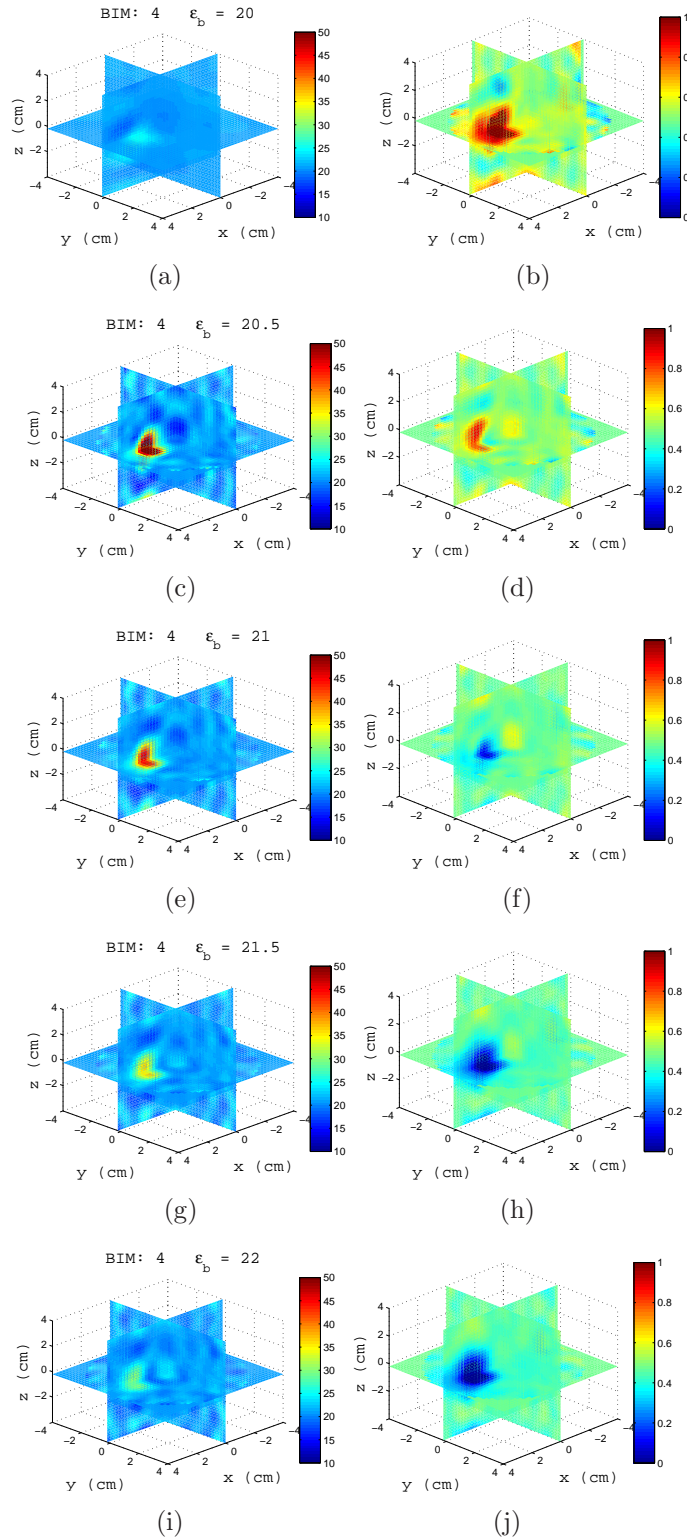


Figure 7.18: Image reconstruction sensitivity to background permittivity. Left and right columns are relative permittivity and conductivity, respectively. Data was generated in background of $(21, 0.475)$. Reconstructions with background relative permittivities of $\{20, 20.5, 21, 21.5, 22\}$ for rows 1 through 5 respectively. Recovered contrasts of the sphere oscillate about the background.

present. Given that the imaging algorithm could recover the single sphere using HFSS data, we can attribute these discrepancies to differences between the experiment and the model.

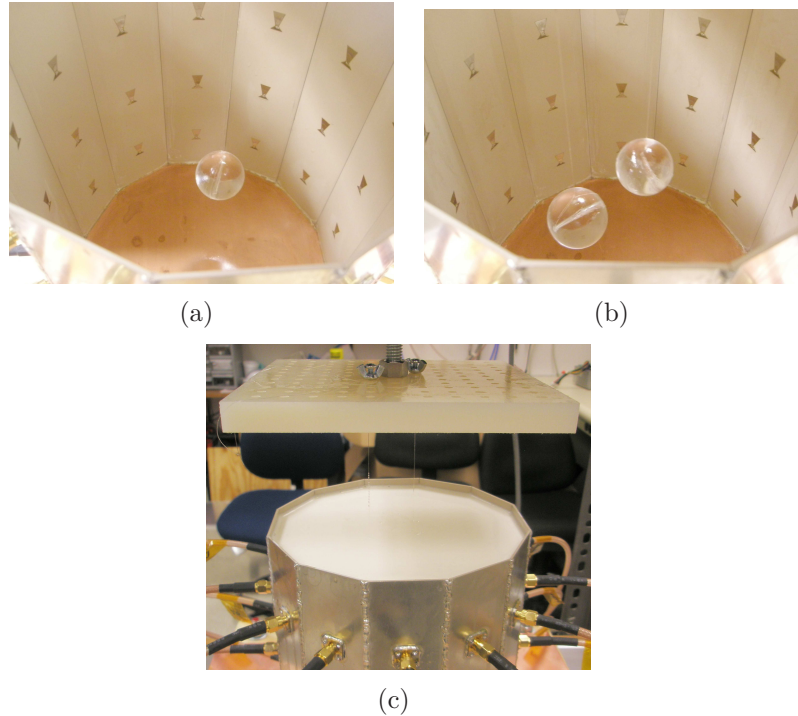


Figure 7.19: Test objects and coupling fluid for Experiment 1. a) Single suspended acrylic sphere. b) Two acrylic spheres. c) Cavity filled with the coupling medium. Objects are suspended and rotated from the nylon platform.

Experiment 2: Finally, while the primary system concerns a cavity having antennas which operate at 2.75 GHz, we also built a lower frequency cavity where the antennas operate at 915 MHz. This cavity was numerically characterized using the same methods. Figure 7.22 shows the cavity with three acrylic spheres. Two spheres are located in the x-y plane, while the third is positioned at approximately $(x,y,z) = (4 \text{ cm}, -3 \text{ cm}, 5 \text{ cm})$. We imaged the relative permittivity and conductivity and the results after 2 iterations are shown in Figure 7.23. The shape and permittivity of the two in-plane spheres are well recovered. The third sphere is also detected but cut off at the upper left of the imaging domain. Artifacts are also present, but this example better demonstrates that the numerical characterization, BIM, and free-space

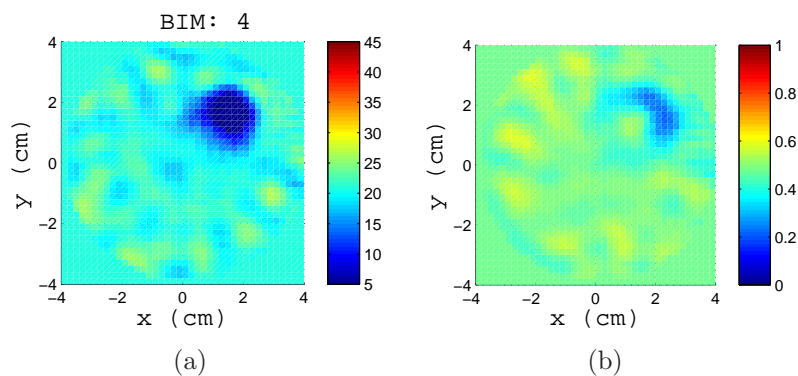


Figure 7.20: Reconstructions of the single acrylic sphere of Experiment 1 shown in Figure 7.19(a). Left: relative permittivity. Right: conductivity. The permittivity is recovered well but the shape in the conductivity is not

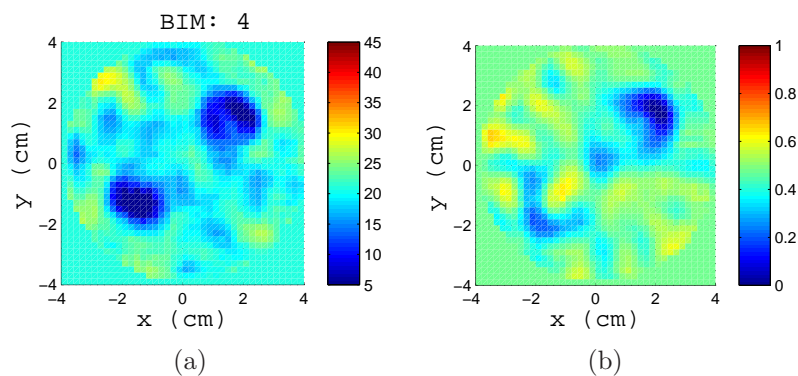


Figure 7.21: Reconstructions of the two acrylic spheres of Experiment 1 shown in Figure 7.19(b). Left: relative permittivity. Right: conductivity. The permittivity is again recovered well but the shape in the conductivity is not.

Green's function are capable of recovering objects in this cavity and source geometry. It should be noted that images formed with data at 915 MHz are less susceptible to modeling errors because the cavity and objects are electrically smaller, but the resolution is reduced.



Figure 7.22: Second cavity with antennas designed to operate at 915 MHz of Experiment 2. Three acrylic sphere are suspended (one visible). Cavity is filled with fluid for imaging.

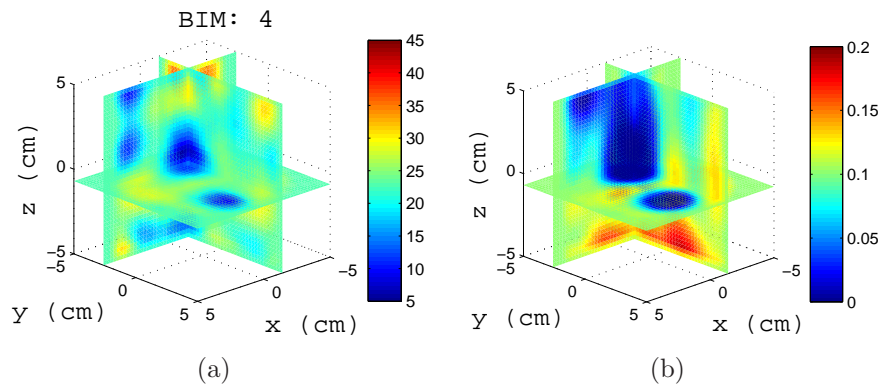


Figure 7.23: Reconstruction of the relative permittivity and conductivity of three acrylic spheres using a cavity operating at 915 MHz from Experiment 2. The two spheres in plane are well recovered, and the third detected at the upper left of the image.

7.5.3 Discussion

Overall, the imaging algorithm, numerical characterization and experiment worked with some success, and there are several areas for continued investigation.

First, Examples 1 and 2, and also Experiments 1 and 2, validate the technique described in this chapter showing that the numerical characterization of the cavity incident fields and the use of the vector Green's function formulation linking the incident fields to the inverse scattering algorithm can be used to successfully form images in a cavity geometry. Examples 1 and 2 demonstrate the consistency of the method using synthetic scattered field S-parameter data. Experiments 1 and 2 show that the characterization and experiment agreed enough for the BIM to recover the location and permittivity of the test objects. More realistic phantoms and lower contrast phantoms will help further confirm the methodology.

Second, in Example 1, although some permittivity and conductivity combinations of the sphere were recovered, others were not. Given that the data was synthetic, this points to inherent imaging ambiguities in the simultaneous retrieval of both permittivity and conductivity in the inverse scattering problem. Possible solutions are increasing the number of unique data, or including prior information about the relations between permittivity and conductivity in tissue.

Third, the success of the algorithm in Example 2 in recovering the partial breast phantom suggests that our use of the lossy free-space dyadic Green's function in the forward solver of the BIM did not grossly affect image reconstruction in this case. This is keeping in mind that the synthetic scattered field S-parameter data did include any multiple scattering between the phantom and the cavity.

Fourth, in light of the successful reconstruction of the simple phantom in Example 2, the failure of the algorithm to recover the more complete breast phantom in Example 3 points to the need to model the chest wall. This can be done by including it in the incident field computations but it may also be necessary to estimate the cavity dyadic Green's function. This is an area to be investigated.

Lastly, Example 4 shows that we must know the background relative permittivity to within 5% of the actual or else risk incorrectly estimating whether the contrasts

are higher or lower than the background. An equivalent error can arise from a correct background permittivity but incorrectly measuring the dimensions of the cavity. We suspect that the very high recovered conductivity values in both Experiments 1 and 2 may be due in part to these types of systematic errors. This demonstrates the difficulty in achieving the necessary consistency between the model, experiment, characterization, and imaging algorithm to accurately form microwave breast images of diagnostic quality.

7.6 Conclusion

In this chapter, we used the vector Green's formulation and numerical simulation to characterize an experimental breast imaging cavity. We used HFSS to numerically estimate the incident fields of the antennas in the cavity and used our understanding of the vector Green's function to interface the numerical characterization with our imaging algorithm and S-parameter based experimental setup. The imaging algorithm recovered both the numerical and experimental test objects with some success.

Though much work remains in developing methods to help better match the model to the physical setup, this experiment shows that the techniques developed in the previous chapters were successful in providing a clear path in order to characterize near-field microwave breast imaging systems. Any current or future cavity based imaging systems can take advantage of some of these techniques.

CHAPTER VIII

Acoustic Inverse Scattering Experiment

8.1 Introduction

In this chapter, we will give the analogous treatment to acoustics as we did to the electromagnetic inverse scattering problem in Chapters IV-VII in an effort to carry the formalism from those chapters to the task of calibrating an acoustic inverse scattering experiment. The acoustic source-scattering matrix formulation will be presented along with a propagation model. Next we will discuss acoustic source characterization and a new self-calibration technique based on the nonlinear inversion of the acoustic propagation model. We will derive the acoustic analogue of the vector Green's function from Chapter V. Finally, results from the application of the self-calibration technique to commercial ultrasound transducer probes will be presented, as well as images of simple targets from the inverse scattering algorithm.

There are several key differences between the experimental acoustic and microwave problems that should be pointed out, especially with regard to source characterization.

First, we are unable to simulate acoustic transducers as completely as we can simulate antennas. The transducer elements of both single-element focused transducers as well as commercial ultrasound probes are complicated amalgams of piezoelectric material, backing, and matching materials. It is possible to X-ray the transducer for spatial size, but this does not give us information about the boundary conditions. In

Table 8.1: Comparison between ultrasound and microwave spatial scales

	Background Velocity	Frequencies	Wavelengths	$\lambda/10$
Microwave	$3 \times 10^8 / \sqrt{(20)}$ m/s	1 - 3 GHz	7cm - 2 cm	O(mm)
Ultrasound	1500 m/s	1 - 3 MHz	1.5 mm - 0.5 mm	O(10 μ m)

the microwave problem HFSS gave us a precisely defined way of comparing experiment and simulation through S-parameters. We do not have an analogous simulator in acoustics.

Second, the acoustic problem size and operator frequencies differ greatly from the microwave problem, as listed in Table 8.1. While the GHz operating frequencies and speed of light are the primary challenge for microwave circuits, the spatial wavelengths and antenna sizes are on the order of centimeters, making the construction of antennas and setups by hand accurate enough. For the acoustic problem, the operating frequencies are MHz making for simpler electrical components, however the acoustic wavelengths in water are submillimeter. Thus positioning and alignment are often done with optical equipment and cannot be done by hand or by eye, because distances are hundreds of wavelengths.

Last, the acoustic source-scattering formulation gives the same transmission line treatment to the feed of the acoustic transducer as we had in the microwave case. However, for the acoustic problem, the electrical length in the circuit is so large that microwave network analysis is not necessary. Also, acoustic measurements are typically not taken with a network analyzer, only an oscilloscope, nor are the transmission lines calibrated as would be necessary to carry out network analysis. Thus, instead of dealing with left and right going waves on the transmission line, we only deal with the total line voltage in experiment. Thus, we need to modify the source-scattering model somewhat to account for this.

8.2 Multipole Propagation Model for Acoustics

In this section, we will first present the same source scattering matrix formulation as was presented in Chapter IV but for acoustic sources. Using it we will derive a similar propagation model relating the transmit coefficients of two acoustic transducers to the voltage measurements between them.

8.2.1 Field Expansion and Translation Relations

The free-space scalar wave functions are given by, [52]

$$\psi_{lm}(\mathbf{r}) = z_l(kr)Y_{lm}(\theta, \phi) \quad (8.1)$$

where $z_l(x)$ is any one of $j_l(x)$, $y_l(x)$, $h_l^{(1)}(x)$, $h_l^{(2)}(x)$ and $Y_{lm}(\theta, \phi)$ are the spherical angular harmonics. A pressure field can be expanded about a source in terms of incoming and outgoing wave functions as

$$\phi(\mathbf{r}) = \sum_{lm} (a_{lm}\Re\psi_{lm}(\mathbf{r}) + b_{lm}\psi_{lm}(\mathbf{r})) \quad (8.2)$$

where a_{lm} and b_{lm} are the multipole coefficients for incoming and outgoing harmonics, respectively, and \Re means the regular part of the corresponding Bessel function.

In the case where we have a field radiating from a frame i and incoming in frame j the fields in each frame are given by

$$\phi(\mathbf{r}_i) = \sum_{lm} b_{lm}^i \psi_{lm}(\mathbf{r}_i) \quad (8.3)$$

$$\phi(\mathbf{r}_j) = \sum_{lm} a_{lm}^j \Re\psi_{lm}(\mathbf{r}_j) \quad (8.4)$$

$$(8.5)$$

Then, from the addition theorem for scalar wave functions, the coefficients of each

frame are related by

$$a_{l'm'}^j = \sum_{lm} \alpha_{l'm',lm}^{ji} b_{lm}^i \quad (8.6)$$

where $\alpha_{l'm',lm}^{ji}$ is the translation matrix given in [52] and is evaluated with the vector that points from frame i to frame j .

8.2.2 Acoustic Source Scattering Matrix Formulation

Following [83], and analogous to the antenna source scattering matrix formulation, the acoustic source is connected to a shielded transmission line, where a_o and b_o are complex outgoing and incoming modes, respectively, on the transmission line. We relate the modes on the transmission line to the pressure field expansion coefficients through a linear model

$$b_o = \Gamma a_o + \sum_{lm} u_{lm} a_{lm} \quad (8.7)$$

$$b_{lm} = t_{lm} a_o + \sum_{l'm'} S_{lm,l'm'} a_{l'm'} \quad (8.8)$$

where t_{lm} and u_{lm} are the transmit and receive coefficients, respectively, and $S_{lm,l'm'}$ captures the passive scattering properties of the acoustic source, much like a T-matrix. Also, Γ is the reflection coefficient seen looking into the device.

From electro-acoustic reciprocity, the following relations between the transmit and receive coefficients can be derived, [83],

$$u_{lm} = \frac{Z_o}{2\rho_o c k^2} (-1)^m t_{l,-m} \quad (8.9)$$

$$S_{l,m,l'm'} = (-1)^{m+m'} S_{l-m,l',-m'} \quad (8.10)$$

where ρ_o , c , and k are the background density, sound speed, and wave number, respectively, and Z_o is the characteristic impedance of the line.

8.2.3 Relation to Total Line Voltage

The source scattering matrix formulation is derived using the left and right traveling line voltages feeding the acoustic source. This was advantageous for the microwave problem because it made the extension to S-parameters quite natural. Given the long electrical wavelengths at ultrasound operating frequencies (1-3 MHz), full network analysis is not usually performed; there is no need to define a reference plane on the transmission line, and we use oscilloscopes to measure only the total line voltage. However, the electrical impedance (and so reflection coefficient) of the acoustic source does play a part. Here we will outline the assumptions necessary to deal with the source scattering matrix in terms of the total line voltage.

The total line voltage is given as $V_o = a_o + b_o$. If the acoustic device is purely receiving, we expect no input mode, $a_o = 0$ so $b_o = V_o$, which we define as the total output voltage on the line V_{out} .

$$V_{out} = b_o = \sum_{lm} u_{lm} a_{lm} \quad (8.11)$$

If the device is purely transmitting, and no other device is transmitting so there are not other incoming waves ($a_{lm} = 0$), then $b_{lm} = t_{lm} a_o$ and $b_o = \Gamma a_o$. Defining the total line voltage now as V_{in}

$$b_{lm} = t_{lm} \frac{1}{1 + \Gamma} V_{in} \quad (8.12)$$

It is enough to lump the effects of the reflection coefficient into the reciprocity relations where the source model is now

$$V_{out} = \sum_{lm} u_{lm} a_{lm} \quad (8.13)$$

$$b_{lm} = t_{lm} V_{in} \quad (8.14)$$

with

$$u_{lm} = c_r (-1)^m t_{l,-m} \quad (8.15)$$

$$c_r = \frac{Z_o(1 + \Gamma)}{2\rho_o c k^2} \quad (8.16)$$

where we define c_r as the reciprocity constant.

It may be difficult or impossible to measure Z_o , Γ , and possibly the other coefficients accurately (especially with commercial ultrasound probes). However, we see that u_{lm} and t_{lm} are simply linearly proportional by systematic constants. The important part of the reciprocity relation is the dependence between u_{lm} and t_{lm} on $-m$.

8.2.4 Propagation Model

Let there be two acoustic sources, which could be transducers elements on a scan head, one transmitting in frame i , the other receiving in frame j , both have their own field expansion and set of transmit and receive coefficients. Assume no multiple scattering between the sources. Using Eqn. (8.6), the input and output voltage of the two devices are related by

$$V_{out}^j = V_{in}^i \sum_{l'm'} u_{l'm'}^j \sum_{lm} \alpha_{l'm',lm}^{ji} t_{lm}^i \quad (8.17)$$

Substituting Eqn. (8.15) and taking $m' \rightarrow -m'$ we have the acoustic propagation

model

$$V_{out}^j = V_{in}^i c_r^j \sum_{l'm'} (-1)^{m'} t_{l'm'}^j \sum_{lm} \alpha_{l',-m',lm}^{ji} t_{lm}^i \quad (8.18)$$

which is analogous to the antenna propagation model derived in Chapter IV. Here, c_r^j depends on the characteristic line impedance and reflection coefficient on the receiver side.

8.3 Ultrasound Source Characterization

In the antenna characterization problem, we took advantage of the fact that we could make our commercial simulation package (HFSS), network analyzer, and antenna construction completely consistent from end to end. In the ultrasound problem, however, we are hard pressed to do any one of these three. First, we do not fabricate the ultrasound transducers ourselves. They are a complicated assortment of piezoelectric resonator, matching layer (to water), impedance matching (to driving circuit), grounding layer, plastic membrane, water proofing, and focusing lens, [5]. It is possible to obtain a rough mechanical layout by X-raying a given transducer, but the exact material properties and boundary conditions are nearly impossible to reverse engineer. Also, the mechanical scales are submillimeter. Second, even if all the mechanical properties are known, simulating the electro-acoustic response requires a multi-physics simulation package which can handle anisotropic piezoelectric material. Last, because we do not calibrate an oscilloscope as we do a vector network analyzer, linking the simulation to the measurements is difficult. A well known package called Field II [140], can simulate the free space radiation of a prescribed array of transducer apertures. It is a widely popular method for simulating beam patterns and apodizations. However, it is based simply on the linear impulse response of ideal apertures. It is unclear how to properly link the results of Field II to measurements in a way

that yields absolute phase calibration of the transducer incident field over hundreds of wavelengths, especially given the uncertainty in the transducer features and their sizes. The point is, we want to avoid having to make too many assumptions in our method of characterizing the transducer; we are seeking a method that keeps close to the formalism of the source-scattering matrix and multipole propagation model because of the rigor and versatility they provide if the transmit coefficients can be found.

Without a full electromechanical simulation of our transducers, we are left with two options in characterizing our transducers and finding the transmit coefficients: direct field measurements using a hydrophone, or inverting the propagation model. We will briefly discuss hydrophone field measurements, but will concentrate mainly on the inversion of the propagation model. The latter represents a new multi-source self-calibration technique which we have studied in some depth.

8.3.1 Hydrophone Characterization

Here we describe our early attempts of transducer characterization with a hydrophone and some thoughts for future work in this area.

Figure 8.1 shows one of our early attempts to characterize a large transducer element with a hydrophone. The transducer has a focal spot approximately 2 cm from the face of the lense. The idea was to find an equivalent source that, given an arbitrary voltage input, would appear to radiate from the focal spot. The transducer was mounted on a micropositioner and gimbal and a filament was used to place the focus at the center of rotation of the rotator. The hydrophone was positioned on a 3-axis automated positioner so that it could be aligned coincident with the bore site of the transducer. A pulse was sent to the transducer, and both it and the hydrophone response were recorded. The transducer was then rotated about its focus for another data acquisition. The reason for doing this is that the hydrophone is not a point, but

has a finite sensing face and its own radiation pattern. The best way, at the time, of minimizing the need to account for the hydrophone pattern was to keep it always pointing radially at the transducer. A Cartesian 3D scan of the field of a stationary transducer would require an extra calibration step to account for this.



Figure 8.1: Photo of an early hydrophone characterization experiment. A transducer is gimbaled and mounted on a translator. The focus of the transducer is positioned at the center of rotation of the rotational stage. A hydrophone is also gimbaled and positioned with a 3-axis micropositioner.

At the time of this experiment, the source-scattering matrix was not known to us, but the goal remained the same in that we were seeking an equivalent source. The approach was to fit the measured hydrophone time traces with a series of Gaussian windowed sinusoids emanating from a compact array of point sources near the focal spot of the transducers. This fitting procedure was successful, but using it in an inverse scattering experiment was not possible at the time.

Had the source-scattering matrix formulation been known to us at the time, then the approach would be to solve a linear inverse problem for the transmit coefficients

given the pressure fields measured by the hydrophone,

$$\phi(\mathbf{r}_n) = V_n \sum_{lm} t_{lm} \psi_{lm}(\mathbf{r}_n) \quad (8.19)$$

where \mathbf{r}_n are the locations of N hydrophone pressure field measurements V_n . Here, V_n is the frequency component of the recorded voltage time trace.

The main challenges with hydrophone characterization are 1) alignment and positioning, 2) removing the effects of the hydrophone, and 3) repeatability. Repeating a hydrophone characterization is difficult, say for instance if someone drops the transducer warranting another characterization, because alignment is so time consuming. Furthermore, unless the hydrophone has been absolutely calibrated (which it often is), then its pattern and frequency response must be taken out.

More recently in the BRS Ultrasound group, a 6-axis robotic arm was used in the hydrophone characterization of CMUT (capacitive micromachined ultrasound transducer) arrays. The robotic arm, with its isocentric software, allows taking samples of the radiated pressure field with the hydrophone radially pointed at a stationary transducer, along the radial arc. Alignment is still a challenge, but this setup approaches an ideal measurement setup.

Interestingly, given the simplicity of a CMUT structure, successful electro-mechanical simulations have been performed which agree with measurement, [141]. This opens up the possibility of using simulation to obtain the transmit coefficients and be able to apply more of the techniques of Chapter IV to ultrasound devices. This is left for future work.

8.3.2 Nonlinear Inversion of the Propagation Model

In the absence of hydrophone characterization of ultrasonic transducers, the next idea is to stay within the formalism of the source-scattering matrix and attempt to invert the propagation model directly for the transmit coefficients. This represents

a hydrophone-less characterization, and could prove quite useful. The envisioned setup is to have two or more transducers in a water bath, with known locations and properly measured transmit and receive line voltages, in which we measure the pairwise response and build an inverse problem around Eqn. (8.18).

The advantages of this approach are that all the necessary physics are contained in the propagation model: the translation matrices capture wave propagation, and reciprocity relates the different transmit coefficients to each other. The disadvantage is that because we are dealing with absolute phase, the locations of the transducer reference frames must be known with submillimeter accuracy. Also, the propagation model is nonlinear in the transmit coefficients. In the case of identical transducers, the problem is polynomial nonlinear, but solvable. In the case of distinct transducers, the problem is nonlinear and non-unique.

8.3.2.1 Forward Model

The cost function for a nonlinear problem is, generally, [55]

$$2S(\mathbf{m}) = \|\mathbf{g}(\mathbf{m}) - \mathbf{d}\|_D^2 + \|\mathbf{m} - \mathbf{m}_a\|_M^2 \quad (8.20)$$

The elements of the forward model and data vectors from the propagation model are, respectively,

$$g^{ji}(\mathbf{m}) = c_r^j \sum_{l'm'} (-1)^{m'} t_{l'm'}^j \sum_{lm} \alpha_{l',-m',lm}^{ji} t_{lm}^i \quad (8.21)$$

$$d^{ji} = \frac{V_{out}^j}{V_{in}^i} \quad (8.22)$$

where we always exclude the self term. The vector of model parameters \mathbf{m} contains the transmit coefficients of the k th transducer, written in vector form over all harmonics

as

$$\mathbf{m} = \begin{bmatrix} \mathbf{t}_1 \\ \mathbf{t}_2 \\ \vdots \\ \mathbf{t}_k \end{bmatrix} \quad (8.23)$$

The forward model is a nonlinear function of the transmit coefficients, but only polynomial nonlinear to second order. In the case that all the transducers in the problem are identical, then it has quadratic form, where we are essentially solving the problem $c = x^2$. However, for multiple distinct transducer elements, where each transducer has its own set of transmit coefficients, the forward model takes the form $c = xy$. In the former case, the answer is unique to within a sign. For the latter, it is impossible to uniquely separate the product of two unconstrained variables.

The weakly nonlinear properties of the forward model point to two things: 1) we should attempt to solve a self characterization problem only when we can assume all the transducers are identical, or when we can correct the data so the elements appear identical (as in Figure 8.16 shown later in the experimental section), and 2) the polynomial form of the forward model means that we will be able to derive an analytical expression for the step length in a conjugate gradient minimization, enabling a fast gradient search.

To facilitate the derivations which follow, we can write the forward model in matrix notation as

$$g^{ji}(\mathbf{m}) = \mathbf{t}_j^t \mathbf{N} \boldsymbol{\alpha}_{ji} \mathbf{t}_i \quad (8.24)$$

where $()^t$ is vector transpose, \mathbf{N} is a diagonal matrix containing $c_r(-1)^m$, and the rows of $\boldsymbol{\alpha}_{ji}$ are evaluated at $m' \rightarrow -m'$.

8.3.2.2 Gradients

Assuming the data are independent, the gradient vector is given by

$$\hat{\gamma} = \sum_{ji} \left(\frac{\partial g^{ji}}{\partial \mathbf{m}} \right)^* \frac{1}{\sigma_{ji}^2} (g^{ji}(\mathbf{m}) - d^{ji}) + \mathbf{C}_M^{-1} (\mathbf{m} - \mathbf{m}_a) \quad (8.25)$$

where $\partial g^{ji}/\partial \mathbf{m}$ is the vector of partial derivatives of the forward model with respect to the model parameters.

We can compute the partial derivatives of Eqn. (8.24) with the help of the following matrix identities

$$\frac{\partial \mathbf{x}^T \mathbf{B} \mathbf{x}}{\partial \mathbf{x}} = (\mathbf{B} + \mathbf{B}^T) \mathbf{x} \quad (8.26)$$

$$\frac{\partial \mathbf{x}^T \mathbf{a}}{\partial \mathbf{x}} = \frac{\partial \mathbf{a}^T \mathbf{x}}{\partial \mathbf{x}} = \mathbf{a} \quad (8.27)$$

If the transducers are identical, $\mathbf{t} = \mathbf{t}_j = \mathbf{t}_i$, for all i and j then

$$\frac{\partial g^{ji}}{\partial \mathbf{t}} = (\mathbf{N} \boldsymbol{\alpha}_{ji} + (\mathbf{N} \boldsymbol{\alpha}_{ji})^t) \mathbf{t} \quad (8.28)$$

If the transducers are different, then the gradients are

$$\frac{\partial g^{ji}}{\partial \mathbf{t}_i} = (\mathbf{N} \boldsymbol{\alpha}_{ji})^t \mathbf{t}_j \quad (8.29)$$

$$\frac{\partial g^{ji}}{\partial \mathbf{t}_j} = \mathbf{N} \boldsymbol{\alpha}_{ji} \mathbf{t}_i \quad (8.30)$$

8.3.3 Conjugate Gradient Updates

Regardless of whether we are solving for identical or different transducer transmit coefficients, the conjugate gradient updates are defined

$$\mathbf{m}_n = \mathbf{m}_{n-1} - \alpha_n \mathbf{v}_n \quad (8.31)$$

$$\mathbf{v}_n = \gamma_n + \beta_n \mathbf{v}_{n-1} \quad (8.32)$$

where α_n is the step length and γ_n is the steepest decent vector. β_n is given by

$$\beta_n = \frac{\langle C_M^{-1}(\gamma_n - \gamma_{n-1}), \gamma_n \rangle}{\langle C_M^{-1} \gamma_{n-1}, \gamma_{n-1} \rangle} \quad (8.33)$$

where \langle, \rangle is a simple dot product.

8.3.4 Step length

We choose α_n to minimize the cost function at each step. Substituting the expression for \mathbf{m}_n into the cost function

$$2S(\mathbf{m}_n) = \|\mathbf{g}(\mathbf{m}_{n-1} - \alpha_n \mathbf{v}_n) - \mathbf{d}\|_D^2 + \|\mathbf{m}_{n-1} - \alpha_n \mathbf{v}_n - \mathbf{m}_a\|_M^2 \quad (8.34)$$

Because this forward model is only slightly nonlinear (polynomial), we will obtain a polynomial in α , the minimum of which can be found using standard algebraic techniques. To help the bookkeeping, we first write the the forward model in matrix notation with two generic model vectors representing receivers and transmitters

$$g^{ji}(\mathbf{a}, \mathbf{b}) = \mathbf{a}_j^t \mathbf{N} \alpha_{ji} \mathbf{b}_i \quad (8.35)$$

where \mathbf{a} and \mathbf{b} are model vectors for receiver and transmitter positions respectively. After substituting the update step, and rearranging it can be shown that

$$\mathbf{g}(\mathbf{m}_n) = \mathbf{g}(\mathbf{m}_{n-1}, \mathbf{m}_{n-1}) - \alpha_n (\mathbf{g}(\mathbf{m}_{n-1}, \mathbf{v}_n) + \mathbf{g}(\mathbf{v}_n, \mathbf{m}_{n-1})) + \alpha_n^2 \mathbf{g}(\mathbf{v}_n, \mathbf{v}_n) \quad (8.36)$$

Substituting this into the cost function we have

$$2S(\mathbf{m}_n) = \|\mathbf{r}_{n-1} - \alpha_n \mathbf{g}_1 + \alpha_n^2 \mathbf{g}_2\|_D^2 + \|\mathbf{c}_{n-1} - \alpha_n \mathbf{v}_n\|_M^2 \quad (8.37)$$

where

$$\mathbf{r}_{n-1} = \mathbf{g}(\mathbf{m}_{n-1}, \mathbf{m}_{n-1}) - \mathbf{d} \quad (8.38)$$

$$\mathbf{g}_1 = \mathbf{g}(\mathbf{m}_{n-1}, \mathbf{v}_n) + \mathbf{g}(\mathbf{v}_n, \mathbf{m}_{n-1}) \quad (8.39)$$

$$\mathbf{g}_2 = \mathbf{g}(\mathbf{v}_n, \mathbf{v}_n) \quad (8.40)$$

$$\mathbf{c}_{n-1} = \mathbf{m}_{n-1} - \mathbf{m}_a \quad (8.41)$$

The term $\mathbf{g}(\mathbf{m}_{n-1}, \mathbf{v}_n)$ is treating \mathbf{m}_{n-1} as receivers and \mathbf{v}_n as sources, while $\mathbf{g}(\mathbf{v}_n, \mathbf{m}_{n-1})$ is the opposite. Writing out the vector norms

$$\begin{aligned} 2S(\mathbf{m}_n) &= \|\mathbf{r}\|_D^2 - \alpha(\mathbf{r}, \mathbf{g}_1)_D + \alpha^2(\mathbf{r}, \mathbf{g}_2)_D \\ &\quad - \alpha(\mathbf{g}_1, \mathbf{r})_D + \alpha^2\|\mathbf{g}_1\|_D^2 - \alpha^3(\mathbf{g}_1, \mathbf{g}_2)_D \\ &\quad + \alpha^2(\mathbf{g}_2, \mathbf{r})_D - \alpha^3(\mathbf{g}_2, \mathbf{g}_1)_D + \alpha^4\|\mathbf{g}_2\|_D^2 \\ &\quad + \|\mathbf{c}\|_M^2 - \alpha(\mathbf{c}, \mathbf{v})_M - \alpha(\mathbf{v}, \mathbf{c})_M + \alpha^2\|\mathbf{v}\|_M^2 \end{aligned} \quad (8.42)$$

and using the fact that $(\mathbf{a}, \mathbf{b}) = (\mathbf{b}, \mathbf{a})^*$, we can write this as a quartic polynomial in α_n

$$S(x) = ax^4 + bx^3 + cx^2 + dx + e \quad (8.43)$$

where

$$x = \alpha \tag{8.44}$$

$$a = \|\mathbf{g}_2\|_D^2 \tag{8.45}$$

$$b = -2\Re(\mathbf{g}_1, \mathbf{g}_2)_D \tag{8.46}$$

$$c = \|\mathbf{g}_1\|_D^2 + 2\Re(\mathbf{r}, \mathbf{g}_2)_D + \|\mathbf{v}\|_M^2 \tag{8.47}$$

$$d = -2\Re(\mathbf{r}, \mathbf{g}_1)_D - 2\Re(\mathbf{c}, \mathbf{v})_M \tag{8.48}$$

$$e = \|\mathbf{r}\|_D^2 + \|\mathbf{c}\|_M^2 \tag{8.49}$$

Next, we must find the minimum of $S(x)$ with respect to x . The first and second derivatives of the quartic are given by

$$S'(x) = 4ax^3 + 3bx^2 + 2cx + d \tag{8.50}$$

$$S''(x) = 12ax^2 + 6bx + 2c \tag{8.51}$$

The leading term of the second derivative shows us that this quartic will, globally, always be convex, because a is a square vector norm and always greater than zero. For a convex quartic, there is either one global minimum, or there are at most 2 local minima and 1 local maximum. We can separate these cases by finding the zeros of $S'(x)$, for which there is either 1 real root and two complex conjugate roots (i.e., 1 global minimum of the quartic), or 3 real roots (i.e., 2 local minima and 1 local maximum of the quartic). In the latter case, we find the global minimum by back substitution; any ambiguity that might arise from identical local minima (i.e. different possible step lengths) has not been observed in practice to be a problem.

A cubic is one of the few polynomials for which the zeros can be determined analytically. There are several methods which can be found in math texts; we summarize

one such method here. Given the following definitions for the cubic

$$f = a_3x^3 + a_2x^2 + a_1x + a_o = 0 \quad (8.52)$$

$$q = \frac{3a_3a_1 - a_2^2}{9a_3^2} \quad (8.53)$$

$$r = \frac{9a_3a_2a_1 - 27a_3^2a_o - 2a_2^3}{54a_3^3} \quad (8.54)$$

$$\Delta = q^3 + r^2 \quad (8.55)$$

the roots of the cubic are determined in two cases

$$\begin{aligned} \Delta \geq 0 \quad s &= \sqrt[3]{r + \sqrt{\Delta}} \\ &t = \sqrt[3]{r - \sqrt{\Delta}} \\ \Delta < 0 \quad \rho &= \sqrt{-q^3} \\ \theta &= \arccos(r/\rho) \\ s &= \sqrt[3]{\rho}e^{i\theta/3} \\ t &= \sqrt[3]{\rho}e^{-i\theta/3} \end{aligned} \quad (8.56)$$

where the real part of the cube root is taken. In the first case there is one real root, and two conjugate complex roots. In the second case, there are three real roots. In either case, the zeros are given by

$$z_1 = s + t - \frac{a_2}{3a_3} \quad (8.57)$$

$$z_2 = -\frac{1}{2}(s + t) - \frac{a_2}{3a_3} + \frac{\sqrt{3}}{2}(s - t)i \quad (8.58)$$

$$z_3 = -\frac{1}{2}(s + t) - \frac{a_2}{3a_3} - \frac{\sqrt{3}}{2}(s - t)i \quad (8.59)$$

To summarize, the procedure for finding the step length in this section broadly demonstrates that, for any forward model that is polynomial in the model parame-

ters, the optimal conjugate gradient step length, α_n , can be determined by finding the minimum of a polynomial that is of the forward model order squared. This reduces to a root finding problem, which can be done numerically for any order, but becomes more sensitive to numerical errors for very high order polynomials. This just means that polynomials are a class of nonlinear forward model that do not require line minimization to find the optimal conjugate gradient step length. This can be beneficial for large problems or in trying to carry analytical inversion methods to their limits.

8.3.5 Summary

In this section, we set up and derived a direct nonlinear optimization routine to invert the acoustic propagation model for the transducer transmit coefficients. All of the above steps were used to implement this nonlinear optimization routine. Experimental results of this algorithm follow in the next section.

Much time was spent analyzing this acoustic inversion routine in simulation. These simulations showed that the algorithm was derived correctly. With perfect data and perfect knowledge of the source locations, the transmit coefficients for multiple identical sources could be recovered uniquely to within a sign, from a wide range of initial conditions. It was also determined that when solving for multiple different transducer transmit coefficients, that the synthetic measured data could be fit quite well, but the solution was not correct and dependent on the initial condition, proving the point of non-uniqueness alluded too earlier.

The physical interpretation of the uniqueness of this problem can explained this way. For identical sources, if one source is positioned as the mirror image of the other, then we know that the contribution to the radiation pattern from the measured response should be split evenly in that direction. When identical sources are positioned not as mirrors, but we are given enough angular looks and the associated source orientations, then we can still recover the pattern correctly. For the case of different

sources, a null in the radiation pattern of one source can be compensated by a strong beam in the other. This effect cannot be separated by pair wise-measurements alone.

It should also be noted that this entire derivation was also carried out and studied for the electromagnetic antenna problem. The only major difference is the addition of more terms in the forward model, but the overall form, subsequent conjugate gradient minimization, and interpretations are otherwise the same.

8.4 Ultrasound Probe Characterization Experiment

To test the nonlinear source characterization in the previous section, we built the setup shown in Figure 8.2. This setup was also used for the inverse scattering (next section) so that the characterization and imaging were performed in identical geometries. Two commercial Phillips ATL L7-4 transducers are mounted facing each other in a water tank. Each probe has 128 transducer elements in a linear array. The probes are connected to a Verasonics data acquisition system, which was programmed to collect all combinations of transmit and receive signals between the elements. The mount was custom made out of king starboard. The mounting holes, shown in Figure 8.3, are separated by 1 cm to allow linear translation of the probes relative to one another. The blue holders were created with the help of the U-M 3D Lab. The probes were laser scanned and the scan was used to create a 3D CAD model of the holders. The holders were then fabricated with a 3D printing system.

The idea for characterization was to take transmission measurements in probe positions that would sweep out the imaging domain. This would allow us to sample the field at points in the imaging domain and out at the receiver location, the hope being that this would pin down the phase of the transmit coefficients, and so also the incident field, everywhere. This setup, however, also means that we only use data in plane for the characterization, which is a compromise we had to make to avoid going to complicated 3D setups. The transducer elements of the L7-4 probe are known to

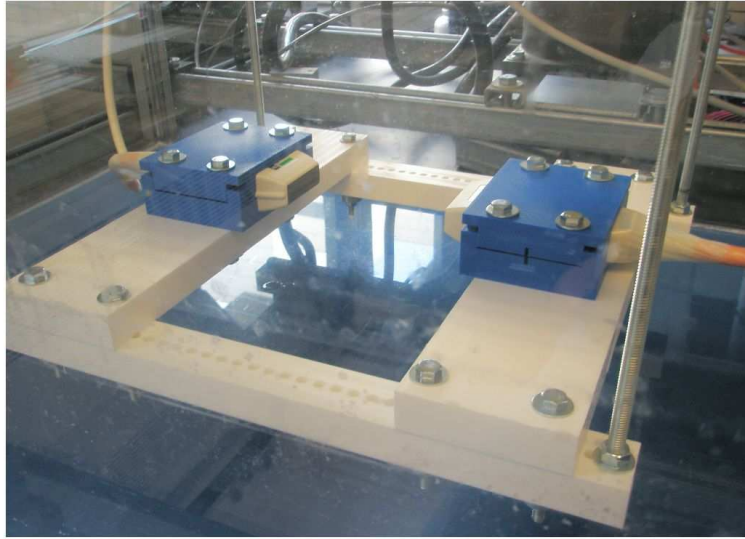


Figure 8.2: Photo of setup for nonlinear source characterization and inverse scattering experiment.

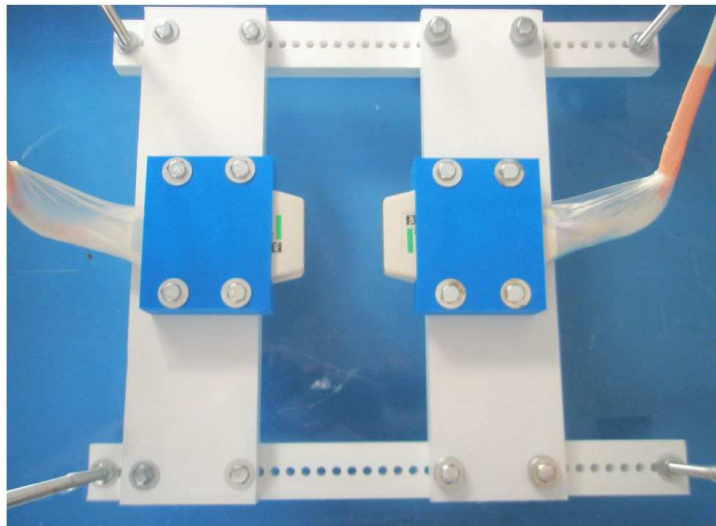


Figure 8.3: Top view of transducer positions. Mounting holes are spaced 1 cm apart.

be 4 mm tall, 0.3 mm wide, with a spacing of 0.4 mm.

8.4.1 Time Domain Data

Figures 8.4 and 8.5 show a typical example of the signals recorded from a water shot, i.e., the incident field. The center transducer element of one probe fired a two cycle pulse and was recorded by all the receivers of the opposite probe. This was repeated for all the elements of the transmitting probe to create an entire data set. The recorded time traces are plotted vertically, for each receiver. Figure 8.6 shows the time trace of the center receive element.

The pulse was a two cycle pulse with a 5 MHz center frequency. The Verasonics was set to sample at 4 samples per wavelength, giving a sample rate of 20 MHz. In water, the wavelength at 5 MHz is $300 \mu\text{m}$, which was the center frequency used for the position inversion in the next section. The characterization and imaging were performed at 3.75 MHz, where the wavelength is $400 \mu\text{m}$ in water.

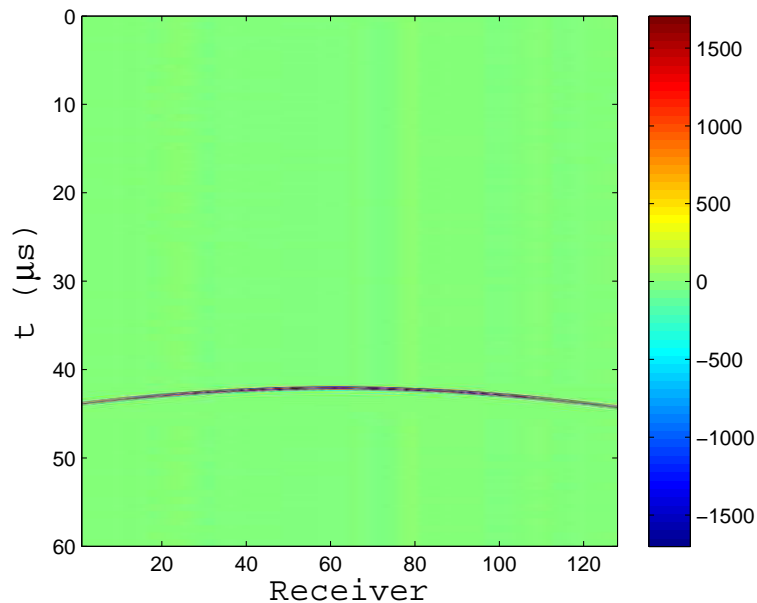


Figure 8.4: Typical time domain data for a water shot. The center element of one probe was fired and the signal was received by all the elements of the opposite probe. The color scale is digitized voltage.

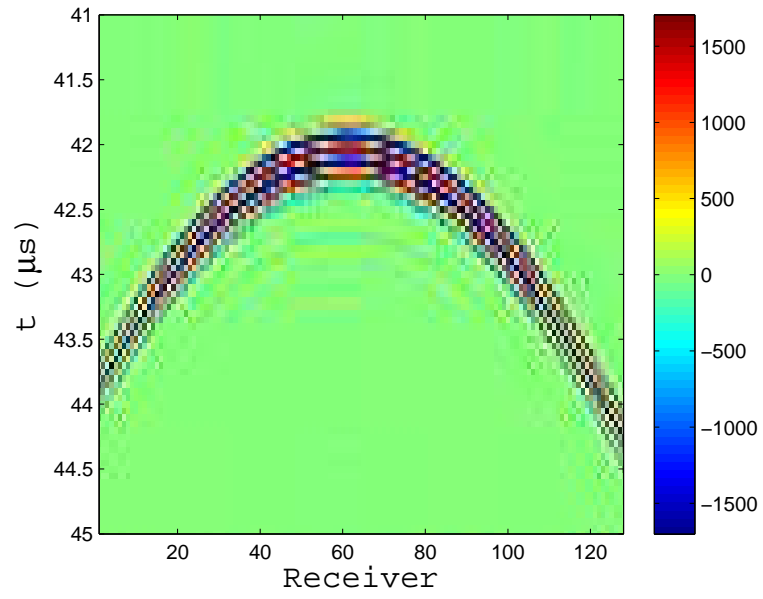


Figure 8.5: Close up of the traces in Figure 8.4.

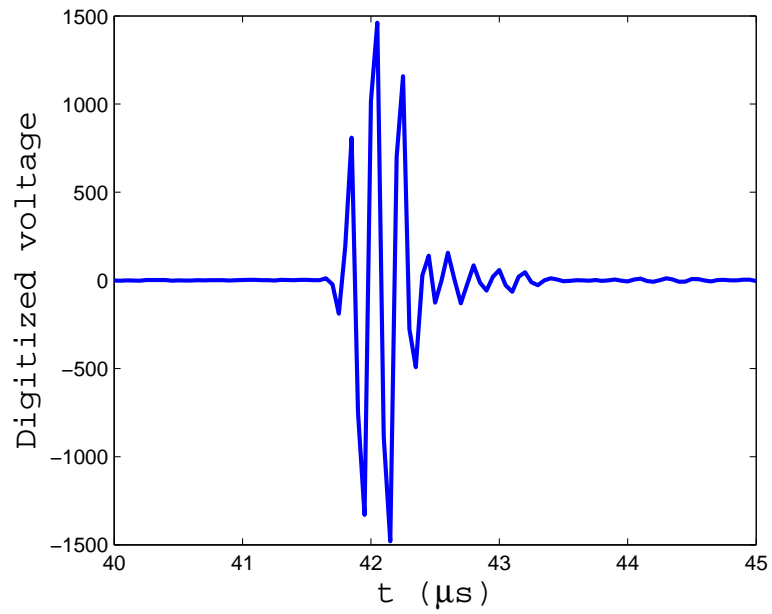


Figure 8.6: Time trace of the center receive element from the data in Figure 8.4.

8.4.2 Position Inversion Setup and Virtual Sources

Before performing the characterization, we must know or assume the locations and orientations of the transducer reference frames. This is not easily done by hand with a micrometer, so we use time of flight, because it is far more accurate. The idea is to record the time of flight of a pulse between all (or many) elements and solve a triangulation problem by inversion for the position and orientation of one array relative to the other. We assume we know the spacing of the array elements and that all the elements lie on a line.

There are several experimental aspects to note at the outset. First, we use time zero of the Verasonics time traces as a common reference. This is because the receive channels of the Verasonics begin recording at the same time on each occurrence of a transmit pulse. This is the only common reference we have between all the transmit and receive data. Second, there is a delay in firing of the transmit pulse equivalent to about one wavelength. Third, each transducer has a lens on its face with a lower speed of sound. This lens is designed to focus the radiation from each element in the elevation direction, so that focused beams used for everyday diagnostic ultrasound are restricted to a thin plane. This lens then introduces a delay on both the transmit and receive signals. Last, the pulse may be delayed in other ways either by the system, the cables, or probe head, that we may not be able to quantify.

We measured the time of flight relative to the beginning of the time trace using a simple envelope-max, shown in Figure 8.7. We accounted for the transmit pulse delay by shifting the zero of the time axis forward. We accounted for the envelope delay by subtracting half a pulse length in water from the time of flight measured at the peak of the envelope. To properly account for the delay induced by the lenses, one must solve Fermat's least action integral for the two-layered boundary. While this effort was undertaken by another member of the group for another project, it was not used here. The effects of not accounting for the lenses, or other delays, in a

time of flight position inversion are that we will find the location of a virtual source behind the actual source location. We rationalize this with the following reasons: 1) accounting for the lens in the propagation model inversion is not trivial and, even if necessary, was deemed beyond the scope of what we wished to derive and test, 2) if the lenses do not adversely effect the radiation pattern in the azimuth plane (the plane of the array), then, using the virtual positions, we can solve for the transmit coefficients of equivalent sources at the virtual locations. In doing so, the effects of the lenses are accounted for by a free-space spatial offset. Finally, if we settle on finding and using virtual source locations and transmit coefficients, we can now also lump the effects of miscellaneous system delays into the virtual source location. This was the reasoning going forward and the assumptions under which we performed our computations. Figure 8.8 shows a diagram of the transition from what we believe to be the actual system to the virtual source configuration.

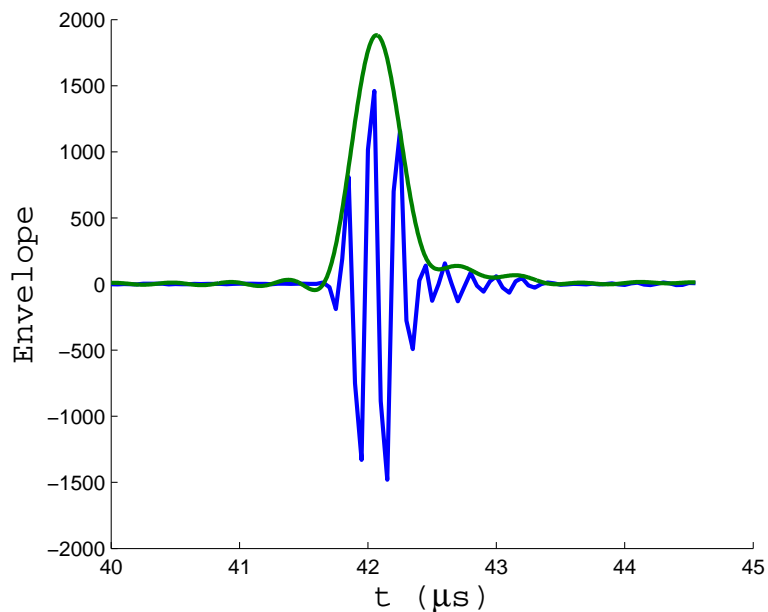


Figure 8.7: Envelope of time trace in Figure 8.6. The time of flight is determined by the time of the envelope maximum less half the pulse width.

The forward model for the position inversion is diagrammed in Figure 8.9 and given by

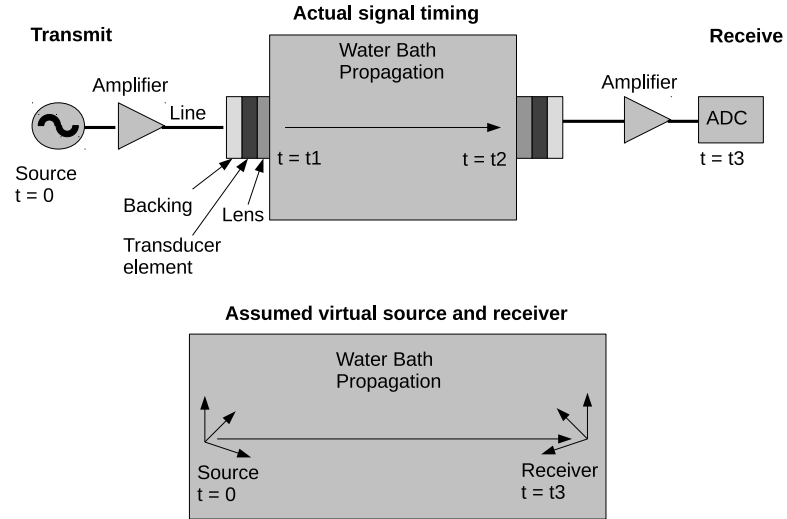


Figure 8.8: Actual and virtual sources and receivers. The signal fires at t_0 , emanates from the transducer at t_1 , arrives at the receiving transducer at t_2 , and is recorded at t_3 . The virtual source and receiver lump any delays into a spatial offset.

$$t_{ij} = r_{ij}/c \quad (8.60)$$

$$r_{ij} = |-(\mathbf{c}_1 + d_i \hat{\mathbf{v}}_1) + \mathbf{c}_2 + d_j \hat{\mathbf{v}}_2| \quad (8.61)$$

$$d_i = ((128 + 1)/2 - i)d, i = 1 \dots 128 \quad (8.62)$$

$$d_j = ((128 + 1)/2 - j)d, j = 1 \dots 128 \quad (8.63)$$

where t_{ij} is the time of flight between two elements, c is the speed of sound of water, and r_{ij} is the distance between two elements. The vectors \mathbf{c}_1 , and \mathbf{c}_2 point to the centers of each array. The vectors $d_i \hat{\mathbf{v}}_1$ and $d_j \hat{\mathbf{v}}_2$ point to the locations of the array elements, with d being the separation of the elements.

To note, many of the modeling problems encountered here are not uncommon in many ultrasound imaging systems. This is because we do not have control over the

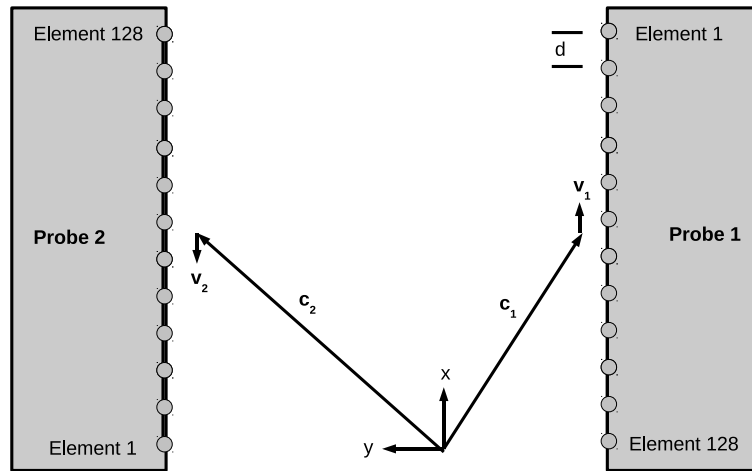


Figure 8.9: Actual and virtual sources and receivers. The signal fires at t_0 , emanates from the transducer at t_1 , arrives at the receiving transducer at t_2 , and is recorded at t_3 . The virtual source and receiver lump any delays into a spatial offset.

construction of the transducers, and the electronic systems are not calibrated with the same care as we calibrate microwave network analyzers. While standard LTI modeling can be used to characterize the electronics of ultrasound systems by solving for appropriate transfer functions, this was not something we were willing to do on the Verasonics system, risking damage, given its recent purchase, heavy use, and cost.

8.4.3 Speed of Sound of Water

The speed of sound of the background water bath was determined two ways: 1) reflection off a plate for a transducer stepped on a micrometer, and 2) measuring the water temperature at the time the data was taken and converting it to speed of sound using a lookup table [142]. Figures 8.10 and 8.11 show the reflection measurement setup. We stepped the transducer on a micropositioner every 0.2" and recorded the time of the zero crossing of the reflected pulse with an oscilloscope. The fit of a set

of reflected pulse travel times is shown in Figure 8.12. The slope is the speed of sound, determined here to be 1495.3 m/s. The temperature of the water for this data was 24.3 °C. Figure 8.13 shows the speed of sound of pure water as a function of temperature from [142]. At 24.3 °C, the sound speed is predicted from the curve to be 1494.8 m/s. In general, these two methods agreed to within 1-2 m/s, which is an error of 0.1% or approximately $\lambda/1000$ at 3.75 MHz. As a result, we routinely relied solely on the temperature to determine the sound speed.



Figure 8.10: Photo of setup to determine the speed of sound of the water bath. From left to right: digital readout thermocouple, oscilloscope, pulser/receiver, micropositioner with transducer and reflection plate.

8.4.4 Position Inversion Results

After determining the time of flights between all elements, we minimized an L1 cost functional over Eqn. (8.60) using the publicly available Matlab function called `fminsearchbnd`. This function modifies the built-in Matlab function `fminsearch` with a nonlinear transformation of the model parameters to enforce bounded limits. We use the L1 norm to automatically eliminate outliers in the time of flights created by the envelop search.



Figure 8.11: Photo of micropositioner with transducer to measure the speed of sound of the water bath.

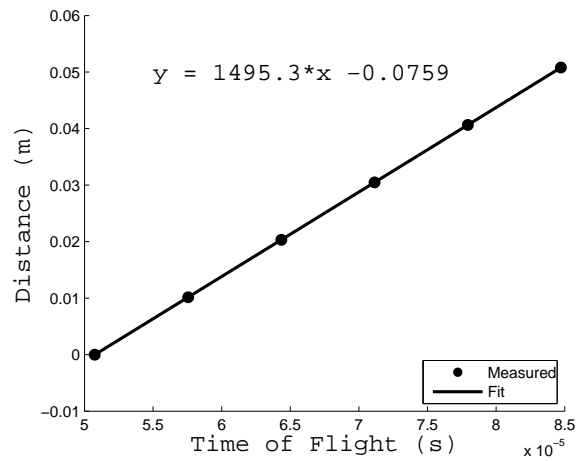


Figure 8.12: Water speed of sound estimation from micropostioner and reflection measurements. Slope of the line is the speed of sound.

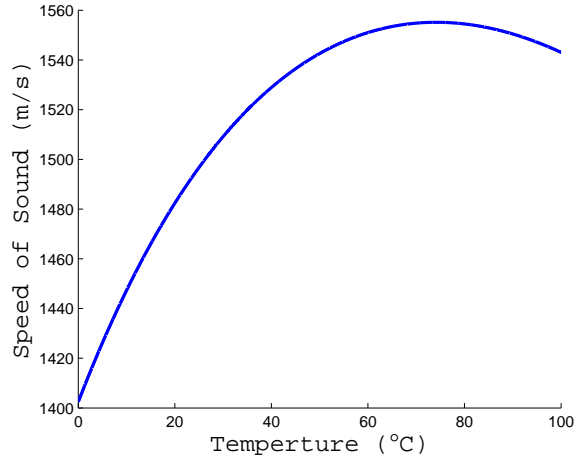


Figure 8.13: Water speed of sound with temperature from literature.

We solved for the location and orientation of the second transducer relative to the first. Thus, we let $\mathbf{c}_1 = 0$ and $\hat{\mathbf{v}}_1 = \hat{\mathbf{x}}$ and the six model parameters are then the elements of the vectors \mathbf{c}_2 and $\hat{\mathbf{v}}_2$. The initial conditions used were $\mathbf{c}_{2,o} = c * t_{center} \hat{\mathbf{y}}$, where t_{center} is the time of flight between the two center elements and $\hat{\mathbf{v}}_{2,o} = -\hat{\mathbf{x}}$ which assumes that the arrays are initially parallel.

This optimization took a few seconds to compute per transducer position on the mount, and was done for each position used for characterization. The results are plotted in Table 8.2 for seven positions spaced approximately 1 cm apart. From the solved y coordinate, we see that the probe separation is consistent with our 1 cm spacing. From the solved x coordinate, we see that the receive array is shifted along the array direction by nearly a millimeter. This was confirmed visually, and corresponds to a translation of the receiver array by several array elements, shown in Figure 8.14. We also confirmed this by inspecting the symmetry of the raw time traces. Finally, from the solved y component of the orientation vector, we see that the receive array is slightly tilted in the x - y plane. The z coordinate offset and z orientation component we ignore, because 1) this inversion is not sensitive to that dimension unless the array is grossly tilted in the x - z plane, and 2) these variations are small compared to variation in the element radiation patterns in the elevation

Table 8.2: Position inversion results for seven transducer positions

Position	$c_{2,x}(cm)$	$c_{2,y}(cm)$	$c_{2,z}(cm)$	$v_{2,x}(m/m)$	$v_{2,y}(m/m)$	$v_{2,z}(m/m)$
1	0.11	1.27	0.01	-0.999	-0.002	-0.001
2	0.07	2.24	0.01	-0.999	-0.003	0.000
3	0.07	3.25	0.02	-0.999	-0.004	0.000
4	0.08	4.25	0.00	-0.999	-0.004	0.001
5	0.09	5.24	0.00	-0.999	-0.005	0.000
6	0.10	6.24	0.01	-0.999	-0.005	0.003
7	0.11	7.25	0.03	-0.999	-0.003	0.001

direction.

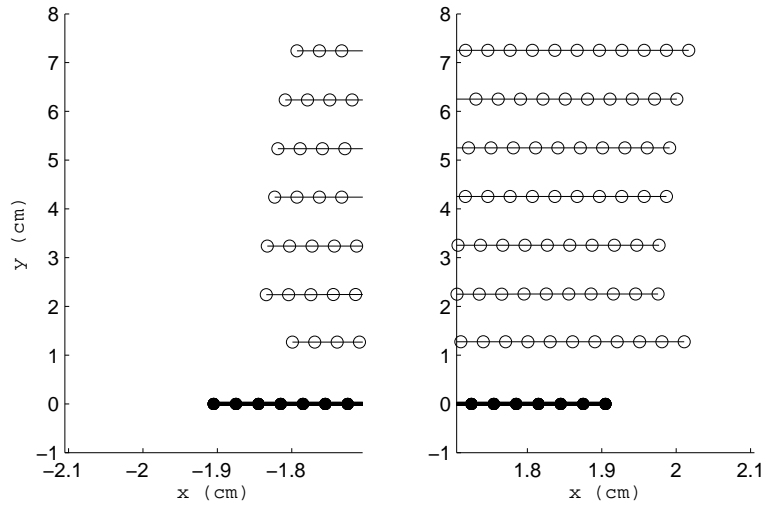


Figure 8.14: Split plot of the probe element positions. Bottom line and filled circles are the element locations of probe 1 (reference). Open circles are the element locations of probe 2 for all seven positions based on the position inversion values of Table 8.2. The y-axis is compressed.

8.4.5 Characterization Results

Having estimated the locations of sources, we can now invert the propagation model for the transmit coefficients. We do this in the frequency domain at 3.75 MHz. This means that we will only be able to form images at this frequency. While more frequencies will help the inverse scattering algorithm, a single frequency is sufficient to confirm if the characterization and imaging algorithm pair are working together,

without the added computation cost. We chose this frequency because it was the lowest frequency at which we could drive the transducers for clean signals. The lower the frequency, the more leniency we are allowed for phase and position errors.

8.4.5.1 Characterization Data

Figure 8.15 shows the magnitude and real part of the incident field spectral component at 3.75 MHz for one position between all combinations of transmit-receive pairs. The anti-diagonal band is due to the fact that the elements are numbered the same on each probe but the probes face each other. Notice the striations in the data, especially the magnitude. This is attributed to inconsistencies in the Verasonics receive chain duplexing. The striations must be filtered before using this data for characterization. In order to filter this effect, we smooth the complex data along each anti-diagonal, because we expect the data to vary smoothly if we were to select any transmit/receive pair and then step along each array. The filtered data are shown in Figure 8.16 and are the data we use for characterization.

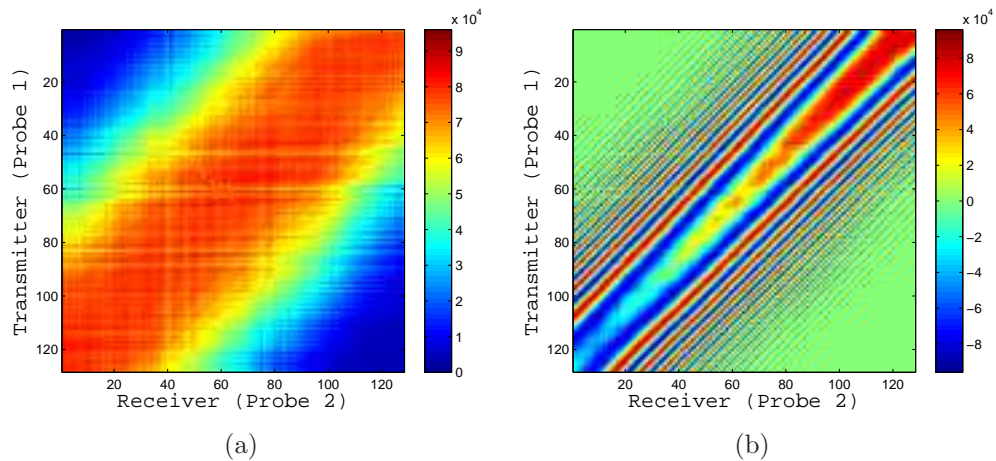


Figure 8.15: Magnitude (a) and real part (b) of the incident field at 3.75 MHz for all transmit/receive pairs. Scale is magnitude and real part of digitized voltage.

We can use this data to look at the intrinsic alignment of the transducer arrays, by looking at phase of the complex frequency component of each signal, shown in

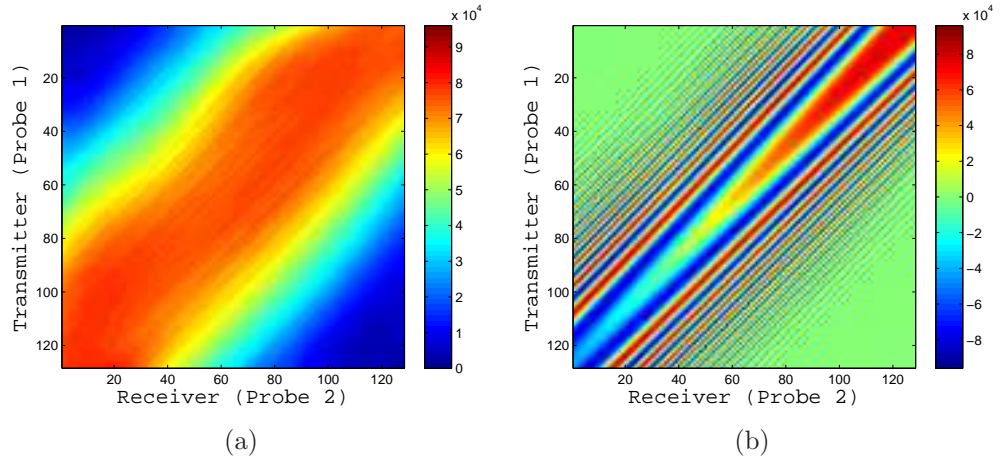


Figure 8.16: Data of Figure 8.15 smoothed along the anti-diagonals.

Figure 8.17. The main anti-diagonal, which represents elements directly across from each other, shows a progressive phase shift of about half a wavelength, which is about $150 \mu m$. This is corroborated by the position inversion and means that we were able to align the probes parallel to within about $\lambda/2$ with the mount alone. However, this also validates the need to use the position inversion.

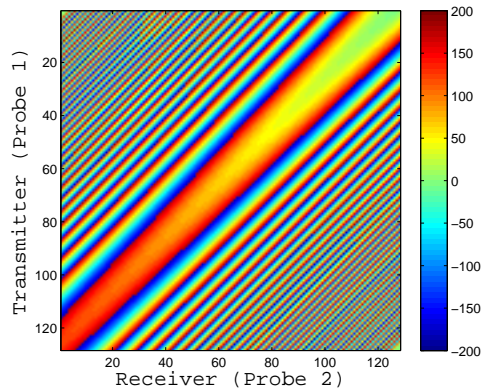


Figure 8.17: Phase of incident field at 3.75 MHz. Anti-diagonal shows that the probes are not quite parallel and rotated about the z-axis.

8.4.5.2 Inversion Results

Here we give some results of the inversion of the propagation model with the measured data above. Because we cannot take data out of plane, we only need to

describe the radiation pattern in the imaging plane, and so we chose to invert for multipole harmonics out to $L = 8$. We assume all the elements are the same, so we are effectively assuming that we use the same source to sample the fields at all points along the face of the probe.

Also, the elements of the second probe are rotated by about 180 degrees, so rotation matrices were included in the propagation model to account for this based on the position inversion results. These are the same rotation matrices used in the antenna model, because rotation of the $Y_{l,m}$ angular harmonics is the same for vector and scalar wave functions. After many trials, we found best results by using data from a subset of elements from each probe. We used data from every tenth element and two positions to obtain the results below.

Figure 8.18 shows the residual with each iteration of conjugate gradient minimization. The residual drops monotonically, meaning that our algorithm was coded correctly. The behavior of the residual is more complicated than for a typical linear problem; the residual of a linear problem would look smoothly logarithmic.

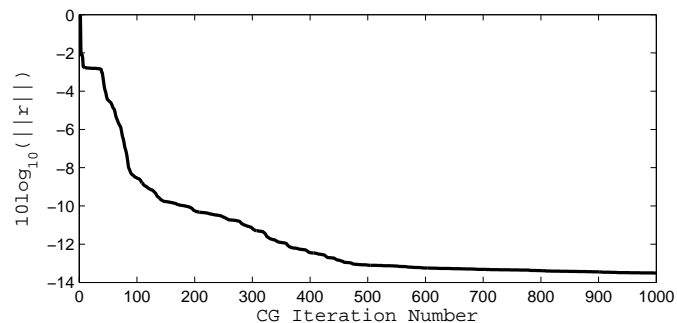


Figure 8.18: Normalized residual as a function of conjugate gradient iteration number.

Figure 8.19 shows the real and imaginary parts of the obtained transmit coefficients. This plot is essentially the spectral power of each multipole in the radiation pattern.

Figure 8.20 shows the measured and predicted magnitude and phase of the data for a subset of transmitter-receiver pairs. The groupings are receivers per transmitter

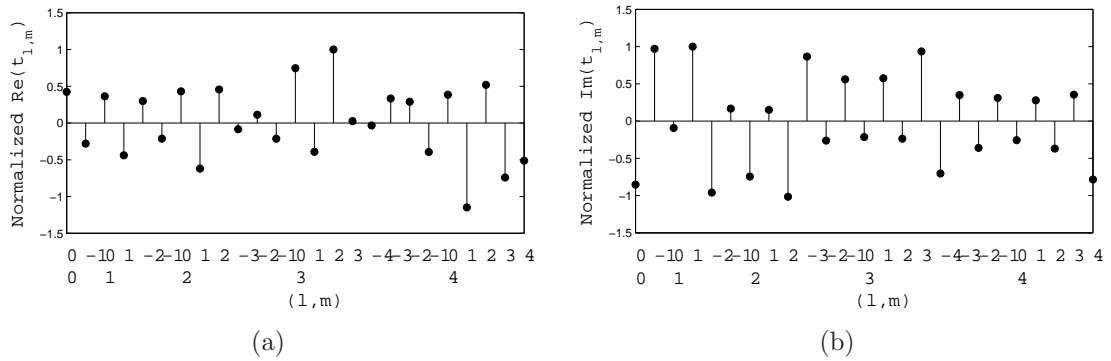


Figure 8.19: Normalized transmit coefficients. a) real part, b) imaginary part. Horizontal axis is the (l, m) harmonic index.

for the two positions. We see that the overall shape of the magnitude is well fitted, and that the phase is fit quite well, to within 20 degrees. This again indicates that the inversion procedure was working to correctly fit the data.

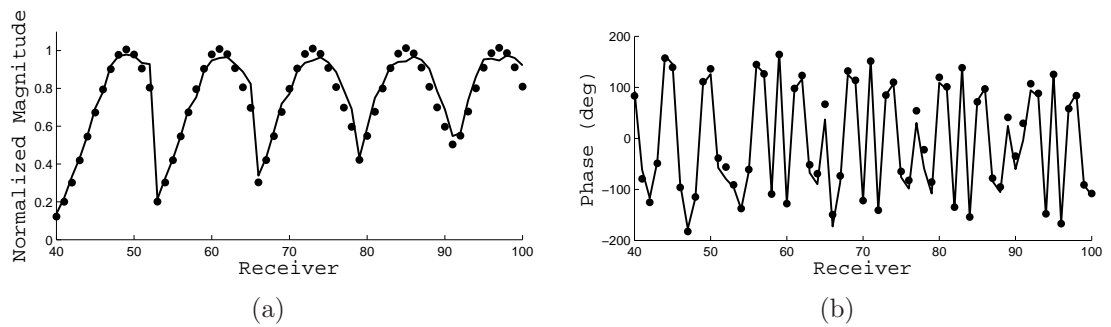


Figure 8.20: Magnitude and phase of measured and predicted data for a sampling of transmit and receive elements. a) Magnitude, b) phase. The apparent groups in the magnitude plot are receivers for a given transmit element.

The pressure field computed with the transmit coefficient is shown in Figure 8.21. This is the normalized magnitude in the plane of the probes, and is the incident field we will use in the inverse scattering algorithm. The side lobes come from having incomplete information in those directions; in other words, the fields are only constrained where we took data with the second probe.

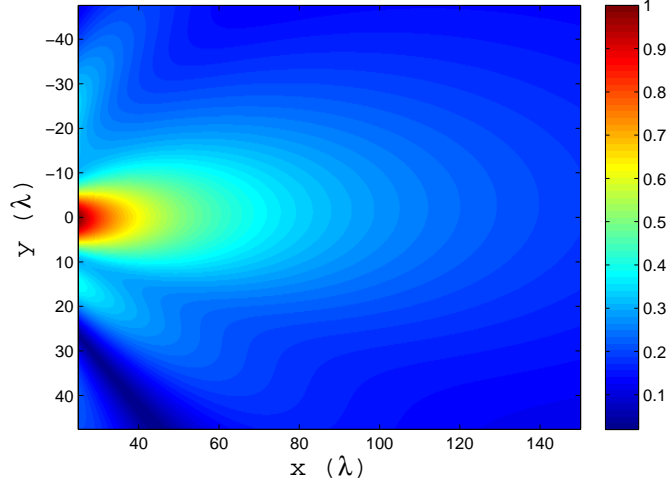


Figure 8.21: Normalized magnitude of acoustic field in the transducer plane computed with the solved transmit coefficients.

8.5 ”Vector Green’s” Formulation for Acoustics

Before turning to the inverse scattering algorithm, we must derive the proper use of the incident field in the volume integral equations. Like Chapter V, where we derived a vector Green’s function kernel to directly link the electrical properties of an object to microwave S-parameter measurements, we can derive the analogous operator for the acoustic problem which will link the acoustic properties of an object to measured voltages by way of the acoustic source model. This kernel will be a single argument scalar function specific to the receiver. We will again see that only the normalized incident field is required to fully characterize an acoustic setup for inverse scattering, provided that it is known accurately enough.

8.5.1 Setup

The scattered pressure field due to an inhomogeneous object is given from Chapter II as

$$\phi_{sca}(\mathbf{r}) = \int g(\mathbf{r}, \mathbf{r}') O(\mathbf{r}') \phi(\mathbf{r}') dV' \quad (8.64)$$

where we define the object function $O(\mathbf{r})$ as the linear operator

$$O(\mathbf{r}) = k_o^2 \left(\delta\kappa(\mathbf{r}) + i \frac{\delta\alpha(\mathbf{r})}{\kappa_o \omega} \right) + k_o^2 \nabla' \cdot \delta\rho^{-1}(\mathbf{r}) \nabla'. \quad (8.65)$$

Let the pressure field about a transducer be written in terms of the multipole expansion as

$$\phi(\mathbf{r}) = \sum_{lm} (a_{lm} \Re\psi_{lm}(\mathbf{r}) + b_{lm} \psi_{lm}(\mathbf{r})) \quad (8.66)$$

with the accompanying transducer model

$$V_{out} = \sum_{lm} u_{lm} a_{lm} \quad (8.67)$$

$$b_{lm} = t_{lm} V_{in} \quad (8.68)$$

We next define the normalized incident pressure field by substituting the transducer model into the field expansion when the transducer is purely transmitting

$$\phi_{inc}(\mathbf{r}) = \sum_{lm} b_{lm} \psi_{lm}(\mathbf{r}) \quad (8.69)$$

$$= V_{in} \sum_{lm} t_{lm} \psi_{lm}(\mathbf{r}) \quad (8.70)$$

$$= V_{in} \hat{\phi}_{inc}(\mathbf{r}) \quad (8.71)$$

where $\hat{\phi}_{inc}(\mathbf{r})$ is the normalized incident field. We next define the normalized total

field which is the total pressure field in the object due to a normalized incident field

$$\hat{\phi}(\mathbf{r}) = \phi(\mathbf{r})/V_{in} \quad (8.72)$$

8.5.2 Vector Green's Function analogue

The addition theorem for the scalar Green's function is given by, [52],

$$g(\mathbf{r}, \mathbf{r}') = ik \sum_{lm} \Re \psi_{lm}(\mathbf{r}) \psi_{lm}^*(\mathbf{r}') \quad (8.73)$$

where we have taken the case $|\mathbf{r}| < |\mathbf{r}'|$. Substituting Eqn. (8.73) into Eqn. (8.64) and rearranging, we can write the scattered field in the frame of a transducer in terms of incoming waves as

$$\phi_{sca}(\mathbf{r}) = \sum_{lm} a_{lm} \Re \psi_{lm}(\mathbf{r}) \quad (8.74)$$

where the multipole coefficients are

$$a_{lm} = ik \int \psi_{lm}^*(\mathbf{r}') O(\mathbf{r}') \phi(\mathbf{r}') dV' \quad (8.75)$$

Substituting Eqn. (8.75) into the transducer model when in receive mode, Eqn. (8.67), we have the output voltage as

$$V_{out} = ik \sum_{lm} u_{lm} \int \psi_{lm}^*(\mathbf{r}') O(\mathbf{r}') \phi(\mathbf{r}') dV' \quad (8.76)$$

Rearranging this we can identify the acoustic analogue of the vector Green's function, which we label as $\hat{g}(\mathbf{r}')$,

$$V_{out} = \int \hat{g}(\mathbf{r}') O(\mathbf{r}') \phi(\mathbf{r}') dV' \quad (8.77)$$

$$\hat{g}(\mathbf{r}') = ik \sum_{lm} u_{lm} \psi_{lm}^*(\mathbf{r}') \quad (8.78)$$

Finally, let there be two transducers, one transmitting in frame i , the other receiving in frame j . The total pressure field in the object is due to the transmitter. Dividing both sides of Eqn. (8.77) by the transmit voltage we can write the scattered field integral equation in terms of the normalized total field of the transmitter and the input and output line voltages as

$$\frac{V_{out}^j}{V_{in}^i} = \int \hat{g}_j(\mathbf{r}') O(\mathbf{r}') \hat{\phi}_i(\mathbf{r}') dV' \quad (8.79)$$

where $\hat{g}_j(\mathbf{r}')$ is the kernel for the receiver.

8.5.3 Reciprocity Relation

Last, by reciprocity, we can show that $\hat{g}_j(\mathbf{r}')$ is related to the incident field of the receiver. Substituting the relations between transmit and receive coefficients, Eqn. (8.15),

$$\hat{g}(\mathbf{r}') = ikc_r \sum_{lm} (-1)^m t_{l,-m} \psi_{lm}^*(\mathbf{r}') \quad (8.80)$$

and using the relation $Y_{lm}^* = (-1)^m Y_{l,-m}$ in the wave function it can be shown that

$$\hat{g}(\mathbf{r}') = ikc_r \sum_{lm} t_{l,m} \psi_{lm}(\mathbf{r}') \quad (8.81)$$

which is the expansion for the normalized incident pressure field multiplied by a scaling factor

$$\hat{g}(\mathbf{r}') = ikc_r \hat{\phi}_{inc}(\mathbf{r}') \quad (8.82)$$

Finally, we can write the scattered field transmit/receive voltage ratio in terms the normalized incident field of the receiver and normalized total field of the transmitter as

$$\frac{V_{out}^j}{V_{in}^i} = ikc_r \int \hat{\phi}_{inc,j}(\mathbf{r}') O(\mathbf{r}') \hat{\phi}_i(\mathbf{r}') dV' \quad (8.83)$$

This is the scattered field integral equation we will use in the cost function of the inverse scattering algorithm.

8.6 Ultrasound Inverse Scattering Experiment

We use the same acoustic inverse scattering algorithm presented in Chapter II to form images of compressibility and absorption. Several objects were used to test the inverse scattering algorithm. The objects are made of metal, plastic, and worm rubber. The hard objects are used to test resolution. The worm rubber has a speed of sound less than that of water and attenuation greater than water and serves to test the contrast. The objects were rotated with a robotic manipulator arm to provide multiple views. First we explain how the rotator was aligned, then present imaging examples.

8.6.1 Rotator alignment

We form images with transmission data only. Due to the limited angle acquisition geometry of the facing probes, we must rotate the probes or the object in order to adequately sample the scattered fields. This is now akin to X-ray or ultrasound CT, where two parallel arrays of sensors are rotated around the object. We rotated the objects using the six-axis robotic arm shown in Figure 8.22.

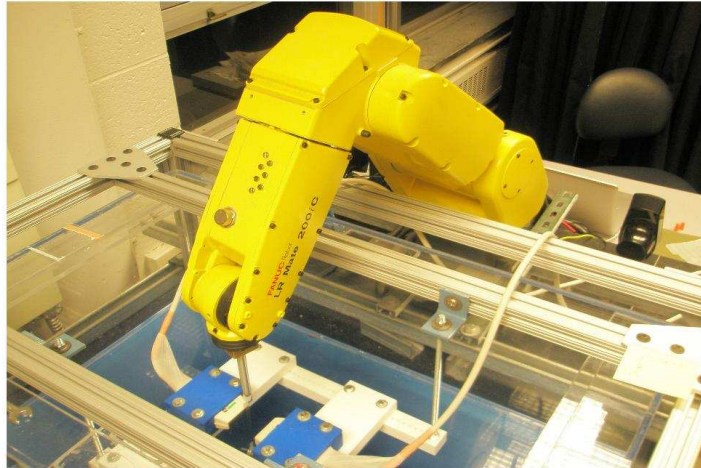


Figure 8.22: Photo of 6-axis positioning arm used to place and rotate objects.

Given the sensitivity of the algorithm to position errors, we must align the center of rotation as best we can at the coordinate center of the object domain. A smooth metal cylindrical rod is attached to the center of the last arm axis which is used for alignment and for attaching and rotating objects, shown in Figure 8.23.

We first align the rod vertically. This is done by eye, and using the global internal reference frame of the robot. Not only must the rod rotate symmetrically, but we must know the location of the center of rotation relative to the first probe (similar to the position inversion). We translate the rod to a point between the probes and take reflection measurements off the rod from symmetric sets of receivers, shown in Figure 8.24, as we finely adjust the position of the arm. If the reflections do not shift in time, then the rod is at the center of rotation and is rotating symmetrically about it. Then any object suspended from it will also rotate about the center of rotation. Reflections recorded from the first probe align the rod in the x-direction. Comparing the reflections of opposing elements on the second probe aligns the cylinder in the y-direction.



Figure 8.23: Close-up of metal rod. Rod is translated and rotated to

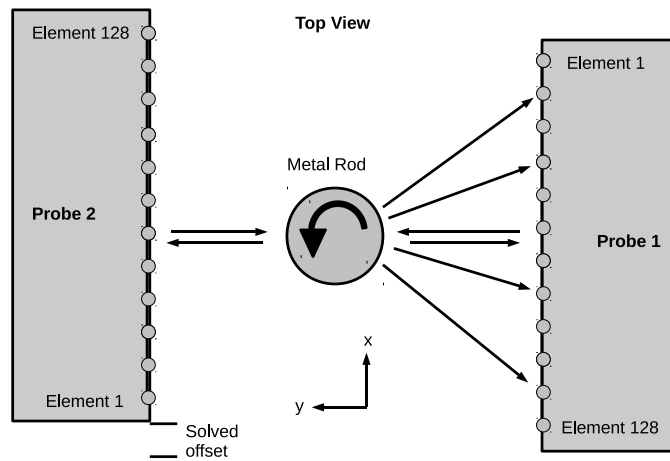


Figure 8.24: Diagram of transmissions and reflections used to align the rotator.

8.6.2 Image Reconstructions

We form images of the 2D cross section of cylindrical targets using the full 3D inverse scattering algorithm. An assortment of these objects is shown in Figure 8.25. The objects hang from the metal rod and are weighed down. We assume the imaging domain is very thin, so ignore any out of plane scattering.



Figure 8.25: Assorted targets of worm rubber, brass rods, and fishline to image.

We form images at 3.75 MHz using 12 or 36 object rotations and a subset of transmitters and receivers on each probe. The imaging domain was about 2 cm on a side, shown in Figure 8.26.

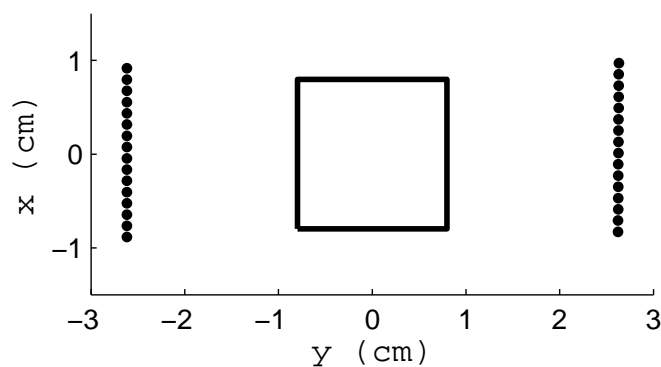


Figure 8.26: Diagram of sources and receivers used in the inverse scattering algorithm. The box outlines the imaging domain.

8.6.2.1 Example 1: Worm rubber cylinder

The first object we imaged was a cylinder of worm rubber, shown in Figure 8.27. The cylinder is approximately 4 mm in diameter. From mass/volume measurements of worm rubber samples, the measured density of the material was 1.0164 g/cm^3 . The speed of sound was estimated from differential time of flight through a known thickness to be 1406 m/s . From this the compressibility was determined to be $4.977 \times 10^{-10} \text{ 1/N}$, which equates to a contrast relative to the background as defined in Chapter II of 0.102. Attenuation measurements were not performed, but worm rubber is known to have positive attenuation contrast.

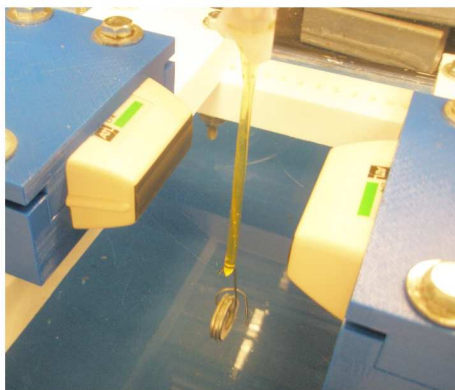


Figure 8.27: Photo of worm rubber target.

For this object we used 12 rotations of 30 degrees each. We subtract the same incident field from the total field for each rotation. The magnitude of the scattered field for all transmitter and receiver pairs is shown in Figure 8.28. These images are similar to the sinograms formed in X-ray CT. The object is off center, and this is evident by tracing the peak scattered field through the different rotations. Also, it is interesting to note, that given the cylindrical nature of this particular object, the side-lobes of the scattered field radiation pattern are visible.

Figure 8.29, shows images of compressibility and absorption formed by the inverse

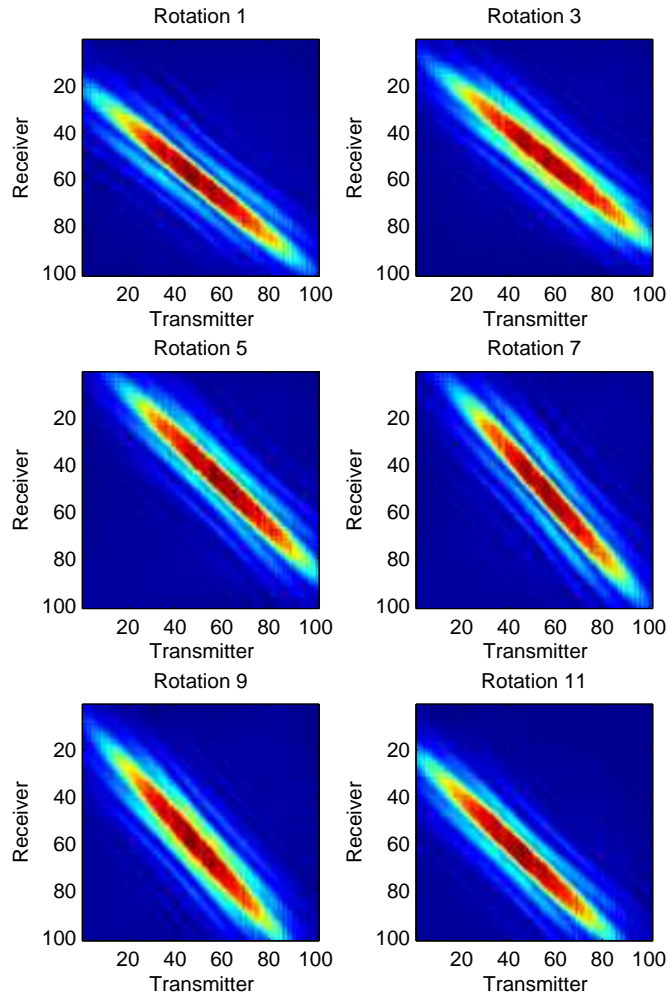


Figure 8.28: Magnitude of the scattered field for select rotations of the object in Figure 8.27.

scattering algorithm. The inverse scattering algorithm was terminated after 12 BIM steps with 12 conjugate gradient steps per iteration. The object location and shape of the object are recovered. The value of compressibility is too large and the absorption shows a ring artifact. These are most likely due to the thin imaging domain, where the recovered values are trying to compensate the predicted scattered fields. However, the signs of the two contrasts are correct, which indicates that the acoustic 'vector Green's' analogue was derived correctly. Similar effects will be present in the examples that follow. Also, the streaks along the outside of the imaging domain are artifacts from the rotations.

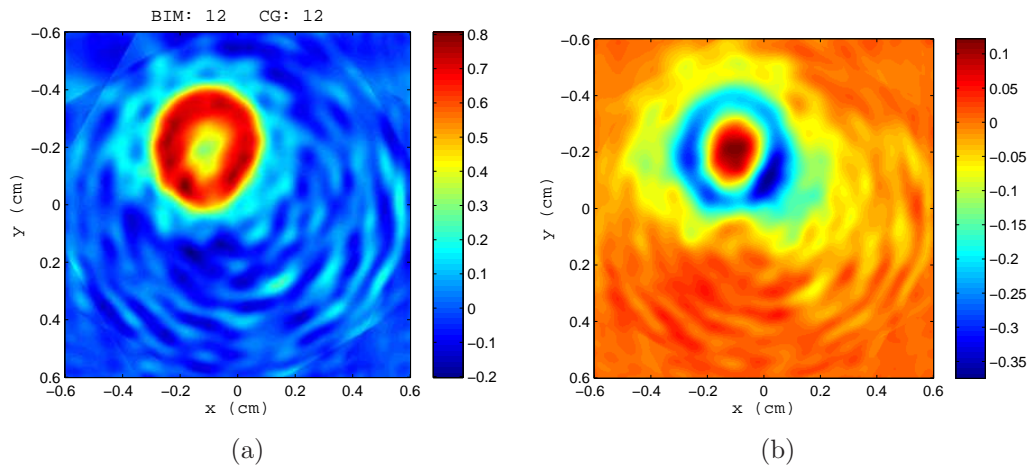


Figure 8.29: Recovered compressibility and absorption contrast for the object in Figure 8.27. a) Compressibility. b) Absorption.

8.6.2.2 Example 2: Two metal filaments

We imaged two thin metal filaments to test resolution even though the material hardnesses are not captured by the physics of the algorithm. The filaments are shown in Figure 8.30. The rods are brass with 0.5 mm diameter and separated by approximately 2 mm.

Figure 8.31, shows images of compressibility and absorption. The inverse scattering algorithm was terminated after 5 BIM steps. The object location and shape

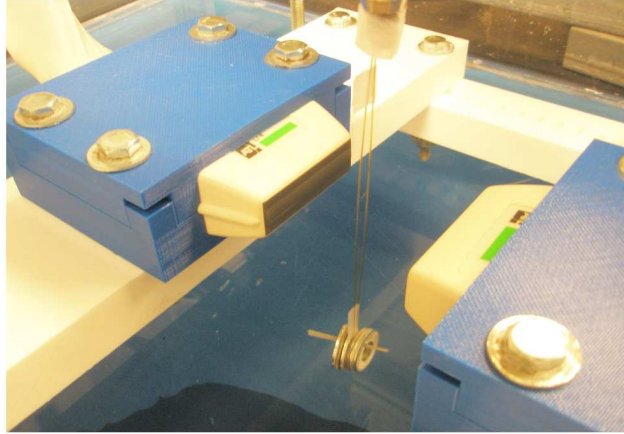


Figure 8.30: Photo of two metal filaments.

of the object are recovered. The compressibility contrast is negative and absorption is positive. This is the correct direction for compressibility because we expect the compressibility of brass to be less than water. The ringing artifacts and streaks are due to the use of only twelve rotations.

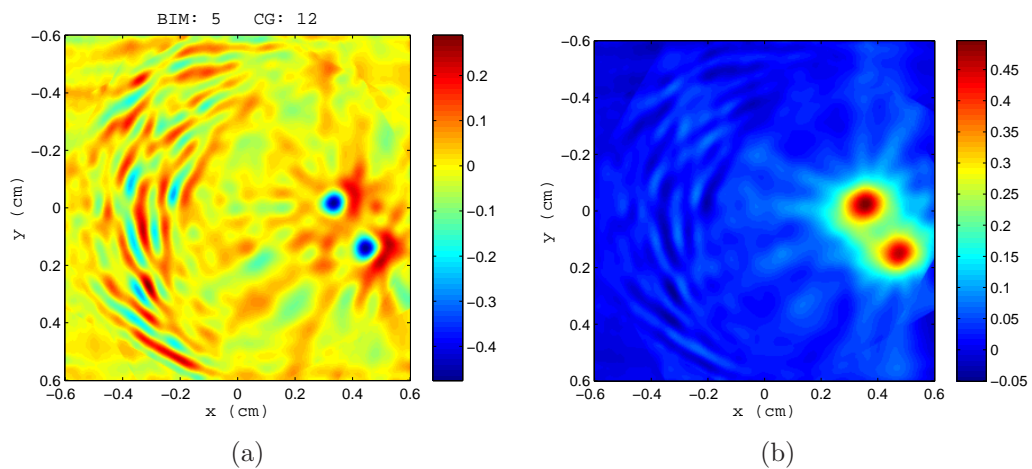


Figure 8.31: Recovered compressibility and absorption contrast for the object in Figure 8.30. a) Compressibility. b) Absorption.

8.6.2.3 Example 3: Two fish line filaments

We imaged two plastic fish line filaments. Again, the material hardnesses are not captured by the physics of the algorithm. The filaments are shown in Figure 8.32. The filaments are 1 mm diameter and separated by approximately 2 mm.

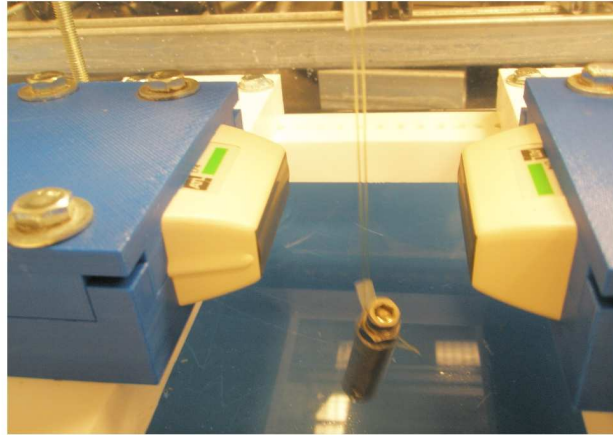


Figure 8.32: Photo of two fish line filaments.

Figure 8.33, shows images of compressibility and absorption. 36 rotations were used and the inverse scattering algorithm was terminated after 5 BIM steps. The object location and shape were not recovered as well as the metal rods. The compressibility contrast is negative and absorption is positive, which is consistent with the results of the brass rods. The images are blurred more than the rods which we attribute to object motion. While this experimental deficiency could have been better addressed, this and the following images are included for completeness.

8.6.2.4 Example 4: The Cheshire cat

For this example, the object was a crescent of worm rubber. This was made as the result of a failed attempt to create a cylinder of worm rubber by pouring molten worm rubber into a metal tube. The target is shown in Figure 8.34.

Figure 8.35, shows images of compressibility and absorption. 36 rotations were

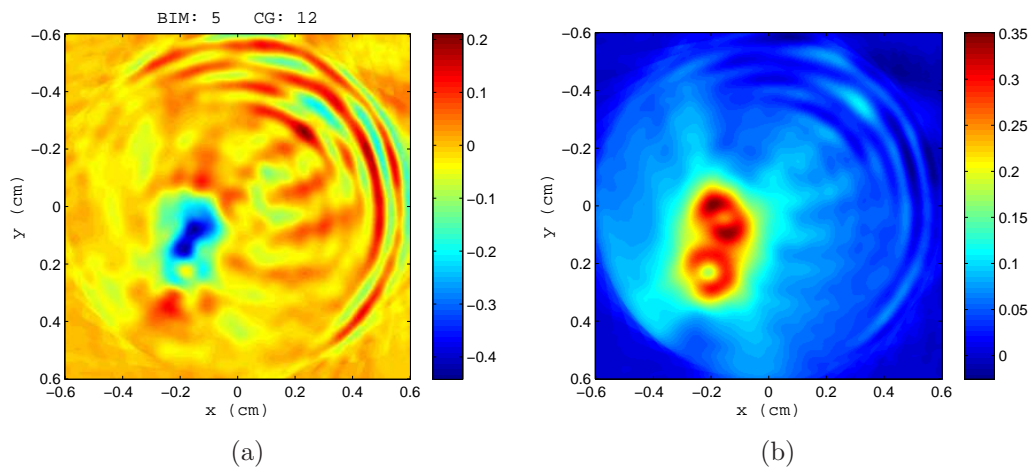


Figure 8.33: Recovered compressibility and absorption contrast for the object in Figure 8.32. a) Compressibility. b) Absorption.

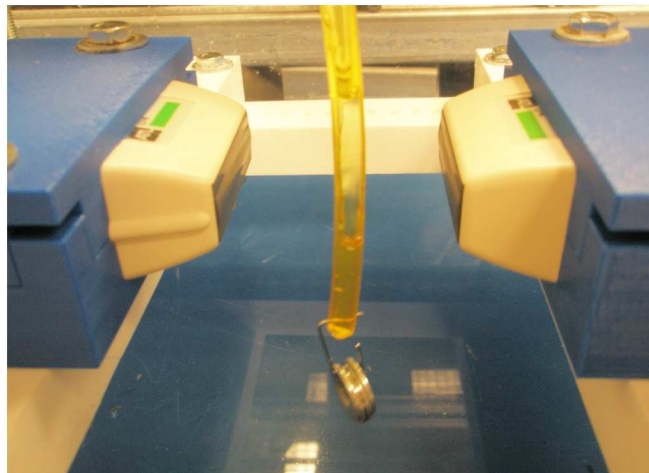


Figure 8.34: Photo of worm rubber crescent.

used and the inverse scattering algorithm was terminated after 12 BIM steps. The compressibility image shows a positive contrast of a crescent, however the negative contrast dip and its similar appearance on the absorption image should not be there. The meaning of this artifact is unclear. While an air bubble could have been trapped in the target, none was visibly present. It might again be due to motion.

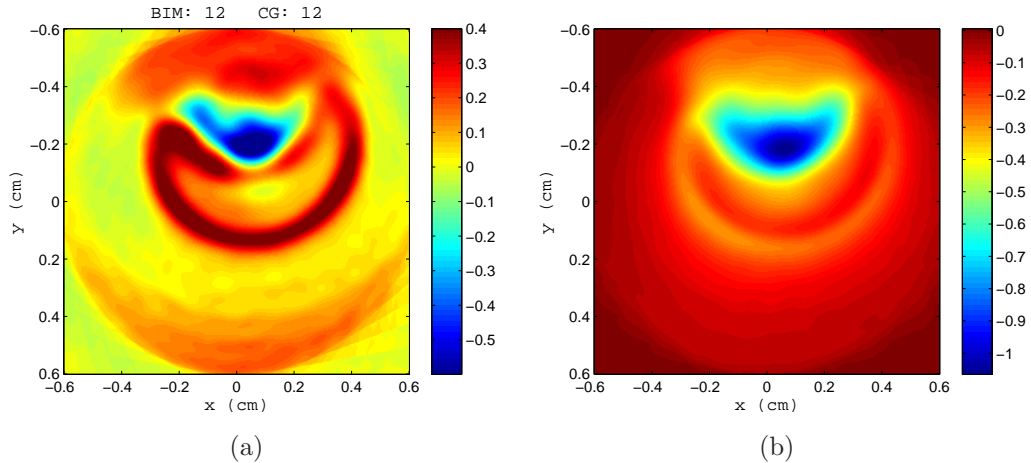


Figure 8.35: Recovered compressibility and absorption contrast for the object in Figure 8.34. a) Compressibility. b) Absorption.

8.6.2.5 Example 5: Combination

Here we imaged a combination of metal rod and a cylinder of worm rubber. The target is shown Figure 8.36.

Figure 8.37 shows images of compressibility and absorption. 36 rotations were used and the inverse scattering algorithm was terminated after 12 BIM steps. The compressibility image shows the correct positive contrast of worm rubber and also the correct locations of the metal rods. The sign of the contrast of the worm rubber absorption is positive and correct, however the rods were not picked up as clearly as when imaged by themselves. This begins to suggest that the alignment of robotic arm may not have been as good for this example as it was for the first few examples.

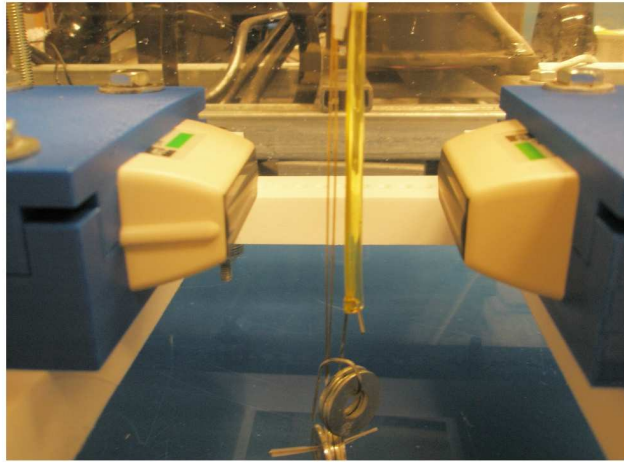


Figure 8.36: Photo of metal rod and worm rubber combination.

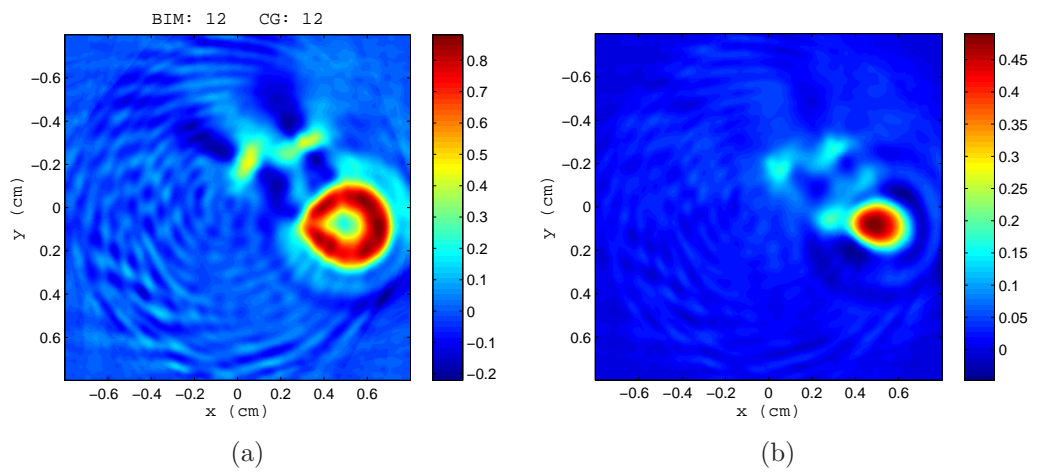


Figure 8.37: Recovered compressibility and absorption contrast for the object in Figure 8.36. a) Compressibility. b) Absorption.

8.6.2.6 Example 6: Worm rubber rectangle.

Last we imaged a rectangle of worm rubber. The target is shown Figure 8.38.

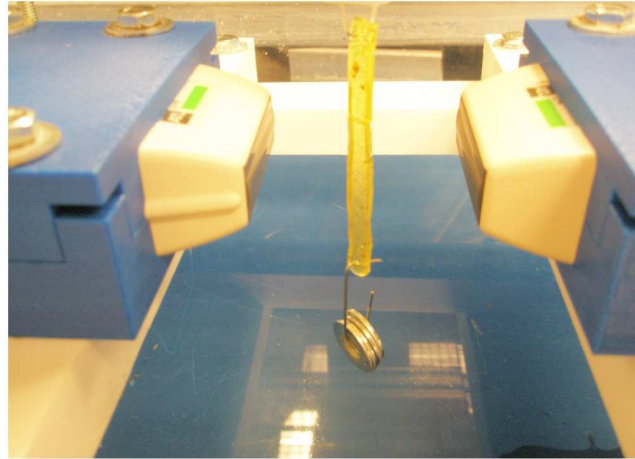


Figure 8.38: Photo of worm rubber rectangle.

Figure 8.39, shows images of compressibility and absorption. 36 rotations were used and the inverse scattering algorithm was terminated after 12 BIM steps. The object borders are not well defined. The object in the absorption image is filled in, while there is an apparent hole in the compressibility image. Given that the object is the same material and nearly the same size as the target in Example 1, we would have expected the images to be similar. Suspected again are motion artifacts, especially if not enough time was allowed for the object settle between rotations.

To summarize the results from these images, we can say that the algorithm, source characterization, 'vector Green's' analog formulation, together with the assumptions of the experiment worked with mixed success. The objects were mostly recovered, and the quantitative values follow some physical intuition. However, the images were not recovered well enough where a detailed evaluation of resolution or quantitative accuracy is appropriate.

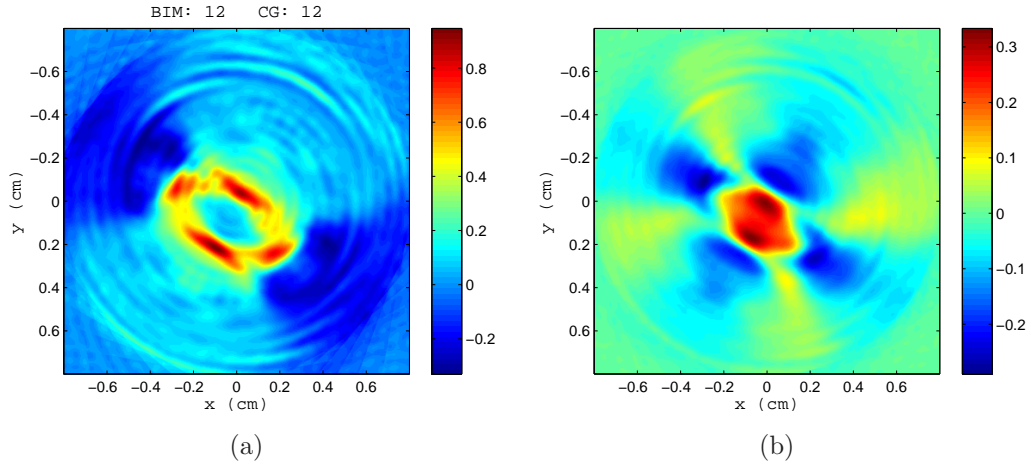


Figure 8.39: Recovered compressibility and absorption contrast for the object in Figure 8.38. a) Compressibility. b) Absorption.

8.7 Conclusion

The overall goal of the work in this chapter was to test the acoustic inverse scattering algorithm that was presented in Chapter II in experiment. The two main difficulties of doing this, as compared to the microwave problem, are 1) dealing with the small spatial scales of acoustic waves and 2) the need to characterize the transducers using measurements as opposed to simulation.

We knew from the outset that we would be required to characterize our sources and receivers. Given the success of the microwave propagation model, source-scattering formulation, and vector Green's function, we also wanted to do as much as possible to remain within these formalisms when testing the acoustic experiment. While we briefly described hydrophone characterization of ultrasonic transducers, the system that was at our disposal for the inverse scattering experiment was the Verasonics Data Acquisition system. The main benefit of using it was the ease and quality with which we could take all combinations of transmit and receive waveforms from commercial ultrasound probes. As such, we needed to characterize these probes and the system, so pursued a path using a new self-characterization technique based on the nonlinear inversion of the acoustic propagation model. To aid the characterization inversion,

we used an additional inversion to solve for the positions of the transducers using the incident field time of flight. The inverse scattering algorithm ultimately worked with some success.

There were many caveats to the experiment as performed. While the characterization inversion appeared to fit the data well, admittedly, we did not have independent confirmation of its accuracy. Thus, in a sense, we were running the forward model blind in the inverse scattering algorithm. Confirming the forward model would have required knowing the precise position and material of targets, with spatial accuracies on the order of 10s of micrometers. For the geometry of the experiment, this would also have required us to model the 3D scattering of 2D objects. This can be done quite nicely in the context of the source-scattering formulation, propagation model and T-matrix methods, but is not trivial to accomplish.

A major assumption which probably had the most effect on image quality and interpretation was solving for a 2D slice of a 3D object. With the cylindrical nature of the objects, we wanted to ignore out of plane scattering. This assumption was probably much of the reason the contrasts values were too high or flipped. Also, motion artifacts turned out to be more of a problem than first anticipated.

While we were mostly interested in testing the self-characterization method of inverting the propagation model, given more time, there are several other methods that could have been tried to characterize this type of experiment. First, the flexibility in the transmit control of the Verasonics system allows one to fire all elements at once. This can be used for plane wave excitation. Plane wave excitation is easily calibrated by comparing the receiver response to theoretical plane wave incidences. However, this method usually requires one to ignore the radiation pattern of the receivers. Given the large wavelength scale of this experiment, these approximations may have worked well. Second, because the transmit and receive elements are in the far-fields of each other, this is a situation where targets could be used to calibrate the transducer

response by normalizing the scattered field response with theoretical scattered fields. Last, we could characterize the probes with traditional hydrophone measurements in the context the source scattering formulation as mentioned at the beginning of this chapter. The robotic arm is well suited for this, but involves a serious investment in alignment and trigger synchronization.

Overall, the methods presented here worked with some success but further investigation is required to better evaluate the performance of the nonlinear characterization and acoustic imaging algorithm.

CHAPTER IX

Conclusion and Future Work

9.1 Conclusion

The purpose of this thesis was to investigate the use of acoustic and microwave inverse scattering imaging techniques in the problem of forming quantitative images for breast cancer detection. The rationale for using inverse scattering has been the hypothesis that if benign and malignant tissue have different material properties, then imaging these properties directly could provide better diagnostic information than is available today. Inverse scattering methods include the complete physical description of wave propagation through material, and so they offer the most rigorous and potentially fruitful path to imaging material properties directly.

There are several algorithmic difficulties in trying to apply inverse scattering to medical breast imaging. First, even with perfect data, inverse scattering algorithms are non-linear and non-unique. This is because images must be formed indirectly through iterative optimization procedures and the metrics used to compare forward model predictions to data are, for all intents and purposes, arbitrary. This just means the images have their own artifacts and interpretations. For instance, these images do not have speckle, but are often blurred. Second, in the case of acoustic and microwave medical imaging, we are interested in imaging more than one material property. For example, we image both permittivity and conductivity with microwaves, and both

compressibility and absorption with ultrasound. This is done for additional diagnostic information but it must also be done to properly describe the scattering phenomena in tissue. However, the simultaneous inversion of two physical properties based on the algorithms investigated here is inherently ambiguous without additional prior information. Last, the computational complexity of inverse scattering algorithms grows nonlinearly with the number of addition data.

The difficulties mentioned so far are purely algorithmic and can be mitigated to some effect. We know that the ill-posedness and non-uniqueness can be reduced by taking more scattered field measurements in both space and frequency. The ambiguity in simultaneous retrieval of two materials is aided by priors. Computation, of course, is improved using more efficient code or more computational resources.

Algorithmic difficulties aside, however, the major question that remained was how does one perform an inverse scattering experiment in the first place? That is, how does one properly calibrate an inverse scattering system so that we achieve meaningful images? This is the one question that needed to be addressed before evaluating the true efficacy of inverse scattering for breast imaging, or any other application. It is also the one question never really addressed in the literature. There are hundreds of papers describing inverse scattering algorithms in theory. These algorithms almost ubiquitously assume two things: 1) the incident fields are known, and 2) the data are field quantities. Oddly, no one, in the history of physics, has ever measured a field quantity directly. At the outset of this work, it was clear that there was a disconnect between the algorithms in theory and the measurements in experiment, and there was never a point to building an experimental system until there was some path to solving them. As a result, the main thrust of this thesis became trying to address these two assumptions in order to make inverse scattering experimentally viable, all the while trying to create experimental systems aimed at breast imaging. These contributions are summarized next.

The work in Chapters II and III contain our modifications to the traditional Born Iterative Method inverse scattering algorithm. These modifications made the algorithm more experimentally realistic. The original cost function of this algorithm was designed around the inversion of a large matrix which was regularized with turning parameters. Instead, by using a multi-variate covariance-based cost function we could, 1) minimize the functional with conjugate gradients avoiding the need to build and store a large matrix, and 2) use the Gaussian interpretation to give us physically meaningful regularization, the values of which come from experiment, eliminating the need for tuning parameters. We also found the Neumann series solution of the forward scattering problem to be particularly useful, especially with the speed up from the Shanks transformation. We applied these modifications to both the acoustic and microwave inverse scattering algorithms which were successfully demonstrated in simulation.

Chapter IV describes our answer to the antenna modeling question. The work was based on the source-scattering matrix formulation. While the formulation is well known in near-field antenna characterization, we contributed three things of very practical importance. First, we used the formulation to derive a propagation model directly predicting microwave S-parameters between two antennas. Second, we used simulation to find the antenna model parameters. Third, we showed how to integrate object T-matrices to predict object scattering. The first and second attributes make this model inexpensively accessible to small laboratory setups. S-parameters are widely used and now expensive near-field antenna ranges are not required to obtain these specific antenna model parameters. Most importantly, we can compute the antenna incident field anywhere away from the antenna, addressing the first major calibration problem of an experimental inverse scattering system. The third attribute allows investigators to very simply evaluate T-matrix methods in the lab. This is also useful for system diagnostics, which we used in Chapter VI.

Chapter V is perhaps the most significant contribution of this thesis. The vector Green's function derived in this chapter effectively solved one of the outstanding calibration problems in experimental microwave inverse scattering, which was the second calibration issue mentioned above. It gave us a rigorous and formal link between the material properties of the objects we wished to image and the scattered field voltage quantities we measured, namely S-parameters. Furthermore, it was shown that the vector Green's function is valid for cavity-like geometries; this would prove to be instrumental in characterizing our near-field microwave breast imaging system in Chapter VII.

In Chapter VI, we wanted to prove the use of the vector Green's function with a free-space inverse scattering experiment. We first modified the cost function and forward model of the BIM to include the vector Green's function. We then constructed a ring of antennas, explained how to make the experimental setup and antenna model consistent, and successfully formed dielectric images of plastic objects without the use of calibration targets.

Chapter VII was the culmination of the microwave calibration and inverse scattering algorithm in a cavity-based breast imaging prototype system. We constructed an imaging cavity and accompanying switching matrix to image simple targets in a lossy coupling medium. We characterized the cavity using simulation and integrated the results with the vector Green's function and inverse scattering algorithm. The imaging was evaluated in both simulation and experiment. Simulation showed the validity of the method and the experiment worked with some success.

In Chapter VIII we returned to the acoustic inverse scattering problem. Given the success of the microwave analysis, we adapted the antenna propagation model and vector Green's function to acoustics. We investigated a new self-characterization technique based on the non-linear inversion of the propagation model to the problem of characterizing commercial ultrasound transducers. We integrated this into the

acoustic inverse scattering algorithm and constructed an experiment in which we rotated objects between two ultrasound probes. Even though we formed images of several targets, given the many assumptions made in the acoustic experiment due to the length scale and nature of the data acquisition, it remained unclear how successfully the methods worked for acoustics.

Overall, much headway was made improving and understanding the calibration of inverse scattering systems, but several questions remain regarding their use in breast imaging. First, even though we know how to calibrate the microwave system, we still do not know if the resolution or image quality is good enough for diagnosis. This is mostly because accurately characterizing a system using absolute phase, as we do, and getting the model to match the experiment, is very difficult. For the ultrasound inverse scattering problem, more work needs to be done on basic calibration. The major problem encountered in this work was that the acoustic wavelengths were too small, and so the spatial uncertainties too large, for the methods we tried. The small wavelength is ultrasound's great strength by providing safe imaging with superior resolution, but it may also exclude techniques such as ours which depend so heavily on accurate phase calibration and crude targets to confirm the forward models. However, because there is little question about the diagnostic potential of the acoustic properties of tissue, further work in acoustic inverse scattering imaging methods should be pursued.

9.2 Future Research Directions

There are several new paths of investigation building on and inspired by this work. Some are specific improvements that can be made on the immediate findings or setups, others are new directions based on some of the conclusions herein, listed below in no particular order.

1. Inverse scattering algorithms

Inverse scattering remains an open topic as researchers are continually looking for faster and more accurate algorithms. They are also searching for new regularization methods. First, having successfully applied the multi-variate covariance-based cost function to the BIM, an area for investigation is how it can be applied to other inversion algorithms, such as the popular CSI algorithm, [69]. It would also be interesting to see how the covariance operators can be generalized or related to non-linear regularization techniques, such as total variation. Second, the computational complexity of gradient based inverse scattering algorithms continues to be nonlinearly proportional to the problem size. This is something that cannot be improved by advances in computation alone. Investigating direct inversion techniques, such as those in diffuse optical tomography, offer a promising direction for rapid imaging but require modifications for acoustic or electromagnetic inverse scattering.

2. System modeling

One of most difficult aspects of the experiments in this dissertation was system modeling. Uncertainties in the source locations, microwave substrate parameters, coupling medium parameters, network analyzer calibration, transducer materials, etc, percolated through the inversion algorithms to adversely affect image reconstruction quality. In addition, multiple scattering between the unknown objects and the surrounding structures went unmodeled. This was the case in both the free-space microwave experiment and the cavity experiment.

There is much that can be contributed to methods which help improve our accuracy of the parameters in system models. One idea is to use inversion techniques as the basis for data driven rapid model correction. For example, in the cavity experiment, even with independent measures of the dielectric properties of the

coupling fluid, we still had to make small, iterative adjustments to our HFSS model after comparing measurements to numerical predictions. A fast inverse perturbation method using incident field measurements might have allowed us to fine tune this parameter on the fly for every experiment. These methods would be especially useful for estimating properties or parameters which are not stable, such as the coupling fluid properties, or structural motion of setups. The other question we encountered was whether to model the multiple scattering in the imaging cavity. Efforts should be undertaken to evaluate the effects on image quality of including multiple scattering or not, and developing ways of estimating or approximating background dyadic Green's functions for arbitrarily complex structures.

3. Ultrasound

Much of the work in this dissertation concentrated on the microwave problem. While microwave breast imaging is still an exploratory area, ultrasound is quite established and actually stands to profit the most from any applications of inverse scattering in clinical settings. This is because ultrasound is used every day to diagnosis or monitor many more medical conditions than breast cancer. Thus, a continued and concerted effort should be made to keep applying full-wave and inverse scattering techniques to improve ultrasound images. The aim should be to provide new quantitative imaging as well as to sharpen traditional B-mode images. In particular, calibration methods for full-wave ultrasound need to be improved so they are simpler and more robust.

4. Microwave breast systems continued

While we were successful in building a prototype microwave breast imaging system, more complete testing remains to be done. First, the system needs to be tested with more realistic breast phantoms. Our coupling medium provides

the basis for this, because we can tune the medium properties by changing the oil/water ratio, but creating realistic breast phantoms is still a difficult process. Another problem encountered with the imaging system was that, because the antenna geometry was fixed, and, because we used a single operating frequency, the scattered field data sets given to the inverse scattering algorithm were extremely sparse. The inverse problem was underdetermined by one order of magnitude or more, and the artifacts in both the images from the numerical and experimental data were a result of this. Better data collection strategies, such as more antennas or mechanical scanning, are needed if inverse scattering is going to be successful for breast imaging.

Other work in the group involved focused microwave breast thermal therapy. While this work continues, an application for microwave breast imaging, in addition to diagnosis, is to aid the planning and accuracy of focused thermal therapy. This requires advances in fast inverse scattering techniques, because images must be formed in a matter of minutes. One approach is to take advantage of the high background conductivity and the lower operating frequencies of the thermal system, which make the electrical size of the problem small, in order to develop fast, approximate inverse scattering solutions.

APPENDICES

APPENDIX A

Operator Transpose for Electromagnetic Inversion

A.1 Operator transpose for point receivers

Here we derive the electromagnetic operator transpose in the context of the weighted spaces, [55]. We assume the field is constant and the integral acts on the object. Writing the scattered field volume integral equation as

$$\mathbf{E}_{sca}(\mathbf{x}_r) = c \int \overline{\mathbf{G}}(\mathbf{x}_r, \mathbf{x}') \cdot O(\mathbf{x}') \mathbf{E}(\mathbf{x}') d^3 \mathbf{x}' \quad (\text{A.1})$$

where c and $O(\mathbf{x})$ are one of the two object functions and their multiplying constant. The above is written for only one, three-vector data point at \mathbf{x}_r . To derive the transpose, we use the relation between the model and data space norms

$$(\mathbf{d}, \mathbf{G}\mathbf{m})_D = (\mathbf{G}^\dagger \mathbf{d}, \mathbf{m})_M \quad (\text{A.2})$$

This is written in terms of the adjoint operator, $\mathbf{G}^\dagger = \mathbf{C}_M \mathbf{G}^* \mathbf{C}_D^{-1}$. If we assume the covariance matrices are the identity, then the adjoint is equal to the transpose. Next, take the model space as a continuous space over the object function, and the

data space also continuous over all possible points of the scattered field. These norms can be defined for continuous scalar functions as

$$(u, v)_D = (u, v)_M = \int u(\mathbf{x})^* v(\mathbf{x}) dV \quad (\text{A.3})$$

In the case that the data are vectors, the conjugate is a vector transpose and dot product

$$(\mathbf{u}, \mathbf{v})_D = (\mathbf{u}, \mathbf{v})_M = \int \mathbf{u}(\mathbf{x})^* \cdot \mathbf{v}(\mathbf{x}) dV \quad (\text{A.4})$$

We start by writing out the data norm, interchanging the order of integration, and aim to arrive at a norm over the model space. Let $\mathbf{d} = \mathbf{E}_{sca}(\mathbf{x})$ and \mathbf{Gm} be a single predicted scattered field three-vector, then

$$(\mathbf{d}, \mathbf{Gm})_D = \int \mathbf{E}_{sca}^*(\mathbf{x}) \cdot c \int \overline{\mathbf{G}}(\mathbf{x}, \mathbf{x}') \cdot \mathbf{E}(\mathbf{x}') O(\mathbf{x}') d^3 \mathbf{x}' d^3 \mathbf{x} \quad (\text{A.5})$$

again $*$ is the conjugate vector transpose for the field, and we take the object out of the dot product. Next, interchange the order of integration

$$(\mathbf{d}, \mathbf{Gm})_D = \int \int \mathbf{E}_{sca}^*(\mathbf{x}) \cdot c \overline{\mathbf{G}}(\mathbf{x}, \mathbf{x}') \cdot \mathbf{E}(\mathbf{x}') O(\mathbf{x}') d^3 \mathbf{x}' d^3 \mathbf{x} \quad (\text{A.6})$$

and use the definition of the matrix-vector transpose $\mathbf{u}^* \mathbf{v} = (\mathbf{v}^* \mathbf{u})^*$.

$$(\mathbf{d}, \mathbf{Gm})_D = \int \int \left((c \overline{\mathbf{G}}(\mathbf{x}, \mathbf{x}') \cdot \mathbf{E}(\mathbf{x}'))^* \cdot \mathbf{E}_{sca}(\mathbf{x}) \right)^* O(\mathbf{x}') d^3 \mathbf{x}' d^3 \mathbf{x} \quad (\text{A.7})$$

$$= \int \int \left(c^* \mathbf{E}^*(\mathbf{x}') \cdot \overline{\mathbf{G}}^*(\mathbf{x}, \mathbf{x}') \cdot \mathbf{E}_{sca}(\mathbf{x}) \right)^* O(\mathbf{x}') d^3 \mathbf{x}' d^3 \mathbf{x} \quad (\text{A.8})$$

$$= \int \left(c^* \mathbf{E}^*(\mathbf{x}') \cdot \int \overline{\mathbf{G}}^*(\mathbf{x}, \mathbf{x}') \cdot \mathbf{E}_{sca}(\mathbf{x}) d^3 \mathbf{x} \right)^* O(\mathbf{x}') d^3 \mathbf{x}' \quad (\text{A.9})$$

Which is the norm over M , so we identify the transpose operator as

$$\mathbf{G}^* \mathbf{d} = c^* \mathbf{E}^*(\mathbf{x}) \cdot \int \overline{\mathbf{G}}^*(\mathbf{x}, \mathbf{x}') \cdot \mathbf{E}_{sca}(\mathbf{x}) d^3 \mathbf{x} \quad (\text{A.10})$$

For the scattered field measured at a point we can write

$$\mathbf{E}_{sca}(\mathbf{x}) \rightarrow \mathbf{E}_{sca} \delta(\mathbf{x} - \mathbf{x}_r) \quad (\text{A.11})$$

and evaluate the integral to give

$$\mathbf{G}^* \mathbf{d} = c^* \mathbf{E}^*(\mathbf{x}) \cdot \overline{\mathbf{G}}^*(\mathbf{x}, \mathbf{x}_r) \cdot \mathbf{E}_{sca}(\mathbf{x}_r) \quad (\text{A.12})$$

The above maps a three vector scattered field data point from a single receiver back to the model space (i.e., the object domain). Numerically, the result is usually multiplied by a factor of a volume element.

APPENDIX B

Vector Wave Functions

B.1 Vector Wave Functions

B.1.1 Wave Function Conventions

From [52], the scalar wave function is

$$\psi_{lm}(\mathbf{r}) = Y_{lm}(\theta, \phi) z_l(kr) \quad (\text{B.1})$$

where $z_l(x)$ is any of $j_l(x)$, $y_l(x)$, $h_l^{(1)}(x)$, $h_l^{(2)}$. The vector wave function is defined

$$\mathbf{M}_{lm}(\mathbf{r}) = \nabla \times [\mathbf{r}\psi_{lm}(\mathbf{r})] = [\nabla\psi_{lm}(\mathbf{r})] \times \mathbf{r} \quad (\text{B.2})$$

Also

$$\mathbf{N} = \frac{1}{k} \nabla \times \mathbf{M} \quad (\text{B.3})$$

$$\mathbf{M} = \frac{1}{k} \nabla \times \mathbf{N} \quad (\text{B.4})$$

Written out the vector wave functions are

$$\mathbf{M}_{lm} = N_{lm} z_l(kr) e^{im\phi} \left(\frac{im}{\sin \theta} P_l^m(\cos \theta) \hat{\theta} + \sin \theta P_l^{m'}(x) \Big|_{x=\cos \theta} \hat{\phi} \right) \quad (\text{B.5})$$

$$\mathbf{N}_{lm} = N_{lm} e^{im\phi} \left[\frac{z_l(kr)}{kr} l(l+1) P_l^m(\cos \theta) \hat{r} + \left(\frac{1}{x} z_l(x) + z_l'(x) \right) \Big|_{x=kr} \cdot \right. \\ \left. \left(-\sin \theta P_l^{m'}(x) \Big|_{x=\cos \theta} \hat{\theta} + \frac{im}{\sin \theta} P_l^m(\cos \theta) \hat{\phi} \right) \right] \quad (\text{B.6})$$

with

$$N_{lm} = \sqrt{\frac{2l+1}{4\pi} \frac{(l-m)!}{(l+m)!}} \quad (\text{B.7})$$

The Condon-Shortly phase is included in the definition of the Associated Legendre polynomials. This is consistent with the vector wave function definitions used to derive the translation and rotation recurrence relations, see Appendix B.1.4.

The $l(l+1)$ factor in the reciprocity relations comes from integrating products of these waves functions over the sphere when evoking then reciprocity theorem. The radially independent vector wave harmonics as given in [113] are

$$\mathbf{X}_{lm} = \frac{1}{i\sqrt{l(l+1)}} (\mathbf{r} \times \nabla) Y_{lm}(\theta, \phi) \quad (\text{B.8})$$

with orthonormality over the sphere as

$$\int \mathbf{X}_{l'm'} \cdot \mathbf{X}_{lm}^* d\Omega = \delta_{l'l} \delta_{m'm} \quad (\text{B.9})$$

$$\int (\mathbf{X}_{l'm'} \times \mathbf{X}_{lm}^*) \cdot \mathbf{r} d\Omega = 0 \quad (\text{B.10})$$

The Condon-Shortly phase does not affect the orthonormalization. If neither term is conjugate, then a factor of $-(-1)^m$ remains from the integration in (B.9). In terms of \mathbf{X} , \mathbf{M}_{lm} is written

$$\mathbf{M}_{lm} = -i\sqrt{l(l+1)}z_l(kr)\mathbf{X}_{lm} \quad (\text{B.11})$$

Thus, when integrating dot products of \mathbf{M}_{lm} and \mathbf{N}_{lm} over the sphere for reciprocity integrals, see [83], in which neither is conjugate, we get a factor of $l(l+1)(-1)^m$ multiplying $\delta_{l'l}\delta_{m'm}$.

B.1.2 Translation Addition Theorem

The translation relations for the vector wave functions are

$$\mathbf{M}_{lm}(\mathbf{r}) = \sum_{l'm'} [\mathbf{M}_{l'm'}(\mathbf{r}')A_{l'm',lm} + \mathbf{N}_{l'm'}(\mathbf{r}')B_{l'm',lm}] \quad (\text{B.12})$$

$$\mathbf{N}_{lm}(\mathbf{r}) = \sum_{l'm'} [\mathbf{N}_{l'm'}(\mathbf{r}')A_{l'm',lm} + \mathbf{M}_{l'm'}(\mathbf{r}')B_{l'm',lm}] \quad (\text{B.13})$$

where $A_{l'm',lm}$ and $B_{l'm',lm}$ are given in [52]. The following identities were confirmed numerically for the translation coefficients

$$|A_{l'm'lm}^{ji}| = |A_{l'm'lm}^{ij}| \quad (\text{B.14a})$$

$$|B_{l'm'lm}^{ji}| = |B_{l'm'lm}^{ij}| \quad (\text{B.14b})$$

$$A_{l'm'lm}^{ij} = (-1)^{l+l'} A_{l'm'lm}^{ji} \quad (\text{B.14c})$$

$$B_{l'm'lm}^{ij} = -(-1)^{l+l'} B_{l'm'lm}^{ji} \quad (\text{B.14d})$$

$$A_{l'm'lm}^{ji} = c_{l,l'} (-1)^{l+l'+m+m'} A_{l,-m,l',-m'}^{ji} \quad (\text{B.14e})$$

$$B_{l'm'lm}^{ji} = -c_{l,l'} (-1)^{l+l'+m+m'} B_{l,-m,l',-m'}^{ji} \quad (\text{B.14f})$$

$$A_{l',-m',l,m}^{ji} = c_{l,l'} (-1)^{m+m'} A_{l,-m,l',m'}^{ij} \quad (\text{B.14g})$$

$$B_{l',-m',l,m}^{ji} = c_{l,l'} (-1)^{m+m'} B_{l,-m,l',m'}^{ij} \quad (\text{B.14h})$$

where $c_{l,l'} = l(l+1)/l'(l'+1)$. Equations (B.14g) and (B.14h) are used in Appendix B.2 and can be derived using (B.14c)-(B.14f).

B.1.3 Rotation Addition Theorem

The rotation addition theorems for both scalar and vector wave harmonics are given by [90, 85, 91, 92],

$$\mathbf{M}_{lm}(r, \theta, \phi) = \sum_{p=-l}^l D_{lmp}(\alpha\beta\gamma) \mathbf{M}'_{lp}(r', \theta', \phi') \quad (\text{B.15})$$

where (α, β, γ) are the three Euler angles describing a Z-X-Z rotation from unprimed to primed coordinate systems. The rotations transform across m for a given l . In other words, D_{lmp} can be written as a block diagonal matrix with blocks spanning m and p for a particular l , zero otherwise. Specifically,

$$D_{lmp}(\alpha\beta\gamma) = e^{im\alpha} d_{lmp}(\beta) e^{ip\gamma} \quad (\text{B.16})$$

where

$$\begin{aligned}
d_{lmp}(\beta) &= \sqrt{\frac{(l+p)!(l-p)!}{(l+m)!(l-m)!}} \sum_u \binom{l+m}{l-p-u} \binom{l-m}{u} \\
&\cdot (-1)^{l-p-u} \left(\cos \frac{\beta}{2}\right)^{m+p+2u} \left(\sin \frac{\beta}{2}\right)^{2l-m-p-2u}
\end{aligned} \tag{B.17}$$

The sum is over all u for positive arguments of the binomial coefficients.

In matrix form, if \mathbf{a} are the outgoing wave coefficients in the i frame, and \mathbf{a}' are those in the rotated i' frame, then

$$\mathbf{a}' = \mathbf{D}_i \mathbf{a} \tag{B.18}$$

where \mathbf{D}_i describes the rotation from i to i' . \mathbf{D}_i is unitary, so $\mathbf{D}_i^{-1} = \mathbf{D}_i^*$, and the inverse relation is

$$\mathbf{a} = \mathbf{D}_i^* \mathbf{a}' \tag{B.19}$$

B.1.4 Computation of Addition Theorems

Recursion relations exist for quickly computing the translation and rotation matrices. For the translation matrices, we use the recursion relations in [143, 144]. For the rotation matrix, we use the recursion relations in [145].

B.2 Reciprocity for Two Fixed Antennas

The goal is to show $S_{ji} = S_{ij}$. Starting with Eqn. (4.23),

$$\begin{aligned}
S_{ji} &= \sum_{l'm'} c_r n_{l'm'} \left[t_{(a)l'm'}^j \sum_{lm} \left(A_{l',-m',lm}^{ji} t_{(a)lm}^i + B_{l',-m',lm}^{ji} t_{(b)lm}^i \right) \right. \\
&\quad \left. + t_{(b)l'm'}^j \sum_{lm} \left(B_{l',-m',lm}^{ji} t_{(a)lm}^i + A_{l',-m',lm}^{ji} t_{(b)lm}^i \right) \right]
\end{aligned} \tag{B.20}$$

Rearranging the sums and writing out the normalization constant,

$$\begin{aligned}
S_{ji} &= \sum_{lm} c_r \cdot \left[t_{(a)l,m}^i \sum_{l'm'} n_{l'm'} \cdot \left(A_{l',-m',lm}^{ji} t_{(a)l'm'}^j + B_{l',-m',lm}^{ji} t_{(b)l'm'}^j \right) \right. \\
&\quad \left. + t_{(b)l,m}^i \sum_{l'm'} n_{l'm'} \cdot \left(B_{l',-m',lm}^{ji} t_{(a)l'm'}^j + A_{l',-m',lm}^{ji} t_{(b)l'm'}^j \right) \right]
\end{aligned} \tag{B.21}$$

Applying (B.14g) and (B.14h) to the translation matrices, we get

$$\begin{aligned}
S_{ji} &= \sum_{lm} c_r n_{lm} \left[t_{(a)l,m}^i \sum_{l'm'} \left(A_{l',-m',l'm'}^{ij} t_{(a)l'm'}^j + B_{l',-m',l'm'}^{ij} t_{(b)l'm'}^j \right) \right. \\
&\quad \left. + t_{(b)l,m}^i \sum_{l'm'} \left(B_{l',-m',l'm'}^{ij} t_{(a)l'm'}^j + A_{l',-m',l'm'}^{ij} t_{(b)l'm'}^j \right) \right] \\
&= S_{ij}
\end{aligned} \tag{B.22}$$

which is the reciprocity relation for a passive, linear, two-port network.

We confirmed numerically that Eqn. (4.31), which includes rotation matrices, is also reciprocal.

APPENDIX C

Special Cases of Vector Green's Function VIE

C.1 Special Cases of Vector Green's Function Integral

Here we consider three special cases of the scattered field integral equation using the vector Green's function: 1) either the transmitter or the receiver is in the far-field, 2) we make the Born approximation, and 3) the antennas are in the far-field and we make the Born approximation.

C.1.1 Far-Field

When either the transmitter or the receiver is in the far-field, we can simplify the expression for its normalized incident field by using the far-field approximations of the free-space vector wave functions, $\mathbf{M}_{lm}(\mathbf{r})$ and $\mathbf{N}_{lm}(\mathbf{r})$. Similar to [89], these are given by

$$\mathbf{M}_{lm}(\mathbf{r})|_{kr \rightarrow \infty} \approx \frac{e^{ikr}}{kr} \mathbf{C}'_{lm}(\theta, \phi) \quad (\text{C.1})$$

$$\mathbf{N}_{lm}(\mathbf{r})|_{kr \rightarrow \infty} \approx \frac{e^{ikr}}{kr} \mathbf{B}'_{lm}(\theta, \phi) \quad (\text{C.2})$$

where

$$\mathbf{C}'_{lm}(\theta, \phi) = i^{-l-1} \nabla \times [\mathbf{r} Y_{lm}(\theta, \phi)] \quad (\text{C.3})$$

$$\mathbf{B}'_{lm}(\theta, \phi) = i^{-l} r \nabla [Y_{lm}(\theta, \phi)] = \hat{\mathbf{r}} \times \mathbf{C}'_{lm}(\theta, \phi) \quad (\text{C.4})$$

The vector functions \mathbf{B}'_{lm} and \mathbf{C}'_{lm} have only $\hat{\theta}$ and $\hat{\phi}$ components and do not depend on the distance r . Prime indicates that we use angular harmonics with the conventions of [52] instead of [89]. We can then write the normalized incident field as

$$\mathbf{e}_{inc}(\mathbf{r})|_{kr \rightarrow \infty} = \sum_{lm} (t_{(a)lm} \mathbf{M}_{lm}(\mathbf{r}) + t_{(b)lm} \mathbf{N}_{lm}(\mathbf{r})) \quad (\text{C.5})$$

$$\approx \frac{e^{ikr}}{kr} \mathbf{f}(\theta, \phi) \quad (\text{C.6})$$

where

$$\mathbf{f}(\theta, \phi) = \sum_{lm} (t_{(a)lm} \mathbf{C}'_{lm}(\theta, \phi) + t_{(b)lm} \mathbf{B}'_{lm}(\theta, \phi)) \quad (\text{C.7})$$

$$= f_{\theta}(\theta, \phi) \hat{\theta} + f_{\phi}(\theta, \phi) \hat{\phi} \quad (\text{C.8})$$

where f_{θ} and f_{ϕ} are complex amplitudes resulting from summing the angular harmonics over the transmit coefficients. The vector function $\mathbf{f}(\theta, \phi)$ represents the far-field radiation pattern of the antenna, but which is phased properly for S-parameter measurements and our antenna characterization. This expression for the normalized incident field can be used either for the vector Green's function when the receiver is in the far-field, or used in a forward solver when the transmitter is in the far-field.

C.1.2 Born Approximation

Under the Born approximation for weakly scattering objects, the total field in the object is approximated by the incident field. Using Eqn. (5.33) which is given in terms of the normalized incident and total fields, the scattered field S-parameters are given by

$$S_{ji} \approx \frac{iZ_0^j}{2\omega\mu} \int f_{ji}(\mathbf{r}') O(\mathbf{r}') dV' \quad (\text{C.9})$$

where

$$f_{ji}(\mathbf{r}') = \mathbf{e}_{inc,j}(\mathbf{r}') \cdot \mathbf{e}_{inc,i}(\mathbf{r}') \quad (\text{C.10})$$

Note that while the variable \mathbf{r}' simply keeps track of the integration location, the dot product of the two incident fields must be computed in the same coordinate system. For instance, when the normalized incident fields are computed using the multipole expansion for antennas in two different reference frames, the vector components seen from each frame must be projected to a common frame for the dot product.

C.1.3 Far-Field and Born Approximation

Let the object be in its own reference frame. If we make far-field approximations for the normalized incident fields in Eqn. (C.10), and we further assume that the incident fields can be approximated by plane waves in the object domain, then it can be shown that

$$S_{ji} \approx \frac{iZ_0^j}{2\omega\mu} \frac{e^{ik(r_j+r_i)}}{k^2 r_j r_i} \mathbf{f}_j(\theta_j, \phi_j) \cdot \mathbf{f}_i(\theta_i, \phi_i) \int e^{-ik(\hat{\mathbf{r}}_j \cdot \mathbf{r}' + \hat{\mathbf{r}}_i \cdot \mathbf{r}')} O(\mathbf{r}') dV' \quad (\text{C.11})$$

where the vectors \mathbf{r}_j and \mathbf{r}_i point from the object frame to the receiver and transmitter frames, respectively, and the vector functions $\mathbf{f}_j(\theta_j, \phi_j)$ and $\mathbf{f}_i(\theta_i, \phi_i)$ are measured with respect to the vectors $-\mathbf{r}_j$ and $-\mathbf{r}_i$ which point from the antennas to the object. This expression can be used for 3D diffraction tomography where scattered field S-parameters are used as data.

APPENDIX D

Cost Function of Linear Inverse Problems

D.1 Cost Function and Step Length for a General Linear Problem

D.1.1 Cost Function

Here we summarize the major points of [55] for minimizing a weighted least-squares cost functional of a linear operator using conjugate gradients. The cost function is, generally,

$$2F(\mathbf{m}) = \|\mathbf{G}\mathbf{m} - \mathbf{d}\|_D^2 + \|\mathbf{m} - \mathbf{m}_a\|_M^2 \quad (\text{D.1})$$

The vector norms $\|\cdot\|_D^2$ and $\|\cdot\|_M^2$ are defined over the data and model spaces through the inverse data and model covariance operators, \mathbf{C}_D^{-1} and \mathbf{C}_M^{-1} , respectively as

$$\|\cdot\|_D^2 = (\mathbf{u}, \mathbf{v})_D = \mathbf{u}^* \mathbf{C}_D^{-1} \mathbf{v} \quad (\text{D.2})$$

$$\|\cdot\|_M^2 = (\mathbf{u}, \mathbf{v})_M = \mathbf{u}^* \mathbf{C}_M^{-1} \mathbf{v} \quad (\text{D.3})$$

The gradient vector and steepest descent vector are given by

$$\hat{\boldsymbol{\gamma}} = \mathbf{G}^* \mathbf{C}_D^{-1} (\mathbf{G} \mathbf{m} - \mathbf{d}) + \mathbf{C}_M^{-1} (\mathbf{m} - \mathbf{m}_a) \quad (\text{D.4})$$

$$\boldsymbol{\gamma} = \mathbf{C}_M \mathbf{G}^* \mathbf{C}_D^{-1} (\mathbf{G} \mathbf{m} - \mathbf{d}) + \mathbf{m} - \mathbf{m}_a \quad (\text{D.5})$$

The adjoint is defined as $\mathbf{G}^\dagger = \mathbf{C}_M \mathbf{G}^* \mathbf{C}_D^{-1}$. Norms over the two spaces are related through the adjoint as

$$(\mathbf{d}, \mathbf{G} \mathbf{m})_D = (\mathbf{G}^\dagger \mathbf{d}, \mathbf{m})_M \quad (\text{D.6})$$

The conjugate gradient updates of the model parameters are given by

$$\mathbf{m}_n = \mathbf{m}_{n-1} - \alpha_n \mathbf{v}_n \quad (\text{D.7})$$

$$\mathbf{v}_n = \boldsymbol{\gamma}_n + \beta_n \mathbf{v}_{n-1} \quad (\text{D.8})$$

where β_n can take one of a number of forms, [55].

D.1.2 Step Length

We solve for the step length by substituting the model update vector into the cost function, and minimize with respect to the step length. A similar result appears in [46], but here we outline and explain the steps in the context of weighted spaces. Substituting Eqn. (D.7) into Eqn. (D.1) we have

$$2F(\mathbf{m}_n) = \|\mathbf{G}(\mathbf{m}_{n-1} - \alpha_n \mathbf{v}_n) - \mathbf{d}\|_D^2 + \|\mathbf{m}_{n-1} - \alpha_n \mathbf{v}_n - \mathbf{m}_a\|_M^2 \quad (\text{D.9})$$

$$\begin{aligned} &= \alpha_n^2 \|\mathbf{s}_n\|_D^2 - \alpha_n (\mathbf{s}_n, \mathbf{r}_{n-1})_D - \alpha_n (\mathbf{r}_{n-1}, \mathbf{s}_n)_D + \|\mathbf{r}_{n-1}\|_D^2 \\ &\quad + \alpha_n^2 \|\mathbf{v}_n\|_M^2 - \alpha_n (\mathbf{v}_n, \mathbf{c}_n)_M - \alpha_n (\mathbf{c}_n, \mathbf{v}_n)_M + \|\mathbf{c}_n\|_M^2 \end{aligned} \quad (\text{D.10})$$

where $\mathbf{r}_{n-1} = \mathbf{G}\mathbf{m}_{n-1} - \mathbf{d}$, $\mathbf{s}_n = \mathbf{G}\mathbf{v}_n$, and $\mathbf{c}_n = \mathbf{m}_{n-1} - \mathbf{m}_a$. Taking the derivative with respect to α_n .

$$\begin{aligned} \frac{\partial}{\partial \alpha_n} (2F(\mathbf{m}_n)) &= 2\alpha_n \|\mathbf{s}_n\|_D^2 + 2\alpha_n \|\mathbf{v}_n\|_M^2 - \\ &\quad 2\Re \{ (\mathbf{s}_n, \mathbf{r}_{n-1})_D + (\mathbf{v}_n, \mathbf{c}_n)_M \} \end{aligned} \quad (\text{D.11})$$

Setting this equal to zero and solving for α_n

$$\alpha_n = \frac{\Re \{ (\mathbf{s}_n, \mathbf{r}_{n-1})_D + (\mathbf{v}_n, \mathbf{c}_n)_M \}}{\|\mathbf{s}_n\|_D^2 + \|\mathbf{v}_n\|_M^2} \quad (\text{D.12})$$

We can simplify the numerator by using the conjugate of Eqn. (D.6),

$$(\mathbf{s}_n, \mathbf{r}_{n-1})_D + (\mathbf{v}_n, \mathbf{c}_n)_M = (\mathbf{G}\mathbf{v}_n, \mathbf{r}_{n-1})_D + (\mathbf{v}_n, \mathbf{c}_n)_M \quad (\text{D.13})$$

$$= (\mathbf{v}_n, \mathbf{G}^\dagger \mathbf{r}_{n-1})_M + (\mathbf{v}_n, \mathbf{c}_n)_M \quad (\text{D.14})$$

$$= (\mathbf{v}_n, \mathbf{G}^\dagger \mathbf{r}_{n-1} + \mathbf{m}_{n-1} - \mathbf{m}_a)_M \quad (\text{D.15})$$

$$= (\mathbf{v}_n, \boldsymbol{\gamma}_n)_M \quad (\text{D.16})$$

The step length becomes

$$\alpha_n = \frac{\Re \{ (\mathbf{v}_n, \boldsymbol{\gamma}_n)_M \}}{\|\mathbf{s}_n\|_D^2 + \|\mathbf{v}_n\|_M^2} \quad (\text{D.17})$$

This is easily modified to account for two, independent contrast functions.

D.2 Vector Green's function operator transpose

To derive the transpose operator in the context of the Vector Green's function volume integral equation, we first let $\mathbf{C}_M^{-1} = \mathbf{C}_D^{-1} = \mathbf{I}$, so that the adjoint is equal to the transpose, and we can write Eqn. (D.6) as

$$(\mathbf{d}, \mathbf{G}\mathbf{m})_D = (\mathbf{G}^*\mathbf{d}, \mathbf{m})_M \quad (\text{D.18})$$

For our problem, the data norm is a sum over discrete data points, namely S-parameter quantities, and the model norm is a volume integral over the contrast functions. Although we discretized the integral in practice, for the derivation of the transpose we can treat the contrast as a continuous function. We start by writing out the left hand side of Eqn. (D.18), using Eqns (6.6) and (6.7). For now, we will only consider the permittivity contrast.

$$(\mathbf{d}, \mathbf{G}_1\mathbf{m}_1)_D = \sum_{ji} S_{ji}^* c_1 \int \mathbf{g}_j(\mathbf{r}) \cdot \delta\epsilon(\mathbf{r}) \mathbf{e}_i(\mathbf{r}) dV \quad (\text{D.19})$$

We exchange the order of integration and summation,

$$(\mathbf{d}, \mathbf{G}_1\mathbf{m}_1)_D = \int \sum_{ji} S_{ji}^* c_1 \mathbf{g}_j(\mathbf{r}) \cdot \delta\epsilon(\mathbf{r}) \mathbf{e}_i(\mathbf{r}) dV \quad (\text{D.20})$$

We then rearrange the integrand to make the integral look like a norm over the model space (i.e. a volume integral over two spatial functions)

$$(\mathbf{d}, \mathbf{G}_1\mathbf{m}_1)_D = \int \left(\left(c_1 \sum_{ji} \mathbf{g}_j(\mathbf{r}) \cdot \mathbf{e}_i(\mathbf{r}) \right)^* S_{ji} \right)^* \delta\epsilon(\mathbf{r}) dV \quad (\text{D.21})$$

$$= (\mathbf{G}_1^*\mathbf{d}, \mathbf{m}_1)_M \quad (\text{D.22})$$

from which we identify the transpose

$$\mathbf{G}_1^* \mathbf{d} = c_1^* \sum_{ji} (\mathbf{g}_j(\mathbf{r}) \cdot \mathbf{e}_i(\mathbf{r}))^* S_{ji} \quad (\text{D.23})$$

where $*$ is simply conjugate. The transpose for the conductivity differs only by a constant.

BIBLIOGRAPHY

BIBLIOGRAPHY

- [1] Breast imaging reporting and data system, 1995.
- [2] M. S. NassAiver W. B. Carter M. Bhargavan R. S. Lewis O. B. Ioffe W. A. Berg, L. Gutierrez. Diagnostic accuracy of mammography, clinical examination, us, and mr imaging in preoperative assessment of breast cancer. *Radiology*, 233(3):830–849, 2004.
- [3] W. Burke S. Harms M. O. Leach C. D. Lehman E. Morris E. Pisano M. Schnall S. Sener R. A. Smith E. Warner M. Yaffe K. S. Andrews C. A. Russell D. Saslow, C. Boetes. American cancer society guidelines for breast screening with mri as an adjunct to mammography. *CA: A Cancer Journal for Clinicians*, 57(2):7589, 2007.
- [4] Breast imaging reporting and data system - ultrasound, 2003.
- [5] E. P. Papadakis. *Ultrasonic Instruments and Devices*. Academic Press, 1999.
- [6] F. A. Duck. *Physical Properties of Tissue*. Academic Press, 1990.
- [7] et. al. W. Weiwand. Direct measurement of sound velocity in various specimens of breast tissue. *Inv. Rad.*, 35(12):721–726.
- [8] A. Swarup S. S. Chaudhary, R. K. Mishra and J. M. Thomas. Dielectric properties of normal and malignant human breast tissues at radiowave and microwave frequencies. *Ind. J. Biochem. & Biophys.*, 21:76–79, 1984.
- [9] J. R. Barr A. J. Surowiec, S. S. Stuchly and A. Swarup. Dielectric properties of breast carcinoma and the surrounding tissues. *IEEE Trans. Biomed. Eng.*, 35,:257–263, 1988.
- [10] D. Popovic C. B. Watkins M. J. Lindstrom J. Harter S. Sewall A. Magliocco J. H. Booske M. Okoniewski M. Lazebnik, L. McCartney and S. C. Hagness. A large-scale study of the ultrawideband microwave dielectric properties of normal breast tissue obtained from reduction surgeries. *Phys. Med. Biol.*, 52:26372656, 2007.
- [11] W. A. Wells B. W. Pogue P. M. Meaney A. Hartov C. A. Kogel S. K. Soho J. J. Gibson S. P. Poplack, T. D. Tosteson and K. D. Paulsen. Electromagnetic breast imaging: Results of a pilot study in women with abnormal mammograms. *Radiology*, 243(2):350359, 2007.

- [12] et. al. N. Duric. Breast imaging with ultrasound tomography: clinical results at the karmanos cancer institute. *Int. Conf. BioMedical Eng. and Info.*, pages 713–716, 2008.
- [13] et. al. M. P. Andre. High-speed data acquisition in a diffraction tomography system employing large-scale toroidal arrays. *Int. J. Imag. Sys. and Tech.*, 8:137–147, 1997.
- [14] N. Duric F. Simonetti, L. Huang. Transmission and reflection diffraction tomography in breast imaging. *Int. Conf. BioMedical Eng. and Info.*, pages 723–727, 2008.
- [15] et. al. M. Andre. Performance of an automated whole-breast ultrasound imaging system employing full-wave 3d inverse-scattering ct. In *RSNA*, pages LL–PH2151–R09, 2008.
- [16] et. al. S. A. Johnson, 1999.
- [17] C. R. Meyer W. Jobe B. Samuels D. D. Adler P. L. Carson, A. L. Scherzinger. Lesion detectability in ultrasonic computed tomography of symptomatic breast patients. *Inverst. Rad.*, (6):421–427, 1988.
- [18] L. Huang C. Li, N. Duric. Breast imaging using transmission ultrasound: reconstructing tissue parameters of sound speed and attenuation. *Int. Conf. BioMedical Eng. and Info.*, pages 708–712, 2008.
- [19] et. al. N. Duric, P. Littrup. Development of ultrasound tomography for breast imaging: technical assessment. *Med. Phys.*, 32(5):1375–1386, 2005.
- [20] et. al. R. R. Leach Jr. Comparison of ultrasound tomography methods in circular geometry. *Proc. of SPIE, Med. Img.: Ultra. Img. and Sig. Proc.*, pages 362–377, 2002.
- [21] S. C. Hagness B. D. Van Veen E. J. Bond, X. Li. Microwave imaging via space-time beamforming for early detection of breast cancer. *IEEE Trans. Antennas Propagat.*, 51(8):1690–1705, 2003.
- [22] S. C. Hagness M. A. Stuchly E. C. Fear, X. Li. Confocal microwave imaging for breast cancer detection: localization of tumors in three dimensions. *IEEE Trans. Bio. Eng.*, 49(8):812–822, 2002.
- [23] C. M. Rappaport P. Kosmas. Fdtd-based time reversal for microwave breast cancer detection-localization in three dimensions. *IEEE Trans. Microwave Theory and Techniques*, 54(4):1921– 1927, June 2006.
- [24] E. Bishop P. Kosmas, C. M. Rappaport. Modeling with the fdtd method for microwave breast cancer detection. *IEEE Trans. Microwave Theory Tech.*, 8(8):1890– 1897, 2004.

- [25] J. E. Bridges S. C. Hagness, A. Taflove. Two-dimensional fdtd analysis of a pulsed microwave confocal system for breast cancer detection: fixed-focus and antenna-array sensors. *IEEE Trans. Biomedical Engineering*, 45(12):1470–1479, 1998.
- [26] J. Li P. Stoica Y. Xie, B. Guo; L. Xu. Multistatic adaptive microwave imaging for early breast cancer detection. *IEEE Trans. Biomedical Engineering*, 53(8):1647–1657, 2006.
- [27] P. Meincke K. D. Paulsen T. Rubaek, P. M. Meaney. Nonlinear microwave imaging for breast-cancer screening using gauss-newton’s method and the cgls inversion algorithm. *IEEE Trans. Antennas Propagat.*, (8):2320–2331, 2007.
- [28] K. D. Paulsen F. Qianqian, P. M. Meaney. Microwave image reconstruction of tissue property dispersion characteristics utilizing multiple-frequency information. *IEEE Trans. Microwave Theory and Techniques*, 52(8):1866– 1875, 2004.
- [29] Q. H. Liu Z. Q. Zhang. Three-dimensional nonlinear image reconstruction for microwave biomedical imaging. *IEEE Trans. Bio Eng.*, 51(3):544–548.
- [30] Susan C. Hagness Jacob D. Shea, Panagiotis Kosmas and Barry D. Van Veen. Three-dimensional microwave imaging of realistic numerical breast phantoms via a multiple-frequency inverse scattering technique. *Med. Phys.*, 37:4210 – 4248, 2010.
- [31] J. LoVetri C. Gilmore, P. Mojabi. Comparison of an enhanced distorted born iterative method and the multiplicative-regularized contrast source inversion method. *IEEE Trans. Antennas and Propagation*, 57(8):2341–2351, 2009.
- [32] E. L. Miller R. Firoozabadi. A shape-based inversion algorithm applied to microwave imaging of breast tumors. *IEEE Trans. Antennas and Propagation*, 59(10):3719–3729, 2011.
- [33] E. L. Miller M. El-Shenawee. Spherical harmonics microwave algorithm for shape and location reconstruction of breast cancer tumor. *Medical Imaging, IEEE Transactions o*, 25(10):1258–1271, 2006.
- [34] A. Sabouni J. Aronsson G Thomas S Pistorius A. Ashtari, S. Noghalian. Using a priori information for regularization in breast microwave image reconstruction. *IEEE Trans. Biomedical Engineering*, 57(9):2197–2208, 2010.
- [35] E. M. Ali K. H. Awadalla H. A. Sharshar S. H. Zainud-Deen, W. M. Has-sen. Breast cancer detection using a hybrid finite difference frequency domain and particle swarm optimization techniques. In *2008 National Radio Science Conferenc*, 2008.

- [36] S. Noghianian P. Thulasiraman S. Pistorius A. Sabouni, X. Meilian. Efficient microwave breast imaging technique using parallel finite difference time domain and parallel genetic algorithms. In *2007 IEEE Antennas and Propagation Society International Symposium*, pages 2176–2179, 2007.
- [37] O. S. Kim T Rubaek and P. Meincke. Computational validation of a 3-d microwave imaging system for breast-cancer screening. *IEEE Trans. Antennas and Propagation*, 57(7):2105–2115, 2009.
- [38] W. Hu T. M. Habashy P. M van den Berg C. Gilmore, A. Abubakar. Microwave biomedical data inversion using the finite-difference contrast source inversion method. *IEEE Trans. Antennas Propagat.*, 57(5):1528–1538, 2009.
- [39] M. A. Stuchly E. C. Fear, J. Sil. Experimental feasibility study of confocal microwave imaging for breast tumor detection. *IEEE Trans. Microwave Theory Tech.*, 51(3):887– 892, 2003.
- [40] E. C. Fear J. M. Sill. Tissue sensing adaptive radar for breast cancer detection - experimental investigation of simple tumor models. *IEEE Trans. Microwave Theory Tech.*, 53(11):3312– 3319, 2005.
- [41] D. Li S. P. Poplack K. D. Paulsen P. M. Meaney, M. W. Fanning. A clinical prototype for active microwave imaging of the breast. *IEEE Trans. Microwave Theory Tech.*, 48(11):1841–1853, 2000.
- [42] J. A. Leendertz A. Preece M. Klemm, I. J. Craddock and R. Benjamin. Radar-based breast cancer detection using a hemispherical antenna array-experimental results. *IEEE Trans. Antennas and Propagation*, 57(6):1692–1704, June 2009.
- [43] T. D. Mast. Empirical relationships between acoustic parameters in human soft tissues. *Acoust. Res. Let. Online*, 1:37–42, 2000.
- [44] W. C. Chew M. Moghaddam. Simultaneous inversion of compressibility and density in the acoustic inverse scattering problem. *Inverse Problems*, 9:715–730, 1993.
- [45] W. C. Chew G. Otto C. Lu, J. Lin. Image reconstruction with acoustic measurement using distorted born iteration method. *Ultrasonic Imaging*, 18:140–156, 1996.
- [46] R. E. Kleinman P. M van den Berg. A contrast source inversion method. *Inverse Prob.*, 13:1607–1620, 1997.
- [47] M. D’Urso T. Isernia, L. Crocco. New tools and series for forward and inverse scattering problems in lossy media. *IEEE Geosci Remote Sensing Lett.*, 1(4):327– 331, Oct 2004.

- [48] M. Donelli D. Franceschini P. Rocca, M. Benedetti and A. Massa. Evolutionary optimization as applied to inverse scattering problems. *Inverse Problems*, 25(12):123003.
- [49] M. Pastorino S. Caorsi, A. Massa and M. Donelli. Improved microwave imaging procedure for nondestructive evaluations of two-dimensional structures. *IEEE Trans. Antennas Propagat.*, 52(6):1386–1397, 2004.
- [50] A. Martini M. Pastorino A. Rosani M. Benedetti, M. Donelli and A. Massa. An innovative microwave-imaging technique for nondestructive evaluation: Applications to civil structures monitoring and biological bodies inspection. *IEEE Transactions on Instrumentation and Measurement*, 55(6):1878–1883, 2006.
- [51] X. X. Yin W. Hong R. J. Cui, W. C. Chew. Study of resolution and super resolution in electromagnetic imaging for half-space problems. *IEEE Trans. Antennas Propagat.*, 52(6):1398–1411, 2004.
- [52] W. C. Chew. *Waves and Fields in Inhomogeneous Media*. IEEE Press, 1995.
- [53] L. Crocco T. Isernia O. M. Bucci, N. Cardace. Degree of nonlinearity and a new solution procedure in scalar two-dimensional inverse scattering problems. *J. Opt. Soc. Am. A*, 18(8), 2001.
- [54] P. Kosmas B. D. Van Veen S. C. Hagness D. W. Winters, J. D. Shea. Three-dimensional microwave breast imaging: dispersive dielectric properties estimation using patient-specific basis functions. *IEEE Trans. Med. Imag.*, 28(7):969–981, 2009.
- [55] A. Tarantola. *Inverse Problem Theory*. SIAM, 2005.
- [56] M. Oristaglio M. Moghaddam, W. C. Chew. Comparison of the born iterative method and tarantola’s method for an electromagnetic time-domain inverse problem. *Int. J. Imag. Sys. Tech.*, 3:318–333, 1991.
- [57] M. L. Oelze R. J. Lavarello. Density imaging using inverse scattering. *J. Acoust. Soc. Am.*, 125(2):793–802, 2009.
- [58] F. Squartini L. Landini, R. Sarnelli. Frequency-dependent attenuation in breast tissue characterization. *Ultrasound in Med. & Bio.*, 11(4):599–603, 1985.
- [59] A. J. Devaney. A filtered backpropagation algorithm for diffraction tomography. *Ultrasonic Imaging*, 4:336–350, 1982.
- [60] W. C. Chew M. Moghaddam. Variable density linear acoustic inverse problem. *Ultrasonic Imaging*, 15:255–266, 1993.
- [61] D. Liu M. Tabie A. I. Nachman R. C. Waag T. D. Mast, L. P. Souriau. A k-space method for large-scale models of wave propagation in tissue. *IEEE Trans. Ultrason., Ferroelect., Freq. Contr.*, 48(2):341–354, 2001.

- [62] T. D. Mast. Two- and three-dimensional simulations of ultrasonic propagation through human breast tissue. *Acoust. Res. Lett. Online*, 3(2):53–58, 2002.
- [63] P. M van den Berg R. E. Kleinman, G. F. Roach. Convergent born series for large refractive indices. *J. Opt. Soc. Am. A*, 7(5):890–897, 1990.
- [64] W. Hong T. J. Cui, W. C. Chew. New approximate formulation for em scattering by dielectric objects. *IEEE Trans. Antennas Propagat.*, 52(3):684–692, 2004.
- [65] Z. Q. Zhang and Q. H. Liu. Two nonlinear inverse methods for electromagnetic induction measurements. *IEEE Trans. Geosci. Remote Sensing*, 39(6):1331–1339, 2001.
- [66] T. Wang G. Ybarra L. W. Nolte J. A. Bryan W. T. Joines Q. H. Liu, Z. Q. Zhang. Active microwave imaging i: 2-d forward and inverse scattering methods. *IEEE Trans. Microwave Theory Tech.*, 50(1):123–133, 2002.
- [67] M. S. Zhdanov. *Geophysical Inverse Theory and Regularization Problems*. Elsevier Science, 2002.
- [68] S. J. Norton. Iterative inverse scattering algorithms: methods of computing frechet derivatives. *J. Acoust. Soc. Am.*, 106(5):2653–2660, 1999.
- [69] A. Abubakar P. M. van den Berg, A. L. van Broekhoven. Extended contrast source inversion. *Inverse Prob.*, 15:1325–1344, 1999.
- [70] P. C. Hansen. Analysis of discrete ill-posed problems by means of the l-curve. *SIAM Review*, 34(4):561–580, 1992.
- [71] A. Neubauer H. W. Engl, M. Hanke. *Regularization of Inverse Problems*. Springer, 2000.
- [72] J. J. Mallorqui A. Abubakar, P. M. van den Berg. Imaging of biomedical data using a multiplicative regularized contrast source inversion method. *IEEE Trans. Microwave Theory Tech.*, 50(7):1761–1771, 2002.
- [73] W. C. Chew and Y. M. Wang. Reconstruction of two-dimensional permittivity distribution using the distorted born iterative method. *IEEE Trans. Medical Imaging*, 9(2), 1990.
- [74] W. C. Chew M. Moghaddam. Nonlinear two-dimensional velocity profile inversion using time domain data. *IEEE Trans. Geo. Rem. Sen.*, 30(1):147–156, 1992.
- [75] L.-P. Song L. Fenghua, Q.H. Liu. Three-dimensional reconstruction of objects buried in layered media using born and distorted born iterative methods. *IEEE Geoscience and Remote Sensing Letters*, 1(2):107– 111, April 2004.

- [76] D. Shanks. Non-linear transformation of divergent and slowly convergent sequences. *Journal of Mathematics and Physics*, 34:1–42, 1955.
- [77] D. M. Pozar. Closed-form approximations for link loss in a uwb radio system using small antennas. *IEEE Trans. Antennas Propagat.*, 51(9):2346–2352, Sept 2003.
- [78] K. Kim A. Medour T. K. Sarkar, Z. Ji and M. Salazar-Palma. A survey of various propagation models for mobile communications. *IEEE Antennas Propag. Mag.*, 45(3):51–82, June 2003.
- [79] A. O. Boryszenko and D. H. Schaubert. Antenna link transfer function factorization applied to optimized channel design. *IEEE Trans. Antennas Propagat.*, 54(54):2878–2889, Oct 2006.
- [80] J. Aberle S. Rogers and D. Auckland. Two-port model of an antenna for use in characterizing wireless communications systems obtained using efficiency measurements. In *Proc. IEEE AP-S Intl. Symp.*, 2002.
- [81] F. Las-Heras Y. Alvarez and M. R. Pino. Reconstruction of equivalent currents distribution over arbitrary three-dimensional surfaces based on integral equation algorithms. *IEEE Trans. Antennas Propagat.*, 55(12):3460–3468, Dec 2007.
- [82] E. Heyman A. Shlivinski and R. Kastner. Antenna characterization in the time domain. *IEEE Trans. Antennas Propagat.*, 45(7):1140–1149, July 1997.
- [83] A. D. Yaghjian. Scattering-matrix analysis of linear periodic arrays. *IEEE Trans. Antennas Propagat.*, 50:1050–1064, August 2002.
- [84] R. A. Shore and A. D. Yaghjian. Scattering-matrix analysis of linear periodic arrays of short electric dipoles. Technical Report AFRL-SN-HS-TR-2004-045, Air Force Research Laboratory In-House Report, 2004.
- [85] J. Hansen. *Spherical Near-field Antenna Measurements*. Electromagnetic Waves 26. IEE, 1988.
- [86] R. L. Lewis. Spherical-wave source-scattering analysis of coupled antennas; a general system two-port solution. *IEEE Trans. Antennas Propagat.*, 35(12):1375–1380, Dec 1987.
- [87] B. Brock. Using vector spherical harmonics to compute antenna mutual impedance from measured or computed fields. Sandia report SAND2000-2217-Revised, Sandia National Laboratories, 2001.
- [88] W. C. Chew. An n^2 algorithm for the multiple scattering solution of n scatterers. *Microwave and Optical Technology Letters*, 2(11):380–383, 1989.
- [89] K.-H. Ding L. Tsang, J. A. Kong. *Scattering of Electromagnetic Waves: Theories and Applications*. Wiley, 2000.

- [90] A.R. Edmonds. *Angular Momentum in Quantum Mechanics*. Princeton University Press, 1957.
- [91] S. Stein. Addition theorems for spherical wave functions. *Quart. Appl. Math.*, 19:15–24, 1961.
- [92] J. C.-E. Sten T. J. Dufva, J. Sarvas. Unified derivation of the translational addition theorems for the spherical scalar and vector wave functions. *Progress in Electromagnetic Resesarch*, 4:79–99, 2008.
- [93] B. Peterson and S. Strom. T-matrix for electromagnetic scattering from an arbitrary number of scatterers. *J. Acoust. Soc. Am.*, 50:771–80, 1974.
- [94] V. A. Babenkoc N. G. Khlebtsovd T. Wriedte M. I. Mishchenkoa, G. Videenb. T-matrix theory of electromagnetic scattering by particles and its applications: a comprehensive reference database. *J. Quantitative Spectroscopy and Radiative Transfer*, 88:357 – 406, 2004.
- [95] A. Abubakar R. F. Bloemenkap and P. M. van den Berg. Inversion of experimental multi-frequency data using the contrast source inversion method. *Inverse Problems*, 17:1611–1622, 2001.
- [96] M. G. Cote P. M van den Berg and R. E. Kleinman. Blind shape reconstruction from experimental data. *IEEE Trans. Antennas Propagat.*, 43(12):1389–1396, 1995.
- [97] J. Stang E. Bresslour R. T. George G. A. Ybarra W. T. Joines C. Yu, M. Yuan and Q. H. Liu. Active microwave imaging ii: 3-d system prototype and image reconstruction from experimental data. *IEEE Trans. Microwave Theory and Techniques*, 56(4):991–1000, April 2008.
- [98] F. Pezin P. Sabouroux K. Belkebir, S. Bonnard and M. Saillard. Validation of 2d inverse scattering algorithms from multi-frequency experimental data. *J. Electromagnetic Waves and Applications*, 14:1637–1667, 2000.
- [99] J. J. van Zyl. Calibration of polarimetric radar images using only image parameters and trihedral corner reflector responses. *IEEE Trans. Geosci. Remote Sensing*, 28(3):337–348, May 1990.
- [100] P. Polatin M. W. Whitt, F. T. Ulaby and V. V. Liepa. A general polarimetric radar calibration technique. *IEEE Trans., Antennas Propagat.*, 39(1):62–67, 1991.
- [101] P. Sabouroux P. C. Chaumet H. Tortel H. Giovannini C. Eyraud, J. Geffrin and A Litman. Validation of a 3d bistatic microwave scattering measurement setup. *Radio Science*, 43(RS4018):1–12, 2008.

- [102] M. Yuan C. Yu and Q. H. Liu. Reconstruction of 3d objects from multi-frequency experimental data with a fast dbim-bcgs method. *Inverse Problems*, 25, 2009.
- [103] Chen-To Tai. *Dyadic Green's Functions in Electromagnetic Theory*. IEEE Press, 1994.
- [104] J. Song and W. C. Chew. Error analysis for the truncation of multipole expansion of vector green's functions. *IEEE Microwave and Wireless Components Letters*, 11(7):311–313, July 2001.
- [105] M. Haynes and M. Moghaddam. Multipole and s-parameter antenna and propagation model. *IEEE Trans. Antennas Propagat.*, 59(1):225–235, Jan 2011.
- [106] H. Gan and W. C. Chew. A discrete bcg-fft algorithm for solving 3d inhomogeneous scatterer problems. *Journal of Electromagnetic Waves and Applications*, 9(10):1339–1357, 1995.
- [107] Z. Q. Zhang and Q. H. Liu. Three-dimensional weak-form conjugate- and biconjugate-gradient fft methods for volume integral equations. *Microwave and Optical Technology Letters*, 29(5):350–356, June 2001.
- [108] P. Zwamborn and P. M. van den Berg. The three-dimensional weak form of the conjugate gradient fft method for solving scattering problems. *IEEE Trans. Microwave Theory and Techniques*, 40(9):1757–1766, Sept 1992.
- [109] D. Sullivan. *Electromagnetic Simulation Using the FDTD Method*. Wiley-IEEE Press, 2000.
- [110] D. M. Pozar. *Microwave Engineering*. Addison Wesley, 1990.
- [111] M. Kisliuk. The dyadic green's functions for cylindrical waveguides and cavities. *IEEE Trans. Microwave Theory and Techniques*, 28(8):894–898, Aug 1980.
- [112] R. Haberman. *Applied Partial Differential Equations*. Pearson Prentice Hall, 4th edition, 2004.
- [113] J. D. Jackson. *Classical Electrodynamics*. Wiley, 3rd edition, 1999.
- [114] J. W. Brown and R. V. Churchill. *Complex Variables and Applications*. McGraw-Hill, 2004.
- [115] W. C. Chew M. Moghaddam. Study of some practical issues in inversion with the born iterative method using time-domain data. *IEEE Trans. Antennas and Propagation*, 41(2):177–184, Feb 1993.
- [116] W. C. Chew G.P. Otto. Microwave inverse scattering - local shape function imaging for improved resolution of strong scatterers. *IEEE Trans. Microwave Theory and Techniques*, 42(1):137–141, Jan 1994.

- [117] J.P. Hugonin N. Joachimowicz, C. Pichot. Inverse scattering: an iterative numerical method for electromagnetic imaging. *IEEE Trans. Antennas and Propagation*, 39(12):1742–1753, Dec 1991.
- [118] C. Pichot R. Ferraye, J.-Y. Dauvignac. An inverse scattering method based on contour deformations by means of a level set method using frequency hopping technique. *IEEE Trans. Antennas and Propagation*, 51(5):1100– 1113, May 2003. pichot2.
- [119] A. Massa M. Pastorino, S. Caorsi. A global optimization technique for microwave nondestructive evaluation. *IEEE Trans. Instrumentation and Measurement*, 51(4):666– 673, Aug 2002.
- [120] P. Sabouroux J. M. Geffrin. Continuing with the fresnel database: experimental setup and improvements in 3d scattering measurements. *Inverse Problems*, 25:1–18, 2009.
- [121] C. Eyraud J.-M. Geffrin, P. Sabouroux. Free space experimental scattering database continuation: experimental set-up and measurement precision. *Inverse Problems*, 21:117–130, 2005.
- [122] W. C. Chew J.-H. Lin. Ultrasonic imaging by local shape function method with cgfft. *IEEE Trans. Ultrasonics, Ferroelectrics, and Frequency Control*, 43(5), 1996.
- [123] B.-K. Chung B.-K. Ang. A wideband e-shaped microstrip patch antenna for 5-6 ghz wireless communications. *Progress in Electromagnetics Research*, 75:397407, 2007.
- [124] M. Moghaddam M. Haynes. Large-domain, low-contrast acoustic inverse scattering for ultrasound breast imaging. *IEEE Trans. Biomedical Engineering*, 57(11):2712–2722, Nov 2010.
- [125] P. M. Van Den Berg A. Abubaker. Total variation as a multiplicative constraint for solving inverse problems. *IEEE Trans. on Image Processing*, 10(9):1384–1392, 2001.
- [126] P. Meincke K. D. Paulsen T. Rubk, P. M. Meaney. Nonlinear microwave imaging for breast-cancer screening using gaussnewton’s method and the cgl inversion algorithm. *IEEE Trans. Antennas and Propagation*, 55(8):2320–2331, 2007.
- [127] A. Zakaria M. Ostadrahimi C. Kaye S. Noghalian L. Shafai S. Pistorius J. LoVetri C. Gilmore, P. Mojabi. A wideband microwave tomography system with a novel frequency selection procedure. *IEEE Trans, Biomedical Engineering*, 57(4):894–904, April 2010.

- [128] Q.H. Liu G.A. Ybarra R.T. George M. Yuan J. Stang, W.T. Joines and I. Leonhardt. A tapered microstrip patch antenna array for use in breast cancer screening. In *Proc. IEEE Antennas and Propagation Society Int. Symp. AP-S*, June 2009.
- [129] C. Gilmore A. Zakaria S. Noghianian S. Pistorius M. Ostadrahimi, P. Mojabi and J. LoVetri. Analysis of incident field modeling and incident/scattered field calibration techniques in microwave tomography. *IEEE Antennas and Wireless Propagation Letters*, 10:900–903, 2011.
- [130] S. C. Hagness N. Behdad S. M. Aguilar, M. A. Al-Joumayly. Design of a miniaturized dual-band patch antenna as an array element for microwave breast imaging. In *IEEE Antennas and Propagation Society International Symposium (APSURSI)*, July 2010.
- [131] D. Baumann-I. J. Craddock M. Klemm, C. Fumeaux. Time-domain simulations of a 31-antenna array for breast cancer imaging. In *IEEE International Symposium Antennas and Propagation (APSURSI)*, pages 710–713, July 2011.
- [132] P. M. Meaney G. Vecchi E. A. Attardo, A Borsic. Finite element modeling for microwave tomography. In *IEEE International Symposium Antennas and Propagation (APSURSI)*, pages 703–706, July 2011.
- [133] M. Moghaddam M. Haynes, S. Clarkson. Electromagnetic inverse scattering algorithm and experiment using absolute source characterization. *IEEE Trans. Antennas and Propagation*, in press.
- [134] Q. H. Liu X. Millard. A fast volume integral equation solver for electromagnetic scattering from large inhomogeneous objects in planarly layered media. *IEEE Trans. Antennas and Propagation*, 51(9):2393– 2401, Sep 2003.
- [135] D. C. Rebenaque J. P. Garcia A. A. Melcon F. D. Q. Pereira, P. C. Castejon. Numerical evaluation of the green’s functions for cylindrical enclosures by a new spatial images method. *IEEE Trans. Microwave Theory and Techniques*, 53(1):94–105, Jan 2005.
- [136] M. W. Fanning D. Li P. M. Meaney, S. A. Pendergrass and K. D. Paulsen. Importance of using a reduced contrast coupling medium in 2d microwave breast imaging. *J. of Electromagn. Waves and Appl.*, 17:333–355, 2003.
- [137] C. Ward M. Fabiilli M. Haynes P. Carson M. Moghaddam J. Stang, L. van Nieuwstadt. Customizable liquid matching media for clinical microwave breast imaging. *Physics in Medicine and Biology*, in preparation (planned submission date: 11/15/2011).
- [138] J. Stang and W. T. Joines. Tapered microstrip patch antenna array for microwave breast imaging. In *IEEE MTT-S International Microwave Symposium*, June 2008.

- [139] J. Stang. *A 3D active microwave imaging system for breast cancer screening*. PhD thesis, Dept. Elect. and Comp. Eng., Duke Univ, Durham NC, 2008.
- [140] J.A. Jensen and N. B. Svendsen. Calculation of pressure fields from arbitrarily shaped, apodized, and excited ultrasound transducers. *IEEE Trans. Ultrason., Ferroelec., Freq. Contr.*, 39:262–267, 1992.
- [141] Amin Nikoozadeh Goksen G. Yaralioglu, Baris Bayram and Butrus T. P. Khuri-Yakub. Finite element modeling of capacitive micromachined ultrasonic transducers. In *Proc. SPIE 5750*, volume 77, 2005.
- [142] N. Bilaniuk and G. S. K. Wong. Speed of sound in pure water as a function of temperature. *J. Acoust. Soc. Am.*, 93(3):1609–1612, 1993.
- [143] W. C. Chew. Recurrence relations for three-dimensional scalar addition theorem. *J. Electromeg. Waves Appl.*, 6(2):133–142, 1992.
- [144] W. C. Chew and Y. M. Wang. Efficient ways to compute the vector addition theorem. *J. Electromagnetic Waves and Applications*, 7(5):651–665, 1993.
- [145] M. S. Gordon C. H. Choi, J. Ivanic and K. Ruedenberg. Rapid and stable determination of rotation matrices between spherical harmonics by direct recursion. *J. Chemical Physics*, 111(19):8825–8831, 1999.